START-TO-END SIMULATIONS OF HYBRID LASER- AND BEAM-DRIVEN PLASMA WAKEFIELD ACCELERATION AND FREE ELECTRON LASERS

Dissertation

Zur Erlangung des Doktorgrades
an der Fakultät für Mathematik, Informatik und Naturwissenschaften
des Fachbereichs für Physik
der Universität Hamburg

Vorgelegt von

Georg Wittig

Hamburg

2017

Nur wenige wissen, wie viel man wissen muss, um zu wissen, wie wenig man weiß.

— Werner von Heisenberg

Plasma physics is usually not a precise science. It is rather a web of overlapping points of view, each modeling a limited range of behavior. Understanding of plasmas is developed by studying these various points of view, all the while keeping in mind the linkages between the points of view.

— Paul M. Bellan. Fundamentals of Plasma Physics

Dedicated to my loving wife, Nelli
and my children, Levon
and Albert Theodor.

ABSTRACT

Plasma wakefield acceleration has experienced a rapidly growing interest and raised high expectations to become the next generation of particle accelerators with high energies, producing possibly better quality beams at an affordable cost. To approach these far-reaching goals, this work investigates the—in the opinion of the author—best implementations of plasma wakefield acceleration.

Therefore, the physical requirements to drive a particle-beam-driven plasma wakefield accelerator (PWFA), which can provide very high-quality electron bunches, with a laser-driven plasma wakefield accelerator (LWFA), will be investigated in detail for the first time. This hybrid plasma wakefield accelerator can avoid the necessity of an expensive, large-scale particle accelerator to generate a suitable PWFA drive beam, by generating the drive-beam with a much cheaper high-power laser in a LWFA. The high-quality electron bunches are generated by the underdense plasma photocathode injection (Trojan Horse) technique in PWFA, which was recently demonstrated experimentally.

In addition, a novel injection technique, which was recently published by the author and others, will be discussed. With this technique, shortly after the publication appeared, it was possible to not only successfully inject charge into a PWFA, but to provide the crucial synchronization in the proof-of-principle experiment that demonstrated the Trojan Horse injection.

Finally, the high-quality bunch from the hybrid plasma wakefield accelerator is further processed and utilized as the driver for a free-electron laser (FEL), to demonstrate the application of the generated electron bunch. In this thesis, the hybrid LWFA-PWFA stage, a subsequent electron-bunch transport line, and the FEL will be described mathematically and accurately modeled by three-dimensional simulations.

ZUSAMMENFASSUNG

Die Beschleunigung von Elektronen in Plasmawellen erfuhr ein sehr schnell steigendes Interesse und schürte große Erwartungen, die nächste Generation von Teilchenbeschleunigern mit hoher Energie, möglicherweise höherer Qualität und sogar geringeren Kosten werden zu können. Um sich diesen weitreichenden Zielen zu nähern, erforscht die vorliegende Arbeit die—aus der Sicht des Autors—besten Konzepte der Plasmawellenbeschleunigung und deren Kombination.

Hierfür werden die physikalischen Voraussetzungen zum Treiben von einem Teilchenstrahl getriebenen Plasmawellenbeschleuniger (PWFA), welcher qualitativ sehr hochwertige Elektronenpakete bieten kann, durch einem Laser getriebenen Plasmawellenbeschleuniger (LWFA) zum ersten Mal im Detail untersucht. Dieser hybride Plasmawellenbeschleuniger kann dabei umgehen, dass ein großer, kostenintensiver konventioneller Teilchenbeschleuniger benötigt wird, um einen geeigneten Treiber für den PWFA zu erzeugen, dadurch, dass dieser Treiber mit einem besser verfügbaren Hochenergie-Laser in einem LWFA erzeugt wird. Die qualitativ hochwertigen Elektronenpakete können dann in dem PWFA durch die Plasma-Photokathode Injektion (Trojan Horse) erzeugt werden, die vor kurzem experimentell bestätigt wurde.

Zusätzlich wird eine neue Injektionstechnik diskutiert, welche von dem Autor und anderen publiziert wurde. Mit dieser Methode gelang es nicht nur kurz nach der Publikation erfolgreich Elektronen in einen PWFA zu injizieren, sondern auch die anspruchsvolle Synchronisation zur Verfügung zu stellen, welche ausschlaggebend zum Erfolg des ersten Trojan Horse Experiments beitragen konnte.

Zuletzt wird das in dem hybriden Plasmawellenbeschleuniger erzeugte qualitativ hochwertige Elektronenpaket dazu verwendet, einen freien Elektronen Laser (FEL) zu treiben, um die Leistungsfähigkeit des erzeugten Elektronenpakets zu demonstrieren. In dieser Arbeit werden die hybride LWFA-PWFA Stufe, eine anschließende Elektronenpaket-Transportstrecke und der FEL mathematisch beschrieben, in dreidimensionalen Computersimulationen genau modelliert und abschließend visualisiert und analysiert.

ACRONYMS

PIC   Particle-In-Cell

Ti:Sa   Titanium Sapphire

RF   radio-frequency [212]

CERN   Conseil Europen pour la Recherche Nucléaire https://home.cern/about

PWFA   particle-beam-driven plasma wakefield acceleration [38]

LWFA   laser-pulse-driven plasma wakefield acceleration [49]

SLAC   Stanford Linear Accelerator Center

FACET   Facility for Advanced Accelerator Experimental Tests, at SLAC [99]

FEL   free-electron laser [126]

SASE   self-amplified spontaneous emission

BSI   barrier suppression ionization [13]

ADK   Ammosov-Delone-Krainov [5]

MPI   multi-photon ionization

rms   root mean square, i.e. $x_{rms} = \sqrt{\langle x^2 \rangle}$, is equal to the standard deviation for a centered mean value $\langle x \rangle = 0$

FWHM   full-width half-maximum

LIT   low ionization threshold

HIT   high ionization threshold

TH   Trojan Horse, or underdense plasma-photocathode injection [93]

VSim   multi-physics cross-platform computational simulation framework [169]

ELEGANT   ELEctron Generation ANd Tracking [25]

FDTD   finite-difference time-domain

GENESIS   fully time-dependent three-dimensional FEL code [186]

PMQ   permanent magnet quadrupole

EMQ   electromagnet quadrupole

FODO   focusing drift defocusing drift

CONVENTIONS

- All vectors will be expressed as bold **r**. Their components are r_x, r_y and r_z.

- z denotes the direction of propagation.

- SI units will be used unless otherwise stated.

- The conventions $\frac{\partial x}{\partial z} \equiv x'$ and $\frac{\partial x}{\partial t} \equiv \dot{x}$ are used.

- The $=$ sign is used if the value is exact,
  the $\approx$ sign is used if the value is rounded at the last digit, while
  the $\sim$ sign is used if the value cannot be given more precisely or is an estimate.

- In the nonlinear plasma wakefield regime, the first plasma-wave cavity is nearly electron-free and therefore often referred to as the "blowout"[109, 193] in the context of particle-beam-driven plasma wakefield acceleration [38] (PWFA), and as the "bubble" in the context of laser-pulse-driven plasma wakefield acceleration [49] (LWFA) [185].

- A *bunch* denotes a compact, approximately spherical bundle of electrons, e.g. the accelerating high-quality witness bunch. To avoid confusion the driver of the wakefield is named the drive *beam*.

- The accelerating bunch is often referred to as witness bunch within the literature and throughout this thesis.

- The root mean square, i.e. $x_{rms} = \sqrt{\langle x^2 \rangle}$, is equal to the standard deviation for a centered mean value $\langle x \rangle = 0$ (rms), is often used as a synonym for the standard deviation in beam and plasma physics [67], see chapter C.

- The indices b:particle beam, l:laser, p:plasma are used.

CONTENTS

Part I

PHYSICS OF HYBRID PLASMA WAKEFIELD ACCELERATION AND FREE-ELECTRON LASERS

1. MATHEMATICAL DESCRIPTION OF PLASMAS After an introduction to particle accelerators, the theoretical and mathematical background will be given to describe charged, many-particle systems and their interaction with electromagnetic fields. Plasmas will be characterized, the properties of plasma waves will be given and relevant interaction processes will be discussed.

2. EMPLOYING PLASMA WAVES AS PARTICLE ACCELERATORS The utilization of plasma wakefield accelerators will be motivated, and the two major methods to drive plasma waves will be discussed. For both methods, techniques will be presented to inject electron bunches into the wakefield and to sustain the acceleration. Special attention will be paid to the possibility to couple both methods and to generate high-quality bunches using the underdense plasma photocathode scheme.

3. OPTICAL PLASMA-TORCH INJECTION Special emphasis will be given to a novel injection technique in electron-beam-driven plasma wakefield acceleration that was first proposed by the author and shortly thereafter experimentally verified at the Stanford Linear Accelerator Center.

4. THEORY OF FREE-ELECTRON LASERS The basic concepts of a free-electron laser will be elaborated. Effectively driving a short-wavelength, coherent light source with a high-quality electron bunch from a plasma wakefield accelerator will be discussed, starting from self-amplified spontaneous emission.

5. COMPUTATIONAL METHODS The methods of the particle-in-cell algorithm, and the basic physical model used in this thesis will be provided.

MATHEMATICAL DESCRIPTION OF PLASMA

Within this work, plasmas will be employed to accelerate particles. Therefore, particle accelerators will be introduced first, followed by the theoretical description of charged particles and electromagnetic fields, including the description of charged particle beams and Gaussian laser pulses. Then, the characterization of plasmas by fundamental plasma parameters will be given. Based on these parameters and a given density and temperature, the most important physical properties can be inferred. This is of high importance to allow efficient computation of these versatile, highly complexly interacting systems

A plasma is a common state of matter that is composed of unbound positively and negatively charged particles.

1.1 ON THE IMPORTANCE OF PARTICLE ACCELERATORS

The use of different types of probe beams has enabled scientists to resolve the structure of matter in more and more detail. Beginning from the visible range of electromagnetic radiation towards smaller wavelengths, and therefore higher energies, the probing of matter has revealed the structure of minerals, biological samples, and the physical behavior of molecules and atoms in current experiments. Besides the temporal and spatial resolution of matter, the interaction and decay of particles has been intensively studied in the past, using particle accelerators to uncover particles produced by high-energy collisions, thanks to the energy-mass equivalence. Because radiation with extremely short wavelengths can be emitted by charged particles with high energy, both applications—particle colliders for the investigation of new particles, and short-wavelength radiation for imaging—were enabled by the development and advance of particle accelerators.

The simplest method of particle acceleration is to generate voltage by separating charges with opposite signs e. g. in a cathode-anode setup, so that electrons emitted by the cathode are attracted and accelerated to the anode. The normal unit of energy, eV, is defined by the simple picture of the energy that a single electron gains by being accelerated by a potential difference of 1 Volt. The unit of the strength of the accelerating field, V/m, is the distance in meters at which an electron reaches one eV of energy.

The long development of accelerators has led to the modern radio-frequency [212] (RF) accelerator structure, in which an electromagnetic wave propagating within conducting cavities is used to accelerate charged particles. As the electromagnetic wave in the accelerator propagates with the speed of light, electrons must be pre-accelerated to a relativistic energy before they can co-propagate with the wave and become fur-

ther accelerated. The frequencies that are used correspond to wavelengths from $30\,\text{cm}$ down to $2.73\,\text{mm}$. Therefore, the sinusoidal accelerating field is nearly constant over the length of a typical bunch on the sub-millimeter scale, and all electrons experience nearly the same accelerating force. This results in a small variance of the energy amongst electrons within the bunch, a very important feature, as will be seen later in this work. By going to smaller wavelengths in the accelerator—as in the case of the plasma wakefield accelerator—a typical electron bunch will experience an increasing difference in the accelerating field between its front and its rear.

The fundamental parts of modern particle accelerators, the RF-cavities, are aligned in linear groups in the case of TESLA consisting of 9 cavities, which are assembled in either linear or circular geometry. A circular accelerator has the advantage that particles can be accelerated by the the same components again and again in many cycles. However, the magnetic field strength, B, that is required to bend the trajectory of a relativistic electron to a radius, R, is $R = E/(ecB)$, and the magnetic field has a technical limit of about $B \sim 1.5\,\text{T}$ for conventional magnets [239], and up to $B \sim 8\,\text{T}$ for super conducting magnets as in the Large Hadron Collider (LHC). The electric breakdown at the

L-band
(30 − 15 cm),
S-band
(15 − 7.5 cm),
X-band
(3.75 − 2.5 cm),
V-band
(7.5 − 4 mm),
and W-band
(4 − 2.73 mm).
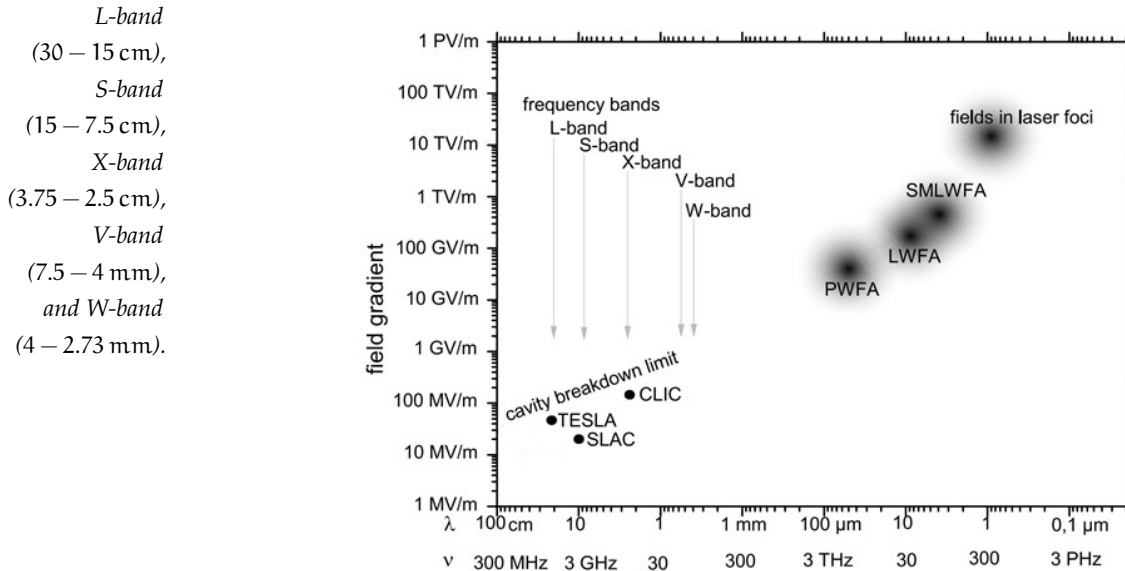
Figure 1: Accelerating gradients of different accelerators against the applied wavelength, λ, and frequency, ν (SMLWFA is a shortcut for self-modulated LWFA [61, 122], and applies a high-power laser that is longer than the plasma wavelength in the self-guided regime). Image adapted from [90].

cavity walls (Kilpatrick limit [114]) limits the maximum operating voltage and thereby the maximum energy gain within one accelerating RF-cavity. This makes the length of linear particle accelerators grow proportional to the desired energy. For higher frequencies (as at the planned Compact Linear Collider (CLIC) [1]), the maximum voltage can be increased before breakdown, as the time at peak field strength is shortened in the accelerator (see figure 1). However, at higher frequencies the surface resistance of the cavity walls also rapidly increases, resulting in a rapidly increasing energy loss. This

effectively limits the maximum attainable field strength to about $100\,\mathrm{MV/m}$ in current RF-accelerators.

Besides the maximum applicable accelerating field strength, a second important issue is the energy that charged particles emit in form of synchrotron radiation when being accelerated. The emitted power from a relativistic particle with charge q and rest mass m_0, that is transversely accelerated is given by

$$P_{syn} = \frac{q^2 c}{6\pi\epsilon_0} \frac{1}{(m_0 c^2)^4} \frac{W^4}{R^2}, \tag{1}$$

which is a function of its energy, W, and the radius of its trajectory, R. Note, particles emit synchrotron radiation also in the forward direction when being longitudinally accelerated, $P_{syn,\parallel} \propto (dW/dz)^2$, but fortunately this effect is negligible for all reasonable accelerating gradients. More importantly, the synchrotron power (1) scales with $1/m_0^4$ and as a result, light particles loose much more energy than heavy particles when forced onto a curved trajectory. Like the power, the energy loss from synchrotron radiation scales with the fourth power of the particle energy, $\Delta W_{syn} = \frac{q^2}{3\epsilon_0(m_0 c^2)^4} \frac{W^4}{R} \propto W^4$. Consequently, it is far more efficient to accelerate electrons in a linear accelerator, although this looses the gain from repeated acceleration on each circuit of the ring. Heavy particles, such as protons, can be accelerated in circular accelerators, such as the currently largest accelerator at the Conseil Europen pour la Recherche Nucléaire https://home.cern/about (CERN) without large losses of energy due to synchrotron radiation.

In a synchrotron, electrons are accelerated in a circle and the strength of the magnetic field that forces the electrons onto a trajectory with constant radius must be synchronized to the energy of the electrons, as dictated by $R = E/(ecB)$.

1.2 MATHEMATICAL DESCRIPTION OF CHARGED PARTICLES AND ELECTROMAGNETIC FIELDS

In plasma wakefield acceleration, an intense driver (particle-beam driver: PWFA, or laser-pulse driver: LWFA) creates a very strong electromagnetic wave by separating charged particles in a plasma wave. For the description of these highly complex systems, a summary of the theoretical foundations of electromagnetic waves and the theory of interacting many-particle systems will be given in the following. Beginning with the precise description of the evolution of electromagnetic fields in vacuum and the behavior of single charged particles in such fields, the formalism will be extended to the fundamental description of many interacting particles, particle bunches and lasers. Thereafter, the microscopic picture of a plasma will be considered. By averaging over the single-particle variables, a macroscopic description can be derived. Because plasmas behave very differently depending on their temperature and density, the classification of plasmas will be discussed. Finally, this theory will be applied to restrict the physical regime to the part that is relevant for this work.

1.2.1 Maxwell's equations

The dynamics of electric and magnetic fields are inseparably coupled by Maxwell's equations

$$\nabla \cdot \mathbf{E} = \frac{\rho}{\epsilon_0} \qquad\qquad \text{(Gauss's law)} \tag{2}$$

$$\nabla \cdot \mathbf{B} = 0 \qquad\qquad \text{(Gauss's law for magnetism)} \tag{3}$$

$$\nabla \times \mathbf{E} = -\frac{\partial \mathbf{B}}{\partial t} \qquad\qquad \text{(Faraday's law)} \tag{4}$$

$$\nabla \times \mathbf{B} = \mu_0 \left(\mathbf{j} + \epsilon_0 \frac{\partial \mathbf{E}}{\partial t} \right) \qquad \text{(Ampère's law),} \tag{5}$$

where $c^2 = 1/\epsilon_0 \mu_0$ is the speed of light in vacuum, ϵ_0 and μ_0 are the electric permittivity and magnetic permittivity in vacuum, respectively and henceforth throughout this thesis. This set of coupled, first-order, partial-differential equations includes all information on sources and curls of electromagnetic fields in vacuum. Gauss's law (2) identifies the charge density, ρ, as the source of the electric field, and Faraday's law (4) describes how a change in magnetic field, $\frac{\partial \mathbf{B}}{\partial t}$, with time causes a curl in the electric field. The absence of magnetic mono poles is expressed in the second equation (3), stating that the magnetic field is always source-free. Ampère's law (5) expresses that curls of the magnetic field can only be generated by the current density $\mathbf{j}$ and the change with time of the electric field, $\frac{\partial \mathbf{E}}{\partial t}$. This set of equations is invariant when introducing a scalar, Φ, and a vector potential, $\mathbf{A}$, which are defined by

$$\mathbf{E} = -\frac{\partial}{\partial t}\mathbf{A} - \nabla \Phi, \qquad\qquad \mathbf{B} = \nabla \times \mathbf{A}. \tag{6}$$

Putting these definitions into Maxwell's equations, the wave equations for the new potentials

$$\left[\nabla^2 - \frac{1}{c^2} \left(\frac{\partial^2}{\partial t^2} \right) \right] \begin{bmatrix} \mathbf{A} \\ \Phi \end{bmatrix} = - \begin{bmatrix} \mathbf{j}\mu_0 \\ \rho/\epsilon_0 \end{bmatrix}, \tag{7}$$

can be derived using the Lorenz gauge $\nabla \mathbf{A} + (1/c)\partial_t \Phi = 0$. The current density, $\mathbf{j}$, and the charge density, ρ, are determined by the locations and the velocities of all charged particles within the system.

Solving equation (7) in the absence of any charge and current ($\rho = \mathbf{j} = 0$), results in the plane wave

$$\begin{aligned} \mathbf{E}(\mathbf{z}, t) &= \mathbf{E_o}\sin\left(\omega t - \mathbf{kz} + \phi\right) \\ \mathbf{B}(\mathbf{z}, t) &= \mathbf{B_o}\sin\left(\omega t - \mathbf{kz} + \phi\right) \end{aligned} \tag{8}$$

with $\mathbf{B_o}$, and $|\mathbf{E_o}| = c\,|\mathbf{B_o}|$ being the wave amplitudes, ω denoting the angular frequency, $\mathbf{k}$ the wave vector, and ϕ a phase of the wave that propagates in the $\mathbf{z}$ direction. It

follows from equation (7), and (8) that $\mathbf{E} \perp \mathbf{B} \perp \mathbf{k}$, and that the *dispersion relation* for light in vacuum reads

$$|\mathbf{k}| = \frac{\omega}{c}. \tag{9}$$

Inserting the definition of the potentials, introduced in equation (6), into equation (2) and applying the Coulomb gauge, $\nabla \mathbf{A} = 0$, gives the *Poisson equation*

$$\nabla^2 \Phi = -\frac{\rho}{\epsilon_0}, \tag{10}$$

which gives the scalar potential, Φ, for a given charge distribution, ρ.

1.2.2 *Electromagnetic fields and forces on charged particles*

Electromagnetic fields exert forces on charged particles, while charged particles themselves generate electromagnetic fields. The electric field originating from a charge distribution, ρ, can be derived from Gauss's law (2)

$$\mathbf{E}(\mathbf{r}) = \frac{1}{4\pi\epsilon_0} \int \rho(\mathbf{r}') \frac{(\mathbf{r} - \mathbf{r}')}{|\mathbf{r} - \mathbf{r}'|^3} d\mathbf{r}', \tag{11}$$

and is also referred to as *Coulomb's law*. Equation (11) simplifies to the well known form $\mathbf{E}(\mathbf{r}) = q/(4\pi\epsilon_0)(\mathbf{r}/r^2)$ in case of a point-charge q, and the resulting static electric force on another charged particle is given by $\mathbf{F}(\mathbf{r}) = q\mathbf{E}(\mathbf{r})$. Similarly, the magnetic field is generated by a current density according to *Biot-Savart's law*

$$\mathbf{B}(\mathbf{r}) = \frac{\mu_0}{4\pi} \int_V \mathbf{j}(\mathbf{r}') \times \frac{(\mathbf{r} - \mathbf{r}')}{|\mathbf{r} - \mathbf{r}'|^3} dV', \tag{12}$$

and can be derived from equation (5), where dV is a volume element. The force induced by a magnetic field that acts on a charged particle is given by $\mathbf{F}(\mathbf{r}) = q\mathbf{v} \times \mathbf{B}$ and always acts perpendicularly to the direction of propagation. The combined force

$$\mathbf{F}(\mathbf{r}) = q\left(\mathbf{E} + \mathbf{v} \times \mathbf{B}\right) \tag{13}$$

is called the *Lorentz force*.

1.2.3 *Propagation of a Gaussian laser pulse in vacuum*

Thanks to Planck [179] and Einstein [58], we know that all electromagnetic waves (including light) can only occur in quantized (discrete) portions called *photons*, which carry energy $E_{ph} = \hbar\omega$ and momentum $\mathbf{p}_{ph} = \hbar\mathbf{k}$ ($\hbar$ is the Planck constant). The generation of a pulse of coherent photons was achieved in the past century by the development of lasers and has enabled numerous applications in technology and science.

In vacuum, a focused Gaussian laser pulse that propagates in the z direction undergoes a spot radius evolution according to

$$w(z) = w_0 \sqrt{1 + \frac{z^2}{z_R^2}} \tag{14}$$

where w_0 denotes the spot radius at focus, and

$$z_R = \frac{\pi w_0^2}{\lambda_l} \tag{15}$$

is known as the *Rayleigh length*—the distance over which the spot radius increases by $\sqrt{2}$. In equation (6), the electrostatic scalar and vector potentials have been introduced; here it is convenient to use the normalized potentials $\phi = e\Phi/m_e c^2$ and $\mathbf{a} = e\mathbf{A}/m_e c^2$. The transverse electric field of a Gaussian laser pulse in paraxial approximation, that is polarized in the x direction, can be expressed as [218]

$$E_x(x, y, z, t) = \mathcal{E}_0 \frac{w_0}{w(z)} \exp\left(-\frac{x^2 + y^2}{w(z)^2}\right) \exp\left(-\frac{(z - ct)^2}{2\sigma_z^2}\right) \times$$
$$\cos\left(\omega_l t - k_l z - k_l \frac{r^2}{2R(z)} + \phi(z)\right) \hat{\mathbf{e}}_x \tag{16}$$

with ω_l, k_l, and $\mathcal{E}_0$ being the frequency, wave number and amplitude of the laser, respectively, σ_z the standard deviation of the pulse length, $w(z)$ the waist (14), $R(z) = z\left(1 + z_R^2/z^2\right)$ the wave-front curvature, and $\phi(z) = \arctan(z/z_R)$ the Gouy phase. The first line of equation (16) is considered as the *envelope* of the laser pulse comprising the slowly varying part, while the second line is the rapidly oscillating part including the phase of the laser. The motion that an electron undergoes in the rapidly oscillation
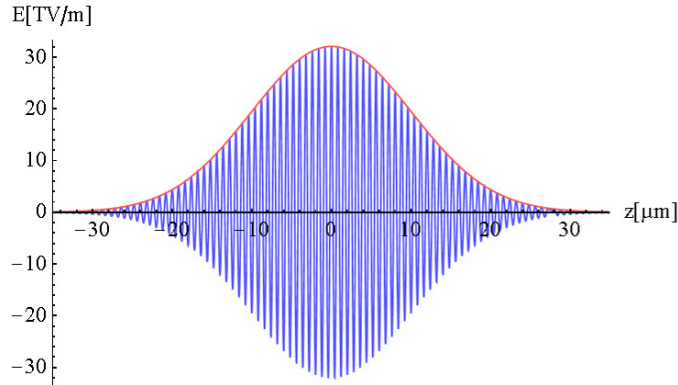

Figure 2: The laser electric field (blue) and envelope (red) from equation (16). The laser parameters are given in Table 11

field of a laser is called the *quiver motion* and its maximum velocity is given by

$$\mathbf{v}_q = \frac{e\mathcal{E}_0}{m_e \omega_l}. \tag{17}$$

The peak values of the characteristic parameters of a Gaussian laser are given by [77]

$$\mathcal{E}_0 = \mathcal{B}_0 c = a_0 \omega_l \frac{m_e c}{e} \quad \Leftrightarrow \quad a_0 = \frac{e\mathcal{E}_0}{\omega_l m_e c}, \tag{18}$$

$$\mathcal{I}_0 = \frac{\epsilon_0 c}{2}\mathcal{E}_0^2 = \frac{\epsilon_0 c}{2}a_0^2\omega_l^2\left(\frac{m_e c}{e}\right)^2 \tag{19}$$

$$\mathcal{P}_0 = \frac{\pi w_0^2 \mathcal{I}_0}{2} \tag{20}$$

$$W = \mathcal{P}_0 \sigma_t \sqrt{2\pi} \tag{21}$$

$\mathcal{E}_0[V/m]$ being the peak electric field strength, $\mathcal{I}_0[W/m^2]$ the peak intensity, $\mathcal{P}_0[W]$ the peak power, and $W[J]$ the total energy. For example, a modern Titanium Sapphire (Ti:Sa) laser with 0.2 J of energy (normalized intensity of $a_0 = 0.15$) and $\lambda = 800\,\text{nm}$ wavelength, focused to a spot size of $w_0 = 50\,\mu\text{m}$ and being compressed to $\tau = 100\,\text{fs}$ full-width half-maximum (FWHM) duration, has a peak intensity of $\mathcal{I}_0 \approx 4.8 \times 10^{16}\,\text{W/cm}^2$, and carries 8.1×10^{17} photons per pulse. This laser exerts a significant light pressure $P = \mathcal{I}_0/c \approx 16\,\text{Mbar}$, which exceeds even the pressure inside the core of the earth, which is $\approx 3.6\,\text{Mbar}$. Its field strength of $\mathcal{E}_0 \approx 6.0 \times 10^{11}\,\text{V/m}$ is almost twice the field strength that ties an electron to the core of a hydrogen atom of $\approx 3.14 \times 10^{11}\,\text{V/m}$. Indeed, present lasers of many orders of magnitude higher energy are in operation (see Table 9), where extreme pressures in excess of 400 Mbar are reached, together with up to $1 \times 10^{19}\,\text{W/cm}^2$ intensities at the focal point, and more than 100 TW power.

1.2.4 *Propagation of a relativistic electron beam*

From equation (11), it follows that a charge distribution that is considered as axially symmetric and infinitely long, $\rho(x, y, z) = \rho(r)$, produces an electric field

$$E_r(r) = \frac{1}{\epsilon_0 r}\int_0^r \rho(r')r'dr' \tag{22}$$

that, for symmetry reasons, has only a radial component $E_r(r)$. The beam current is given by $\mathbf{j}(x, y, z) = j(r)\mathbf{e}_z$, where $\mathbf{e}_z$ denotes the unit vector in the direction of propagation, z. Assuming a mono-energetic electron bunch with a uniform longitudinal velocity $\mathbf{v}_z = \beta_z c\mathbf{e}_z$ (with $\beta_z = v_z/c$), the radial dependence of the current is determined by the charge density $\mathbf{j}(r) = \rho(r)\beta_z c\mathbf{e}_z$. From equation (12), it follows that the azimuthal component of the magnetic field can be expressed as

$$B_\theta(r) = \frac{\mu_0 \beta_z c}{r}\int_0^r \rho(r')r'dr', \tag{23}$$

and therefore

$$\beta_z E_r(r) = cB_\theta(r). \tag{24}$$

Considering the *paraxial approximation*, where $\beta^2 = \beta_x^2 + \beta_y^2 + \beta_z^2 \approx \beta_z^2$, the Lorentz force, $F_r = e(E_r - \beta_z c B_\theta)$ (e denoting the elementary charge), is reduced to

$$F_r = eE_r(1 - \beta_z^2) = e\frac{E_r}{\gamma^2}, \tag{25}$$

where $\gamma^2 = 1/(1 - \beta^2)$ is the Lorentz factor. This is a very important finding, which shows that the focusing electric force and the defocusing magnetic force becomes equal for relativistic electron beams and that therefore the Lorentz force vanishes as $1/\gamma^2$. This has the effect that electron beams stay better focused, the higher their energy. Otherwise, particle accelerators would have to fight strongly diverging particle beams, increasing the cost and engineering requirements drastically. A magnetic field of $B = 1\,T$ exerts the same force on a relativistic electron beam as an electric field of $E \approx 3 \times 10^8\,V/m$. Because nowadays field strengths of $1\,T$ are fairly easy to generate, whereas an electric field of $0.8\,GV/m$ is far beyond technical limits, magnets are normally used to steer electron beams rather than electric fields. On the other hand, because the force that a magnetic field exerts on a charge, $\mathbf{F}(\mathbf{r}) = q\mathbf{v} \times \mathbf{B}$, always acts perpendicularly to its velocity, it cannot do work or transfer energy to the particle. Consequently, only electric fields can be employed to accelerate particles, whereas magnetic fields are best suited to steer particle beams.

In analogy to equation (14), the focusing that a relativistic, Gaussian electron beam undergoes can be described by

$$\sigma_r(z) = \sigma_{r0}\sqrt{1 + \frac{z^2}{\beta^{*2}}}, \tag{26}$$

with focal position at $z = 0$, a minimum spot size of σ_{r0}, and $\beta^* = \sigma_{r0}^2\gamma/\epsilon_n$ (ϵ_n is the emittance[1], the beam β-function that is analogous to the Rayleigh length, z_R.

The transverse charge-density distribution for a Gaussian bunch is

$$\rho_b(r) = \rho_{b,0}\exp\left(\frac{-r^2}{2\sigma_r^2}\right), \tag{27}$$

where the maximum charge density is given by

$$\rho_{b,0} = \frac{Q}{(2\pi)^{3/2}\sigma_z\sigma_r^2}, \tag{28}$$

including its total charge Q, and its transverse, σ_r, and longitudinal size, σ_z. The radial electric *space-charge field* follows from integration of equation (22)

$$E_r(r) = \frac{\rho_{b,0}\sigma_r^2}{\epsilon_0 r}\left(1 - \exp\left(\frac{-r^2}{2\sigma_r^2}\right)\right). \tag{29}$$

---

1 The emittance is defined in terms of the beam phase space by $\epsilon = \sqrt{\langle x^2 \rangle \langle x'^2 \rangle - \langle xx' \rangle^2}$, where x is a coordinate perpendicular to the direction of motion and x' is its rate of change in this direction, see section 2.3.1.

It vanishes at the bunch center, increases linearly inside the bunch until roughly σ_r, and falls like $1/r$ for large distances (see figure 3). Its maximum is located at $r \approx 1.5852\sigma_r$ (see figure 3) and has the value

$$\max(E_r) = E_r(1.5852\sigma_r) \approx 0.45\frac{\rho_{b,0}\sigma_r}{\epsilon_0} = 0.45\frac{I_p}{2\pi\epsilon_0\beta c\sigma_r}, \tag{30}$$

using the bunch peak current (35). These values are particularly important measures when it is required to estimate if the maximum fields of a bunch transcend a certain ionization threshold. The space-charge force connected with an electron beam causes plasma electrons to be pushed away from the drive-beam axis in PWFA and sets up the plasma wakefield.
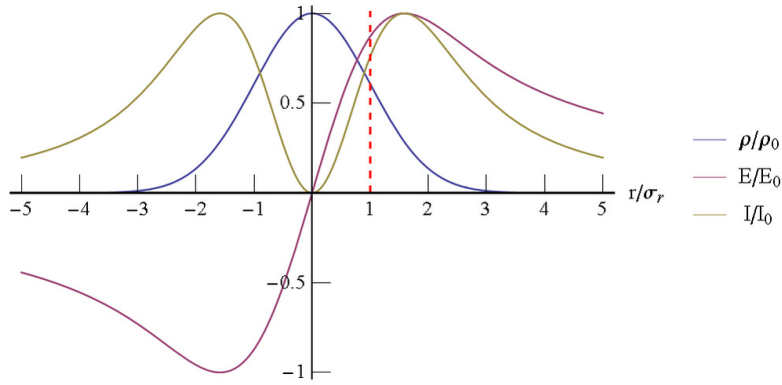
Figure 3: The charge distribution of a Gaussian bunch, equation (27), its transverse electric field, equation (29), and the corresponding intensity $I \propto E^2$ are displayed in normalized units.

When adding the forward direction with a Gaussian profile and its propagation in the z-direction, the temporal development in vacuum reads

$$\rho_b(z, r, t) = \rho_{b,0}(z)\exp\left(\frac{-r^2}{2\sigma_r(z)^2}\right)\exp\left(\frac{-(z-\beta ct)^2}{2\sigma_z^2}\right), \tag{31}$$

including the decrease of the peak density $\rho_{b,0}(z) = Q/((2\pi)^{3/2}\sigma_z\sigma_r(z)^2)$ along z, where $\sigma_r(z)$ is given in equation (26). The full expression for the transverse electric field strength in vacuum is

$$E_r(z, r, t) = \frac{Q}{(2\pi)^{3/2}\sigma_z\epsilon_0 r}\left(1 - \exp\left(\frac{-r^2}{2\sigma_r(z)^2}\right)\right) \times$$
$$\exp\left(\frac{-(z-\beta ct)^2}{2\sigma_z^2}\right). \tag{32}$$

The current of a charge distribution, ρ, traveling at speed $v_z = \beta_z c$, is determined by $I = \beta_z c\rho(z)$, where $\rho(z)[C/m] = \int_A \rho(x, y, z)dA$ is the total charge in perpendicular plane, A, at the position z. Integrating the charge distribution over this surface gives

This description is equivalent to the definition $I = dQ/dt$.

$$\int_A \rho(z, r, t)dA = 2\pi\int_0^\infty r\rho(z, r, t)dr = \frac{Q}{\sqrt{2\pi}\sigma_z}\exp\left(\frac{-(z-\beta_z ct)^2}{2\sigma_z^2}\right), \tag{33}$$

and therefore the current of the Gaussian bunch reads

$$I_b(z,t) = \beta_z c \frac{Q}{\sqrt{2\pi}\sigma_z} \exp\left(\frac{-(z-\beta_z ct)^2}{2\sigma_z^2}\right), \tag{34}$$

and the *peak current* is simply given by

$$\max(I_b) = \beta_z c \frac{Q}{\sqrt{2\pi}\sigma_z} \equiv I_p. \tag{35}$$

Note that the peak current does not depend on the transverse dimension of the bunch, $\sigma_r(z)$, but on the length of the bunch, σ_z, and the contained electrons Q, and therefore stays constant during transverse oscillations of the bunch. The transport of non-relativistic high-current beams is limited by the magnetic field generated, which acts back onto the current. The *Alfvén current* [3]

$$I_A = \frac{4\pi m_e c}{\mu_0 e} \approx 17\text{kA} \tag{36}$$

marks a soft limit for a non-relativistic beam of charged particles to be transportable.

1.3 PHYSICS OF PLASMAS

A plasma is one of the four fundamental phases of matter including solid, liquid, and gas. Most elements pass through these states when raising the temperature, where the plasma state is eventually reached at very high temperatures. However, the very low-density interstellar gas is also a plasma, since once atoms are ionized, the probability that they find another electron for recombination is extremely small. For very high densities, gases also begin to ionize when the energy level of the continuum becomes smaller than a bound state (Mott transition). All of this shows that a plasma is a very common state of matter, and in fact, more than 99% of observable matter is in this state. It is convenient to assume a plasma to be *quasi-neutral*, without loosing generality by equating the amount of positive and negative charges $n_e = Zn_i$, where n_e, n_i are the free electron, and ion density, respectively, and Z is the atomic number of the ions.

1.3.1 *Characteristics of plasmas*

For a comprehensive formulary see NRL PLASMA FORMULARY 2016 by J. D. Huba. A transition between two phases of matter only occurs when a certain threshold of density, n, or temperature, T, is exceeded; this is also true for less visible transitions, such as a jump in the conductivity. The connection of these two variables to the volume and the pressure is called the equation of state (EOS), and is well known in the case of an ideal gas[2] $pV = nRT$ ($R = 8.314\,\text{J}\,\text{mol}^{-1}\,\text{K}^{-1}$ being the gas constant, p the pressure,

---

2 The ideal gas is assumed to contain point-like particles that interact only with elastic collisions. Under normal conditions, many gases i. e. noble gases, hydrogen, nitrogen, and oxygen can be treated as ideal gases.

and V the volume). Another fundamental feature of plasmas is the mass ratio between ions and electrons, $m_i/m_e \approx 1836$, which gives rise to a different behavior based on different reaction times of each species. In the following, the most important plasma parameters that are used to separate plasmas into regions on the temperature-density plane within which differing physical models apply will be introduced.

Degeneracy

The quantum effect of degeneracy drastically changes the behavior of a plasma when the thermal energy, $k_B T$, gets smaller than the *Fermi energy*

$$\epsilon_F = \frac{\hbar^2}{2m_e} \left(3\pi^2 n\right)^{2/3}, \tag{37}$$

which is the highest energy level occupied by electrons at zero temperature (completely degenerate). The corresponding *degeneracy parameter* is a measure of how much the quantum nature comes into play, and is given by

$$\Theta = \frac{k_B T}{\epsilon_F} = \frac{2m_e}{\hbar^2} \frac{k_B T}{(3\pi^2 n)^{2/3}} \propto \frac{T}{n^{2/3}}. \tag{38}$$

If the thermal energy is much larger than the Fermi energy i.e. $\Theta \gg 1$, the system can be considered classical, otherwise for $\Theta \ll 1$, the quantum nature is no longer negligible and the system must be considered degenerate. The Fermi energy for a density of $10^{17}\,\mathrm{cm}^{-3}$ amounts to $\epsilon_F = 0.786\,\mathrm{meV}$. Therefore, the degeneracy of a plasma at or above room temperature, $T \sim 25\,\mathrm{meV}$, can be neglected and only classical plasmas will be considered in the following.

Screening

Statistically, every particle in a plasma is surrounded by more particles with the opposite charge. As a consequence, every charge is screened by the surrounding particles such that its electric field decreases faster than the pure Coulomb potential in vacuum. The length within which the field of an electron in a plasma is compensated by $1/e$ ($e = 2.71828$ being Euler's number) compared to the un-screened field,

$$\lambda_D = \sqrt{\frac{\epsilon_0 k_B T}{n e^2}}, \tag{39}$$

is called the *Debye length* [123], and the screened potential decreases as $e^{-r/\lambda_D}/r$. For a plasma with a density of $n = 1 \times 10^{17}\,\mathrm{cm}^{-3}$ at room temperature, $T = 25\,\mathrm{meV}$, the Debye length amounts to $\lambda_D \approx 3.75\,\mathrm{nm}$.

The number of particles within a sphere of radius λ_D is given by the fundamental *plasma parameter*

$$\Lambda = \frac{4\pi}{3} n \lambda_D^3 = \frac{4\pi}{3} n \left(\frac{\epsilon_0 k_B T}{n e^2}\right)^{3/2} \propto \frac{T^{3/2}}{n^{1/2}}. \tag{40}$$

At low densities and high temperatures, there are many particles within this sphere, $\Lambda \gg 1$, and the plasma can be considered as weakly coupled or *ideal*. In such a plasma, collective electrostatic interactions dominate over binary collisions, allowing interactions to be treated as the interaction with a smooth background field. Another way to see this is that, in a weakly coupled plasma, the kinetic energy of the particles is much bigger than their potential energy and particles can freely move through the system.

On the other hand, at high densities and low temperatures, the Debye sphere is sparsely populated, $\Lambda \ll 1$, and the plasma must be considered strongly coupled. Then, the plasma is strongly affect by binary collisions between particles. At room temperature, and $n = 1 \times 10^{17}\,\mathrm{cm}^{-3}$, $\Lambda = 0.022$, which is less than one, so that a strongly correlated plasma must be assumed.

In a plasma that cannot be considered ideal (or weakly coupled), the energy of free electrons is no longer given only by their kinetic energy, but is lowered by the interaction with other plasma electrons. In this case, again all electrons can be considered as ideal, but with a lower energy (self-energy) [123]. The effective ionization energy, ξ_{eff}, is therefore lowered by the same amount, and can in the simplest approximation for hydrogen be calculated as [26]

$$\xi_{\mathrm{eff}} = \xi_{\mathrm{ion}} - \frac{e^2}{4\pi\epsilon_0}\sqrt{\frac{2}{\lambda_{\mathrm{D}}^2}}, \tag{41}$$

where ξ_{ion} is the unperturbed ionization energy (see figure 4).
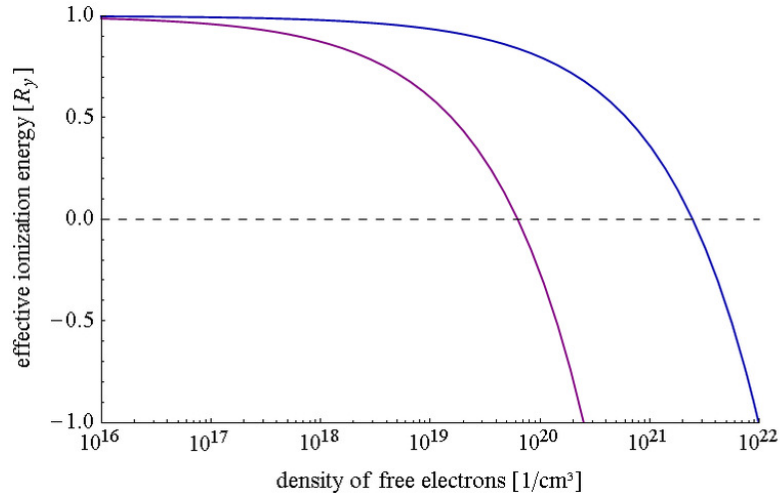
Figure 4: Lowered effective ionization energy of hydrogen for room temperature $T = 25\,\mathrm{meV}$ (violett), and $T = 1\,\mathrm{eV}$ (blue); full ionization is reached at $n = 6.27 \times 10^{19}\,\mathrm{cm}^{-3}$ and $n = 2.47 \times 10^{21}\,\mathrm{cm}^{-3}$, respectively (where $\xi_{\mathrm{eff}} = 0$).

Consequently, a neutral gas undergoes the phase transition to a plasma in both directions in the temperature-density plane. At high temperatures, when the thermal energy reaches the ionization energy, and at high densities, when atoms are ionized due to high pressure.

Relativistic corrections need to be considered at high temperatures. When

$$\frac{m_e c^2}{k_B T} \lesssim 1, \tag{42}$$

the thermal energy becomes larger than the rest mass, where the mean *thermal velocity* is given by

$$v_{th} \approx \sqrt{\frac{k_B T}{m_e}}. \tag{43}$$

This can be deduced from the Maxwell-Boltzmann velocity distribution of an ideal gas in equilibrium (the exact mean velocity of the Maxwell-Boltzmann distributions is $v_{th} = \sqrt{8 k_B T / (\pi m_e)}$, omitting $\sqrt{8/\pi} \approx 1.6$). For room temperature, $v_{th} \approx 66\,883\,m/s$ and therefore $m_e c^2 / k_B T \approx 0.511\,MeV / 25\,meV \gg 1$, so that no relativistic corrections are required.

In plasma wakefield experiments, the temperature is typically not below room temperature, $T \approx 25\,meV$. The media under consideration within this thesis are hydrogen and lithium. As the latter is not in the gaseous phase under normal conditions, it needs to be vaporized to be used in plasma wakefield experiments [167]. For lithium, the boiling point of $1603\,°K \approx 0.14\,eV$ might be considered as the lower temperature-limit in equilibrium. However, since plasmas undergo highly non-equilibrium states interacting with high-power lasers and electron beams, orders of magnitude higher temperatures might occur locally. For instance, in the Particle-In-Cell (PIC) simulations presented later in this work, the energy of free electrons at the boundary of the plasma wave is typically on the order of $100\,keV$.

The temperatures that are relevant for plasma wakefield acceleration can be considered to be $T \in \{25\,meV, 100\,keV\}$. Applied densities are typically $n \in \{10^{15}, 10^{19}\}\,cm^{-3}$, corresponding to a plasma wavelength (see next section) of $\lambda_p = 1.06\,mm$, and $\lambda_p = 10.6\,\mu m$, for the two extreme densities considered. This results in $\Lambda \in \{2.15 \times 10^{-3}, 5.44 \times 10^{13}\} \lessgtr 1$, $\Theta \in \{1.48, 2.74 \times 10^{12}\} > 1$, and $\frac{m_e c^2}{k_B T} \in \{5.1 \times 10^{-3}, 2.04 \times 10^7\} \lessgtr 1$. Consequently, the plasma can be considered as not degenerate, but for $n = 10^{19}\,cm^{-3}$ and room temperature, e.g. before passage of the drive beam, the plasma is only slightly above the critical value, $\Theta = 1.48$. As regards relativistic effects, electrons definitely have speeds close to c within the boundary of the plasma wave, but not in equilibrium. Finally, the plasma must be considered as strongly correlated in the state of equilibrium and can behave as ideal at the very high temperatures occurring after the interaction with the driver. Ionization due to high densities (Mott effect) might occur for low-ionization-threshold media with threshold within regions of increased density; however, these atoms are usually ionized before the perturbation of the driver. High-ionization-threshold media might show a lowered ionization threshold at regions of increased density (e. g. at the back of the plasma wave).

The eigenfrequency of plasma

Every plasma responds in a characteristic time that can be seen as the time an electron needs to pass a Debye length, λ_D, when it propagates with a mean thermal velocity, v_{th}, $\lambda_D/v_t = \sqrt{(\epsilon_0 m_e k_B T)/(e^2 n_e K_B T)} = \sqrt{\epsilon_0 m_e/(e^2 n_e)} \equiv \omega_p^{-1}$. This frequency is the *plasma frequency*

$$\omega_p = \sqrt{\frac{e^2 n_e}{\epsilon_0 m_e}} = \frac{2\pi c}{\lambda_p} = k_p c, \tag{44}$$

the collective eigenfrequency of all plasma electrons in the potential of the static ions. Moreover, connected to the plasma frequency, ω_p, is the corresponding *plasma wavelength*, $\lambda_p = 2\pi c/\omega_p$, the response time, ω_p^{-1}, and the *skin depth* $k_p^{-1} = c/\omega_p$, which is analogous to the skin depth of conductors. The latter is the depth to which electromagnetic radiation can penetrate in overdense plasmas, or equivalently, the length that a relativistic electron beam or laser propagates in underdense plasmas until the plasma reacts. In analogy, the reaction time and eigenfrequency of the ions can be calculated if the electron mass, m_e, is replaced by the mass of the ions. For instance, for hydrogen at a gas density of $1 \times 10^{17}\,\mathrm{cm}^{-3}$, which is typical for plasma accelerators, the reaction time of electrons is $56.05\,\mathrm{fs}$, while the reaction of the protons takes $2.40\,\mathrm{ps}$. The corresponding electron-plasma frequency is $\omega_p \approx 17.84\,\mathrm{THz}$, and the plasma wavelength $\lambda_p \approx 105.6\,\mathrm{\mu m}$.

One of the most important features in plasma physics is the big difference between the masses of electrons and ions. The smallest possible ratio is for pure hydrogen, $m_p/m_e \approx 1836.15$; all other elements have bigger ratios. Due to this big difference in the response time between electrons and ions, the heavy particles can be considered as stationary over the time scale of the electrons. This allows the electron dynamics to be decoupled from that of the ions and enables a wide range of plasma dynamics to be described. This is also known as the *two-fluid* approximation. Note that, when the electron velocity approaches the speed of light, the relativistic correction $\omega_p^2 \to \omega_p^2/\gamma$ must be considered.

Dispersion in plasmas

In equation (9) the dispersion in vacuum was given. The dispersion of an electromagnetic wave with frequency ω, and wave vector, k, in a plasma

$$\omega^2 = c^2 k^2 + \omega_p^2, \tag{45}$$

is altered by the interaction with plasma particles. As a result, $k = \omega/c\sqrt{1 - \omega_p^2/\omega^2}$ can become imaginary when $\omega > \omega_p$ and light cannot penetrate the plasma (see figure 5). The point where $\omega = \omega_p = \sqrt{n_e e^2/\epsilon_0 m_e}$ defines the *critical density*

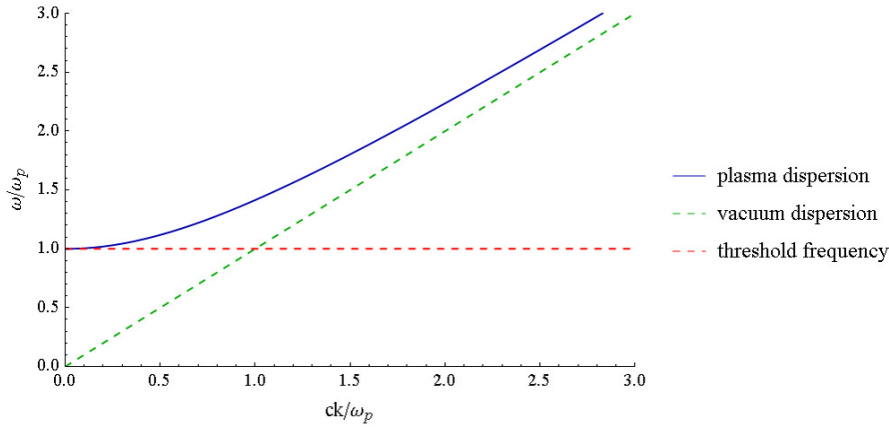$$n_c = \frac{\epsilon_0 m_e}{e^2} \omega^2. \tag{46}$$

Figure 5: Dispersion in vacuum and plasma.

Thus, a laser with the frequency $\omega = \omega_l$ can no longer propagate for $n > n_c$ and immediately couples to the plasma frequency and gets reflected (this allows a plasma to be used as a mirror for high-intensity lasers). For a Ti:Sa laser, this critical density is at 1.74×10^{21} cm^{-3}.

The term "underdense" is used for a plasma density that is transparent for the considered laser frequency $\omega_l \ll \omega_p$.

1.3.2 Kinetic equation

The physical description of a plasma can be formulated on different levels of detail. The lowest level of this description—called the microscopic picture—is given by the full six-dimensional phase space of all particles, combined in the N-particle distribution function. The full evolution of this function, given by its total derivative, is known as the *Boltzmann equation*.

Holding the complete information about the positions and momenta of all N particles in a system for any time, the N-particle distribution function $f(\mathbf{r}^N, \mathbf{p}^N, t) = f(\mathbf{r}_1, \mathbf{r}_2, \ldots \mathbf{r}_N, \mathbf{p}_1, \mathbf{p}_2, \ldots, \mathbf{p}_N, t)$ (here $\mathbf{r}^N$, and $\mathbf{p}^N$ are used as a shortcut for all spatial positions and momenta of all N particles) is exact, but enormously complicated. This function spans the $6N + 1$-dimensional phase space, including 3N-spatial, 3N-momentum-type dimensions and the time, and is the foundation of statistical physics. It can be expressed as the sum

Following the description in [128].

$$f(\mathbf{r}^N, \mathbf{p}^N, t) = \sum_s f_s(\mathbf{r}^N, \mathbf{p}^N, t)$$

$$= \sum_s \sum_{i=1}^{N_s} \delta(\mathbf{r}^N - \mathbf{r}_i(t))\delta(\mathbf{p}^N - \mathbf{p}_i(t)) \tag{47}$$

over all positions and momenta of all N_s particles of all s species, where this particles are considered point like and therefore can be represented as delta functions. Consid-

ering only the species s, its total time derivative describes the evolution of this system and is also known as the *Boltzmann equation*

$$\left(\frac{\partial}{\partial t} + \mathbf{v}\nabla_{\mathbf{r}} + q^n\left(\mathbf{E} + \mathbf{v}\times\mathbf{B}\right)\nabla_{\mathbf{p}}\right)f_s(\mathbf{r}^n,\mathbf{p}^n,t) = \left.\frac{\partial f_s}{\partial t}\right|_{\text{collision}}. \tag{48}$$

This equation describes the change of the phase space due to collisions (right-hand side), diffusion ($\mathbf{v}\nabla_{\mathbf{r}}$), and the external Lorentz force ($\mathbf{F}\nabla_{\mathbf{p}}$). If the right-hand side of this equation can be neglected, e. g. for a collisionless plasma, equation (48) becomes the *Vlassov equation*.

One fundamental feature of this phase-space function is the conservation of phase space volume, given by *Liouville's Theorem*

$$\frac{\partial f_s}{\partial t} + \nabla f_s = 0. \tag{49}$$

Because it is impossible to measure the full N-particle distribution function, and it is unnecessary to know all details of the system, it is crucial that the macroscopic properties can be obtained by averaging over this function:

$$\rho(\mathbf{r},t) = \sum_s q_s \int d\mathbf{p} f_s(\mathbf{r}^N,\mathbf{p}^N,t) \tag{50}$$

$$\mathbf{j}(\mathbf{r},t) = \sum_s q_s \int d\mathbf{p}\mathbf{v}^N f_s(\mathbf{r}^N,\mathbf{p}^N,t), \tag{51}$$

where s is used to denote the particle species of the charge q_s, and the superscript N, again, denotes a coordinate in the 6N-dimensional phase space of all N particles.

1.3.3 *Relevant interaction processes*

In an inelastic collision, part of the energy is transferred to or from inner degrees of freedom of an atom or molecule. Otherwise it is called an elastic collision.

Most of the collisions between photons and atoms or molecules are elastic and do not change the energy (color) of light. This process, also known as *Rayleigh scattering* is dependent on the wavelength and reflects small wavelengths (blue) better than large—the reason why the sky is blue. In contrast, the inelastic *Raman scattering* that changes the energy (wavelength) of the photon is three to four orders of magnitude less probable. The photon either gains energy (*Stokes*, blue-shifting its wavelength), or looses energy (*Anti-Stokes*, red-shifting the wavelength) to the loss or benefit of the inner energy of its collisional partner. When the scattering partner is a free electron. this inelastic scattering process is also called *Compton scattering*.

Once an atom or molecule is excited via an inelastic collision, its excitation may decay, emitting a photon, or transferring the energy to another atom or molecule to which it might be bound. This process is purely statistical and follows a certain probability distribution as a function of time, and is known as *fluorescence* when a photon is emitted. On the other hand, the photoemission can be induced by another impacting particle or photon. The latter enables the functionality of a *laser*, which utilizes this mechanism by

pumping a medium such that many more electrons are in an excited state than in the ground state and then using photons to trigger induced emission and clone the incident photon. Because plasmas do not occur under normal conditions, the ionization of gases is of crucial importance for plasma wakefield acceleration and will be discussed in the following.

Photoionization

At short wavelengths and moderate intensities, multiple photons, each carrying less than the ionization energy $\hbar\omega < \xi_{ion}$, can collectively ionize one atom. This is possible only when the photons overlap spatially and temporally such that it is possible to transfer the energy of more than one photon without violating the conservation laws within the quantum uncertainty. To achieve this high spatial and temporal overlap, multi-photon ionization (MPI) requires a high photon flux. In the common single-photon ionization process, only one photon with energy $\hbar\omega \geqslant \xi_{ion}$ is needed to free a valence electron with binding energy ξ_{ion}, and the photon is thereby absorbed. However, because the binding energy is very high, very short-wavelength photons are required. For example, hydrogen with a binding energy of $\xi_{ion} = 13.6\,eV$, requires wavelengths of $\lambda < 91\,nm$, which is beyond commonly available laser wavelengths.

Tunnel ionization

At long wavelengths and high electric field strengths, the potential of atoms can be distorted such that an electron can have a lower energy when it crosses a short potential barrier. The electron has a significant probability to cross the potential barrier of the atom if it is distorted over a sufficiently long time and the barrier length is short. The *Keldysh parameter* [112, 178]

$$\gamma_K = \omega_l \sqrt{\frac{2m_e\xi_{ion}}{e^2E_l^2}} \tag{52}$$

is often used to distinguish between the MPI and the tunnel ionization regime, where ω_l and E_l are the laser frequency and electric field, respectively, and ξ_{ion} is the ionization energy. The regime $\gamma_K \gg 1$ corresponds to a high probability for multi-photon ionization to occur, whereas for $\gamma_K \ll 1$, tunnel ionization is more likely. The tunnel-ionization rate is given by the quasi-static approximation of the MPI rate, where the oscillation of the electric field can be considered as constant on the time scales of the tunneling process, i.e. the limit of the MPI model when the Keldysh parameter approaches zero. Both ionization methods have been united in the Yudin-Ivanov (YI) model [250]; however, as tunnel ionization is far more likely in the considered regime, MPI is ne-

glected in this work. A popular formalism for the Ammosov-Delone-Krainov [5] (ADK) ionization process was adapted for use in PIC simulations [29] to give

$$W_{ADK}[s^{-1}] \approx 1.52 \times 10^{15} \frac{4^{n^*} \xi_{ion}[eV]}{n^* \Gamma(2n^*)} \times$$

$$\left(20.5 \frac{\xi_{ion}^{3/2}[eV]}{E[GV/m]} \right)^{2n^*-1} \exp\left(-6.83 \frac{\xi_{ion}^{3/2}[eV]}{E[GV/m]} \right) \tag{53}$$

with the ionization energy ξ_{ion}, the electric field strength E, the extended factorial function, Γ, and $n^* \approx 3.69 \times Z/\sqrt{\xi_{ion}[eV]}$, the corrected principal quantum number, which takes into account that the ionization potential is shielded in more complex atoms. The ADK model is considered valid until the field strength reaches

$$E_{c,ADK} = E_a(\sqrt{2}-1)|\xi_{ion}/\xi_a|^{3/2} \approx 1.50|\xi_{ion}[eV]|^{3/2} \frac{GV}{m}, \tag{54}$$

with the atomic field $E_a = \frac{m_e^2 e^5}{(4\pi\epsilon_0)^3 \hbar^4} \approx 5.14 \times 10^{11} \frac{V}{m}$, and the Hartree energy $\xi_a = \frac{m_e e^4}{(4\pi\epsilon_0\hbar)^2} \approx 27.2\,eV$. Figure 10 shows this ADK-rate for different elements.

Barrier-suppression ionization

Formula 53 is applicable for moderate field strengths of slowly oscillating fields (compared to atomic time-scales, $\tau_{atom} = \hbar/2R_y \simeq 24\,as$, R_y being the Rydberg constant). Ionization will occur with certainty, if the field strength rises above the ionization energy (i.e. several $V/\text{Å} = 10^{10}V/m$, Å being typical the spatial dimension of atoms). This can be understood as lowering the potential well below the bound-state energy of the electron, also known as barrier suppression ionization [13] (BSI). This ionization process is faster than tunneling, and results in immediate and complete ionization. The critical field strength for this ionization to occur is given by

$$E_{c,BSI} = \frac{4\pi\epsilon_0}{e^3} \frac{\xi_{ion}^2}{4Z} \tag{55}$$

with $\xi_{ion}[J]$ the ionization energy and Z, the atomic number after ionization (i.e. equal to the number of ionized electrons) [13, 52]. Therefore, in order for tunnel ionization to be the dominant ionization mechanism, the conditions $\gamma_K < 1$ and $E < E_{c,ADK}$ must be fulfilled. In plasma wakefield accelerators, typically the tunnel ionization method is most effective within the parameter range considered here. When the field strength of the ionization laser or ionizing particle bunch exceeds the critical BSI field strength, tunnel ionization has usually already ionized all atoms.

So far, the main ionization mechanisms discussed are induced by photons. However, the impact of an electron with sufficient energy can also efficiently ionize atoms. The cross section of this *impact ionization* strongly depends on the energy of the electron and becomes negligible for electrons with energies that are far beyond the required ionization energy.

All interaction processes that require the movement of heavy particles such as ions and atoms are neglected, since the collision time is typically much longer than the time scales under consideration within this work. Similarly, the recombination of ions and electrons takes much longer, as it involves the interaction of two ions and one electron, so the second ion can carry away the excess energy. Also on a larger time scale is the inverse process of photo-ionization, which might occur with the emission of a photon. Within this work, it is assumed that neutrals are ionized only via the ADK process, the remaining ions are treated as stationary and the freed electrons interact only with the electromagnetic fields caused by other particles or lasers. Once the gas is ionized, it reacts to a strong laser if its duration, τ_l, is longer than the characteristic time of the plasma response, $\omega_p \tau_l > 1$ and the plasma is transparent at the wavelength of the laser. The plasma wave thereby generated will be described in section 2.2.

For an overview of these processes see [102].

EMPLOYING PLASMA WAVES AS PARTICLE ACCELERATORS

The necessity for new concepts of particle acceleration arises from the circumstance that the cost for projected new colliders based on conventional RF-based techniques has become very large. The crucial point is the attainable accelerating gradient, which reaches its physical limits in RF cavities at around 100 MV/m due to break-down con the cavity walls. The application of plasma waves as particle accelerators, which might solve this problem by providing orders of magnitude higher accelerating gradients, is investigated in this thesis.

For instance, considering the dimensions of the currently largest particle accelerator, the Large Hadron Collider (LHC) at CERN with 27 km long circumference and a final energy of 6.5 TeV, build by a collaboration of over 10 000 scientist and engineers from over 100 countries, funding an even larger accelerator (in addition) would be extremely challenging. It becomes obvious that a much larger circular accelerator of this type is currently unaffordable. The next large-scale accelerator currently being discussed is the International Linear Collider (ILC), which will accelerate electrons and positrons to 500 GeV energy in two separate 12 km long linear accelerator (linac) arms, each of which contains a total of 8 000 superconducting cavities, which need to be cooled to 2.15°K [17].

The bottleneck of today's accelerators, the limitation of the accelerating field, can be overcome if one looks for a completely different direction in which higher field strengths can be attained that are simultaneously capable of accelerating particles. Because electric fields are generated by the separation of charged particles, the idea of examining plasmas seems natural. Here, the field strength can be very high, but requires a microscopic system that tends to require the control of very complex and chaotic behavior. The basic concept of utilizing the high accelerating fields in plasma, is to excite a strong plasma wave that propagates nearly with the speed of light [49, 219]. Surprisingly, such a plasma wave has a region in which strong accelerating and focusing fields occur; both are required to contain and accelerate particles. In fact, the plasma wave acts as a transformer that converts the transverse field of a driver into the axial accelerating electric field of the plasma wave. However, to generate and maintain a strong plasma wave is challenging—the most promising methods under investigation are LWFA and PWFA, applying a strong laser or particle beam to drive a wakefield.

2.1 GENERATING PLASMA WAKEFIELDS

One basic requirement of plasma wakefield acceleration, is that the dimensions of the driver must be similar to the plasma wavelength, which is $\lambda_p = 105.6\,\mu m$ for a typical density of $n = 10^{17}\,cm^{-3}$. This raises the need for highly compressed ($\sim 30\,\mu m$ or $\sim 100\,fs$ long), strongly focused, high-energy lasers, or electron beams. However, it is not trivial to maintain this compactness as the plasma acts back on the driver, leading to loss of energy and changing the transverse dimensions [62, 104].

It is common to differentiate between two distinct regimes in plasma wakefield accelerators, the *linear* and the *nonlinear* regime. The linear plasma wave, also known as a Langmuir wave, is excited by a moderately strong driver, has a sinusoidal form and travels with phase velocity $v_{ph} \lesssim c$. The maximum field amplitude in the linear regime, E_0, can be estimated by assuming that all electrons oscillate with the same frequency $\omega_p = ck_p$. The resulting maximum field amplitude is called the *cold nonrelativistic wave-breaking field*

$$E_0 = \frac{m_e c \omega_p}{e}, \tag{56}$$

and can be obtained in the framework of cold fluid dynamics [49]. Equation (56) limits the accelerating field in the linear regime. However, the producible accelerating gradient is already three orders of magnitude larger than in conventional RF-based accelerators, e. g. $E_0 \approx 30.4\,GV/m$ for a density of $10^{17}\,cm^{-3}$. This means that electrons could be accelerated to $30\,GeV$ within only one meter, provided a meter-long wakefield can be sustained. The linear regime is obtained for normalized peak amplitudes of $a_0 \leqslant 1$ (see equation (18)) for laser drivers, and by $n_b < n_p$ for particle-beam drivers (n_b being the peak density of the drive beam, and n_p the ambient plasma density). The plasma wave, as a response to a stronger driver, will eventually break and become a nonlinear wave that exceeds the value of E_0, and can no longer be described within the theory of cold fluid dynamics.

Many authors refer to the (non)linear regime also as (non)relativistic regime, referring to (non)relativistic velocities in the perpendicular electron motion.

Higher field strengths can be gained in the nonlinear regime. Using the nonlinear, relativistic, cold fluid equations in one dimension, the plasma wave has a maximum amplitude of [2, 62]

$$E_{WB} = E_0 \sqrt{2(\gamma_p - 1)}, \tag{57}$$

with the relativistic factor of the plasma wake, $\gamma_p = \left(1 - v_{ph}^2/c^2\right)^{-1/2} > 1$, a function of the plasma wave phase velocity v_{ph}.

2.1.1 *Characteristics of a plasma wakefield*

In the following section, first a phenomenological description will introduce the physics of plasma wakefields, followed by simplified analytical models. A complete analytical

description in all three dimensions including all relevant physical interactions is not possible. However, with certain simplifications, analytical descriptions can be found using plasma-fluid theory, e. g. in the one-dimensional nonlinear regime [19, 33, 209]. Lu et. *al.* [144] developed a phenomenological semi-analytical description for a non-evolving driver in the three-dimensional nonlinear regime. For the full temporal development of a three-dimensional, nonlinear plasma wakefield including the evolution and energy loss of the driver, usually PIC simulations are required [169, 184].

The ponderomotive force of a strong laser (72), and the space-charge force of a relativistic electron beam ($F_r(r) = eE_r(r)$ with the electric field given in equation (29)) can expel plasma electrons. This displacement of the plasma electrons creates an electron-free plasma cavity, featuring a strong electromagnetic field, which pulls the electrons back towards the propagation axis. Meanwhile, the plasma ions experience the same force, but do not react to it as fast as the electrons due to their larger mass, and therefore act as a positively charged homogeneous background during the passage of the plasma wave. In LWFA and PWFA, the generated plasma wave looks similar, with the important difference that a laser pulse typically travels more slowly ($v_g/c < 1$ see equation (77)) than a relativistic electron beam ($\beta \approx 1$) and the excited plasma wave.

In this work, the nonlinear regime will be exploited in both, LWFA and PWFA, because of the advantage of accelerating fields in excess of E_0. The stronger accelerating field allows electrons to be accelerated to the speed of the plasma wave within less than half a plasma wavelength, allowing electrons that are injected into the plasma cavity to become *trapped* in the same cavity. In the nonlinear regime, the gradient of the accelerating field becomes approximately linear over a significant part of the plasma wave and, simultaneously, the focusing part is enlarged. This creates a larger region where both acceleration and focusing fields support stable acceleration of electrons.

The highly nonlinear regime

For an extremely strong driver, $a_0^2 \gg 1$ in case of a laser and $n_b \gg n_p$ for an electron beam, with small transverse size, $\sigma_r k_p \ll 1$, a highly nonlinear wakefield is excited whose shape becomes a sphere. In this regime, plasma electrons gain a relativistic transverse velocity during the interaction with the strong driver. The longitudinal field—which in the linear case is sinusoidal—becomes sawtooth-like, featuring a linear accelerating field within the plasma cavity. Within this cavity, the electric and magnetic fields reduce to an longitudinal electric field, E_z, and the transverse component becomes $E_r - cB_\theta$, because $j_\theta = 0$ and therefore also $E_\theta = B_r = B_z = 0$ (in cylindrical coordinates, θ, r, and z, with rotational symmetry). In general, the plasma wave can accelerate electrons in the forward direction when $E_z < 0$ and focus them when

In the nonlinear regime, the first plasma wave cavity is electron-free and therefore often referred to as "blowout"[109, 193] in the context of PWFA and as "bubble" in the context of LWFA [185].

$E_r - cB_\theta > 0$. The radial and longitudinal fields are connected by the *Panofsky-Wenzel theorem* [111, 177]

$$\frac{\partial E_z}{\partial r} = \frac{\partial (E_r - cB_\theta)}{\partial z}. \tag{58}$$

Inserting the angular component of the Maxwell equation (5) in cylindrical coordinates [28]

$$\frac{\partial B_\theta}{\partial z} = -\mu_0 j_r + \frac{1}{c}\frac{\partial E_r}{\partial z} \tag{59}$$

into equation (58) gives

$$\frac{\partial E_z}{\partial r} = \mu_0 c j_r, \tag{60}$$

the connection between the longitudinal field, E_z, and the radial current, j_r [16]. The accelerating field is therefore given by

$$E_z(r,z) = -\mu_0 c \int\limits_r^\infty j_r(r',z)\,dr', \tag{61}$$

Note that current is defined as the moving direction of positive charges.

using $\int E_z(r)\,dr = E_z(\infty) - \int_r^\infty E_z(r')\,dr'$, and $E_z(r \to \infty) = 0$. Thus, the transverse current, j_r, is the source of the longitudinal accelerating field. When the driver expels plasma electrons, it generates a radial negative currentand therefore a positive longitudinal field is created, that decelerates electrons. Likewise, the returning electrons provide a positive current, generating a negative longitudinal field that accelerates electrons (see figure 6). The point where the electrons in the boundary of the plasma cavity (sheath) reach their largest displacement, $R = R_{max}$, and the radial current becomes zero, is therefore also the position where the longitudinal field is zero and switches its sign. The function $R = R(\xi)$ denotes the radius of the plasma cavity. As a result, the plasma wave converts the energy of the driver (which puts energy into the radial expulsion of the electrons), into the accelerating field of the plasma wave. In the case of an electron driver, the expulsion of plasma electrons therefore also immediately creates the decelerating field, which reduces the energy of the driver during the propagation within the plasma. Inside the plasma cavity, there is no radial current, $j_r(r < R) = 0$, (except for possibly the electron drive beam) and therefore $\frac{\partial E_z}{\partial r} \approx 0$ (see equation (60)). Similarly, the focusing field is linear in the radial direction, $(E_r - cB_\theta)/E_0 = k_p r/2$ and constant in the longitudinal direction, $\frac{\partial}{\partial \xi}(E_r - cB_\theta) \approx 0$, inside the plasma cavity (see figure 6 (a)), which can be derived with the use of Maxwell's equations in conjunction with equation (58). The fact that the radially focusing fields are linear in the nonlinear regime has the big advantage over the linear regime that the normalized emittance is

In LWFA, $R_{max} \approx w_0$ [146], whereas in PWFA $R_{max} \approx \sigma_r\sqrt{\frac{n_b}{n_p}}$, with n_p, and n_b, the plasma and beam density, respectively, and σ_r its transverse extension [104]

preserved (the emittance will be introduced in section 2.3.1). The slopes of these fields are given by [120, 144]

$$\frac{E_z(\xi)}{E_0} = \frac{k_p \xi}{2} \tag{62}$$

$$\frac{E_r(r)}{E_0} = \frac{k_p r}{4} \tag{63}$$

$$\frac{cB_\theta(r)}{E_0} = -\frac{k_p r}{4}, \tag{64}$$

using the co-moving coordinate $\xi \equiv z - ct$. Note that the focusing force inside the plasma cavity is therefore $F_r = e(E_r - cB_\theta) = eE_0 k_p r/2$. In equation (61), it has been shown that the longitudinal field, E_z, is proportional to the radial current, and therefore to the radial velocity $v_r = \frac{\partial r}{\partial t} = -c\frac{\partial r}{\partial \xi}$. Lu et. *al.* [144] exploited this behavior to describe the nonlinear three-dimensional plasma wave in therms of the blowout radius, $R(\xi)$, in a semi-analytical approach. With the approximation that the current, which contributes to the wakefield, is concentrated within a thin sheath in the boundary of the plasma cavity, Lu et. *al.* conclude $E_z \propto \frac{\partial R}{\partial \xi}$. The nearly circular shape of a highly nonlinear wakefield can be approximated by a parabola near the center; its derivative, and therefore the longitudinal field, E_z, is approximately linear in this region. For larger distances from the center, the slope of a circle increases faster than that of a parabola, and its derivative, the longitudinal field, therefore decreases faster than linearly at later positions in the blowout (such as in figure 6 (b), or as illustrated by the central blue lines in figure 34).

In the slightly nonlinear regime, shown in figure 6 (a), in the rear of the wave $R(\xi)$ has a lower slope and the longitudinal field therefore has not a sharp maximum as in the highly nonlinear case (remember $E_z \propto \frac{\partial R}{\partial \xi}$). The transverse field switches its sign approximately at the position where the axial field has its extrema, and vanishes directly on axis (see figure 6 (a)).
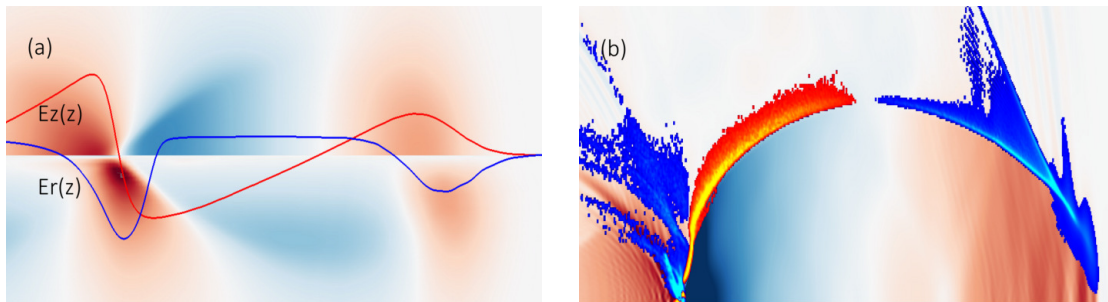
Figure 6: Example PWFA simulations in the slightly nonlinear (a), and in the extreme nonlinear "blowout" regime (b), illustrating where the fields and the currents are positive (red) or negative (blue). (a): the longitudinal electric field, E_z, (top half, the red curve shows the central E_z values) and the transverse electric field, E_r, (bottom half, the blue curve shows E_r in longitudinal direction slightly off-axis). (b): the radial current, j_r, (bright-blue: negative, bright-red: positive) and the corresponding longitudinal field, E_z in the background (confer equation (61)).

The region that can be exploited for the acceleration of electrons, is where the wakefield is simultaneously accelerating ($qE_z > 0$) and focusing ($q(E_r - cB_\theta) < 0$). In the linear regime, the longitudinal wakefield can be described as a sine function and the transverse field as a cosine function in the longitudinal direction; the region where the fields satisfy this condition is therefore only 1/4 of the plasma wavelength. In the highly nonlinear regime, the overlap of the focusing and accelerating phase increases until both almost merge and reach nearly half of the plasma wavelength [106]. Therefore, the highly nonlinear regime is very promising for plasma wakefield acceleration and operation in this regime led to the breakthrough experiments in LWFA, featuring quasi mono-energetic beams [64, 74, 153].

To model the full propagation appropriately in three dimensions, including the self-consistent evolution of the driver, requires numerical simulations e. g. with fully three-dimensional PIC simulations, as used in this thesis. However, the one-dimensional formalism that will be introduced in the following, is particularly useful to show the basic physical properties of a plasma wave.

Wave equations

In the limit of a quasi-static wakefield [209] and a highly relativistic driver ($\gamma_p^2 \gg 1$ with $\gamma_p^2 = (1 - (v_p/c)^2)^{-1}$ denoting the relativistic factor of the wave, and v_p, its phase velocity), the Poisson equation in one dimension can be expressed in the form [33, 62, 209]

$$\frac{1}{k_p^2}\left(\frac{\partial^2 \phi(\xi)}{\partial \xi^2}\right) = \frac{n_b(\xi)}{n_0} + \frac{1+a(\xi)^2}{2(1+\phi(\xi))^2} - \frac{1}{2}, \tag{65}$$

with the normalized scalar potential, $\phi(\xi) = \frac{e\Phi(\xi)}{m_e c^2}$, and vector potential, $a(\xi) = \frac{eA(\xi)}{m_e c^2}$, introduced in equation (6); n_0 is the unperturbed ion density. The right-hand side of this equation comprises the source term for plasma distortions by a laser pulse represented by its normalized vector potential $a(\xi)$, or the density distribution, $n_b(\xi)$, of an electron drive beam. The solution of this equation provides the scalar potential, $\phi(\xi)$, from which the other plasma-wave quantities

$$\Delta n_e(\xi) = \frac{1+a(\xi)^2}{(1+\phi)^2} - 1 \tag{66}$$

$$\frac{E_z}{E_0} = -\frac{1}{k_p}\frac{\partial \phi}{\partial \xi} \tag{67}$$

can be derived, where $\Delta n_e(\xi)$ is the relative electron-density variation and E_z is the longitudinal field of the plasma wave. Equation (65) applies for the linear and slightly nonlinear regime in LWFA and PWFA, whereas the highly nonlinear regime is not included.

Figure 7 shows the difference of the linear (left, $a_0 < 1$) and the nonlinear regime (right, $a_0 > 1$), and therefore the influence of the strength of the driver in the case of
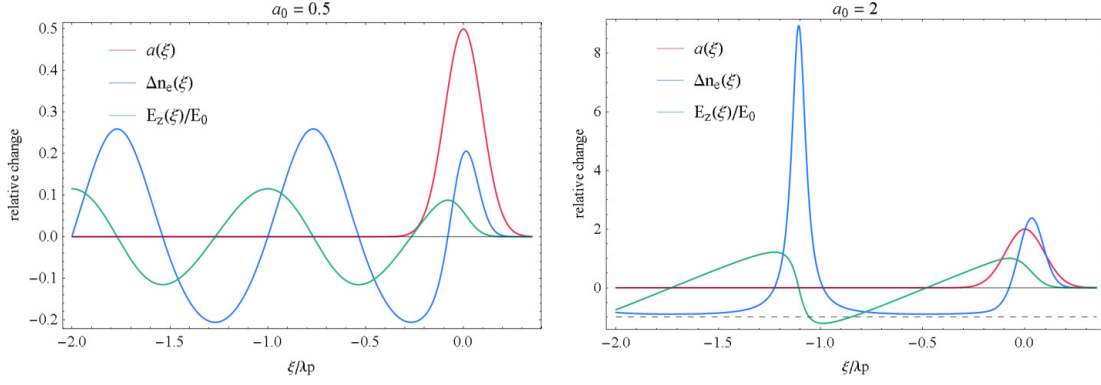
Figure 7: Linear ($a_0 = 0.5$, left) and nonlinear ($a_0 = 2$, right) plasma waves driven by a laser pulse, according to equation (66) and (67) using the solution of equation (65). Numerical methods implemented by Thomas Heinemann.

LWFA. In the linear regime, the sinusoidal form of the longitudinal electric field (green curve), shows an amplitude of significantly less than the cold wave-breaking limit, E_0. In the nonlinear regime, the longitudinal electric field increases beyond E_0 and its slope becomes linear (saw-tooth-like) within the nearly electron-free plasma cavity ($\Delta n_e \approx -1$, blue curve). Simultaneously, the plasma wavelength grows, the curvature of the plasma cavity increases towards a spherical shape and very high density spikes occur at the point where the plasma cavity closes. At the transition from the linear to the nonlinear regime, the trajectories of plasma electrons begin to cross, leading to a singularity in the cold fluid equations, which can be remedied as soon as finite temperatures are assumed [142]. Importantly, the breaking of the plasma wave also enables the trapping of plasma electrons in LWFA (self-injection) [222]. The length of the extended plasma cavity can be estimated by [61]

$$\lambda_{p,NL} \approx \lambda_p \frac{2}{\pi} \frac{E_{max}}{E_0} \quad \text{for} \quad E_{max} \gg E_0, \tag{68}$$

where E_{max} denotes the maximum accelerating field strength, and $E_0 = m_e c \omega_p / e$, the cold non-relativistic wave-breaking field. Note that for electrons, the maximum accelerating field is the minimum longitudinal field, $E_{z,min}$. The maximum amplitude of the slightly nonlinear plasma wave was approximated by the cold relativistic wave-breaking field given by equation (57) in a one-dimensional quasi-linear approach. In the highly nonlinear regime, the definition of this maximum accelerating field is most reasonably made without taking the narrow peak field at the rear of the plasma cavity into account, which cannot be effectively used for acceleration. In the case of LWFA, the maximum usable accelerating field is estimated by the linear continuation of the slope of the longitudinal field to the rear of the blowout [146]

$$E_{z,max} \simeq E_z(-\lambda_{p,NL}/2) \simeq -E_0 \sqrt{a_0} \tag{69}$$

with the nonlinear plasma wavelength $\lambda_{p,NL} \simeq \lambda_p (2/\pi) \sqrt{a_0}$. Similarly, in the nonlinear regime of PWFA, the accelerating field can be expected to vary as $E_z \propto E_0 \sqrt{I_p}$, as

opposed to $E_z \propto E_0 I_p$, in the linear case [22]. Therefore, the nonlinear regime is also less efficient than the linear regime. The cold non-relativistic wave-breaking field, $E_0 = m_e c \omega_p / e$, shows that the amplitude of the wakefield increases with the plasma density as $E_0 \propto \sqrt{n_e}$, whereas the slope of the accelerating field in the highly nonlinear regime is $\partial E_z / \partial \xi = E_0 k_p / 2 \propto n_e$. Note that the wakefield is only sensitive to the peak current, but not to the transverse extent of the drive beam, as long as it is sufficiently smaller than the transverse extent of the blowout. Consequently, oscillations of the drive-beam do not have a large influence on the wakefield. On the other hand, these oscillations do change the peak transverse fields of the drive beam, which might ionize a neutral background gas.

Efficiency of plasma wakefield accelerators

The accelerating bunch is also often referred to as witness bunch within the literature and throughout this theses.

A typical measure of the efficiency of a plasma wakefield accelerator, the *transformer ratio*, is the quotient of the maximum witness-bunch acceleration, $E_{z,min}$, over the maximum drive-beam deceleration, $E_{z,max}$ [15, 22, 39]

$$T = \frac{E_{z,min}}{E_{z,max}}. \tag{70}$$

Note, the minimum longitudinal wakefield, $E_{z,min}$, is the maximum accelerating field for electrons.

The overall efficiency of a plasma wakefield accelerator is given by the amount of energy that is transferred from the driver to the witness bunch at the end of the acceleration; $\eta = (\gamma_{d,f} + \gamma_w)/\gamma_w < 1$ ($\gamma_{d,f}$, and γ_w denotes the final energy of the drive beam, and the witness bunch, respectively). The maximum energy gain of the witness bunch, $\gamma_w = T\gamma_{b,i}$, is obtained when the decelerating field has completely compensated the initial energy of the drive beam, $\gamma_{b,i}$. In reality, the drive beam cannot transfer all its energy to the wakefield, and the remaining energy of the driver is lost for the acceleration process. On the other hand, the witness bunch usually cannot extract all the energy of the wakefield, again reducing the overall efficiency (see beam-loading discussion below).

Another interesting perspective on the transformer ratio for PWFA is given by

$$T \sim \frac{\Delta \xi_{dec}}{\Delta \xi_{acc}}, \tag{71}$$

where $\Delta \xi_{dec}$ is the distance from the front of the plasma cavity to ξ_0, and $\Delta \xi_{acc}$ is the distance from ξ_0 to the end of the plasma cavity [22], defining $\xi_0 = 0$ to be the position where $E_z(\xi_0) = 0$. If the drive-beam charge is negligible at ξ_0, $\Delta \xi_{acc}$ depends only on the maximum radius of the plasma cavity, which is determined by the peak current of the drive-beam, I_p. However, the length $\Delta \xi_{dec}$ can be influenced by the shape and length of the driver, which therefore can be exploited to increase the transformer ratio.

For instance, if a short drive beam expels plasma electrons very rapidly, some receive a kick that lets them escape the attractive potential of the ion channel and they cannot contribute to the accelerating part of the wakefield. On the contrary, if the drive beam

exerts a gently increasing force on the electrons, fewer electrons are lost. Therefore a long, conically shaped electron bunch provides the best transformer ratio [39, 108, 143], and it can be shown that, for a longitudinally symmetric drive beam, the transformer ratio is limited to $T \leqslant 2$ in the linear regime [197].

So far, the space-charge field of the witness bunch, which lowers the accelerating field at the position of the bunch, was not considered. This *beam-loading* of the wake limits the amount of charge that can be loaded into the plasma wave to the level at which the witness bunch itself excites a plasma wave that fully cancels the wave of the driver (beam-loading limit) [109]. When the witness bunch is capable of completely absorbing the wakefield, the energy-transfer efficiency is at its maximum.

On the other hand, beam loading can be exploited to shape the gradient of the accelerating field [151], and therefore change the energy gain of the witness bunch. This requires the witness bunch to have a density distribution that ideally is matched to the slope of the accelerating field. Such properties have been intensely studied [22, 80, 224, 225] and are provided by an approximately linearly decreasing density of the witness bunch. This technique, however, is only exploitable in a dephasing-free setup such as in PWFA.

Summarizing, for the maximum efficiency, a conically increasing density of the drive beam is required in order that energy should not be lost in setting up the wakefield, while a conically decreasing witness bunch would be ideal to flatten the accelerating gradient; a witness bunch with large charge could fully load the wakefield and absorb nearly all of its energy.

2.2   LASER-DRIVEN PLASMA WAKEFIELD ACCELERATORS

Increasingly fast development of laser technology has triggered many novel research areas, among which laser-plasma-based particle acceleration has shown its potential in numerous research laboratories ever since its introduction in 1979 [219]. Worldwide, experiments have reported electron-beam production featuring hundreds of $MeVs$ of energy gain and broad energy spectra [4, 73, 130, 148, 163, 168, 221, 226], enabled by the availability of sophisticated laser-amplification methods [113, 214]. Switching to the highly nonlinear "bubble" regime [161, 185], led to a major breakthrough in 2004, when three groups independently reported the acceleration of quasi-mono-energetic electron beams [64, 74, 153].

Until today, ultra-high-power lasers [40, 115, 132, 233], advanced accelerator techniques such as self-modulation [4, 90, 122, 163, 168, 221], relativistic self-focusing [118, 210, 216], staging [115, 182, 213], laser guiding by a preformed plasma channel [65, 76, 189] and improvement of the diagnostics [30, 69, 82, 235], have further significantly improved the quality and energy of laser-driven plasma wakefield accelerators. This rapid development has led to the acceleration of high-quality electron beams beyond $1\,GeV$ [43, 115, 133, 134, 233] applying PW laser systems, and advanced techniques to guide the laser over several Rayleigh lengths. A comprehensive list of laser facilities available for LWFA experiments is given in Table 9. In the following, the effect of a high-power laser on plasma and, the effect of the plasma on the laser will be discussed.

2.2.1   *The ponderomotive force*

Within a homogeneous electromagnetic wave, an electron will follow the oscillation of the wave and not gain any net momentum in one or the other direction. For a tightly focused laser, however, the intensity of the laser strongly varies in the transverse direction and an electron will feel a weaker force once it is pushed away from the laser center and will not be pulled back with the same strength. In other words, the electrons react to the field pressure of the laser pulse. This results in a net *ponderomotive force*

$$\mathbf{F}_p = -\frac{e^2}{4m_e\omega_l}\nabla(\mathbf{E}^2),\tag{72}$$

which decreases with ω_l, the frequency of the laser, and grows with the gradient of $I_l \propto \mathbf{E}^2$, the intensity and the electric field strength of the laser [124]. Choosing a much longer wavelength to increase the ponderomotive force was not an option to date, as high-energy lasers are only available for $\approx 0.8-1\,\mu m$ wavelengths in Ti:Sa laser systems. However, new high-power CO_2 lasers with wavelengths of $\lambda_l \approx 10\,\mu m$, are under development and will be deployed for LWFA experiments in the near future e.g. at the Accelerator Test Facility (ATF) at the Brookhaven National Laboratory (BNL) [181]. Operation at much longer wavelengths is limited by the critical plasma density (46), such

that lasers with wavelengths in excess of the plasma wavelength, $\omega_l > \omega_p$, can no longer penetrate the plasma. On the other hand, enhancements in the amplification of lasers, such as the chirped pulse amplification (CPA) technique [214], have enabled laser powers of up to PWs, and intensities in excess of $10^{20}\,\mathrm{W/cm^2}$. For comparison, the solar constant is only $0.137\,\mathrm{W/cm^2}$. These developments increase the ponderomotive force to a level where an amplified laser can excite a strongly nonlinear wakefield.

2.2.2 *Laser-plasma interactions*

When an ultra-short, high-intensity laser propagates through an underdense plasma, its properties are strongly modified [165]. Before discussing these phenomena, it is important to understand the effect of very high intensities, density fluctuations and the fact that the plasma electrons have relativistic velocities on the dispersion and the refractive index of the plasma. Taking account of the relativistic transverse velocities of the electrons, the dispersion in plasma reads [110]

$$\omega^2 = c^2 k^2 + \omega_p^2/\gamma, \tag{73}$$

where γ is the relativistic factor of the plasma electrons. Compared to the nonrelativistic case, where the plasma is transparent for radiation with $\omega > \omega_p$, in the relativistic case, the plasma becomes transparent for electromagnetic waves with $\gamma\omega > \omega_p$ and thus radiation with longer wavelengths can penetrate the plasma. The ratio of the vacuum speed of light and the *phase velocity*

$$v_{ph} \equiv \frac{\omega}{k}, \tag{74}$$

defines the *relativistic refractive index* [77]

$$\eta_0 = \frac{c}{v_{ph}} = \frac{ck}{\omega} = \sqrt{1 - \frac{\omega_p^2}{\gamma\omega^2}}, \tag{75}$$

using equation (73). For an underdense (transparent) plasma, the phase velocity

$$v_{ph} = c\sqrt{1 + \frac{\omega_p^2}{\gamma\omega_l^2}} \tag{76}$$

of a laser with the frequency $\omega = \omega_l$ is always larger than c, while the *group velocity*

$$v_g \equiv \frac{\partial\omega}{\partial k} = c\sqrt{1 - \frac{\omega_p^2}{\gamma\omega_l^2}}, \tag{77}$$

is always smaller and denotes the velocity of the laser within the plasma. From equation (77), it can be seen that the velocity of the laser slows down for $\gamma\omega_l \to \omega_p$ and eventually will reach zero for $\gamma\omega_l = \omega_p$, marking the point at which the plasma becomes opaque. The maximum relativistic factor of plasma electrons under the influence

The terms "ultra-short" and "high-intensity" laser pulses have been reconsidered several times in the past, as soon as pulses with shorter duration and higher intensities became available.

of a strong laser with normalized amplitude a_0 is $\gamma = \sqrt{1 + a_0^2/2}$, assuming only the contribution from the transverse motion, $\gamma \approx \gamma_\perp \gg \gamma_\parallel$.

From equation (75), it can be seen that the refractive index is altered due to a change in the density, $\omega_p = \omega_p(n)$, the frequency, ω, and relativistic velocities of the plasma electrons, γ [51, 165]. In addition, the refractive index changes based on the intensity within dispersive media [234]

$$\eta = \eta_0 + \eta_2 \mathcal{J}_0. \tag{78}$$

For very high laser intensities, $\mathcal{J}_0 \propto a_0^2 \omega_l^2$, η_0 denotes the linear, and $\eta_2 > 0$ the non-linear and intensity-dependent portion of the refractive index, respectively. All these contributions to the refractive index react back on the local laser phase, and group velocity and significantly change the propagation of the laser.

Relativistic self-focusing

Assuming a laser pulse with a Gaussian intensity distribution, $a(r) = a_0 \exp(-r^2/w_0^2)$ in the transverse direction, the diffraction angle of the laser is given by $\Theta = \sqrt{2}/(k_l w_0)$. With the use of the resulting r-dependent relativistic factor $\gamma(r) = \sqrt{1 + a(r)^2/2}$, the refractive index (75) becomes a function of r as well, with its maximum on axis, $r = 0$. Therefore, $d\eta/dr < 0$, and a strong laser can be guided based on relativistic velocities of the plasma electrons [216]. The maximum angle of this *relativistic self-focusing* is given by $\alpha = a_0 \omega_p/(\sqrt{8}\omega_l)$, and the diffraction of a laser can therefore be compensated when $\alpha = \Theta$ or $a_0^2 w_0^2/8 \geqslant 4/k_p^2$. Since $\mathcal{P}_0 \propto a_0^2 \omega_0^2$, a critical power for relativistic self-focusing

$$P_c[\mathrm{GW}] \approx 17.4 \left(\frac{\omega_l}{\omega_p}\right)^2 \propto \frac{1}{\lambda_l^2 n_p} \tag{79}$$

can be derived, when considering the average angle instead of the maximum angle (α) for self-focusing [210]. This critical power increases with lower plasma densities, n_p, and smaller laser wavelengths, λ_l. For $P_l/P_c < 1$, the laser diffracts, for $P_l/P_c = 1$ its transverse size is matched and for $P_l/P_c > 1$ the plasma focuses the laser pulse. In the case of a Ti:Sa laser in a $n_p = 10^{17} \, \mathrm{cm}^{-3}$ dense plasma, the critical power is $P_c \approx 303.2 \, \mathrm{TW}$.

However, there is another effect that leads to an effective focusing of the rear part of the laser pulse, which arises from the transverse density gradient of the plasma wave itself [216]. The less dense center thereby results in a maximum of the refractive index on axis, $d\eta/dr < 0$, and is therefore focusing. In contrast, the opposite density profile (with a higher density on axis) can occur if a Gaussian laser pulse ionizes several consecutive ionization thresholds, leading to *ionization defocusing*.

Another method to guide a high-power laser is therefore the use of a preformed plasma channel [18]. Ways to generate such a channel include the use of hydrodynamic expansion after heating by a laser [57, 76, 208], a fast high-current discharge (z-pinch) [100],

or a slow capillary discharge waveguide [107, 141, 172, 207]. The pre-formed channel has the advantage over the relativistic self-guiding mechanism that, the entire pulse and not only the back is guided, and that there is no need for the extremely high critical power, P_c, especially for low plasma densities. Further, the channel can be used to flatten the accelerating field, mitigate emittance growth via Coulomb collisions and reduce the focusing fields and therefore the divergence of the obtained bunch [202]. However, it also involves the need to generate a long and stable plasma channel.

Relativistic self-phase modulation and longitudinal bunching

In LWFA, the plasma density increases towards the front of the drive laser and in the transverse direction, as electrons are pushed aside by the ponderomotive force. The resulting density gradient along the propagation axis also changes the relative speed between the front and the back of the laser pulse, as dictated by the group velocity (77). The lower density at the back of the pulse leads to a higher group velocity than at the front, so the laser pulse becomes longitudinally bunched. This *longitudinal bunching* can be used to drive a high-amplitude wakefield by a laser pulse that is long compared to the plasma wavelength in a dense plasma in the self-guided regime, $P \geqslant P_c$ [90, 148, 163]. The z-dependence of the laser group velocity then results in a modulation of the laser intensity with the period of the plasma wavelength, which in turn reinforces the wakefield and is called *Self-Modulated LWFA*.

The change of the density also changes the local phase velocity (74) of the laser. As the driving laser always experiences a positive density gradient, the phase velocity at the back is slower than that at the front, and the wavelength of the laser pulse is stretched. The increase of the wavelength effectively removes energy from the laser pulse and is the physical mechanism by which the excitation of the wakefield extracts energy from the laser. The part of the laser pulse whose wavelength is stretched also slows down, as dictated by the group velocity, and begins to elongate the entire laser pulse, resulting in a mismatch of the plasma wavelength and laser duration. When the laser has reached this point, the excitation of the wakefield ends together with the depletion of the power of the laser $\mathcal{P}_0 \propto \lambda_l^{-2}$ and its compactness. Besides these straightforward physical instabilities in LWFA, there are several higher-order laser-plasma instabilities that can spoil the acceleration [61]. The most important instabilities in this context are the *laser-hosing* [211] and the *Raman forward and backward scattering* [10].

A negative density gradient, e. g. at a position at the rear of a plasma wave, can therefore also reduce the wavelength of a laser and "accelerate photons".

2.2.3 *Driver matching conditions*

For an axially symmetric laser pulse, the plasma wake will be excited most efficiently when the laser pulse ends approximately at the center of the bubble. In the one dimensional, quasi-static description given in equation (10),

$$k_p \sigma_z \simeq 1 \tag{80}$$

maximizes the accelerating field of a linearly polarized Gaussian laser pulse [61]. In the highly nonlinear case, $a_0 > 1$, the elongation of the plasma wave, $k_{p,NL} = 2\pi/\lambda_{p,NL}$ (68), must be considered. However, the amplitude of the wake is not changed much by moderate variations of the duration of the laser, especially for high laser amplitudes.

Matching of the transverse size in the strongly nonlinear regime is aimed at mitigating oscillations of the driving laser, which is not easy, considering the number of effects that are involved. The relativistic self-focusing force balances the diffraction of a Gaussian laser pulse, when $k_p w_0 \simeq 2\sqrt{8}/a_0$, as discussed in the context of the critical power (79). In contrast to an electron-beam driver in PWFA, which has its maximum transverse field at $\approx 1.6\sigma_r$ off axis, the maximum field of a Gaussian laser pulse is on axis. This requires the laser to be broader than a comparable electron beam to push plasma electrons equally far off-axis. A laser spot size with $w_0 \approx R$ is therefore optimal, assuming a spherical blowout with radius R [146].

2.2.4 *Physical limitations*

The final energy of the electron bunch, ΔW, after acceleration is determined by the length of the acceleration, L_{acc}, and the averaged accelerating field, $\overline{E}_z$, that the electrons have witnessed.

$$\Delta W = e\overline{E}_z L_{acc}. \tag{81}$$

The acceleration is terminated by the energy loss (*depletion*) and the *diffraction* of the driving laser pulse, as well as the *dephasing* of the trapped electrons in the plasma wave. In the following, the distance after which the acceleration terminates, because of these effects will be discussed in detail.

Diffraction

If no guiding is provided, the acceleration will end as soon as the driving laser diffracts sufficiently that its peak intensity becomes insufficiently large to drive the wakefield. A Gaussian laser pulse in vacuum undergoes a spot size evolution according to equa-

tion (14) with the characteristic length, $z_R = \pi w_0^2/\lambda_l$. Neglecting any influence of the plasma, the *diffraction length* can be estimated by [61]

$$L_{diff} \simeq \pi z_R = \frac{\pi^2 w_0^2}{\lambda_l}. \tag{82}$$

For typical laser and plasma parameters, this shortens the acceleration length more than dephasing and pump depletion. For example, a Ti:Sa laser that is focused to a spot size of $w_0 = 50\,\mu m$ will be able to drive a plasma wakefield only for $L_{acc} = L_{diff} \approx 3.1\,cm$. As discussed above, diffraction of the laser can be avoided when using very high laser powers, $P \geqslant P_c$ [210, 216], or laser guiding in a pre-formed plasma channel [57, 76, 82, 189].

Dephasing

The next limit on the acceleration length, is the distance electrons need to outrun the accelerating phase of the wakefield. In LWFA, the wakefield moves approximately with the group velocity of the driving laser, $v_g = c\sqrt{1 - \omega_p^2/(\gamma\omega_l^2)} < c$, whereas the accelerating witness bunch propagates with nearly the vacuum speed of light. The difference in these velocities and the length of the accelerating phase, $\sim \lambda_{p,NL}/2$, therefore defines an appropriate estimate for the *dephasing length*

$$L_{deph} \simeq \frac{1}{2}\frac{\lambda_p^3}{\lambda_l^2} \times \begin{cases} 1 & \text{for} \quad a_0^2 \ll 1 \\ (\sqrt{2}/\pi)a_0 & \text{for} \quad a_0^2 \gg 1 \end{cases} \tag{83}$$

assuming a linearly polarized Gaussian laser in the one-dimensional limit [61]. In the linear regime, the phase that is simultaneously focusing and accelerating is only $\sim \lambda_p/4$. For the highly nonlinear case, $a_0^2 \gg 1$, the dephasing lengths scales as $L_{deph} \propto a_0 n^{-3/2}$, which means that the acceleration length can be increased with a higher laser intensity and more importantly, a lower plasma density. The latter simultaneously increases the length of the accelerating phase, $\lambda_p \propto \sqrt{n}$, and the velocity of the wakefield, according to $v_g = c\sqrt{1 - \lambda_l^2/(\lambda_p^2\gamma)}$. However, for lower plasma densities, relativistic self-focusing requires ever higher laser powers, and laser guiding by a pre-formed plasma channel becomes inevitable at some point. Alternatively, if a drive-laser with a smaller wavelength, $\lambda_l \ll \lambda_p$, is available it can be used to increase the group velocity, but then the ponderomotive force, $F_p \propto \lambda_l$, also decreases. To further increase acceleration length for a fixed laser intensity and density, the plasma density can be modified to increase at a rate that compensates the dephasing of the witness bunch by constantly shrinking the plasma wavelength, keeping the witness bunch at the same phase of the wakefield [189, 208]. This increases the potentially available length of the accelerating phase to the entire plasma wavelength at the start of the acceleration, but the laser is then unable to drive the wakefield efficiently for all densities.

Laser-energy depletion

The least severe limitation is the depletion of the energy of the laser itself [32]. The physical reason for the energy loss is the increase of the laser wavelength as a result of the difference in the phase velocities along the propagation axis, as discussed in the context of laser-plasma interactions. The increasing wavelength of parts of the laser pulse, decreases the group velocity and hence the relative speed, inducing a rapid lengthening of the laser pulse at the end of the acceleration [165, 206]. Then, the resonance between the laser and the plasma gets lost and the power of the driving laser pulse is reduced. A characteristic length after which the laser energy is depleted to a level where the acceleration terminates, can be estimated to be

$$
L_{depl} \simeq \frac{\lambda_p^3}{\lambda_l^2} \times \begin{cases} 2/a_0^2 & \text{for} \quad a_0^2 \ll 1 \\ (\sqrt{2}/\pi)a_0 & \text{for} \quad a_0^2 \gg 1 \end{cases}
\tag{84}
$$

assuming a linearly polarized Gaussian laser in the one-dimensional limit [61]. For instance, a laser pulse with $a_0 = 8$ (as used later in this thesis), has a dephasing length of $L_{deph} = 3.3\,m$, and a depletion length of $L_{depl} = 6.6\,m$ in a $n_p = 1 \times 10^{17}\,cm^{-3}$ dense plasma.

Because the pump depletion length is twice the dephasing length and much longer than the diffraction length, it is the least restrictive limit on the acceleration length. The only way to increase the energy of the witness bunch further, is to use a new laser pulse in a subsequent plasma accelerator stage. First experiments using a two-stage setup in LWFA have been conducted [115, 140, 182, 213]. However, to preserve the quality of the witness bunch during the transition between the plasma accelerator stages, specialized plasma profiles are required [160, 236] . The single-stage energy gain can now be deduced based on these estimates for the acceleration length and the maximum accelerating field.

The maximum energy gain and accelerated charge

The most severe limitation of the acceleration length from the phenomena discussed above is the diffraction of the laser pulse. Operating in the highly nonlinear and relativistic self-focusing regime, $P \geqslant P_c$, the acceleration length is determined by the dephasing length, and the maximum accelerating field is given by $E_{z,max} \simeq \sqrt{a_0}m_e c\omega_p/e$ (given in equation (69)). The dephasing of the witness bunch ends the acceleration approximately at the center of the bubble, where it has traveled approximately the same distance as the radius of the bubble, $R \simeq w_0$. Since the accelerating field decreases nearly linearly in the forward direction, the witness bunch experiences on average roughly half the peak field, $E_{z,max}/2$. The total energy gain (81) during one stage can

therefore be estimated by $\Delta W \approx \frac{2}{3} mc^2 \left(\frac{\omega_l}{\omega_p}\right)^2 a_0 \propto a_0/n$, assuming $L_{acc} = L_{deph} \approx \frac{2}{3}\frac{\omega_l^2}{\omega_p^2}R$, or in more practical units [146]

$$\Delta W[GeV] \approx 1.7 \left(\frac{P_l[TW]}{100}\right)^{1/3} \left(\frac{10^{18}}{n[cm^{-3}]}\right)^{2/3} \left(\frac{0.8}{\lambda_l[\mu m]}\right)^{4/3}. \tag{85}$$

Therefore, approximately $1.7\,GeV$ final energy is predicted by this formula for a $100\,TW$ Ti:Sa laser in a $n_p = 1 \times 10^{18}/cm^3$ dense plasma. Here, it is also evident that the achievable energy gain increases faster by lowering the plasma density, n_p, than by increasing the laser power, P_l. Decreasing the laser wavelength, λ_l, would have the largest impact on increasing the final energy, provided an corresponding laser is available. By equating the energy of the wakefield with the energy N particles absorb after acceleration over one dephasing length, the amount of charge that can be accelerated can be estimated as

$$Q[nC] \approx 0.40 \frac{\lambda_l[\mu m]}{0.8} \sqrt{\frac{P_l[TW]}{100}}, \tag{86}$$

assuming the matching conditions $k_p w_0 \simeq k_p R \simeq 2\sqrt{a_0}$ are fulfilled, again in practical units [146]. This shows that the previously assumed $100\,TW$ Ti:Sa laser is capable of accelerating approximately $0.4\,nC$ of charge, corresponding to 2.5×10^9 electrons. When comparing the energy of the driving laser, $W_l \propto a_0^2$, with the total energy that is contained in the witness bunch with N electrons of $\Delta W \propto a_0$ energy, the scaling of the overall energy efficiency can be derived, $N\Delta W/W_l \propto 1/a_0$. This shows that the overall efficiency decreases with the strength of the laser, as measured by the normalized amplitude of its vector potential, a_0. Physically, this can be understood as an increasing percentage of electrons being accelerated so much in the transverse direction by the high laser intensity that they do not return. These scalings for the expected energy and charge have been experimentally reproduced, and the approximate order of magnitude confirmed for a wide range of laser energies [157].

2.2.5 *Injection methods*

One fundamental difference of LWFA and PWFA is that the velocity of the plasma wave is typically slower in LWFA, as it equals the group velocity of the driving laser. This naturally leads to the possibility, that relativistic electrons can enter the wave from behind [31].

This *self-injection* occurs in the non-linear regime when the plasma wave breaks, and has produced the low-energy-spread bunches in the breakthrough experiments of LWFA [64, 74, 153]. Self-injection relies on the electrons that are statistically scattered into the plasma cavity by the extremely high-density peak at the point where electrons first cross the axis in the rear of the plasma cavity. The onset of self-injection was reported to coincide with a laser power exceeding three times the critical power

for relativistic self-focusing, $P_l > 3P_c$ [69], whereas the maximum charge is limited by beam-loading [75]. Until the beam-loading limit is reached, the wake continuously fills with electrons, resulting in a large energy spread. Low energy-spread bunches are only possible if self-injection can be confined within a small region. To apply other injection techniques and avoid self-injection that could contaminate the quality of the obtained witness bunch, it is necessary to either operate beyond the critical wave-breaking point, or suppress further self-injection via beam-loading. Bearing this in mind, many other ionization techniques have been proposed.

Ionization injection [36] was used to ionize high-ionization-threshold (HIT) states at the peak fields of the driving laser in high-Z gases [37, 43, 175], in a spatially confined dopant gas [140, 173], or in an injector stage which is separated from the accelerator stage [115, 182, 213]. More recently, *two-color ionization injection* of HIT electrons by a second trailing laser pulse was proposed to enhance the quality of the witness bunch, using different wavelengths for the driving and ionization laser [27, 201, 248]. Earlier, the use of a second laser to trap plasma electrons whose trajectories are altered by the laser's ponderomotive force was considered [227].

To start or enhance self-injection, a density decrease can be used, termed *density down-ramp injection* [31, 71, 215], e. g. to fully load the plasma wave at once, or to temporarily enable self-injection in a linear wakefield. An increasing plasma density can be used either to reduce or stop self injection in a nonlinear plasma wakefield. The required density transitions can be realized by locally heating a plasma using a strongly focused laser causing subsequent thermodynamic expansion [65], or by creating shock fronts with a sharp edge in a gas jet [199], or application of capillaries to longitudinally tailor the plasma density [81, 171]. All these techniques are of a hydrodynamic nature, and therefore rely on the movement of ions, which consequently prohibit a fast build-up process and are difficult to control precisely because of turbulence. Further injection techniques such as *colliding pulse injection* [60, 66, 70] and *external injection* [84, 103, 196], have been proposed and experimentally realized.

This completes the theoretical basis of LWFA that is needed for this thesis and which will be applied in the simulations section, chapter 6 of this work. In the following, a similar overview will be given for PWFA, where the key injection technique of this work, Trojan Horse, or underdense plasma-photocathode injection [93] (TH) injection, will be discussed. Thereafter, the possibility of combining the advantages of LWFA and PWFA in a *hybrid LWFA-PWFA scheme* will be discussed.

2.3 ELECTRON-BEAM-DRIVEN PLASMA WAKEFIELD ACCELERATORS

Plasma wakefield acceleration [38, 197] is of great interest since its first observation [194], mainly due to its major advantage over LWFA of being free from dephasing and not requiring additional guiding of the driver. Here, the plasma wave travels with the speed of the highly relativistic electron drive beam, which is approximately c, and once electrons are trapped, they do not change their position within the wakefield during acceleration. Therefore, the acceleration length is not limited by dephasing and, in addition, it is not limited by the divergence of the driver, thanks to the strong focusing fields within the plasma wave.

Unfortunately, the electron beams with high energy (several GeV) and high currents (several kA) needed to drive a PWFA are currently only available at a few conventional large-scale accelerator facilities. If an accelerator already exists, there seems to be no point in also having a PWFA facility. However, if the plasma accelerator can provide a better quality or a higher energy than its driver, the effort can be justified. This indeed can be achieved using the *Trojan Horse* injection technique, which promises to provide extremely high-quality bunches and was first demonstrated in a proof-of-principle experiment at Stanford Linear Accelerator Center (SLAC) [53]. The details of this injection technique will be discussed in this chapter after the introduction of PWFA.

Early experiments at SLAC demonstrated metre-scale acceleration in a lithium heat-pipe oven [96, 98, 104, 167] with multi-GeV energy gain [97] and investigated the acceleration and deceleration of the drive beam without injection of additional electrons. This led to the hitherto highest observed energy gain in a metre-scale plasma accelerator, doubling the energy of the rear part of the 42 GeV drive beam [21]. This "afterburner" concept proposes to use plasma wakefield acceleration to further increase the energy of an already accelerated electron bunch [129]. The latest milestone of PWFA was also accomplished at SLAC and showed for the first time the acceleration of a clearly separated bunch of significant charge over one GeV with low energy spread [139].

After the successful demonstration of PWFA at SLAC, European facilities such as the Compact Linear Accelerator for Research and Applications (CLARA) in the UK [41], and the Future-ORiented Wakefield Accelerator Research and Development (FLASH-Forward) at DESY [12] in Germany are joining the list of facilities available to contribute to this area of research. In addition, the accelerator test Facility (ATF) at Brookhaven National Laboratory (BNL) proposes to implement the Trojan Horse injection in their next upgrade of the electron beam-line [127, 181].

In PWFA, the driving force, $F_{sc}(r) = eE_r(r) \propto n_b$, of a Gaussian electron drive beam with peak density, n_b, is simply the bipolar *space-charge* field given in equation (29). The peak density of a Gaussian drive-beam, $n_b = N_b/((2\pi)^{3/2}\sigma_z\sigma_r^2)$, includes the number of electrons, $N_b = Q/e$, its length, σ_z, and its width, σ_r. As in the case of LWFA, in PWFA the strength of the driving force can induce the transition between the

linear and the nonlinear regime. Comparison of n_b to the plasma density, n_p, therefore gives a measure of whether the wakefield is linear, i. e. if $n_b < n_p$. A more accurate measure is given by the normalized beam charge [16, 192]

$$\tilde{Q} \equiv \frac{N_b k_p^3}{n_p} \qquad \begin{cases} \gtrsim 1 & \text{nonlinear wakefield} \\ \ll 1 & \text{linear wakefield} \end{cases} \qquad (87)$$

with N_b, the number of electrons in the drive-beam, n_p, the ambient plasma density, and k_p, the skin depth. $\tilde{Q}$ compares the total number of electrons of the drive-beam with the portion of the plasma electrons that can effectively react to the driver, $n_p k_p^{-3} \propto n_p^{-1/2}$, and is analogous to the a_0 parameter in LWFA. Like a_0, $\tilde{Q}$ is not related to the longitudinal or transverse size of the driver, so that additional conditions are required to excite the plasma wakefield resonantly. The maximum wakefield can be obtained for

$$k_p \sigma_z \simeq \sqrt{2} \qquad (88)$$
$$k_p \sigma_r \lesssim 1, \qquad (89)$$

when the electron drive beam is matched to the plasma density [104, 145]. The radius of the generated plasma cavity is approximately $R_{max} \approx \sigma_r \sqrt{n_b/n_p}$ [104]. Although an electron beam can more easily set up a plasma wave than a laser, its peak electric field is smaller, and therefore it is more difficult for an electron beam to ionize than it is for a laser (see equation (53)). Consequently, the plasma typically cannot be efficiently ionized by the PWFA driver and needs some form of pre-ionization. It was demonstrated that this can be achieved in a heat-pipe oven [167], or by a pre-ionization laser with an extended line focus (e. g. using an Axicon) [53]. Simulations show that a self-ionized PWFA is possible for a large drive-beam charge but indicate that only part of the driver can contribute to exciting the wakefield, resulting in *head erosion* [6, 240, 252].

2.3.1 *Attributes of electron beams*

A bi-Gaussian electron drive beam evolves in vacuum according to equation (31). In the following section, more aspects of its temporal development in plasma and magnetic fields will be discussed.

Phase space and emittance

One of the most important measures of the quality of an electron-beam is the *emittance* [67]. The full phase-space distribution includes all positions, (x, y, z), and momenta, (p_x, p_y, p_z), of an electron bunch and needs to be projected to provide a useful measure. This is usually done by taking statistical moments in both transverse directions, x, y, of the distribution (for details see chapter C) to obtain a simpler description

for the evolution of the electron bunch. As the description in both transverse directions is analogous, the following discussion only considers one direction, but equally applies for the other. Instead of the phase space $\{x, p_x\}$, one typically uses the identity $x' = dx/dz = p_x/p_z$ to measure the emittance in *trace-space* $\{x, x'\}$ [67]. The second trace-space coordinate, x', is equal to the divergence, $\theta = \arctan(p_x/p_z) \approx p_x/p_z$, when the paraxial approximation, $p_x \ll p_z$, applies. For a Gaussian bunch, the distribution in trace-space can be described by an ellipse of the form

$$\gamma x^2 + 2\alpha x x' + \beta x'^2 = \epsilon, \tag{90}$$

with $\pi\epsilon$, the area of the ellipse, and α, β, and γ, the *Twiss parameters* that are related to the shape and orientation of the ellipse as displayed in figure 8. The Twiss parameters
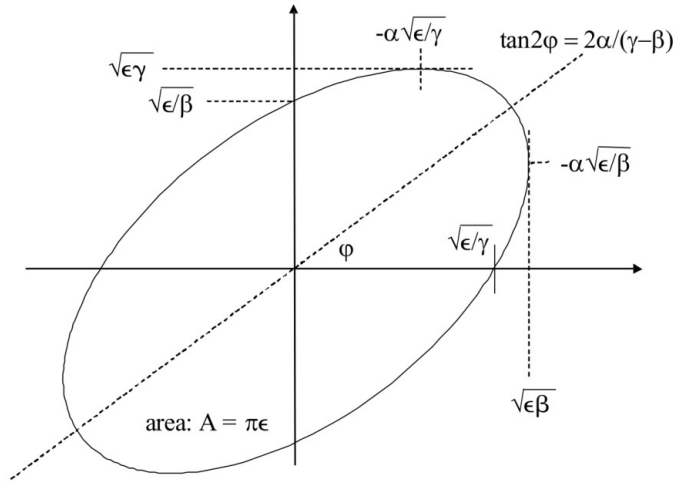

Figure 8: Phase-space ellipse of a Gaussian electron bunch, visualizing the meaning of the Twiss parameters (Picture taken from [238])

can be obtained by the second central moments of the trace-space distribution of N particles (for more details see Appendix chapter C)

$$\epsilon\beta = \sigma_x^2 = \langle x^2 \rangle \equiv \frac{1}{N}\sum_i x_i^2 - \left(\frac{1}{N}\sum_i x_i\right)^2$$

$$\epsilon\gamma = \sigma_{x'}^2 = \langle x'^2 \rangle \equiv \frac{1}{N}\sum_i x'^2_i - \left(\frac{1}{N}\sum_i x'_i\right)^2 \tag{91}$$

$$-\epsilon\alpha = \sigma_{x,x'} = \langle xx' \rangle \equiv \frac{1}{N}\sum_i\sum_j x_i x'_j - \left(\frac{1}{N}\sum_i x_i\right)\left(\frac{1}{N}\sum_j x'_j\right)$$

Because a tilted ellipse is fully described by three parameters, one of the four parameters α, β, γ, ϵ is redundant, and $\beta\gamma - \alpha^2 = 1$. The values of σ_x and $\sigma_{x'}$ correspond to the standard deviation of the electron distribution in the transverse direction, known as the bunch width, and the standard deviation of the divergence, x', respectively. The value of ϵ can now be identified with the rms trace space *emittance*

$\epsilon = \sqrt{\langle x^2 \rangle \langle x'^2 \rangle - \langle xx' \rangle^2}$, by inserting the Twiss parameters into $\beta\gamma - \alpha^2 = 1$. Because $x' = p_x/p_z$ decreases during acceleration (increasing p_z), this emittance is not constant and can be normalized by multiplication with the mean forward momentum

$$\epsilon_n = \frac{\langle p_z \rangle}{m_e c} \sqrt{\langle x^2 \rangle \langle x'^2 \rangle - \langle xx' \rangle^2}. \tag{92}$$

This definition is a good measure of the quality of an electron bunch because it neither changes under linear focusing fields nor during acceleration, and therefore only depends on the generation process of the bunch [36, 117]. Of course, these are idealized assumptions and the emittance is not always constant but might increase and deteriorate the bunch quality in an accelerator or transport beam line due to finite energy spread (phase mixing), thermal effects, and at density transitions e.g. at the exit of the plasma [68, 160, 162].

Another representation of the ellipse equation (90), is given by

$$\epsilon = \mathbf{x}^T \boldsymbol{\sigma}^{-1} \mathbf{x} = (x \quad x') \begin{pmatrix} \beta & -\alpha \\ -\alpha & \gamma \end{pmatrix}^{-1} \begin{pmatrix} x \\ x' \end{pmatrix} \tag{93}$$

were $\boldsymbol{\sigma}$ is the *beam matrix* and the area of the ellipse is given by $A = \pi\sqrt{\det\boldsymbol{\sigma}}$. From the above formalism, it can be seen that the $\boldsymbol{\sigma}$ matrix must have an invariant determinant $\det\boldsymbol{\sigma} = \epsilon^2 = \text{const.}$, which corresponds to the emittance, ϵ, and the area of the ellipse. Liouville's principle (49) states that the particle density in phase space does not change with time if the forces applied are conservative, which is generally fulfilled in particle accelerators. This is another reason why the emittance is conserved.

Equation of motion

The equation of motion of a single particle in a linear focusing field is given by

$$x''(z) + K(z)x(z) = 0, \tag{94}$$

where $K = k + \kappa_x^2$, with $\kappa_x[\text{m}^{-1}] = 0.2998|B[\text{T}]|/(\beta W[\text{GeV}])$, the local curvature of the trajectory, and the field gradient $k[\text{m}^{-2}] = 0.2998g[\text{T/m}]/(\beta W[\text{GeV}])$ (with B, and g, the magnetic field, and magnetic field strength, respectively, $\beta = v/c$, and W, the energy of the electron). For instance, the equations of motion for an electron inside an ion channel are $x'' + e^2 n_p/(2m_e\epsilon_0)x = 0$, and $K = e^2 n_p/(2m_e\epsilon_0)$. Assuming $K = \text{const.} > 0$, the solutions of equation (94) are

$$C(z) = \cos(\sqrt{K}z) \quad S(z) = \frac{1}{\sqrt{K}}\sin(\sqrt{K}z), \tag{95}$$

and for $K < 0$

$$C(z) = \cosh(\sqrt{K}z) \quad S(z) = \frac{1}{\sqrt{K}}\sinh(\sqrt{K}z), \tag{96}$$

which satisfy the initial conditions $C(0) = 1$, $S(0) = 0$, $C'(0) = 0$, and $S'(0) = 1$. The general solution can be written as

$$x(z) = C(z)x_0 + S(z)x_0', \tag{97}$$

$$x'(z) = C'(z)x_0 + S'(z)x_0', \tag{98}$$

were x_0 and $x_0' = dx_0/dz$ define the initial state of the electron [238]. The change of the trace space of an electron, $\mathbf{x}^\mathsf{T} = \{x(z)\ x'(z)\}$, along a beam transport line, can now be calculated in the matrix formalism [238]

$$\mathbf{x}_f = \mathbf{M}\mathbf{x}_i, \tag{99}$$

where the *transport matrix*,

$$\mathbf{M} = \begin{pmatrix} C(z) & S(z) \\ C'(z) & S'(z) \end{pmatrix} \tag{100}$$

is dependent on the type of beam-steering element, and the initial and final state is $\mathbf{x}_i$, and $\mathbf{x}_f$, respectively. The trace space of the electron bunch as a whole is therefore advanced from its initial state $\boldsymbol{\sigma}_i$ to its final state $\boldsymbol{\sigma}_f$ by

For more details see [195], [188], or [238].

$$\boldsymbol{\sigma}_f = \mathbf{M} \cdot \boldsymbol{\sigma}_i \cdot \mathbf{M}^\mathsf{T}. \tag{101}$$

The trajectory of an electron with the trace space coordinates $\{xx'\}$ in a beam transport line is governed by equation (99). This matrix can be used to describe the influence of various linear beam-steering elements, such as dipoles and quadruples. A drift space of length L, for example, can be represented by [238]

$$\mathbf{M}_0 = \begin{pmatrix} 1 & L \\ 0 & 1 \end{pmatrix}. \tag{102}$$

The transport matrix of a focusing quadrupole ($|k| > 0$) of length L is given by

$$\mathbf{M}_{QF} = \begin{pmatrix} \cos\phi & \sin\phi/\sqrt{k} \\ -\sqrt{k}\sin\phi & \cos\phi \end{pmatrix}, \tag{103}$$

with $\phi = \sqrt{|k|}L$, whereas a defocusing quadrupole ($k = -|k|$) is represented by the transport matrix

$$\mathbf{M}_{QD} = \begin{pmatrix} \cosh\phi & \sinh\phi/\sqrt{k} \\ \sqrt{k}\sinh\phi & \cosh\phi \end{pmatrix}. \tag{104}$$

The result from multiple beam elements of a beamline, e. g. the often used beam transport line consisting of a periodic focusing and defocusing lattice (FODO), is obtained by multiplication of all included transport matrices. The trajectory of an electron is than expressed as

Focusing is referred to the x direction.

$$\mathbf{x}_f = \mathbf{M}_{QF} \cdot \mathbf{M}_0 \cdot \mathbf{M}_{QD} \cdot \mathbf{M}_0 \mathbf{x}_i. \tag{105}$$

At a later point in this thesis, a beamline is designed based on this transport matrix. Although all these definitions are based on Gaussian distributions, they are used for arbitrary particle distributions and still represent a valuable measure of beam quality. For other distributions, the rms value no longer includes $\approx 68.27\%$ of the area.

Envelope equation

To follow the evolution of a Gaussian electron-bunch, the equation of motion of a single particle needs to be extended to the evolution of the beam envelope [195]. In equation (101), a formalism was constructed to determine the evolution of a bunch using the transport matrix **M**. However, to ease the inclusion of additional effects, it is more convenient to switch to a differential approach again. The derivatives of the transverse size, σ_x, of a Gaussian bunch are

$$\sigma'_x = \frac{d\sigma_x}{dz} = \frac{1}{2\sigma_x}\frac{\partial}{\partial z}\langle x^2 \rangle = \frac{\sigma_{xx'}}{\sigma_x}, \tag{106}$$

and,

$$\sigma''_x = \frac{1}{\sigma_x}\frac{d\sigma_{xx'}}{dz} - \frac{\sigma^2_{xx'}}{\sigma^3_x} = \frac{\sigma^2_{x'} + \langle xx'' \rangle}{\sigma_x} - \frac{\sigma^2_{xx'}}{\sigma^3_x} = \frac{\epsilon^2}{\sigma^3_x} - \frac{\langle xx'' \rangle}{\sigma_x}. \tag{107}$$

Applied to an electron bunch accelerated and focused inside a plasma wakefield, the *envelope equation*

$$\sigma''_r(z) + k^2_\beta \sigma_r(z) = \frac{\epsilon^2_n}{\gamma^2 \sigma^3_r(z)} \tag{108}$$

can be derived in analogy to equation (94), assuming an axially symmetric ($\sigma_x = \sigma_y \equiv \sigma_r$) Gaussian electron bunch in the paraxial approximation ($\beta_z \gg \beta_r$). Inside the blowout, the bunch undergoes *betatron oscillations* with period $\lambda_\beta = 2\pi/k_\beta$, and betatron frequency $\omega_\beta = ck_\beta = c\frac{k_p}{\sqrt{2\gamma}}$. The first pinching point (focus) of an electron beam inside the blowout can therefore be expected after $\lambda_\beta/2 = \pi/k_\beta$. The special case where the ion-channel focusing is balanced by the diverging trend and the bunch is therefore matched to the plasma, can be found by setting $\sigma''_r(z) = 0$ in equation (108), resulting in

$$\sigma_{r,eq} = \sqrt{\frac{\epsilon_n}{\gamma k_\beta}}. \tag{109}$$

Beam brightness and luminosity

The *normalized Brightness* [188]

$$\mathcal{B}_n = \frac{2I_p}{\pi^2 \epsilon_{n,x}\epsilon_{n,y}} \tag{110}$$

is a combined parameter that is designed to measure the quality of an electron bunch with peak current I_p, and normalized transverse emittances $\epsilon_{n,x}$, and $\epsilon_{n,y}$, whose maximization enhances achievable free-electron laser [126] (FEL) performance. Specifically

for FEL applications, the energy spread of the bunch plays a crucial role and therefore is included in the normalized *6D-Brightness* [54]

$$\mathcal{B}_{n,6D} = \frac{Q}{\epsilon_{n,x}\epsilon_{n,y}\epsilon_{n,z}},$$
(111)

where the longitudinal emittance, $\epsilon_{n,z}$, is added to include the effect of the energy (longitudinal momentum) spread. A higher 6D-Brightness allows FEL-operation at shorter wavelengths and using a shorter undulator. Similarly, the *Luminosity*,

$$\mathcal{L} = \frac{fN^2}{4\pi\sigma_x\sigma_y},$$
(112)

is one measure of the quality of an electron and a positron bunch for application in a collider, with the collision frequency, f. For both bunches, an equal number of particles, N, and equal transverse dimensions, σ_x, σ_y, are assumed. However, for a collider that is based on plasma wakefield acceleration, positrons also need to be accelerated, for which the accelerating and focusing phase is much smaller in nonlinear wakefields [203, 248], which means that it is more difficult to build.

Space-charge

Naturally, the compression of charged particles is made difficult by the repulsive electric Coulomb fields that are given by equation (32) for a Gaussian electron bunch. As discussed in the context of the propagation of charged particle beams, in section 1.2.4, this outward force is damped like $1/\gamma^2$ for relativistic particle beams. To decide whether the *space-charge* force or relativistic damping dominates for a given bunch, the *generalized perveance* [35, 187]

$$\mathcal{K} = \frac{I_p}{I_A}\frac{2}{\beta^3\gamma^3},$$
(113)

is defined, where I_A is the Alfvén current (36), and I_p is the peak current of the electron bunch; i.e. if $\mathcal{K} \ll 1$, the space-charge can be neglected. With. The repulsive space-charge force then results in the equation of motion for a single electron

$$r'' = \frac{\mathcal{K}}{\sigma_r^2}r,$$
(114)

and the envelope equation is given by

$$\sigma_r''(z) + k_\beta^2\sigma_r(z) - \frac{\mathcal{K}}{\sigma_r(z)} - \frac{\epsilon_n^2}{\gamma^2\sigma_r^3(z)} = 0$$
(115)

2.3.2 *Electron-beam-plasma interactions*

Interestingly, there are several driver-plasma interactions in PWFA that are similar to that of LWFA. The fundamental characteristics that are alike are the focusing and deceleration of the driver by the plasma, without which acceleration would not be sustainable. However, some instabilities such as hosing [56, 104, 237] or head erosion [252]

arise in both scenarios based on the mentioned similarities. Firstly, the most prominent effect of a plasma on electron beams, *plasma lensing* [176], will be discussed, which is similar to plasma guiding of laser pulses.

Plasma lensing

The focusing is caused by the interaction of a charged particle beam with a homogeneous plasma (passive plasma lens), or due to the external generation of strong cylindrical magnetic fields inside the plasma by high currents (active plasma lens) [228]. Generally, there are two different regimes, termed *underdense* ($n_p \ll n_b$) and *overdense* ($n_p \gg n_b$) plasma lensing. In the former, the ambient plasma density is less than the density of the electron bunch; for the latter it exceeds it. Using plasma to focus electron beams instead of conventional quadrupole magnets, has the big advantage that the focusing force is in principle unlimited[1] and focuses in both transverse directions simultaneously. High focusing strengths are crucial, as the Lorentz force is damped by $1/\gamma^2$ and therefore becomes increasingly ineffective for highly energetic electron beams. Plasma lenses are therefore promising candidates to work in combination with plasma accelerators, in order to provide for stronger acceleration and focusing than conventional magnet- and solenoid-based solutions.

Here, only passive, underdense ($n_p \ll n_b$) plasma lensing will be considered because it has the advantage over the overdense plasma lensing that the focusing strength only depends on the ambient plasma density (and not also on the bunch density). The criterion $n_p \ll n_b$ effectively puts an upper limit on the density of the plasma that can be applied for a given bunch and with it, on the achievable focusing strength. This condition equals that to set up a highly nonlinear plasma wakefield and the focusing fields inside the generated plasma channel with radius [104]

$$R_{max} \approx \sigma_r \sqrt{\frac{n_b}{n_p}} \tag{116}$$

Note, this differs from the condition to resonantly excite a wakefield, $k_p \sigma_z \sim 1$, and creates a long ion channel rather than a blowout.

are then exploited to guide the electron beam. The passive, underdense plasma lens is most effective for a thin, $k_p \sigma_r \ll 1$, and long, $k_p \sigma_z \gg 1$, bunch. This ensures that the bunch completely fits into the ion channel, i.e. $\sigma_r \ll R_{max}$ and the leading part of the bunch that does not propagate within the electron-free region can be neglected. The leading part of the beam that cannot be focused due to the finite time the plasma electrons need to react to the electron bunch's expelling space-charge force can be estimated to be approximately the plasma skin depth, k_p^{-1}.

The focusing force inside the ion channel is given by

$$F(r) = -\frac{e^2 n_p}{2\epsilon_0} r = -\frac{m_e}{2} \omega_p^2 r, \tag{117}$$

which is also the origin of the *betatron oscillations* that all bunches inside a plasma wakefield undergo during acceleration. To focus short bunches, $k_p \sigma_z \ll 1$, which are

---

1 Until the density cannot be further increased without loosing the properties of a plasma.

typical for plasma accelerators, an active plasma lens can be applied, i.e. within a discharge capillary. This has been experimentally exploited, for instance to focus a LWFA-generated bunch into a second plasma stage for post-acceleration [213, 228]. Further discussions on the focusing behavior of underdense plasma lensing can be found in [89, 104, 121] In the overdense case, $n_b \ll n_p$, the beam is focused by its own magnetic field, while its electric field is effectively screened by the plasma. Overdense plasma lensing can further increase the focusing strength on a given electron bunch. However, the focusing strength becomes also dependent on the bunch density. This implies that the focusing force is a function of the distribution of the charge of the bunch.

Physical limitations

Because in PWFA neither dephasing nor divergence limits the acceleration length, the depletion of the energy of the drive beam ultimately limits the acceleration length, provided other instabilities can be avoided. The *energy loss* of the drive beam can be immediately inferred from the physics of the blowout, discussed in section 2.1.1. It was shown in equation (61) that the radial current of the expelled electrons is directly connected to a longitudinal field, which is decelerating for electrons. The rate at which the electron drive beam is decelerated is therefore given by the maximum of the decelerating field, $E_{z,max}$. The driver will have lost all its energy when $eE_{z,max}L_{acc} = m_e c^2 \gamma_{driver}$. This limits the acceleration length to

$$L_{acc} \simeq \gamma_{driver} \frac{m_e c^2}{eE_{z,max}}. \tag{118}$$

In the case of positron drivers, the plasma electrons are "sucked in" before the first plasma cavity, resulting in a current in the opposite direction, and a field that, again, is decelerating for positrons.

The energy gain of the witness bunch is $eE_{z,max}L_{acc} = \gamma_{driver} m_e c^2 E_{z,max}/E_{z,min}$, where the transformer ratio $T = E_{z,max}/E_{z,min}$ (for symmetric drivers, $T \lesssim 2$) was used. Due to energy conservation, it is obvious that, for fully beam-loaded situations, where the witness bunch has as many electrons as the driver, the witness bunch cannot gain more energy than the driver. To achieve higher energies in the witness bunch, a high transformer ratio is needed and the witness bunch must contain significantly less charge.

2.3.3 *Injection methods*

Because in PWFA, in contrast to LWFA, the driver and plasma wake jointly propagate with approximately the speed of light in vacuum, for electrons it is not possible to enter the blowout from behind (self-injection). Therefore, the acceleration is dephasing free, so that better controlled injection techniques can be applied, and less unwanted charge, often referred to as *dark current*, can be trapped [150]. Three distinct methods have been investigated to inject electrons into PWFA: density down-ramp injection [84, 155, 215,

245], internal ionization injection [92–94, 137, 154, 242, 244] and external injection of a pre-accelerated bunch [85, 91].

So far, the internal underdense plasma photocathode injection, dubbed the "Trojan Horse" method, has drawn much attention and promises a controlled injection of electron bunches with very low emittance and very high brightness. Therefore, a special emphasis will be given to this injection method, which will be described in a separate section 2.4 and is used later in this thesis. Recently, a novel method to inject electrons into PWFA by applying a transverse ionization laser in front of the wakefield for controlled and fast injection was proposed by the author and others [240, 241] and will be discussed in chapter 3. First, however, the conditions needed for electron trapping will be derived, assuming that electrons are liberated inside the blowout and are initially at rest, as in the TH injection method.

Electron trapping

In order to inject electrons into the plasma wakefield, they must be accelerated to the same velocity as the wakefield within the length of its accelerating phase. Because the plasma wave's velocity is equal to the velocity of the electron drive beam, the injected electrons must gain the energy of the driver. However, thanks to the high field strengths and the small electron mass, the difference of the velocities becomes negligible very quickly and the electrons no longer change their relative position within the wakefield noticeably. It can be shown that in the quasi-static approximation

$$\frac{\partial}{\partial t}\left(\gamma - v_{ph}\frac{p_z}{m_e c^2} - \frac{e}{m_e c^2}\left(\Phi - v_{ph}A_z\right)\right) = 0 \tag{119}$$

is a constant of the motion, were γ is the relativistic factor, $p_z = \gamma m_e v_z$ is the forward momentum of the electron, Φ is the scalar potential and A_z is the longitudinal component of the vector potential of the wakefield [164]. With the definition of the *trapping potential*

$$\psi \equiv \frac{e}{m_e c^2}\left(\Phi - v_{ph}A_z\right) = \gamma - \gamma\frac{v_z v_{ph}}{c^2} - \text{const.} \, , \tag{120}$$

which is the third term of equation (119), the potential difference

$$\Delta\psi \equiv \psi_f - \psi_i = \gamma_f - \gamma_f\frac{v_f v_{ph}}{c^2} - \gamma_i + \gamma_i\frac{v_i v_{ph}}{c^2} \tag{121}$$

between the initial (subscript i) and the final (subscript f) state of an electron can be formulated. This allows the condition for trapping to be deduced by demanding that the final velocity of the injected electron must at least be equal to the velocity of the wakefield, $v_f \geqslant v_{ph}$. The required potential difference that the electron needs to traverse to gain this velocity then becomes

$$\Delta\psi \leqslant \frac{1}{\gamma_{ph}} - \gamma_i\left(1 - \frac{v_{ph}v_i}{c^2}\right), \tag{122}$$

with the relativistic factor of the wakefield, $\gamma_{ph} = (1 - v_{ph}^2/c^2)^{-1/2}$. In the simplest form, where the electron is initially at rest, $v_i = 0$, and the wakefield is highly relativistic, $\gamma_{ph} \gg 1$, the *trapping condition* reads

$$\Delta\psi \leqslant -1, \tag{123}$$

and it can be seen that any positive initial velocity, $v_i > 0$, would make trapping easier $\Delta\psi \leqslant -\gamma_i \left(1 - v_{ph}v_i/c^2\right)$. To meet this trapping condition, electron drive beams with high currents are required to excite a highly nonlinear wakefield that generates a deep trapping potential. For instance, considering electrons to travel approximately with the speed of the wakefield when they reached 99% of the speed of light ($\beta = 0.99$, $\gamma \approx 7$), they have an energy of $m_e c^2(\gamma - 1) \approx 3.6\,\mathrm{MeV}$. Therefore, the electron must pass a potential of approximately $3.6\,\mathrm{MV}$ within the plasma cavity to be trapped.

However, an easier way to make trapping possible, e. g. for an electron drive beam with lower current, is to apply a density down-ramp to locally reduce the phase velocity of the wakefield [119, 155]. In a homogeneous plasma, the phase velocity of the wakefield is constant and equal to the velocity of the driver. However, at a region of decreasing density, $dk_p/dz > 0$, the phase velocity is reduced to

$$\frac{v_{ph}}{c} = \left(1 + \frac{\xi}{k_p}\frac{\partial k_p}{\partial z}\right)^{-1}, \tag{124}$$

which can make $1/\gamma_{ph} = \sqrt{1 - v_{ph}^2/c^2}$ large enough to allow for trapping if $\Delta\psi \leqslant (1/\gamma_{ph}) - 1$. This allows self-injection of electrons via wave-breaking [71, 155, 240, 245], or enables TH-injection in an intermediate region using a softer ramp while self-injection is suppressed [119].

It is important to note that with the trapping condition (122), a condition was found that allows, but does not guarantee trapping. As only longitudinal dynamics has been considered so far, in addition it is required that the electrons are trapped at a position where the transverse field is focusing, which does not necessarily coincide with the first condition, e. g. at the rear of the blowout.

2.4 TROJAN HORSE WITNESS-BUNCH GENERATION

One of the most promising witness-bunch generation techniques that is available for plasma wakefield acceleration is the underdense plasma photocathode or "Trojan Horse" method [93]. Similar to the conventional photocathode [55], a tightly focused laser is used to release electrons, in this case, inside the blowout, where $\Delta\psi < -1$, to generate a high-quality electron bunch. In contrast to a conventional photoinjector, in the underdense plasma photocathode, the released electrons can be accelerated very quickly, thanks to the extremely high accelerating fields inside the plasma wakefield of up to hundreds of GV/m. This effectively prevents the deterioration of the emittance of the

witness bunch after ionization because the $1/\gamma^2$ damping of the Lorentz force quickly compensates the space charge and allows for emittances superior by orders of magnitude to conventional techniques.

For an electron source, bound electrons with a high ionization threshold (HIT) are needed inside the blowout. They should be neither affected by the ionization of the low ionization threshold (LIT) atoms that are required to constitute the plasma, nor by the wakefield itself. This is possible only in PWFA, because the fields of the electron drive beam that can set up a highly nonlinear wakefield are well below that of a laser that would excite a similar wakefield and keep states of moderate ionization energy un-ionized. Typically, the driving laser for LWFA can even ionize tightly bound electrons of high-Z atoms [175] and would therefore not leave much to ionize for a trailing ionization laser without requiring challenging laser wavelengths [201, 248] or intensities. The required two distinct ionization energies for TH injection can be that of
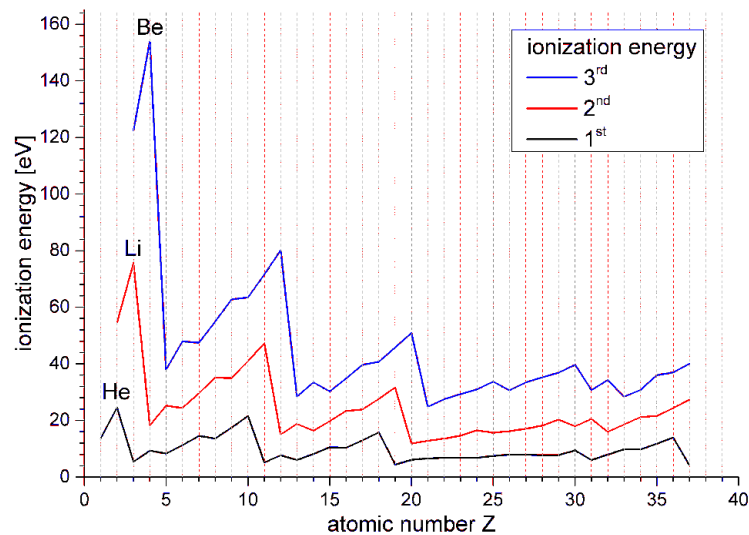

Figure 9: The first three ionization energies of atoms with increasing atomic number.

a single gas species, with a very low first, and a high second ionization energy, such as lithium, or two (or more) gas species, whose first ionization energies substantially differ, like lithium and helium. The use of two gas species has the big advantage that the density of the HIT component can be adjusted independently from the density of the LIT component, which is required to vary the amount of injected electrons. As can be seen from figure 9, the highest first ionization energies can be found for Z = 2(He), 10(Ne), 18(Ar), ..., corresponding to noble gases, which are therefore good candidates for the HIT component. However, in order not to deteriorate the emittance of the witness bunch, extremely high ionization energies should be avoided if possible. Immediately following are alkali metals, Z = 1(H), 3(Li), 11(Na), 19(K), 37(Rb), 55(Cs), ... that have the lowest first ionization energies and show a first ionization energy decreasing with higher atomic number. Alkali metals fortunately also have the highest second ionization energies and are therefore ideal candidates for operation with just one gas

LIT element (ξ_{ion}[eV])		HIT element (ξ_{ion}[eV])		energy gap [eV]	T_{boil}[° C]
ONE COMPONENT					
Li (5.39)		Li$^+$ (75.64)	(Li^{2+} (122.5))	70.25	1330
Rb (4.18)		Rb$^+$ (27.29)	(Rb^{2+} (40.0))	23.11	688
Be (9.32)	Be$^+$ (18.21)	Be^{2+} (153.9)	(Be^{3+} (217.7))	135.7	2969
TWO COMPONENTS					
H (13.6)		He (24.59)	(He$^+$ (54.42))	10.99	
Li (5.39)		He (24.59)	(He$^+$ (54.42))	19.2	1330
Rb (4.18)		He (24.59)	(Rb$^+$ (27.29))	20.41	688

Table 1: Example combinations of LIT and HIT components. To make the ionization of the gas that is required for the plasma wakefield as easy as possible, the lowest LITs are beneficial. The HIT component must stay un-ionized during the ionization of the LIT component, and in the vicinity of the driver and wakefield. Therefore, a sufficiently large energy gap and high HIT is required. The next ionization energy is plotted in parentheses in the central HIT column.

species. If a larger gap between the ionization energies or a larger HIT is required, the third ionization threshold can be used as HIT, and the first two ionization energies can both be combined in the LIT-component, e. g. using beryllium. This is needed when the driver has high, and possibly strongly varying field strengths as a result of betatron oscillations, for example. In fact, the electron drive beam used later in this work ionizes even the second electron of lithium at the beginning. However, to maintain the advantageous possibility for changing the HIT-component density independently from the LIT-component density, the fields of the driver must not ionize helium. For more details of possible LIT and HIT combinations see Table 1, and for a visualization of the available ionization energies see figure 9. Besides the ionization energy, other important chemical aspects such as toxicity, flammability, acidity, boiling temperature and formation of molecules must be considered.

As can be seen in figure 10, operating with hydrogen as LIT, and helium as HIT medium, provides only a narrow gap for useful field strengths for pre-ionization. Much broader gaps are available with Li as LIT component, and He, or Li$^+$ as HIT component. This would relax the restrictions on the allowable field strengths of the driver and makes pre-ionization of the LIT component much easier.

Figure 10 shows the part of the ADK-rate that is strictly valid (continuous lines) and also its continuation for $E > E_{c,ADK}$ (dashed lines). This illustrates that the used computational model for ionization fails with increasing field strength. The applied ADK-rate continues to increase rapidly before reaching a maximum at some $100 - 1000$ ionization
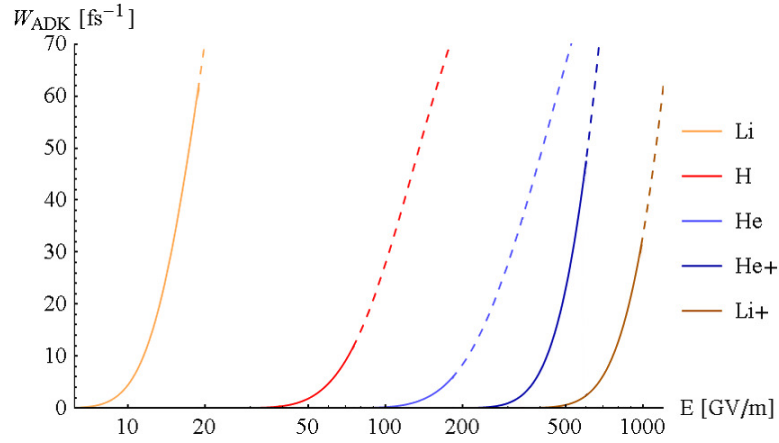
Figure 10: Rates for tunnel ionization from equation (53). The point where the field strength exceeds the critical field strength for ADK, (54) is shown by dashed lines (compare Table 2), whereas solid lines indicate that the ADK model is strictly valid.

events per femto-second (depending on the element under consideration, not shown here), and therefore must result in an underestimation of the ionized charge for significantly higher field strengths. This inaccuracy does not affect the amount of ionized charge if the field increases slowly enough for the ADK rate to fully ionize a gas before it looses its accuracy. However, it will make a difference at rapidly growing fields if BSI quickly becomes the dominant ionization process. A detailed overview of the corresponding values is given in Table 2.

2.4.1 *Features of the Trojan Horse injection method*

In the following, the correlation between the parameters of the TH-laser and the characteristics of the generated witness bunch will be discussed. In addition, two new approximations will be derived that estimate the amount of ionized charge and the scaling of the energy spread.

Ionized charge

A simple estimate of the amount of charge that is ionized by a focused Gaussian laser pulse can be obtained by assuming that the gas is fully ionized when the local laser field strength exceeds a critical field strength, E_c. The contribution of the wakefield to the total field strength will be considered to be negligible.

The envelope of the electric field of the laser is given by $\mathcal{E}_0(w_0/w(z))\exp\left(-r^2/w(z)^2\right)$ (see equation (16)). The positions where the laser field exceeds the critical field, E_c, can then be obtained by equating both field strengths. The result is the function

$$r(z) = w(z)\sqrt{\ln\left(\frac{\mathcal{E}_0}{E_c}\frac{w_0}{w(z)}\right)} = \frac{w_0}{z_R}\sqrt{(z^2 + z_R^2)\ln\left(\frac{\mathcal{E}_0}{E_c}\frac{z_R}{\sqrt{z^2 + z_R^2}}\right)}, \tag{125}$$

which describes the boundary of the ionization volume. The volume in which the laser field strength exceeds the critical field strength is therefore

$$V_{ion} = \pi\int_{-z_0}^{z_0} r(z)^2 dz = 2\pi\frac{w_0^2}{z_R^2}\int_0^{z_0}(z^2 + z_R^2)\ln\left(\frac{\mathcal{E}_0}{E_c}\frac{z_R}{\sqrt{z^2 + z_R^2}}\right)dz, \tag{126}$$

with $r(z_0) = 0$, and the length of the ionized volume in the lab frame

$$2z_0 = 2z_R\sqrt{\frac{\mathcal{E}_0^2}{E_c^2} - 1}. \tag{127}$$

The amount of ionized charge is $q_{ion} = en_{HIT}V_{ion}$, with n_{HIT}, the density of the HIT component. The analytical solution of the integral (126) gives the *ionized charge*

$$q_{ion} = en_{HIT}2\pi\frac{w_0^2}{9z_R^2}\left[6z_R^3\left(\arctan\left(\frac{z_R}{z_0}\right) - \pi/2\right) + \right.$$
$$\left. z_0\left(z_0^2 + 6z_R^2 + 3(z_0^2 + 3z_R^2)\ln\left(\frac{\mathcal{E}_0}{E_c}\frac{z_R}{\sqrt{z_R^2 + z_0^2}}\right)\right)\right], \tag{128}$$

which is a function of the laser (a_0 and w_0), the applied element-specific threshold, E_c, and the density of the considered species, n_{HIT}. Comparison with simulations show that this approach can overestimates the ionized charge by a factor up to 10 when $E_c = E_{c,BSI}$ (see equation (55)) is used. However, a good estimate for the critical field for full ionization is not easy and is not represented accurately by the simple approximations (54) and (55). Either way, the fundamental scaling of the ionization mechanism of the Gaussian laser pulse can be illustrated nicely with this simple approach.

The length over which the laser ionizes, $2z_0$, is a direct measure of the maximum *initial energy spread* of the trapped bunch. Because the first ionized electron has been accelerated over this distance before the last electron is ionized and becomes trapped at approximately the same position. In the following, the term 'initial' is used to denote the properties of the ionization volume, which correspond to the bunch characteristics before trapping. The maximum *initial bunch radius*,

$$\Delta r = r(0) = w_0\sqrt{\ln\left(\frac{\mathcal{E}_0}{E_c}\right)}, \tag{129}$$

in combination with the initial transverse momentum of the released electrons determines the emittance. The maximum *initial bunch length*,

$$\Delta\xi = \sigma_{z,l}\sqrt{2\ln\left(\frac{\mathcal{E}_0}{E_c}\right)}, \tag{130}$$

can be estimated by the distance between the center of the laser ($\xi = 0$, the most likely position of the first and last electron to be ionized), and the point where the longitudinal envelope of the laser at focus, $\mathcal{E}_0 \exp\left(-\xi^2/(2\sigma_{z,l}^2)\right)$, exceeds the critical field strength (approximately the position where the foremost electron will be ionized). The FWHM duration and length of the laser pulse are given by τ and $\sigma_{z,l} = v_g\tau/(2\sqrt{2\ln 2})$, respectively. The effect of variations of the laser peak amplitude, a_0, and spot radius, w_0, on the length of the ionized volume is depicted by the intersection with an assumed critical field, E_c (black line) in figure 11. As can be seen, the properties of the
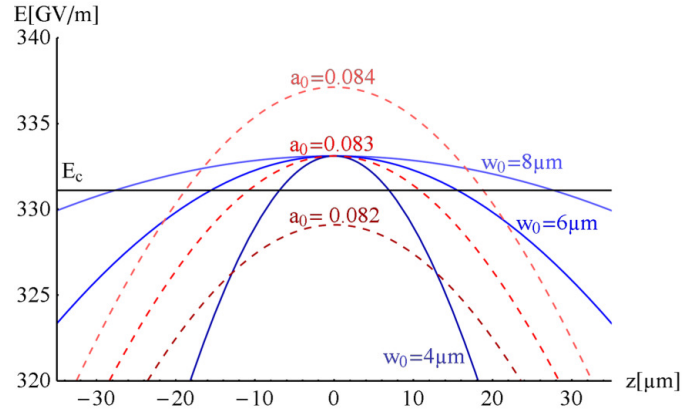

Figure 11: Evolution of the peak electric field strength of a Gaussian laser in the lab frame for different w_0 (blue), and a_0 (red) is shown, including an example threshold for the critical field strength (black line). For all blue curves $a_0 = 0.083$ and for all red curves $w_0 = 5\,\mu m$.

witness bunch, which are determined by the amplitude of the laser and the length and width of the ionized volume, are rather sensitive to the parameters of the TH-laser.

Relative energy spread

In a plasma wakefield accelerator in the highly nonlinear regime, the relative energy spread, $\sigma_W/\langle W \rangle$, of the witness bunch can either increase or decrease, with

$$\sigma_W = \sqrt{\langle W^2 \rangle - \langle W \rangle^2}, \qquad \text{and} \qquad \langle W \rangle = \sum_{i=1}^{n} p_i W_i, \tag{131}$$

were p_i is the probability of the energy W_i (for more details see Appendix chapter C). The relative energy spread decreases during acceleration when

$$\frac{d}{dt}\left(\frac{\sigma_W}{\langle W \rangle}\right) = \frac{\dot{\sigma}_W}{\langle W \rangle} - \frac{\sigma_W}{\langle W \rangle^2}\langle \dot{W} \rangle < 0 \quad \Leftrightarrow \quad \frac{\sigma_W}{\langle W \rangle} > \frac{\dot{\sigma}_W}{\langle \dot{W} \rangle}. \tag{132}$$

Because the relative energy spread is positive, $\frac{\sigma_W}{\langle W \rangle} > 0$, equation (132) is fulfilled when

$$\frac{d\langle W \rangle}{dt} > \frac{d\sigma_W}{dt}, \tag{133}$$

i. e. the energy increases faster than the energy spread. In the case of the blowout regime, the accelerating field is approximately linear over a wide range, $E_z(\xi) = E_0(k_p/2)\xi$, (see equation (62)) and the energy of an electron is given by $W = \beta_z c e E_z t$ ($E_z < 0$, $\xi < 0$, $e < 0$). Assuming a non-evolving wakefield and $\beta_z \approx 1$ for all electrons, the rate at which the mean energy of an electron bunch increases when it is accelerated by this field is given by

$$\frac{d\langle W \rangle}{dt} = \beta_z c e \langle E_z \rangle. \tag{134}$$

The linear accelerating field strength, $E_z(\xi)$, leads to a linear energy chirp, $W(\xi) = \beta_z c e E_0(k_p/2)t\xi$, which increases with time. From this, the connection between the energy spread and the bunch length $\sigma_W = \beta_z c e E_0(k_p/2)t\sigma_z$, and the rate at which the energy spread increases

$$\frac{d\sigma_W}{dt} = \beta_z c e E_0(k_p/2)\sigma_z = \beta_z c e \frac{dE_z}{d\xi}\sigma_z > 0 \tag{135}$$

can be inferred. Combining the results from equation (135) and equation (134), it can be seen that the relative energy spread decreases in a linear accelerating field when

$$\langle E_z \rangle > \frac{dE_z}{d\xi}\sigma_z. \tag{136}$$

The relative energy spread therefore decreases during acceleration when the accelerating gradient, $\frac{dE_z}{d\xi} = E_0(k_p/2)$, times the bunch length, σ_z, is smaller than the mean accelerating field, $\langle E_z \rangle$, at the trapping position of the witness bunch. Because the slope of the accelerating field increases with the density as $\frac{dE_z}{d\xi} \propto n_p$, while the amplitude of the wakefield increases only as $\langle E_z \rangle \propto E_0 \propto \sqrt{n_p}$, the energy spread and the relative energy spread can be lowered by operating at a lower density.

Emittance

The key feature that makes the underdense plasma photocathode a unique accelerator concept is its ability to produce bunches with an ultra-low emittance of $\epsilon_n \sim 10^{-9} - 10^{-8}\,\mathrm{m\,rad}$, and peak brightness values of up to $\mathcal{B}_n \sim 10^{19}\,\mathrm{A\,m^{-2}\,rad^{-2}}$, exceeding the quality of current RF accelerators by at least one order of magnitude [94]. The scaling of the emittance of a TH bunch before trapping was estimated as [93]

$$\epsilon_n \approx w_0 a_0/2^{3/2}, \tag{137}$$

assuming $\epsilon_n \approx \sigma_r \sigma_{p_r}/(m_e c)$. From this, it can be seen that the initial emittance for typical laser intensities required to ionize HITs, $a_0 \sim 0.1$ and $w_0 \sim 5\,\mu m$, would result in $\epsilon_n \sim 20\,\mathrm{nm\,rad}$. However, during the trapping process, phase mixing increases the emittance as $\epsilon_n \propto w_0^2$, still allowing for $\epsilon_n \sim 10^{-8}\,\mathrm{m\,rad}$-level emittances [201, 242]. Including the ionization dynamics of a linearly polarized laser and the influence of

phase mixing during trapping, the thermal emittances parallel and perpendicular to the plane of laser polarization are given by

$$\epsilon_{n,\parallel} = k_{\beta 0} w_0^2 \frac{a_0}{\lambda_l} \frac{3\pi r_e}{4\alpha^4} \left(\frac{\xi_{ion,H}}{\xi_{ion}} \right)^{3/2} \left(1 + \frac{2a_0^2}{(k_{\beta 0} w_0)^2} \right) \tag{138}$$

$$\epsilon_{n,\perp} = k_{\beta 0} w_0^2 \frac{a_0}{\lambda_l} \frac{3\pi r_e}{4\alpha^4} \left(\frac{\xi_{ion,H}}{\xi_{ion}} \right)^{3/2}, \tag{139}$$

where $k_{\beta 0} = k_\beta (z = 0)$, and $k_\beta = k_p / \sqrt{2\gamma}$, and the effect of the ponderomotive force is negligible, i.e. $a_0 \ll 1$.

Because the emittance scales with $w_0^2 a_0$, it increases together with the amount of ionized charge. Bunches with a low emittance typically also have low charge. A freely selectable HIT-component density however allows the emittance to be tweaked independently from the charge (and peak current), which is a key feature to optimize the FEL performance. Although electrons are most likely to be released at the peak field of the rapidly oscillating part of the laser pulse, some are also released some distance before or after it. This leads to a residual transverse momentum after the passage of the laser pulse, as the positive and negative transverse acceleration of the electrons in the field of the laser is no longer on average zero [131]. To minimize this effect, it is advisable to reduce the intensity of the ionizing laser to just slightly above the ionization threshold.

Ionization and trapping dynamics

Assuming that the laser pulse completely ionizes the HIT component on axis, the length over which the degree of ionization jumps from zero to one is significantly shorter than the laser pulse and the electrons are born essentially within a thin, curved surface that changes with time. The shifting of this ionization front with respect to the laser pulse not only determines the initial bunch length, but also results in a crescent-like shape of the initial longitudinal phase space of the generated witness bunch. The orientation of this crescent-like shape thereby depends on whether the TH-laser focus is located within the accelerating or the decelerating phase of the blowout. When the laser releases electrons within the decelerating phase of the wakefield in front of the blowout center, they are first accelerated in the opposite direction (backwards) until the longitudinal wakefield switches its sign. After that, they are slowed down until they stop at the same distance to the blowout center as their release position. From there on, the electrons quickly gain velocity in the forward direction at further increasing field strengths, and eventually become trapped. However, this reverses the order of the electrons—so that the first electron becomes the last and vice versa and the orientation of the crescent-like shape of the longitudinal phase space is reversed.

The first electrons to be free originate from near the center of the Gaussian laser pulse when its continuously increasing electric field strength increases the probability for ionization. While the peak intensity of the laser increases towards its focus, the ionization

front moves forward, whereas behind the focus, the ionization front goes back again and the last electrons are released at a similar position with respect to the laser pulse as the first electrons. However, the electrons that are freed and trapped first have gained energy in the meantime and are therefore separated from the last electrons in longitudinal phase space, which results in the crescent-like shape. This shape is distorted as the first electrons are trapped at the unperturbed accelerating field at the back of the blowout, while all electrons that arrive later feel the reduced combined field strength of the plasma wave and the trapped electrons. If the number of trapped electrons is large enough to cause a significant variation of the wakefield (beam-loading), this results in a shift of the trapping position for the subsequent electrons. Additionally, due to the linearly increasing accelerating field, the electrons at the back of the witness bunch are accelerated faster than those at the front and the longitudinal phase space is tilted throughout the acceleration (energy chirp). Interestingly, the combination of these processes can lead to a folding of the witness bunch in longitudinal phase space, which significantly increases the peak current at the knee.

Recently, the TH-method has been successfully demonstrated using the high-energy electron-beam at the Facility for Advanced Accelerator Experimental Tests, at SLAC [99] (FACET), which is now closed for an upgrade. This major milestone was enabled by the novel optical Plasma Torch technique that allowed for the required fs-level synchronization between the driver and the injection laser. The optical Plasma Torch technique was developed by the author and others [241] and will be discussed separately in chapter 3. The enhancement of the witness-bunch quality towards the theoretically possible, potentially game-changing quality of the Trojan Horse method is one key experiment in upcoming PWFA facilities such as ATF [180], FACET-II and FLASHForward [12].

2.5 THE HYBRID LWFA-PWFA SCHEME

All the discussed advantages of the Trojan Horse method, can only reach their full potential if an appropriate electron drive beam is available to set up a stable, highly nonlinear wakefield. Currently, only one facility, the Stanford Linear Accelerator Center, can provide a suitable drive beam, applying a conventional large-scale linear accelerator based on RF technology to accelerate a $\sim 3\,\mathrm{nC}$ electron beam to about $20\,\mathrm{GeV}$ of energy (for a list of other PWFA facilities see Table 8). Finding alternative PWFA drivers and making them more available and less expensive is therefore one key task in PWFA research. However, this particular field has not been investigated much until now, which leaves many possibilities open for investigation. This work can therefore only provide one part of the necessary research and will discuss how a beam produced in LWFA can be utilized to drive a PWFA. Previously, the transition from LWFA to PWFA within a single plasma stage was investigated by three-dimensional PIC simulations in

which the accelerated electrons drive a wakefield after the LWFA-drive laser has lost its capability to do so [174].

The number of PWFA facilities is small compared to the number of strong laser systems in operation that are capable of driving highly nonlinear plasma wakefields (as shown in Table 9 and figure 47). Making electron beams from LWFA available as drivers for PWFA, would therefore dramatically increase the number of PWFA-facilities. Also, the most severe limitations of LWFA, diffraction and dephasing, can be avoided in PWFA, where witness bunches with potentially much higher quality can be generated via Trojan Horse injection [94, 242].

The driving space-charge force in PWFA is directly proportional to the electric field of the electron-beam, $F_{sc} = eE$, whereas the ponderomotive force, $F_p \propto \nabla(\mathbf{E}^2)$ depends on the gradient of the square of the electric field of the laser pulse in LWFA.

The characteristic length for the divergence in vacuum of an electron bunch, $\beta^* = \sigma_{r,0}^2 \gamma/\epsilon_n \sim 1\,\mathrm{m}$, is significantly longer than that of a laser pulse, $z_R = w_0^2 \pi/\lambda_l \sim 1\,\mathrm{mm}$, for typical parameters. Besides the less pronounced divergence, the electron beam is automatically focused by the plasma and can excite a dephasing-free plasma wave much more efficiently than a laser pulse. This makes a particle beam a significantly better driver for plasma wakefield acceleration than a laser pulse. In particular, beams from LWFA are well suited to drive a PWFA, because they are already very compact and the high energy spread and emittance, which are typical in LWFA, do not spoil the capability of driving a PWFA. Another big advantage is the inherent synchronization between the laser of the LWFA stage and the drive beam of the PWFA stage, which can be used for the synchronization for the TH injection, which is otherwise very challenging. And, last but not least, after it has lost its capability to drive a plasma wakefield, the laser from the LWFA stage could be re-used to pre-ionize part of the second PWFA stage, which is difficult for an electron beam. Now, the requirements for a LWFA beam to be able to drive a PWFA will be discussed.

Producing drivers for PWFA in LWFA

In order to set up a highly nonlinear wakefield ($\tilde{Q} \gg 1$, see (87)), the PWFA drive beam must have a larger charge and peak current than typical LWFA experiments, which reported $\sim 10 - 100\,\mathrm{pC}$, using lasers with energies of a few joules. This is related to the fact that the experiments were designed to produce quasi mono-energetic beams with a good emittance to match the requirements of typical applications. On the other hand, a higher laser power would have been required to accelerate more charge (see equation (86)). However, theory and simulations show that it is possible to generate high-energy, high-charge electron beams in LWFA that are potentially well suited as drivers for PWFA [105, 156, 230]. From detailed PWFA-TH simulation studies with several plausible LWFA bunches, it was found that the drive beam must have at least $0.5\,\mathrm{nC}$ of charge for TH injection to function properly (using a spherical drive beam with $\sigma_x = \sigma_y = \sigma_z = 7\,\mu\mathrm{m}$, and $I_p \approx 8.5\,\mathrm{kA}$). For drive beams with a lower charge, the trapping condition can be fulfilled, but because the wakefield is only slightly nonlinear,

the part of the wake that is simultaneously focusing and accelerating is small and trapping at defocusing fields may occur.

Besides a high charge of the drive beam, a sufficiently high energy is important to sustain the wakefield and to take advantage of the possibility of a longer acceleration length compared to LWFA. To accelerate a witness bunch to more than $1\,\text{GeV}$, which is the chosen minimum energy required for the FEL in this work, the drive beam should have at least the same energy, assuming the effective transformer ratio to be $T \sim 1$ (see equation (70)). The minimum energy that is required for the drive laser in the LWFA stage can be estimated by the energy that is required for the drive beam in the PWFA stage, which can easily be calculated from its total charge and energy via $W_t[J] = Q[nC]W[GeV]$. However, when considering that the overall efficiency of plasma wakefield acceleration is typically only a few percent, the energy of the drive laser must be chosen proportionally higher.

The effective transformer ration is dependent on the trapping position of the witness bunch and beam-loading.

For example, the electron beam at FACET has approximately $3\,\text{nC}$ of charge and $20\,\text{GeV}$ of energy, which is equivalent to a $60\,\text{J}$ laser pulse. Therefore, to accelerate a similar electron beam in a LWFA stage, a laser with significantly more energy than $60\,\text{J}$ would be required. On the other hand, the drive-beam charge and energy that is indeed necessary for PWFA is somewhat lower than that of the FACET driver; i. e. an optimal driver would have around $1\,\text{nC}$ and $10\,\text{GeV}$. The energy of the drive laser that is required to accelerate this electron beam (with $1\,\text{nC}$, and $10\,\text{GeV}$), can therefore be estimated to be $\sim 100\,\text{J}$, assuming the overall efficiency of the LWFA to be $\sim 1\%$. The energy of $10\,\text{GeV}$ for the PWFA drive beam was chosen to approximately balance the need for a stable and long acceleration enabled by the high energy of the drive beam with the necessity to keep the energy of the drive laser within reasonable limits.

Transportation of the LWFA beam

One of the challenges of plasma wakefield accelerators is to capture and transport the witness bunch behind the plasma, because of the typically large divergence, possibly large charge, high energy spread and large shot-to-shot variance [138, 205]. To transport and focus a LWFA beam into a PWFA using conventional methods, is therefore not easy. Experimentally, the separation of a LWFA into an injector and an accelerator stage without beam-steering elements between the plasma stages has been realized, by putting both plasma stages immediately next to each other [140, 182] and producing energies as high as $3\,\text{GeV}$ [115]. Recently, one group demonstrated the transport of an electron beam, using an active plasma lens between two LWFA stages, which were separately driven by two laser pulses [213]. This showed, for the first time, that the coupling of multiple laser wakefield accelerators is possible to achieve higher energies. The setup of this experiment could also easily be used as a hybrid LWFA-PWFA accelerator.

To drive a PWFA, the beam must enter the plasma stage with approximately the correct length to efficiently set up the wakefield (88) and with small enough transverse

dimensions (89) to fit into the blowout. In order to compensate the high transverse momenta of the electrons from LWFA, and to prevent them from escaping from the plasma cavity, a minimum focusing force, $F(r) = -e^2 n_p/(2\epsilon_r)$, and thus density is required in the PWFA. The usable densities of the PWFA stage are therefore determined by the dimensions and the divergence of the generated electron beam. For TH injection, the field strength of the beam must be large enough to enable trapping by setting up a nonlinear wakefield (see (122)), but it must not ionize the HIT species, and ideally, the electron drive beam should be able to pre-ionize the LIT species. To match these requirements, the plasma density and the LIT and HIT species must be chosen appropriately, e.g. using lithium and helium to ensure a broad gap between the ionization energies.

However, if the driver is able to ionize the HIT species, it is not difficult to lower its peak field strength by just letting it diverge in a free drift space. When entering the PWFA stage, part of the drive bunch is then outside the wakefield and no longer contributes to driving it. This can effectively lower the peak field below the HIT and also has the advantage that the drive-beam electrons that are still within the blowout, have a reduced divergence, p_r/p_z, and a higher mean energy, $W \propto p_z^2$. The velocity at which electrons with different energies diverge (or focus) can be increased by the use of the chromatic dispersion of a plasma lens, e.g. for beams with a high energy and accordingly low divergence. However, when energies beyond a certain threshold are truncated, the bunch length is shortened due to the energy chirp.

A detailed discussion of the choices for the simulation parameters will be given in chapter 6 and chapter 7, where three-dimensional simulations are conducted, including all important physical aspects of both plasma stages. In the following chapter, the concept of the optical Plasma Torch injection will be introduced.

OPTICAL PLASMA TORCH INJECTION

The optical Plasma Torch injection was recently introduced by the author and others [240, 241]. This technique is primarily applicable in PWFA, but with some changes it is also viable in LWFA. Compared to other injection methods in PWFA (other than TH), it provides the possibility for high repetition rates and most interestingly, an easy setup that can be aligned and optimized very well until high witness-bunch quality is achieved. The alignment and synchronization is done between the electron drive beam and a laser pulse, and it is therefore also well suited as an intermediate step towards more advanced setups that require a very precise alignment and synchronization such as TH. That is why this technique became a crucial part of the setup of the experimental campaign E210 at FACET that eventually established Plasma Torch and Trojan Horse injection. With the Plasma Torch, it was not only possible to successfully inject charge into a PWFA setup, but also to provide the critical, precise synchronization in the proof-of-principle experiment of Trojan Horse. Due to this great success, the Plasma Torch is also planned to become a part of future experiments, e.g. at the FLASHForward facility.

3.1 FUNCTIONAL PRINCIPLE

The technique uses a moderately intense and focused laser that crosses the axis of the drive beam perpendicularly in a plasma wakefield accelerator (see figure 12). The laser pulse arrives before the electron drive beam and ionizes a high ionization threshold species at the region of its focal point that stays neutral in the vicinity of the fields of the electron drive beam and its wake.
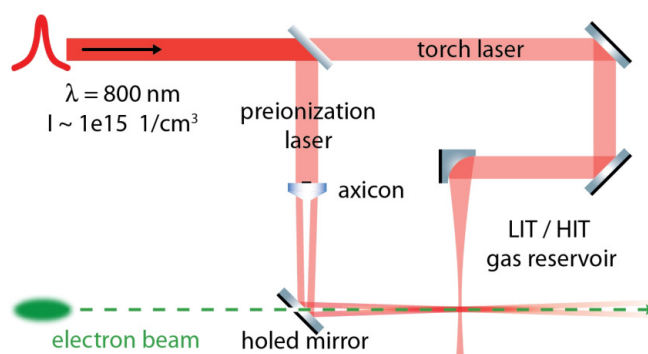

Figure 12: Schematic of the experimental realization of the optical Plasma Torch technique.

The plasma column thereby created, picturesquely named "*optical Plasma Torch*" is very well adjustable in its density, width and position by adjusting the background gas density and the laser. Importantly, it can be adjusted independently from the parameters of the PWFA. During the interaction with the drive beam and wakefield, a controlled injection into the blowout is possible when electrons at the boundary of the plasma wave enter a region where they can continue to be accelerated in the forward direction.

This technique has the advantage that it is easy to get injection, even with badly aligned geometry, and synchronization on the few ns level, by applying a wide laser spot, or shifting the focal position to increase the possible interaction region. It is therefore a very fast and easy method to achieve injection, and allows the generation of high-quality electron bunches, as well as alignment and synchronization of a laser to the electron drive beam. Even if no charge is injected into the wakefield, a deflection of the drive beam could be measurable [104, 166].

Once the signal of the injected charge in seen, the alignment can be adjusted down to the order of 10 microns, enabling high-quality witness-bunch generation, and very good alignment and synchronization that can facilitate advanced injection and acceleration concepts. Naturally, the injection vanishes if the ionizing laser arrives later than the drive beam at the interaction point. This gives the opportunity to reduce the delay until the laser arrives exactly as the plasma wake is produced, making it possible to ionize directly within the wakefield. This creates the possibility to achieve Trojan Horse injection, as only the laser intensity has to be lowered to ionize just within the blowout (for the Trojan Horse method, a lower laser intensity is required when compared to the Plasma Torch).

3.2 DIFFERENT IMPLEMENTATION POSSIBILITIES

Beam-driven plasma-wakefield accelerators can be operated in two modes: either the background gas has to be ionized in front of the drive beam; or, if the drive-beam space-charge fields exceed the ionization threshold of the background gas within a radius larger than the blowout, it may ionize the plasma itself, and simultaneously drive the wakefield. Further, a second gas species with a significantly higher ionization potential can be added to provide the possibility to locally create additional plasma when higher field strengths are applied. As regards the capability of an electron beam to ionize, it must have a comparatively high charge in order to be able to exceed even low ionization thresholds and its space-charge fields must extend over a sufficiently large radius. This is possible only for high-current electron beams (on the order of $10\,\mathrm{kA}$), which also introduces more possible sources of unwanted injected charge from the HIT, gas if present. Also, for the typical Gaussian-like drive beam, the ionization

occurs only near the center of the drive beam at peak electric-field strengths, leaving the head of the beam unused for driving the wakefield, and subject to free transverse expansion. On the the other hand, only the lowest ionization threshold media such as lithium (5.39 eV), or rubidium (4.18 eV) can be utilized. This implies several challenges, such as the need to vaporize it first and toxicity. These issues have been addressed in the first self-ionized PWFA experiments at FACET [167, 173] where a lithium-helium mixture was used and helium ionization and subsequent trapping at driver lensing positions has been shown.

Considering the self-ionized scenario, the Plasma Torch scheme works with a different physical mechanism than in a pre-ionized plasma, based on the fact that the ionization front is not at the beam front but near its center for a Gaussian-like beam. In this case, Plasma Torch injection is possible even when the local plasma column exhibits the same density as in the wakefield, using just one gas. When the drive-beam enters the pre-ionized region of the Plasma Torch, the blowout is shifted to the front of the drive-beam, where no plasma would be otherwise. Thus more drive-beam current contributes to set up the wakefield, resulting in a higher accelerating gradient and amplification of the blowout. At the exit of the Plasma Torch, the blowout shifts back until its front (and the ionization front) is near the drive-beam center again, while the accelerating field is still amplified at the back of the blowout. This creates the possibility that charge can enter the blowout from behind, which is quickly accelerated to relativistic energies and becomes trapped.

In the second possible scheme of pre-ionized PWFA, the torch laser ionizes a HIT component, and therefore the wakefield interacts with locally increased density. This shortens the plasma-wave cavity during passage, and allows electrons to enter from the rear of the plasma cavity as well, similar to the well known density-downramp injection method [215]. The change of the torch density can vary the amount of injected charge—not possible in a single-component gas, where the torch density cannot be adjusted independently from the wakefield. Also a mixed scheme is possible, where a self-ionized PWFA setup is applied and the torch laser ionizes the LIT as well as an additional HIT component, leading to a double-trapezoid plasma-density profile and an injection mechanism that is a combination of both previous cases. For a detailed discussion and simulation results of all cases see [240] and [241].

Using a laser to generate a locally increased plasma density comes with the big advantage that extremely short and sharp ramps can be produced, favorable also with regard to the time scales at which the ramp can be generated, compared with other hydrodynamical solutions that have been applied so far. Density ramps that are short compared to the plasma wavelength are required for effective injection [215].

Because the plasma density profile is a direct measure of the applied laser-intensity profile, it can be controlled very well and even more complex shapes can be realized if required. The delay between the plasma torch and the arrival of the electron bunch

allows the ramp edges to be softened, as equilibration of the plasma density sets in. The relaxation time depends on the plasma density and the temperature of the electrons. This temperature can be regulated by the laser, as electrons exhibit an initial momentum after ionization, and can be additionally heated by absorption due to inverse Bremsstrahlung. Consequently, the most stable optical Plasma Torch is generated if the applied laser power is only slightly above the ionization threshold, and electrons within it stay cold, so the duration of the Plasma Torch is only limited by the recombination time.

Using a high-power laser and applying a delay on the few ns level will set up a strong non-equilibrium state followed by a hydrodynamic equilibration process that can be used to inject electrons also in LWFA. After ionization and heating, the electrons dissipate into the colder surrounding plasma, leaving an electron-depleted region on axis. Ions therefore begin to follow, creating two steep density peaks along the plasma wakefield accelerator axis after $1-2\,ns$ [65]. The whole relaxation process leads to a temporal density evolution that can be compared with the waves on a water surface after throwing a stone into it, where the highest wave occurs immediately after the excitation, featuring the mentioned double-peak profile.

3.3   PLASMA-TORCH TRAPPING CONDITIONS

In the following, only the pre-ionized scenario will be considered, as it clearly provides the best stability and controllability besides producing the highest quality witness bunches [240].

As has been shown in the case of the injection of electrons into the blowout, the trapping condition, $\Delta\psi \leqslant \frac{1}{\gamma_{ph}} - \gamma_i\left(1 - \frac{v_{ph}v_i}{c^2}\right)$, also dependents on the phase velocity of the wake, v_{ph} (and $\gamma_{ph} = (1 - v_{ph}^2/c^2)^{-1/2}$). This phase velocity $\frac{v_{ph}}{c} = \left(1 + \frac{\xi}{k_p}\frac{\partial k_p}{\partial z}\right)^{-1}$ is a function of the density gradient, and density ramps can therefore facilitate trapping.

Given a strong drive beam that can excite a nonlinear wakefield for which the trapping condition (122) is fulfilled within a significant portion of the blowout, naturally trapping disappears when the perturbation exerted by the Plasma Torch becomes too weak. This is the case if the ratio of the Plasma Torch density, and the background density becomes too small, or if the Plasma Torch is too short. Thus, one important figure of merit is the ratio of torch width, L_T, to plasma wavelength within the torch $\lambda_{p,T}$, which should be bigger than one.

$$L_T > \lambda_{p,T} \tag{140}$$

However, the occurrence of trapping is also dependent on the strength of the plasma wave (and therefore its driver) and its capability to quickly accelerate electrons to a relativistic velocity. The inference might therefore be formulated as

"Trapping occurs if the blowout fits into the Plasma Torch ($L_T > \lambda_{p,T}$), and its rear is located at a position where electrons would have been trapped if they were released at this position outside the Plasma Torch ($\Delta\psi < -1$)".

The last part of this condition ensures that the driver is strong enough to excite a wakefield that can trap electrons.

In the following, a simulation series will be shown where a FACET-type drive beam (23 GeV energy, 2% total energy spread, 1 nC of charge and 2.25 mm mrad normalized rms emittance) drives a plasma wake in a pre-ionized hydrogen plasma as LIT medium of 1×10^{16} cm^{-3} density, and helium as HIT medium whose density was varied from 0.1×10^{16} cm^{-3} to 10×10^{16} cm^{-3}. The diameter of the Plasma Torch stays approximately the same at $\approx 400\,\mu m$, while the torch density is altered from 1/10 to 10 times the background density. For the helium densities from 0.1 to 0.6×10^{16} cm^{-3}, no trapping was observed. For helium densities from 0.6 to 1×10^{16} cm^{-3}, electrons were trapped at a position too far towards the rear of the blowout, where they were radially pushed outside the blowout again by its defocusing fields.

This behavior is illustrated in figure 13, where the ratio of helium density to hydrogen density is plotted against the amount of stably trapped charge (left), and the position of the first trapped electron (right). Note that the torch density is $n_H + n_{He}$, but only the helium density was varied, so for convenience the aforementioned ratio of torch density to background density $(n_H + n_{He})/n_H$ is simplified to n_{He}/n_H. The simula-
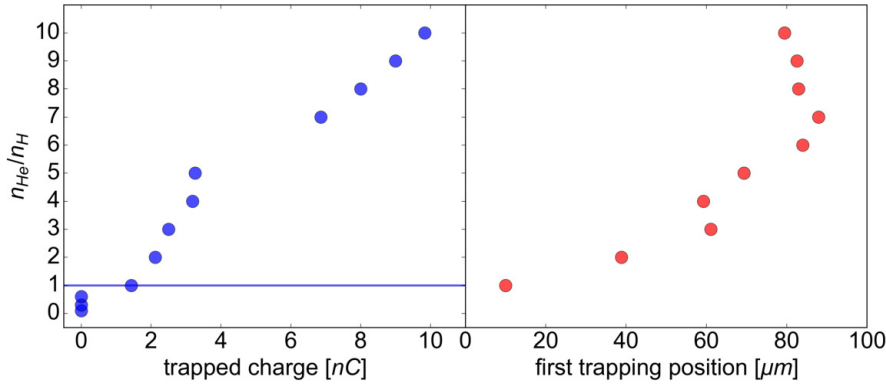
Figure 13: The amount of stably trapped charge behind the torch as a function of density within the torch (left), and the position of the first trapped electrons (right). The threshold for stable injection for a FACET-type driver was $n_H = n_{He} = 1 \times 10^{16}$ cm^{-3} (blue line).

tion with $n_{He} = 6n_H$ was removed due to technical difficulties. After stable trapping sets in at $n_H = n_{He} = 1 \times 10^{16}$ cm^{-3}, the trapped charge scales approximately linearly with the helium density until beam-loading forbids further injection (not yet reached in the figure).

The right sub-figure shows that, in addition to increasing the trapped charge, increasing the density of the Plasma Torch also shifts the trapping position of the foremost electron closer to the blowout center, and longer witness bunches are generated.

It can also be seen in this figure that there is a first and a last possible trapping position in the blowout, limited at the rear by the point were the transverse fields switch to defocusing, and at the front by the distance that electrons need to become trapped when coming from the blowout center. This can be understood as a consequence of the shrinking of the blowout inside the torch when the helium density is increased. So electrons are situated further towards the front of the blowout—compared with a scenario with less helium density—which is their starting point for forward acceleration and trapping when leaving the Plasma Torch. So the higher the helium density within the Plasma Torch, the smaller the plasma blowout and the earlier the trapping position.
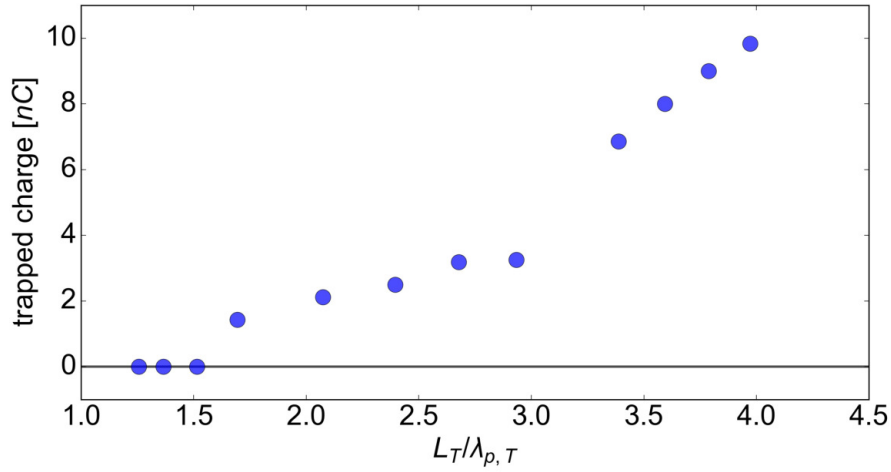

Figure 14: Stably injected charge against the Plasma Torch diameter in units of the plasma wavelength inside the torch, showing that it is not sufficient that the blowout fits inside the Plasma Torch ($L_T/\lambda_{p,T} = 1$) to get injection, but also the driver strength must be taken into account. For $L_T/\lambda_{p,T} \lesssim 1.7$ no stable injection was found.

In conclusion, the amount of trapped charge increases with increase in density within the Plasma Torch up to several nC's, so the wakefield behind the first cavity is mostly compensated by the wakefield of the trapped charge, and only one plasma cavity exists. The ratio of the density within, and outside the Plasma Torch—or the ratio of both plasma wavelengths—also determines the position of the leading edge, and the length of the witness bunch. Further, it is not sufficient that the blowout fits into the length (and width) of the Plasma Torch ($L_T/\lambda_{p,T} > 1$), as shown in figure 14. Depending on the drive beam, the blowout must be significantly smaller than the diameter of the Plasma Torch, which means a higher density of the HIT component. Using a FACET-type drive beam, stable trapping has been observed for $L_T/\lambda_{p,T} \gtrsim 1.7$.

Smaller Plasma Torch density provides the opportunity to produce very short witness bunches, with less charge (compared to the observed nC-level) and trapping in further plasma-wave buckets becomes possible. However, if the trapping position is too far towards the rear of the blowout, the transverse defocusing fields of the blowout can lead to complete destruction of the witness bunch. The witness bunch quality that has been achieved in the simulation series shown above was at the single digit mm mrad emittance level, and the energy spread shortly after the torch was on the order of 10% to several 10%, at approximately $10\,\mathrm{MeV}$ energy. The best witness bunch properties that have been measured in the computer simulations so far were from a bunch with $257\,\mathrm{pC}$ charge, $25\,\mathrm{MeV}$ energy, and 6.4% energy spread, $2.7\,\mathrm{mm\,mrad}$ emittance, and $3.62\,\mathrm{kA}$ peak current extracted $10\,\mathrm{mm}$ after the Plasma Torch [240]. Note that the work discussed here was focused on showing the injection process and resulting witness-bunch quality, but did not consider the acceleration, during which the total energy spread can be continuously decreased (see equation (172)). Further enhancements of these results are possible, for instance with controlled beam loading by applying special Plasma Torch profiles. Also, previous research was performed based only on a strong FACET-type drive beam (of $1-3\,\mathrm{nC}$ charge and many GeV's of energy); varying the driver properties and background plasma density could therefore be another way to enhance the quality of the resulting witness bunch.

4

THEORY OF FREE ELECTRON LASERS

4.1 INTRODUCTION

One promising application of the high-energy, low-emittance TH-bunches is the generation of high-power (GW), short-wavelength (Å) radiation in a free-electron laser (FEL) [126]. The FEL contains an undulator, a long structure of magnets with a periodically switching orientation of the magnetic field (visualized in figure 15). When traversing the undulator, the electrons are forced into a sinusoidal trajectory and therefore emit radiation in the forward direction. The wavelength of this radiation is proportional to the undulator period over the square of the energy of the bunch $\lambda_r \propto \lambda_u/\gamma^2$, and therefore very short wavelengths can be generated. For example, for $\gamma = 1000$ (corresponding to an electron energy of $\approx 511\,MeV$), an undulator period of $\lambda_u = 1\,cm$, and an undulator parameter of $a_u \approx 1$, the emitted radiation has a wavelength as small as $5\,nm$. One other major advantage over conventional laser systems is that the generated wavelength can be continuously tuned by easily accessible parameters. This is one reason why FELs are of growing interest today.

For a comprehensive list of current FEL facilities see http://www. lightsources. org/fels
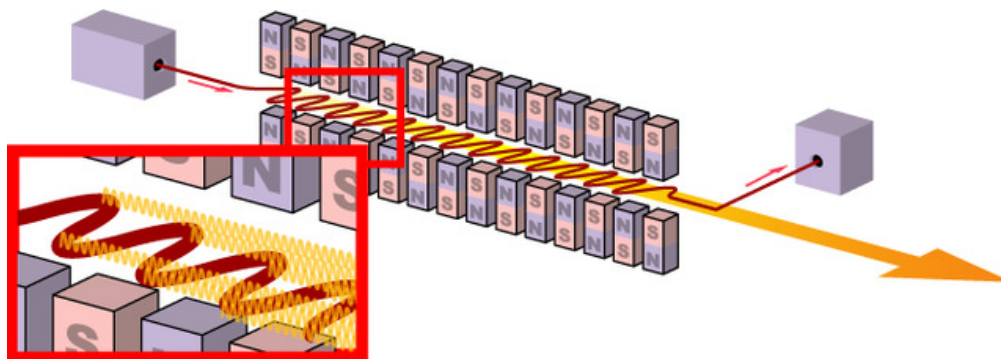

Figure 15: FEL principle by Horst Frank, XFEL.

However, other than conventional laser systems, the FEL requires a very high-quality electron bunch the production of which, so far, needs a large-scale accelerator. Plasma-based accelerators could thus help to make FELs less expensive, more available and smaller. Because the size of the accelerator cavity is much smaller in a plasma-based accelerator than in a conventional accelerator and the accelerating fields are much stronger, the slope of the accelerating field is much steeper. Therefore, an accelerating bunch must either be accordingly shorter in a plasma-based accelerator, or it will feel a larger difference in the accelerating fields within the bunch, which significantly changes the energy gain between the front and the back. Bunches that are accelerated

in a plasma wakefield have therefore typically a large correlated energy spread (chirp), which can be compensated by letting the bunch propagate through a reversed field slope. Even without the compensation of the correlated energy spread, the FEL-process is possible if the fractional energy spread (which is the energy spread within a slice of the bunch), is low enough [204]. In addition, the bunch parameters must be adjusted behind the plasma to match the requirements of the FEL, in particular the large divergence needs to be lowered. Using a plasma accelerator to drive a FEL is therefore not as easy as using a conventional accelerator. First experiments have already shown undulator radiation from bunches produced by plasma wakefield accelerators [72, 198], but for the FEL, significant advances in the quality of the accelerated bunches are required [45].

4.2   ELECTRON MOTION IN AN UNDULATOR

This description mainly follows the well written formalism of [200]. If electrons with the total relativistic energy $\gamma m_e c^2$ are forced onto a sinusoidal trajectory by an altering magnetic field, a periodic transverse acceleration is induced due to the Lorentz force (see equation 13).

$$\gamma m_e \dot{\mathbf{v}} = -e\mathbf{v} \times \mathbf{B}, \tag{141}$$

where $\dot{\mathbf{v}} = \frac{\partial \mathbf{v}}{\partial t}$. Assuming a planar undulator, the magnetic field on the symmetry plane $y = 0$ is given by

$$\mathbf{B} = -B_0 \sin(k_u z)\mathbf{e}_y \tag{142}$$

where B_0 is the magnetic field amplitude, $k_u = 2\pi/\lambda_u$ is the undulator number, and $\mathbf{e}_y$ denotes the unity vector in the y direction. Then, the electron motion is determined by two differential equations of second order

$$\ddot{x} = \frac{e}{\gamma m_e} B_y \dot{z}, \qquad \ddot{z} = -\frac{e}{\gamma m_e} B_y \dot{x}. \tag{143}$$

With the approximation that the velocity in the forward direction is constant $\dot{z} \approx \beta c$ (and $\ddot{z} \approx 0$) throughout the sinusoidal motion, and much faster than the transverse component of the velocity $\dot{z} \gg \dot{y}$,

$$x(t) = \frac{eB_0}{\gamma m_e \beta c k_u^2} \sin(k_u \beta c t), \qquad z(t) = \beta c t \tag{144}$$

Defining the start of the undulator at $z = 0$, $x(0) = 0$ and $\dot{x}(0) = eB_0/\gamma m_e k_u$ results in

$$x(z) = \frac{K}{\gamma \beta k_u} \sin(k_u z), \tag{145}$$

introducing the *undulator parameter*

$$K = \frac{eB_0}{m_e c k_u} = 0.934 \, B_0[\text{T}] \, \lambda_u[\text{cm}] \tag{146}$$

which is one of the key parameters of FELs. It is proportional to the magnetic field strength B_0, and the undulator period $\lambda_u = 2\pi/k_u$ and is a measure of the amplitude of the sinusoidal motion. With this definition, the mean velocity in the forward direction can be expressed as $\bar{v}_z = c\left(1 - \frac{1}{2\gamma^2}\left(1 + \frac{K^2}{2}\right)\right)$. The maximum cone of the emitted radiation, $\Theta_{max} \approx K/\beta\gamma$, is proportional to the undulator parameter, and $1/\gamma$ is the instantaneous opening angle of the radiation from relativistic electrons in a magnetic field. If the opening angle of the undulator motion of the electrons is smaller than one over gamma ($\Theta_{max} \leqslant 1/\gamma, \quad \beta \approx 1 \quad \Rightarrow K \leqslant 1$), the radiation of many positions on a trajectory along the undulator spatially overlap in the forward direction. Consequently, interference of the radiation on axis results in a narrow spectral bandwidth of the fundamental wavelength and its odd higher harmonics. These are the characteristics of the *undulator*, defined by $K \leqslant 1$. This condition usually is a bit relaxed and K-values of 2 or 3 are still counted as undulators.

In a *wiggler*, the amplitude of the oscillatory motion is increased, and thus $K \gg 1$. Here, the cone of the emitted radiation covers a larger angle, the intensity has a minimum on axis, the bandwidth is broader, and the total photon output increases, while the intensity of the fundamental wavelength decreases. As is evident from equation (145), the electron motion in the transverse direction is a sine, with period $k_u/2\pi$ and amplitude of $K/\gamma\beta k_u$, if the small longitudinal oscillation is ignored ($\dot{z} \approx$ const). Thus, to first order, the electron will emit dipole radiation with power

$$P_1 = \frac{e^2 c\gamma^2 K^2 k_u^2}{12\pi\epsilon_0(1 + K^2/2)^2},\tag{147}$$

which is independent of the considered system (moving or stationary). Because this formula does not include the effect of the longitudinal motion, it describes only the power of the first harmonic. The total power of the spontaneously emitted undulator radiation can be derived by summing over all angles and all harmonics

$$P_{total} = \frac{e^2 c\gamma^2 K^2 k_u^2}{12\pi\epsilon_0},\tag{148}$$

and is consistent with the formula for synchrotron radiation. This formula is also valid for wiggler radiation, where the power is increased proportional to K^2, whereas the power contained in the first harmonic decreases as $1/K^2$.

The bandwidth, $\delta\omega/\omega$, of the fundamental wavelength, $\lambda = 2\pi c/\omega$, of the undulator radiation ($K < 1$) decreases with the number of undulator periods, N_u, as

$$\frac{\Delta\omega}{\omega} \approx \frac{1}{N_u}.\tag{149}$$

The angle at which the first harmonic is emitted decreases as well with the number of undulator periods as

$$\sigma_\Theta \approx \frac{1}{\gamma}\sqrt{\frac{1 + K^2/2}{2N_u}},\tag{150}$$

where σ_Θ denotes the rms deviation of the angle of the emitted radiation, Θ. From equation 150, it can be seen that the fundamental wavelength of undulator radiation is significantly better collimated than pure synchrotron radiation, namely by a factor of approximately $1/\sqrt{N_u} \ll 1$.

To better understand why an undulator is capable of producing coherent light, the path differences of the emitted radiation must be considered. Only wavelengths that overlap at an integer multiple of their own wavelength after one undulator period can propagate in the undulator. All other wavelengths interfere destructively. The path difference is also a function of the angle Θ. This restricts the propagation in the forward direction, $\Theta = 0$, to odd harmonics. Near the axis, $\Theta \approx 0$, the wavelengths of the spontaneous undulator radiation are given by

$$\lambda_m = \frac{\lambda_u}{2m\gamma^2}\left(1 + a_u^2 + \gamma^2\Theta^2\right) \quad m = 1,3,5\ldots, \tag{151}$$

with $a_u^2 = K^2/2$ for planar undulators and $a_u^2 = K^2$ for helical undulators. Note that $\lambda_m = \lambda_1/m$, and λ_1 is proportional to λ_u/γ^2, where γ denotes the electron energy, λ_u the undulator period, K the undulator parameter given by equation 146, and Θ is the angle with respect to the propagation axis z. As $\Theta \approx K/\gamma$, the last term in equation 151 is negligible for large gamma. For radiation observed slightly off axis, $\Theta > 0$, all harmonics can occur, $m = 1,2,3\ldots$. The emitted radiation is linearly polarized in the plane of the electron motion for a planar undulator, or circularly polarized for helical undulators.

To transfer energy from the electron to the light wave, the time derivative of the energy of the electrons must be negative

$$dW/dt = -ev_x(t)E_x(t) < 0. \tag{152}$$

This is the case if the transverse velocity of the electron, v_x, and the electric field, E_x, point into the same direction. If this is the case at some point, the light will continue to move forward with c, while the average speed of the electron is $\bar{v}_z = c(1 - (2 + K^2)/(4\gamma^2)) < c$. A continuous transfer of energy is therefore only possible if the transverse velocity of the electron always points into the same direction as the electric field of the light wave. This can be achieved if the phase of the light wave advances by an optical wavelength, λ_r, within one undulator period, λ_u, and the difference of the electron and light travel time fulfills $c\Delta t = c(1/\bar{v}_z - 1/c)(\lambda_u/2) \overset{!}{=} \lambda_r/2$. Rearranging this requirement gives

$$\lambda_r = \frac{\lambda_u}{2\gamma_r^2}\left(1 + a_u^2\right), \tag{153}$$

the only wavelength which provides a sustained energy transfer from an electron with the resonant energy $\gamma = \gamma_r$ to the light wave. The equivalence of equation (151) for $\Theta = 0$, and (153) is an extremely important finding. It means that the resonant wavelength for continuous energy gain of the light wave exactly matches the wavelength

of the undulator radiation in the forward direction. This is the reason why spontaneous undulator radiation can be used to seed the FEL process, enabling self-amplified spontaneous emission (SASE).

In equation 146, the longitudinal motion is neglected, leading to the undulator parameter K. Discarding the assumption of the longitudinal motion being constant, $v_z = v_z(t)$, the modified undulator parameter

$$\widehat{K} = K \left[J_0 \left(\frac{K^2}{4 + 2K^2} \right) - J_1 \left(\frac{K^2}{4 + 2K^2} \right) \right] \tag{154}$$

can be derived, where J_0, and J_1 are Bessel functions of zeroth and first order, respectively. The modified undulator parameter, $\widehat{K}$, is always smaller than K. Note that in a helical undulator, the longitudinal motion is constant and therefore the use of K is justified. Including the oscillatory therm in the longitudinal motion, not only enables the generation of higher harmonics but also has an influence on the gain of the fundamental wavelength, but not on the wavelength itself.

4.3 HIGH-GAIN FEL

For simplicity, only planar undulators will be considered in the following. By using a planar undulator, one direction of the bunch is dominant and can be chosen to be the plane of better bunch quality in case there is a difference, e. g. due to laser polarization. The power of the emitted undulator radiation is [159]

$$P \propto \left| \sum_{j=1}^{N} E_j e^{i\psi_j} \right|^2 = \sum_{j=1}^{N} E_j^2 + \left| \sum_{j=1}^{N} \sum_{k=1}^{N} E_j E_k e^{i(\psi_j + \psi_k)} \right|_{k \neq j}^2 \tag{155}$$

where

$$\psi = (k_u + k_l)z - \omega_l t + \psi_0 \tag{156}$$

is the *ponderomotive phase* of the emitted radiation (k_l, ω_l, and ψ_0 denote the wave number, frequency and the initial phase of the emitted light, respectively), E_j the electric field and $N \gg 1$ the number of electrons. Keeping the ponderomotive phase constant, $d\psi/dt = (k_u + k_l)\overline{v}_z - \omega_l = 0$, is another way to determine the resonant wavelength in equation (153). The first part of the right-hand side of equation (155) is linearly proportional to the number of electrons, $\propto N$, while the second part lets the power increase with the square of the number of electrons, $\propto N^2$. If all electrons have different phases, the second term is small and tends to interfere destructively. This is the case at the start of the FEL process, where incoherent radiation is generated and the total power is approximately the sum of the emitted power of N independent electrons. To profit from the second, potentially much larger term, the phases of all electrons must be correlated such that $\psi_j \approx \psi_k$, which requires that all electrons are periodically bunched

at the resonant wavelength, λ_r. Then, the power increases with N^2, and the radiation is coherent. This constitutes the high-gain regime and justifies calling it a "free-electron laser".

4.3.1 First-order equations

To model the full FEL process, the evolution of the electric field and the phase space of the electrons must be computed. The temporal development of the phase can easily be obtained by taking the derivative of equation (156) $d\psi/dt = (k_u + k_l)\bar{v}_z - \omega_l$, resulting in equation (160). The rate at which the phase of the n-th electron advances is therefore only dependent on the energy of this electron and the undulator period $\lambda_u = 2\pi/k_u$.

As an electron with the resonance energy, γ_r, constantly transfers energy to the light wave, it looses energy and therefore shifts out of resonance. A measure of this energy detuning is given by the relative energy deviation

$$\eta = \frac{\gamma - \gamma_r}{\gamma_r}, \tag{157}$$

where γ_r is the resonance energy, which is coupled to the resonance wavelength by equation (153), and $\gamma = \gamma(t)$ is the energy of the electron that is subject to deceleration. The temporal development of the energy deviation, $d\eta/dt = (1/\gamma_r)(d\gamma/dt)$ is the second important equation that is required to compute the evolution of the FEL process.

The tilde will mark complex quantities in the following.

The energy transfer rate, $d\gamma/dt$, can be determined starting from equation (152), with $W_r = \gamma_r m_e c^2$, considering the complex amplitude of the electric field in the transverse and forward directions to account for the coupling to the light wave and the space charge, respectively. Adding both effects and applying the slowly varying amplitude approximation (which is justified by $\lambda_u \gg \lambda_l$) results in

$$\frac{d\eta}{dz} = -\frac{e}{m_e c^2 \gamma_r} \Re\left[\left(\frac{\hat{K}\tilde{E}_x}{2\gamma_r} + \tilde{E}_z \right) e^{i\psi} \right]. \tag{158}$$

With

$$\tilde{E}_z(z) = -\frac{i\mu_0 c^2}{\omega_l} \tilde{j}_1(z) \tag{159}$$

equation (161) follows. In equation (161), the complex modulated amplitude of the current, $\tilde{j}_1(z)$, of the electron bunch given in equation (163) was used. Note, the current

density can be derived from $j_z = v_z \rho$. The complete set of coupled first-order 1D FEL equations is given by

$$\frac{\partial \psi_n}{\partial z} = 2k_u \eta_n \qquad n = 1...N \tag{160}$$

$$\frac{\partial \eta_n}{\partial z} = -\frac{e}{m_e c^2 \gamma_r} \Re \left[\left(\frac{\widehat{K} \tilde{E}_x}{2\gamma_r} - \frac{i\mu_0 c^2}{\omega_l} \tilde{j}_1 \right) e^{i\psi_n} \right] \tag{161}$$

$$\frac{\partial \tilde{E}_x}{\partial z} = -\frac{\mu_0 c \widehat{K}}{4\gamma_r} \tilde{j}_1 \tag{162}$$

$$\tilde{j}_1 = 2j_0 \frac{1}{N} \sum_N^{n=1} e^{-i\psi_n} \equiv 2j_0 \left\langle e^{-i\psi_n} \right\rangle \equiv 2j_0 b \tag{163}$$

where $\tilde{j}_1 = 2j_0 b$ contains the *bunching factor* $b = \left\langle e^{-i\psi_n} \right\rangle$. As electrons with different phases gain energy from, or lose energy to, the light wave, they begin to periodically bunch depending on their phase. The modulated current distribution thereby induced takes this change of the electron distribution into account by the bunching factor, $0 \leqslant b \leqslant 1$, which is a measure of the obtained phase correlation (see also equation (155)) and enables the high-gain regime. At saturation, the electron distribution has reached the maximum possible bunching that degrades from there on and the energy is transferred from the light wave back to the electrons.

The set of coupled equations (160-162) describes the evolution of the ponderomotive phase ψ_n, the relative energy deviation η_n of the n-th electron, complex modulated current density $\tilde{j}_1$ and the complex amplitude of the radiation field $\tilde{E}_x$, along the undulator axis, z. A periodic (or continuous) electron beam along the undulator is assumed in this set of equations and the drive beam diameter, r_b, is assumed to be large (i.e. $r_b \gg \sqrt{L_{g0} \lambda_l}$, where the gain length, L_{g0}, will be defined in equation (169)). The main physics of the high gain FEL is included in this set of equations; however, no analytical solution is known. Containing micro-bunching, and saturation, these equations can already describe the most important phenomena of the FEL, but the SASE mode cannot be modeled. To predict important quantities like the growth rate of the emitted power, these 1D equations will be generalized in the next section to allow an arbitrary phase-space distribution of the electron bunch.

The set of $2N + 2$ coupled equations (160-163) cannot be solved analytically, and therefore must be integrated numerically. This is done by the fully time-dependent three-dimensional FEL code [186] (GENESIS) that will be used in chapter 8 to simulate the FEL process.

4.3.2   *Third-Order equation*

The set of coupled 1D equations can be transformed into one third-order equation and solved analytically by first-order perturbation theory. A treatment at higher orders would allow for the generation of higher harmonics which are excluded in the present

analysis. First-order perturbation theory can be applied, and the ponderomotive phase, ψ, and the energy spread, η, can be eliminated from the equations, if the density modulation is assumed to be small. This results in the third-order equation of the electric field [200]

$$\frac{\tilde{E}_x'''}{\Gamma^3} + 2i\left(\frac{2k_u}{\Gamma}\eta\right)\frac{\tilde{E}_x''}{\Gamma^2} + \left(\frac{k_{sc}^2}{\Gamma^2} - \left(\frac{2k_u}{\Gamma}\eta\right)^2\right)\frac{\tilde{E}_x'}{\Gamma} - i\tilde{E}_x = 0, \tag{164}$$

which has the advantage that it can be solved analytically. In equation (164), two important parameters have been introduced: the FEL *gain parameter*

$$\Gamma = \left[\frac{\mu_0 \widehat{K}^2 e^2 k_u n_e}{4\gamma_r^3 m_e}\right]^{1/3}, \tag{165}$$

and the *space-charge parameter*

$$k_{sc} = \sqrt{\frac{2k_u \mu_0 n_e e^2 c}{\gamma_r m_e \omega_l}} = \sqrt{\frac{2\lambda_l}{\gamma_r \lambda_u}} \frac{\omega_p}{c}. \tag{166}$$

Usually, the influence of the space charge can be neglected for highly relativistic electron beams, $\gamma \gg 1 \Rightarrow k_{sc} \ll \Gamma$, but even for $k_{sc} = 0.5\Gamma$, the gain length (which will be introduced in equation (169)) is only increased by about 10%.

The coefficient of the relative energy deviation, η, in equation (164) is combined in the famous *FEL, or Pierce parameter* [23, 159]

$$\rho_{FEL} = \frac{\Gamma}{2k_u} = \frac{1}{2\gamma_r}\left(\frac{I_p}{I_A}\right)^{1/3}\left(\frac{\widehat{K}\lambda_u}{\sqrt{2}2\pi\sigma_r}\right)^{2/3}. \tag{167}$$

This is the central parameter in FEL theory and connected to all important physical quantities of the FEL process. The simplest form of equation (164)

$$\frac{\tilde{E}_x'''}{\Gamma^3} - i\tilde{E}_x = 0 \tag{168}$$

is obtained when a mono-energetic ($\eta = 0$), high-energy bunch ($k_{sc} = 0$) is assumed. This simplified equation can be solved with the trial solution $\tilde{E}_x(z) = A e^{\alpha z}$ that leads to $\alpha^3 = i\Gamma^3$, and the general solution $\tilde{E}_x(z) = A_1 e^{(\Gamma/2)(i+\sqrt{3})z} + A_2 e^{(\Gamma/2)(i-\sqrt{3})z} + A_3 e^{-i\Gamma z}$. The real part of this solution is the electric field, and the A_i's are defined by the initial conditions. Only the first eigenvalue of this solution, $\tilde{\alpha}_1 = (i + \sqrt{3})\Gamma/2$, has a positive real part and for large z, leads to an exponential growth of the amplitude of the electric field with power $P(z) \propto |\tilde{E}_x|^2 \propto e^{\sqrt{3}\Gamma z} \equiv e^{z/L_{g0}}$. Now, the important question of how fast the emitted radiation is amplified can be answered, introducing the *ideal gain length*

$$L_{g0} = \frac{1}{\sqrt{3}\Gamma} = \frac{1}{\sqrt{3}2k_u\rho_{FEL}}. \tag{169}$$

This gain length assumes a one-dimensional, highly relativistic electron beam without energy spread. In any realistic FEL, this length is larger because of a finite bunch length,

non-zero energy spread, space charge, betatron oscillations, and radiation diffraction. In this thesis, the formalism of M. Xie [243] is used to estimate the realistic gain length, L_g, of a three-dimensional bunch, including radiation diffraction, the electron-beam transverse emittance and energy spread.

4.4 CHARACTERISTIC FEL PARAMETERS

So far, the exponential growth of the radiation power was discussed, during which the average energy of the electron bunch decreases. The relative energy spread grows at a similar rate as the power, $\sigma_\gamma/\gamma \simeq \rho_{FEL}(P/P_{sat})$, due to the discrete nature of the spontaneous photon emission over a broad energy spectrum (the saturation power, P_{sat}, will be defined in the following). Consequently, the energy of the electrons leaves the resonant bandwidth of the undulator at some point, marking the end of the exponential growth and, thereafter, energy is pumped back from the light wave to the electrons. The distance after which this occurs is reached when $\sigma_\gamma/\gamma \gtrsim \rho_{FEL}$, and is called the *saturation length*. Huang et. *al.* [101] estimated this length to be

$$L_{sat} \approx \frac{\lambda_u}{\rho_{FEL}} = 4\pi\sqrt{3}L_{g0} \approx 21.8L_{g0}, \tag{170}$$

however, it is more common to assume $L_{sat} \approx 20L_{g0}$. The *saturated radiation power* can be estimated by

$$P_{sat} \approx \rho_{FEL}P_b, \tag{171}$$

with $P_b = I_0\gamma_b m_e c^2/e$, the power that is initially contained in the electron bunch. The Pierce parameter can therefore be seen as the overall efficiency of the FEL, which is typically on the order of 10^{-3}. The bandwidth of the undulator radiation decreases with the distance in the undulator as $\sigma_\omega/\omega = 3\sqrt{2}\rho_{FEL}\sqrt{L_{g0}/z} \propto z^{-1/2}$ and is $\sigma_\omega/\omega \approx \rho_{FEL}$ at saturation. A highly efficient FEL therefore produces a broad spectrum.

Similarly, the energy detuning of the electrons that can be tolerated by the undulator is $\eta \lesssim \rho_{FEL}$. In contrast to the space-charge parameter, the energy spread σ_γ/γ (and relative energy deviation $\eta = (\gamma - \gamma_r)/\gamma_r$) has a significant influence on the gain length of the FEL. While a mono-energetic bunch ($\sigma_\gamma = 0$) reaches the ideal value of the gain length, L_{g0}, for $\sigma_\gamma/\gamma = 0.5\rho_{FEL}$, the gain length is already 25% larger than the ideal gain length. For $\sigma_\gamma/\gamma = \rho_{FEL}$, the gain length already increases by more than a factor of two [200]. Because only particles inside a narrow energy window contribute constructively to the FEL-gain process, it is crucial that the energy spread is significantly smaller than the Pierce parameter and an often-used upper limit for the initial relative energy spread is given by

$$\frac{\sigma_\gamma}{\gamma} \leqslant \frac{\rho_{FEL}}{2}. \tag{172}$$

This requirement is essential for good FEL performance; it is a challenge to meet it when applying plasma wakefield accelerators as sources for FEL drive beams.

Slippage

Electrons perform a sinusoidal motion in the undulator (see equation (145)), and therefore travel a longer distance compared to the straight path of the emitted photons. Consequently, electrons have a smaller average velocity in the forward direction and slip back by one resonant wavelength with respect to the photons in every undulator period, as dictated by the resonance condition (153). The instantaneously accumulated *phase slippage*

$$L_s = N_u \lambda_r \tag{173}$$

therefore increases with longer resonant wavelength, λ_r, and number of undulator periods, $N_u = L_{sat}/\lambda_u \approx 1/\rho_{FEL}$. Within an undulator of length $L_{sat} = \lambda_u/\rho_{FEL}$, the total accumulated slippage is simply $L_{s,max} = \lambda_r/\rho_{FEL}$. For the generated radiation to not move out of the electron bunch and thus to overlap within the undulator, the total accumulated slippage should not be larger than the bunch length

$$L_{s,max} = \frac{\lambda_u}{\rho_{FEL}} \leqslant \sigma_z. \tag{174}$$

This is an important condition, as electron bunches from plasma accelerators are typically very short (few microns). If this condition is not fulfilled, the saturation of the lasing process is substantially delayed and the generated light pulse is stretched. In the transverse direction, an analogous condition must be fulfilled [116]

$$\epsilon_n \leqslant \frac{\gamma \lambda_r}{4\pi}, \tag{175}$$

which guarantees transverse overlap by ensuring that the bunch divergence is smaller than the divergence of the emitted photons. This condition also shows the energy and wavelength possibilities for a given bunch, and limits the attainable minimum wavelength through the emittance for a given energy.

Self-amplified spontaneous emission

Interestingly, spontaneous emission of radiation can be interpreted as emission that is stimulated by vacuum fluctuations [88].

The FEL process can be seen as an instability that needs an initial seed to start. This seed can be provided by either a slightly pre-bunched electron distribution, or an external seed laser at the resonant wavelength. The other option is to let the process start from the incoherent shot noise of the initial undulator radiation. This process is called SASE [23] and requires a longer undulator and starting phase of the FEL. The radiation pulse in a SASE-FEL develops phase correlation only within a short range, the *cooperation length*, that is determined by the phase slippage over one gain length

$$L_c = \frac{\lambda_r}{\sqrt{3}4\pi\rho_{FEL}}. \tag{176}$$

These regions develop temporal coherence and cause a spike in the spectrum, so a bunch of length σ_z will show approximately $\sigma_z/(2\pi L_c)$ spikes. This includes the possibility to build a *single spike* SASE-FEL, where a very short bunch with $\sigma_z \approx 2\pi L_c$ is

applied [190, 191]. Then, close attention must be paid to keep the phase slippage as short as the bunch length by using a short undulator and resonant wavelength.

The cooperation length, L_c, has an important role in the applicability of electron bunches with energy chirp in FELs. Because the coherence length in the SASE mode is $\approx 2\pi L_c$, it is sufficient that the energy spread fulfills the condition (172) only within this range. This opens the possibility for electron bunches with an energy spread that in total violates $\sigma_\gamma/\gamma < \rho_{FEL}/2$, to be used in a FEL when the fractional (or slice) energy spread meets this condition. The length of the slices must therefore be about as long as the cooperation length of the considered undulator, and the energy chirp is limited by [204]

$$\frac{\alpha_c}{\sigma_{z,fwhm}}\left(\frac{\lambda_r}{\rho_{FEL}^2}\right) \ll 1 \tag{177}$$

with $\sigma_{z,fwhm} = \sigma_z 2\sqrt{2\ln 2}$ the FWHM bunch length, ρ_{FEL} the Pierce parameter, λ_r the resonant wavelength of the undulator, and the slope of the energy chirp α_c given by

$$\frac{\Delta\gamma}{\gamma} = \alpha_c \frac{\xi}{\sigma_{z,fwhm}}, \tag{178}$$

where $\xi = z - ct$ is zero in the center of the bunch.

COMPUTATIONAL METHODS

5.1 PARTICLE-IN-CELL ALGORITHM

Physicists have largely profited from computational methods that are used to predict the development of physical systems. Especially in very complex systems like plasmas, this has led to large accomplishments, enabled by ever better computer systems. Despite very large modern high-performance computing (HPC) machines, plasma wakefield acceleration is not—and does not need to be—modeled including all details of the system. Usually, a selection of relevant interactions and other simplifying assumptions are made that do not affect the physical processes of interest.

To simplify the computation of a macroscopic weakly coupled plasma, it is convenient to define *macro-particles* that are composed of a large number of physical particles and thereby reduce the number of particles of the system. Another benefit of this technique is the use of finite size particles, instead of using point-like electrons that interact with the Coulomb potential that becomes infinite for zero distance. The macro-particles are designed to avoid this singularity by using an interaction that decreases again as soon as the macro-particles start to overlap and is the same as the Coulomb potential for distances larger than the particle radius. The thereby reduced potential energy in the system is compensated for by using less particles to reproduce the plasma parameter (40).

These macro-particles are used in the PIC method [20, 95], which allows the interaction of three-dimensional collisionless plasmas with relativistic particle beams and high-power lasers to be computed. The PIC method is widely applied in the computation of plasma-based accelerator research and is based on the Maxwell equations (2-5) in combination with the Vlassov equation (equation (48) with the right-hand side set to zero). To give a small error, the Maxwell equations are solved with the finite-difference time-domain (FDTD) method and advanced in time on a Yee-mesh [247]. In this mesh, the values of the magnetic field are defined at the center of the faces of the cells, whereas the values of the electric field and current are defined at the middle of the edges of the cells. In the FDTD method, the time is advanced in half steps, where the electric-field values are computed at half-integer time steps and the magnetic-field values are computed at integer time steps (leap-frog algorithm). Particles are advanced through free space [24].

The fields and the particles are alternately advanced within the PIC cycle. The charge and current densities are deposited onto the grid, followed by solving the Maxwell

equations to calculate the electric and magnetic field values at the respective grid points. Then, the fields are interpolated back onto the locations of the particles to calculate the Lorentz force and the particles are moved after the integration of the equations of motion using the leap-frog method.

Naturally, the spatial size of the cell of the grid must be chosen sufficiently small to resolve all important phenomena. To avoid numerical instability, the time step must fulfill the *Courant-Friedrichs-Lewy* condition [46, 247]

$$c\Delta t < \sqrt{\Delta x^2 + \Delta y^2 + \Delta z^2},$$ (179)

which precludes propagating particles faster than one cell per time step. For the PWFA simulations in this work, the time step $c\Delta t = \Delta z/2$ is used to minimize the growth rate of numerical instabilities associated with a relativistic particle bunch [78]. Other restrictions can arise, e.g. when a high-power laser is used, a smaller time step is required that scales with the laser amplitude [11].

Further, the discretization of the electromagnetic field leads to a minimum wavelength that can be resolved with the chosen cell size. This alters the dispersion at small wavelengths and leads to the artificial effect that particles may travel faster than the numerical speed of their own radiation. Hence, resonant interaction between the light and the particle can lead to the generation of an artificial source of radiation. This *numerical Cherenkov* radiation was studied intensely [47, 78, 86, 135, 249] and can be reduced by a careful choice of the simulation parameters or alternative field solvers. However, the origin of this effect, the discrete nature of the electric field on the grid, cannot be avoided within the PIC method. The minimum wavelength that can be resolved by a grid with the resolution Δz is $\lambda_{min} = 2\Delta z$, restricting the wave numbers to $k < \pi/\Delta z$. In the applied standard Yee-mesh, electromagnetic waves propagate according to the dispersion relation [86]

$$\left(\frac{1}{c\Delta t}\sin\left(\frac{\omega\Delta t}{2}\right)\right)^2 = \left(\frac{1}{\Delta x}\sin\left(\frac{k_x\Delta x}{2}\right)\right)^2 +$$
$$\left(\frac{1}{\Delta y}\sin\left(\frac{k_y\Delta y}{2}\right)\right)^2 + \left(\frac{1}{\Delta z}\sin\left(\frac{k_z\Delta z}{2}\right)\right)^2,$$ (180)

whereas in vacuum the dispersion is $\omega^2/c^2 = k_x^2 + k_y^2 + k_z^2$. This numerical dispersion error significantly slows down the speed of electromagnetic waves near the cut-off frequency. Note that the numerical dispersion is most accurate along the diagonal of the simulation cell and least accurate along the axes.

In this work, the high-performance multi-physics cross-platform computational simulation framework [169] (VSim)[1] was used to compute full three-dimensional laser- and

---

[1] Plasma acceleration package (PA), solely developed to perform large-scale simulations of laser-plasma and beam-plasma acceleration experiments by Tech-X

beam-driven plasma wakefield accelerator scenarios. Within VSim, all operators are local, which enables local communication via the Message Passing Interface (MPI) and proven scaling up to over 30 000 processors. To maintain this proximity on the nodes, the particles are sorted regularly. For the shapes of the macro-particles, b-splines of second order are used [63]. This requires higher-order field interpolation for the Lorentz force to minimize self forces and numerical heating. In addition, the currents are smoothed to reduce numerical heating. The ionization mechanism is implemented using the ADK tunnel ionization theory given in equation (53). This field-ionization mechanism is applied for ionization by lasers and by the space-charge fields of charged particles. Further, the boundaries of the simulation box are equipped with perfectly matched layers (PML) to absorb any outgoing wave energy and prevent reflections back into the simulation domain. To reduce computational cost and to discard regions of no physical relevance, the simulation box was moved with the speed of light along with the plasma wave. In case of the TH simulations, the ionization laser is not fully resolved, but is represented by its envelope to further reduce the computational load and allow for a much faster simulation [48].

5.2 JUSTIFICATION OF APPLIED APPROXIMATIONS

Within the simulations of this thesis, the particles are initially at rest and hence assumed "cold" with $T = 0°K$ before being heated by a laser or a particle beam. However, this is not substantially different from room temperature, $T \approx 22° C \approx 295.15° K \approx 0.0254\,eV$, as the energies that occur shortly after the interaction with the driver are orders of magnitude higher, and the small difference of the initial energy becomes negligible in the regions of interest. This justifies the use of zero temperature instead of room temperature. However, including a finite temperature could smooth the fields at hot spots [142].

CRITICAL FIELDS FOR THE ADK MODEL

species	ionization energy [eV]	$E_{c,ADK}$ [GV/m]	$W_{ADK}(E_{c,ADK})$ [fs^{-1}]
H	13.6	75.26	11.59
He	24.59	182.94	6.02
He+	54.42	602.36	47.78
Li	5.39	18.79	61.76
Li+	75.64	987.13	31.58

Table 2: Critical field values for the applicability of the ADK model for different species, defined in equation (54).

The use of the ADK model for ionization is justified because the Keldysh parameter given in equation (52) indicates the dominance of tunnel ionization over MPI for the used parameters. For instance, in the main PWFA simulation displayed in Table 13, $\gamma_K \approx 0.14 < 1$. For the same simulation, the peak electric field of the laser at focus $\mathcal{E}_0 \approx 482\,\text{GV/m}$ is smaller than the maximum allowable field for ADK, $E_{c,ADK} \approx 987.13\,\text{GV/m}$ (given in equation (54)), also indicating the applicability of the ADK model. If the occurring field strength is beyond the critical value, the ionization process might still be modeled accurately when the tunnel ionization already provided for complete ionization before the critical field strength is exeeded. This, however, needs to be verified manually when using VSim; in the case that the electric field strength rapidly increases beyond the critical BSI field, the applied ADK-model becomes inaccurate.

For hydrogen for example, the critical value is $E_{c,ADK} \approx 75.26\,\text{GV/m}$ and $W_{ADK} \approx 11.59\,/\text{fs}$ (compare table 2). At a density of $10^{23}/\text{m}^3$, the corresponding linear charge density amounts to $\lambda \approx \left(1 \times 10^{23}/\text{m}^3\right)^{1/3} \approx 4.64 \times 10^7/\text{m}$, or 46.4 particles per μm. A laser is therefore passing $46.4\,\mu\text{m/c} \approx 14$ particles per femto-second along the axis. Hence, an ionization rate exceeding $W_{ADK} \gtrsim 14/\text{fs}$ could fully ionize hydrogen with a density of $10^{23}/\text{m}^3$. The use of macro-particles underestimates the amount of charge that is ionized in general, which is especially visible for ionization near the threshold energy. Originating from the fact that only whole macro-particles can be ionized, the maximum error is less than the charge of one macro-particle. When considering the spatial volume that is ionized and its temporal development, this might add up to more than the charge of one macro-particle. In the PWFA simulations shown in figure 34 and 35, 163 840 electrons have been combined in every macro-particle, corresponding to 0.26 pC. Compared to the obtained charge in the generated bunch of 35.9 pC, this error affects at least the last shown digit.

Atoms and ions can also be ionized by collisions with an electron. The cross section for this *impact ionization* has a maximum shortly after the ionization energy, and decreases asymptotically thereafter. Furthermore, it takes more time than tunnel ionization. Thus it is negligible for electrons with energies much larger than the ionization energy $\xi \gg \xi_{\text{ion}}$. Especially the high-energy drive beam is very ineffective in ionizing via impact ionization. However, impact ionization by moderate-energy plasma electrons can be of importance as a second-order effect, e. g. from electrons that are transversely scattered outside the plasma by the driver of the wakefield. In addition, when operating with a gas mixture that includes HIT species, impact ionization of HIT species by plasma electrons must be considered as a source of dark current.

Part II

START-TO-END-SIMULATIONS: FROM HYBRID PLASMA WAKEFIELD ACCELERATION TO UNDULATOR RADIATION

1. PRODUCTION OF A PLASMA WAKEFIELD DRIVE BEAM IN LWFA In the first stage of the hybrid plasma wakefield accelerator, a high-power laser is utilized to accelerate a suited PWFA drive beam. In consideration of the available resources and methods, suitable LWFA simulation parameters are investigated and implemented resulting in a long, fully three-dimensional simulation that will be shown and discussed. The optimal position for the extraction of the obtained electron beam is considered.

2. HIGH-QUALITY ELECTRON-BUNCH GENERATION IN LWFA-BEAM DRIVEN PWFA The preparation and injection of the obtained drive beam into the PWFA stage will be discussed and simulated. In the second stage of the hybrid plasma wakefield accelerator, the sustained excitation of the plasma wakefield without unintentionally injecting electrons will be discussed. To show the influence of the different TH-laser parameters and to find the best witness-bunch, a parameter scan over the ionization laser parameters is conducted and evaluated. Eventually, the acceleration of the high-quality witness bunch will be given and the optimal position to extract this bunch from the plasma will be investigated.

3. GENERATING HIGH-POWER SHORT-WAVELENGTH RADIATION IN AN UNDULATOR In the last stage of the simulation chain, the possibilities of the obtained high-quality bunch to drive a FEL will be considered and an according choice for the undulator design will be discussed. The capturing and matching of the bunch with a conventional beamline will be simulated and analyzed, followed by the simulation of the full FEL process.

4. CONCLUSIONS AND OUTLOOK In the last chapter of this work, the results will be summarized, and important findings will be emphasized. Finally, future improvements on the presented scheme will be discussed.

PRODUCTION OF A PLASMA WAKEFIELD DRIVE BEAM IN LWFA

6.1 COMPUTATIONAL RESOURCES

LWFA simulations are particularly computationally expensive, demanding big amounts of time and core hours. Therefore only one long LWFA simulation could be realized, which will be displayed and discussed in the following. The expenses of the simulations have been covered by the Jülich Supercomputing Centre (JSC), Norddeutsche Verbund für Hoch- und Höchstleistungsrechnen (HLRN), and the National Energy Research Scientific Computing Center (NERSC) that I hereby gratefully acknowledge. The simulations ran on the Supercomputers Gottfried (named after Gottfried Willhelm Leibnitz) provided by HLRN, the Jülich Research on Exascale Cluster Architectures (JURECA) at JSC, and the supercomputer named in honor of Thomas Edison (EDISON) at NERSC.

The latest update from HLRN (HLRN III) runs a Cray XC30 (Intel IvyBridge) and XC40 (Intel Haswell) system with 2.7 petaflops combined peak performance of 85 248 cores[1]. The JURECA installation comes with 2.2 petaflops per second peak performance on 45 216 Intel Haswell cores[2], and Edison, a Cray XC30 with a peak performance of 2.57 petaflops per second on 133 824 compute cores[3].

The simulations are set up under the restrictions of available computational resources and methods and scenarios that would have been too expensive could therefore not be conducted. This effectively restricts LWFA simulations to a minimum density beneath which, no simulations are possible without applying advanced computational methods. For instance, using a frame of reference that is moving with a relativistic velocity along with the wakefield (boosted frame) can significantly reduce the computational load as the wavelength of the laser is stretched and therefore a larger cell size can be used. However, this mixes up the order of time events within the simulation window, making a transformation of the gathered output back into the lab frame very cumbersome, which somewhat compensates the speedup gained during the simulation. This method has therefore not been utilized.

Super computing performance is typically measured in floating point operations per second (flops), computed from the CPU frequency times the number of floating point operations per computing cycle times the number of cores.

---

1 https://www.hlrn.de/home/view/NewsCenter/ArticleNov2013KonradAndGottfried
2 https://www.fz-juelich.de/ias/jsc/EN/Expertise/Supercomputers/JURECA/JURECA_node.html
3 https://www.nersc.gov/users/computational-systems/edison/

6.2   ASPECTS OF THE LASER-DRIVEN ACCELERATOR STAGE

In section 2.2.4, the methods applicable to surmount the physical limitations of LWFA have been introduced, where the most severe limitation of the acceleration length is the diffraction of the laser pulse. Consequently, methods to overcome diffraction will first be evaluated in the following. Further, the change of characteristic parameters with the laser wavelength, as well as the required laser energy and suitable focal spot size and duration will be discussed, including the choice of an appropriate plasma species and its density. Then, a proper electron-beam injection method has to be selected that can inject sufficient charge for PWFA, and that is applicable under the given circumstances.

For an extensive overview of available ultra-high laser systems see figure 47 and Table 9.

Although currently, nearly all laser systems available for LWFA run at the $0.8 - 1.1\,\mu m$ wavelength covered by conventional mode-locked solid-state lasers, it is tempting to consider longer laser wavelengths for LWFA. Then, the laser power that is required to drive the wakefield can be lowered, as the ponderomotive force $F_p \propto \lambda_l$ (equation (72)) and the laser strength parameter $a_0 = e\mathcal{E}_0/(m_e \omega_l c)$ (see equation (18)) is increased simultaneously. Facilities running at longer laser wavelengths have therefore been proposed and will be available in the near future [180, 181].

On the other hand, operation at longer laser wavelengths makes a number of parameters worse for LWFA. The Rayleigh length, $z_R = \pi w_0^2/\lambda_l$, shortens the acceleration length due to diffraction and, at the same time, the power that is necessary for self-guided propagation, $P_c \propto \lambda_p^2/\lambda_l^2$, is increased (see equation (79)). This, however, can be compensated by going to a lower plasma density, where a wider focal spot radius, w_0, can be applied, and the plasma wavelength $\lambda_p \propto n^{-1/2}$ is accordingly increased. Also other LWFA characteristics are altered by a longer laser wavelength. The energy depletion length, $L_{pd} \propto a_0\lambda_p^3/\lambda_l^2$ (84), and the dephasing length, $L_{deph} \propto a_0\lambda_p^3/\lambda_l^2$ (83), is shortened, but again, this can be compensated by lowering the plasma density. The estimated single-stage energy gain (85) can be increased by going to shorter laser wavelengths $\Delta W \propto \lambda_l^{-4/3}$, lower plasma densities $\Delta W \propto n^{-2/3}$, and higher laser powers $\Delta W \propto P_l^{1/3}$, in decreasing order of significance. The amount of charge that can be accelerated (86) grows with laser power $Q \propto P_l^{1/2}$ and laser wavelength $Q \propto \lambda_l$. However, one must also take into account the fact that long-wavelength laser pulses are harder to compress to short durations, as the minimum compression is limited to few cycles of the laser wavelength. For a CO_2 laser, the minimum compression is about $100\,fs$, corresponding to only ~ 3 wavelengths per pulse, using self-chirping induced by the Kerr effect [181]. Therefore, it also is required to operate at lower plasma density (and thus wavelength) when a laser pulse with long wavelength is applied.

Summarizing, the energy gain and the amount of charge increases with laser power, while operating at longer laser wavelengths decreases the achievable energy gain, but increases the amount of charge that can be accelerated. Besides the capability of driving a wakefield more efficiently at a longer laser wavelength, its capability to sustain the

acceleration is decreased. Further, the computational costs to simulate such a scenario is lowered, since the longer the laser wavelength, the larger the cell size that can be used in the simulation. On the other hand, a larger simulation window is necessary because lower plasma densities and thus larger plasma waves need to be monitored, increasing the number of cells.

6.2.1 *Laser guiding*

Laser diffraction in vacuum is determined by the Rayleigh length $z_R = \pi w_0^2 / \lambda_l \approx$ 1.57 mm for $w_0 = 20 \mu m$ at Ti:Sa wavelength. Hence, the acceleration would cease after a few millimeters if laser diffraction is not stopped. This can be done by either guiding the laser within a pre-formed plasma channel [7], or by choosing a laser intensity that is high enough for relativistic effects to set in, which can also lead to self-guiding of the laser pulse [210]. Applying the first method, the required laser energy can be reduced at the cost of having to provide for a plasma channel.

Pre-formed plasma channel

To demonstrate the guiding of a laser pulse by a pre-formed plasma channel, and to achieve the aforementioned reduction in computational time, a simulation with a CO_2 laser with $\lambda_l = 10 \, \mu m$ is implemented. To guide the laser, a hollow parabolic plasma density channel is implemented. For the long wavelength, the strength parameter $a_0 \propto \lambda_l$ is increased and a longer cell size is used. This is shown in figure 16, using $a_0 = 6$, $w_0 = 10 \, \mu m$, $\tau = 100 \, fs$, $\lambda = 10 \, \mu m$, and a hydrogen density of $1 \times 10^{17} \, cm^{-3}$, where the laser is stably guided over many Rayleigh lengths. The plasma channel was implemented by a parabolic plasma profile with a radius of $100 \, \mu m$. Because the plasma wakefield does not self-inject electrons for these conditions, a density down-ramp was implemented to inject electrons into the plasma wave (not shown here). In these simulations, only less than $10 \, pC$ of charge is injected for different peak densities and widths of the downramp. To inject more charge, a higher laser energy is required. In figure 16, the laser focus is chosen very small and results in a tiny Rayleigh length in combination with the $10 \, \mu m$-long laser wavelength. However, this simulation nicely demonstrates the functionality of external guiding of the laser pulse. In addition, using a plasma channel to guide the laser pulse has the beneficial effect that the accelerating field can be flattened, or even reversed to reduce the energy spread of the accelerated bunch [183, 220].

Others reported self-injected charge of several $100 \, pCs$, using simulation of LWFA in a plasma channel [223]. Leemans et. *al.* [133] reported self-injected electrons with up to $4.2 \, GeV$ of energy and up to $50 \, pC$ of charge, using a $16 \, J$ laser in a plasma channel
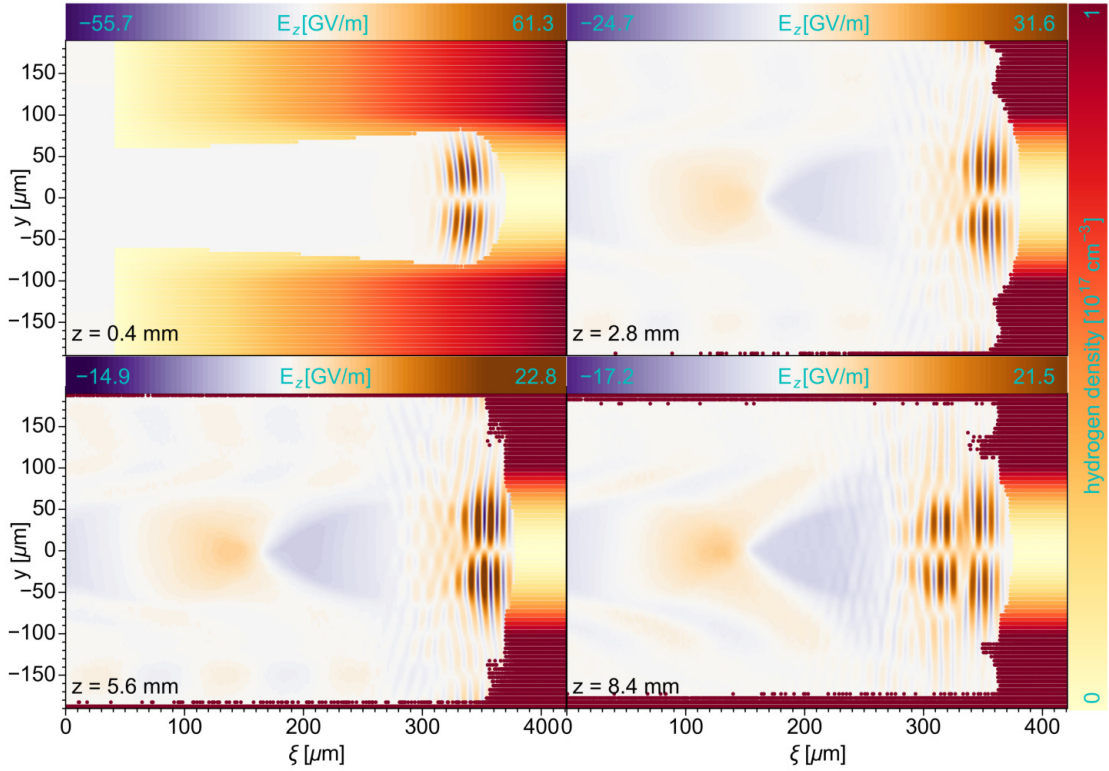
Figure 16: Guiding of a CO₂ laser with ($\lambda = 10\,\mu m$, $a_0 = 6$, $\tau = 100\,fs$, $w_0 = 10\,\mu m$, $W \approx 82.3\,mJ$) in $n_p = 1 \times 10^{17}\,cm^{-3}$ dense neutral hydrogen. The neutral hydrogen (orange-red colored) is shown to visualize the hollow plasma channel with $100\,\mu m$ radius over many Rayleigh lengths ($z_R \approx 31.4\,\mu m$).

generated by capillary discharge. This result is remarkable, as it uses significantly less laser energy than in other experiments [233], while achieving similar results.

External guiding becomes necessary for laser pulses with a power less than the critical power (79), e. g. at a low plasma density. Otherwise, a strongly relativistic laser pulse can be self-guided over a dephasing length with the relativistic self-focusing mechanism [43, 64, 118]. Either way, some form of laser guiding is essential to provide for a sufficiently long acceleration length in LWFA.

6.2.2 Plasma species and density

Neutral hydrogen was chosen as target gas for the LWFA stage, because it can only be ionized once, no higher-order states occur, and it is in gaseous phase under normal conditions. Furthermore, its ionization threshold is sufficiently low to allow the laser to ionize at its very edges and provide a stable and wide plasma for the acceleration. Operating with gases of higher atomic number (Z) might lead to an unfortunate density distribution, where the strong laser peak-electric-field strength required to drive the wakefield (on the order of TV/m) is capable of ionizing many electrons from one nuclei. Therefore, fewer states are ionized at lower field strengths, giving the highest

plasma density on axis. Such a plasma-density profile would strongly defocus a laser pulse (ionization defocusing). Therefore, high-Z gases are usually not beneficial for LWFA (with few exceptions [248]).

In general, extending the dephasing length, $L_{deph} \propto n^{-3/2}$ by operation at low density is favorable to simultaneously increase the achievable energy gain $\Delta W \propto n^{-1}$. However, when going to lower plasma densities, simulations become increasingly challenging, as the required computational resources explode with the requirement of a larger simulation box to fully model the bigger plasma wavelength. In addition, the necessary simulation length is extended as well, quickly making a full three-dimensional standard PIC simulation very ineffective without enhancements in computational methods [156, 230]. Therefore, the plasma density was chosen to be at the lowest level that could be used with the available computational resources, while simultaneously using a high laser energy to quickly accelerate the electrons to a high energy. With this, the laser pulse can also be self-guided and no external plasma channel is required.

A comparable restriction in minimal density applies to experiments as well, arising from the available laser power. So far, the cutting-edge high-power lasers utilized in LWFA experiments, with and without a plasma channel, are on the 100 TW level, only allowing the usage of densities above $n_p \sim 1 \times 10^{18}\,\text{cm}^{-3}$, and restricting the gained energy to approximately the 1 GeV mark [43, 118, 134]. Using a PW-level laser allows a lower plasma density to be used, resulting in a higher achievable energy of potentially up to 10 GeV [233] and beyond [156, 230] if acceleration can be sustained over a sufficiently long distance.

6.2.3 *LWFA injection*

As described in section 2.2.5, electrons can enter the plasma wave from behind when its accelerating field is strong enough to suck them in (self injection). This self injection naturally occurs in nonlinear laser-driven plasma waves, because the plasma wave travels with a velocity below the vacuum speed of light. To implement other injection methods, self injection must therefore first be suppressed or avoided. This can be done by tuning the laser power down to operate in the linear regime, but then external guidance of the laser pulse is required.

Another way to suppress self-injection is to fully load the wakefield with electrons at the start to lower the accelerating field to a level where no electrons can be self-injected (beam loading). Because self-injection is a continuous process, a large amount of charge can be injected with a continuous energy spectrum, which is very bad for most applications, except for driving a plasma wakefield. So, arising from the requirement for high charge and energy, operating at a high density and laser energy in the bubble regime using self injection is the most promising scenario to produce suitable PWFA drivers. In a more advanced scenario, where an external guidance for the laser can be provided,

lower plasma densities would be better to increase the energy of the witness beam in LWFA.

The high energy of the laser was also chosen due to computational reasons, so the self injected electrons are accelerated very rapidly and the total acceleration length can be kept short. Because the final energy is proportional to $\Delta W \propto a_0/n\lambda_l$, and neither the laser wavelength nor the plasma density can be adjusted in the needed direction, tuning up the laser amplitude is the only parameter left to increase the final electron beam energy. Apart from that, a high accelerating field also promises to inject a large amount of charge, which is also crucial for a potential PWFA drive beam. When considering the total energy content of the needed PWFA drive beam, a high demand on total laser energy on the 100 J-level is required (see discussion in section 2.5), especially when taking the expected low efficiency of the LWFA into account.

The spatial dimensions of the laser pulse can be adjusted to the dimensions of the plasma wave to maximize the response and the efficiency of the accelerator. However, as the laser pulse undergoes rapid transformations during the acceleration, and the wakefield does not change much for small variations around the optimum, the spot size and pulse duration optimization is not crucial as long as they are within a reasonable range around the optimum value [61]. As one optimization goal is to also keep the total required laser energy $W_l \propto w_0^2 a_0^2 \sigma_t/\lambda_l^2$ as low as possible, choosing a smaller w_0 and σ_t than demanded by the plasma-response-maximization conditions might save some energy without loosing much of the possible witness energy. This correlation, however, would require a more detailed investigation aimed at enhancing the overall efficiency.

Finally, the density and laser parameters have been chosen such that, according to equation (85) and equation (86), a bunch of 1.4 nC charge can be accelerated to 6.1 GeV in a self-guided LWFA. This bunch would meet the requirements of a PWFA drive bunch very well.

6.3   JUSTIFICATION OF THE SIMULATION SETTINGS

The previous discussion resulted in the setup of a simulation whose parameters are displayed in Table 10 and Table 11. The chosen density of $5 \times 10^{17}\,\text{cm}^{-3}$ is below the density of typical LWFA experiments, and requires a laser spot size that is on the order of half the plasma wavelength [33, 219]. Accordingly, the laser FWHM duration $\tau = 2\sqrt{2\ln(2)}\sigma_z/c$ (σ_z being the standard deviation of the pulse in the forward direction) was chosen to be $\tau = \lambda_p/2c \approx 78.8\,\text{fs}$, and thus $k_p\sigma_z = \pi/(2\sqrt{2\ln(2)}) \approx 1.3$. This is a little larger than the condition to maximize the amplitude of the wakefield $k_p\sigma_z \approx 1$ (for a linear polarized laser in the linear regime) [61]. However, because $a_0 = 8$ indicates the highly nonlinear regime, a longer pulse is reasonable, given the increased nonlinear plasma wavelength ($\lambda_{NL} > \lambda_p$). The laser focal spot radius $w_0 = 23.6\,\mu\text{m} \approx \lambda_p/2$ was chosen to match half the plasma wavelength (so the diameter matches the

plasma wavelength), and is significantly less than the transverse matching condition, $2\sqrt{a_0}/k_p(n_p) \approx 42.5\,\mu m$, which balances the transverse ponderomotive force of the laser pulse by the counteracting ion-channel force [146]. This potentially saves laser energy, $W_l \propto a_0^2 w_0^2$, which would be necessary to reach the same a_0 for $w_0 = 42.5\,\mu m$. The FWHM duration of the laser, $\tau \approx 78.8\,fs$, is significantly larger than the build-up time of the plasma response, $\omega_p^{-1} \approx 25.1\,fs$ and therefore permits self guiding. Further, the very high laser energy of $W_l \approx 100\,J$ results in a power that greatly exceeds the power for self guiding $\mathcal{P}_0/P_c = 20\,206 \gg 1$ (see Table 10), ensuring acceleration over the dephasing length of $L_{deph} \approx 30\,cm$.

The longitudinal cell size of $\Delta z = 5 \times 10^{-8}\,m$ divides the laser wavelength of $\lambda_l = 8 \times 10^{-7}\,m$ into 16 points (8 points for half the period), providing reasonable resolution. The minimal wavelength that can propagate at this resolution is $\lambda_{min} = 2\Delta x = 0.1\,\mu m$. The size of the simulation window was adjusted to include all regions of interest.

The optimized time step $\Delta t = 0.5\Delta x/c \approx 0.167\,fs$ to suppress instabilities in the drive and witness bunches was employed [79]. Apart from that, the high a_0 of the laser would require a better time resolution to satisfy $c\Delta t a_0/\lambda < 1$ [11], however this would have been beyond the available resources. The condition is not fulfilled by $c\Delta t a_0/\lambda_l = 0.5$, but the thereby introduced error in the particle pusher leads to an underestimation of the momentum that plasma electrons gain from the laser field. A smaller time step would thus lead to an even more pronounced blowout, resulting in higher energies in the accelerated electron bunch. Therefore, the chosen time step does not spoil the validity of this simulation, but rather underestimates the final bunch energy. With this, the selected simulation parameters have been justified, and the simulation was set up. The results are displayed and discussed in the following.

6.4 SIMULATION OUTCOME AND DISCUSSION

Figure 17 illustrates the self-guided propagation of the ultra-relativistic laser pulse in a $5 \times 10^{17}\,cm^{-3}$ dense hydrogen plasma by the measured field strength during the simulation. As it is focused directly onto the plasma start at $0.1\,mm$, the laser would diffract immediately within $z_R \approx 2\,mm$ if if is not guided and quickly loose its capability to drive a plasma wakefield. Here, it was demonstrated that this laser can be guided through the plasma via relativistic self-focusing over more than $50\,mm$, due to its peak power of $20\,206$ times the critical power for self guiding (79). Note, the simulation was stopped after a sufficiently high energy and charge of the electron beam was reached, so even longer guiding is possible.

The peak field strength of $\mathcal{E}_0 \approx 32\,TV/m$ (see Table 10) of the vacuum focal point is reached shortly before the first subplot ($z = 0.4\,mm$) in figure 17, where the peak field value is always shown in the top left. Later, $\mathcal{E}_0$ is easily outreached by more than a

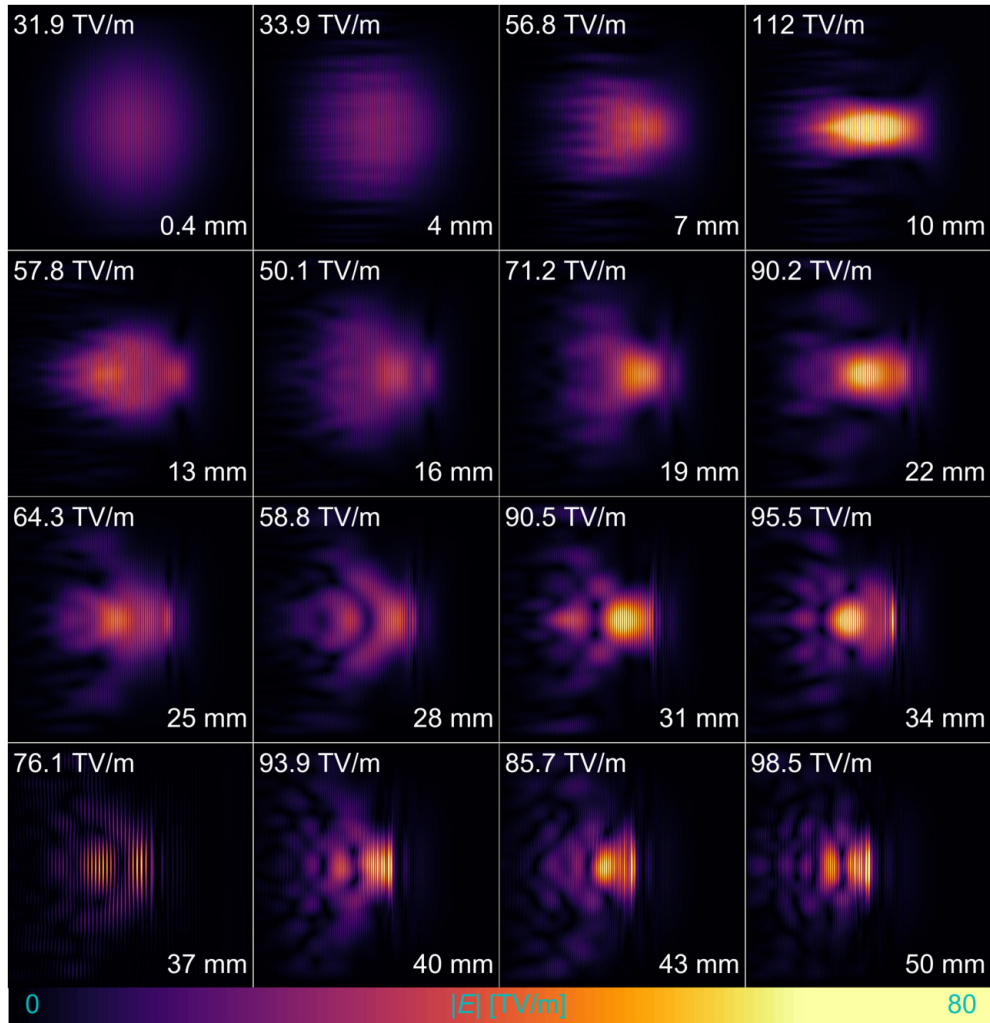Figure 17: Laser field-strength development, showing self guiding of a 100 J, $z_R \approx 2\,\text{mm}$ laser over a length of 50 mm, directly focused 0.1 mm behind the plasma entry. The maximum field strength (upper left) oscillates after the first plasma-lensing focus at 10 mm, attended by increasing filamentation and etching and diffraction of the pulse front.

factor of 3, when the plasma further compresses the laser spot towards its first plasma focus at $z \sim 10\,\text{mm}$, attended by the filamentation of the laser pulse [8, 105, 184].

The front of the laser-pulse is subject to etching, diffraction, compression and increasingly elevated field strength after approximately $z \sim 30\,\text{mm}$ (see figure 18). The backward shift of the laser front as a result of the above described effects can clearly be seen in figure 17, while the self guiding leads to a periodic focusing at about every $\sim 12\,\text{mm}$, which is approximately the position depicted in the right subplots of figure 17.

When the pulse is compressed at its front, its wavelength is subsequently stretched from the loss of energy to the wakefield and propagates at a slower velocity and falls more and more behind, which was described in section 2.2.2. Note, this process can also be understood as an inelastic scattering process, where the laser pulse is collec-

tively scattered by the plasma resonance frequency, resulting in a frequency shift of $\omega_l + n\omega_p$ (n is the scattering order) of the scattered light (Raman forward scattering) and simultaneous excitation of a plasma wave [124]. This scattering process was used to describe the excitation of linear plasma waves in one dimension and was not yet formulated for the nonlinear three-dimensional case [61].
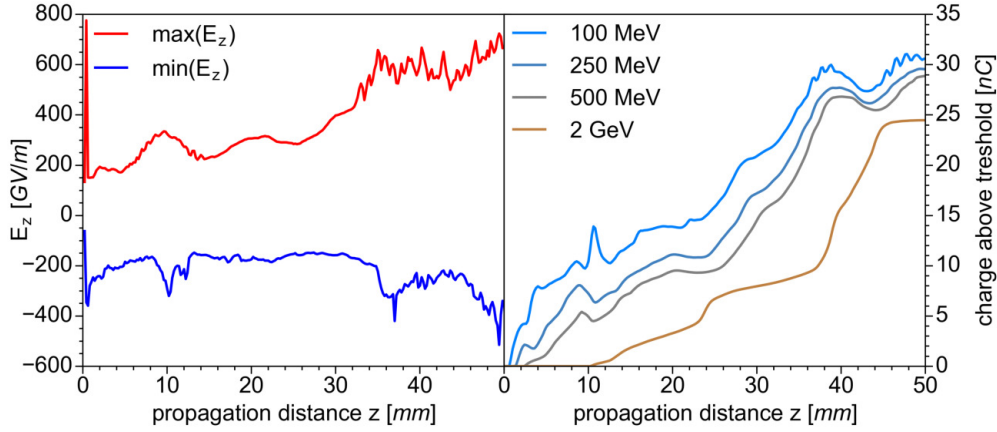

Figure 18: Left figure: evolution of the peak accelerating (blue, negative) and laser-field strength (red) on axis. Right figure: the total amount of trapped charge exceeding an energy of 100, 250, 500, and 2000 MeV throughout the acceleration, visualizing the self-injection.

In figure 18, the repercussions of the laser peak-field strength and the accelerating field on the amount of injected charge is depicted, showing the correlation of increased accelerating field (negative longitudinal field strength) and increased self-injected charge. The left plot displays the peak field strength of the laser (red), and its peak accelerating field (blue, negative) at the position of the witness beam on the propagation axis (see central curves of figure 19-22).

In the right-hand side of figure 18, all charge that exceeds the displayed energy threshold (top left) is counted for every time step of the simulation, showing continuous self injection. When a group of new electrons is self injected due to the evolution of the laser, they quickly reach the first energy threshold of 100 MeV. However, these electrons are not necessarily situated in the bubble, as electrons above 100 MeV can also be found in the second plasma cavity or in the transverse direction when being pushed outside the bubble (see top-right subplot in figure 19). Therefore also electrons with a higher energy thresholds are shown, which are more likely to be trapped within the first plasma cavity. When comparing the charge at the different energy levels, it can be seen what fraction of the lower energy electrons eventually becomes trapped and is accelerated to the next energy threshold.

The first plasma focus of the laser is clearly visible in the left plot of figure 18 by the locally increased maximum field strength $max(E_z)$ at 10 mm. This also increases the maximum accelerating field $min(E_z)$, lengthens the plasma cavity, and therefore

lots of electrons are injected into the plasma-wave cavity, which can be seen in the right plot by a significant amount of electrons exceeding the lowest 100 MeV threshold shortly after this position. Thereafter, part of the initially accelerated electrons cannot be kept in the plasma cavity when the laser looses its peak strength and the cavity shrinks again, visible by the fact, that the amount of charge drops again. Another charge leak of mainly low-energy electrons can be seen after 40 mm of acceleration, when hosing [104, 237] of the meanwhile substantially elongated witness beam leads to an enhanced transverse oscillation. The peak energy of the bunch at this point is already close to 6 GeV (see figure 23).

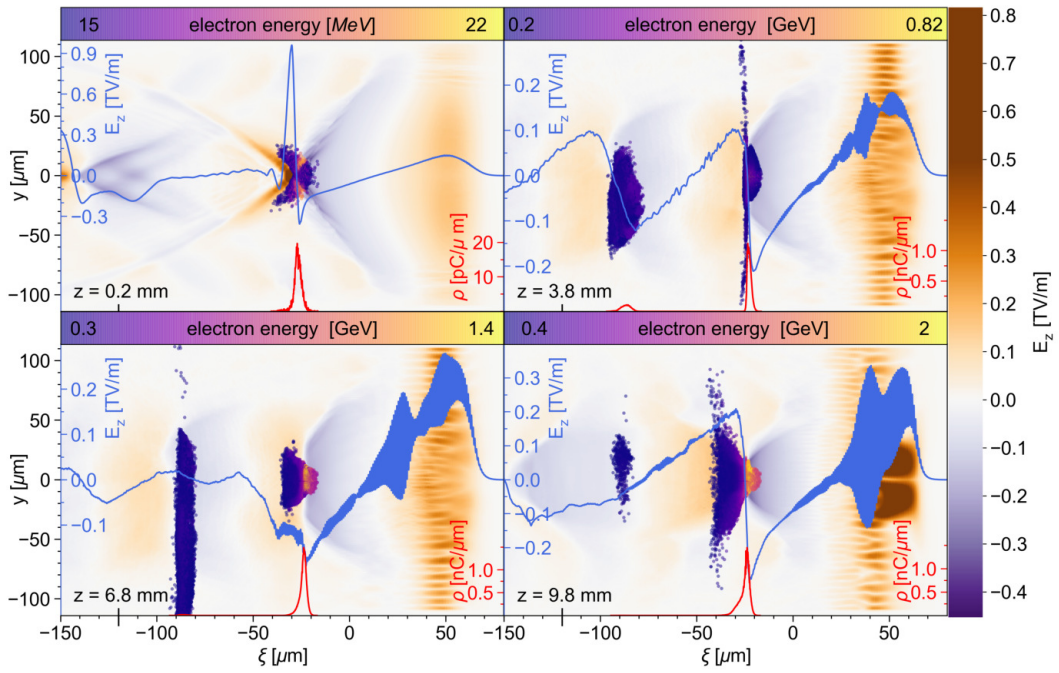*Note that the transverse coordinate, y, is on a different scale than the longitudinal coordinate, ξ.*

Figure 19: Initial laser-wakefield acceleration (accelerating field E_z shown in the background, right colorbar) until 10 mm, featuring electrons (color coded dots, top colorbar) above 15, 200, 300, and 400 MeV. The longitudinal distribution of these electrons (red curves), and the amplitude of the longitudinal accelerating field along the central axis (blue curves) are depicted.

In figure 19-22, the details of each time step of figure 17 are depicted, including the central plane of the longitudinal electric field (right color bar) in the direction of the polarization of the laser and its amplitude along the central axis (blue lines). The electrons that exceed the energy threshold, given as the minimum energy in the top color bars, are projected onto this y-z plane, and in addition are projected again onto the bottom of each subplot (red) to show the longitudinal distribution of the injected charge. Note, the z position is given at the front of the subplots in figure 17, and at the rear in figure 19-22 and shows the same time step. Also, the amplitude of the longitudinal field on axis (blue curves) does not necessarily include the maximum laser field strength.

The plasma starts with a linear 0.2 mm long upramp, and the drive laser is focused directly in the center of this ramp. The peak density at the front of the electron beam is generated at the start, when a large amount of electrons is sucked into the bubble by the peak accelerating fields, which are not lowered by beam-loading at this point. When enough charge is injected, its space-charge force starts to interfere with the electrons in the plasma sheath of the bubble and shifts the end of the bubble further behind. The lengthening of the bubble then makes room for more electrons to be trapped at later positions with increased laser field strength. Note, much less charge would be able to enter the bubble without this effect, because dephasing is too slow to make room for new charge at such a fast rate. In fact, dephasing does not play an important role over the 5 cm of acceleration as the dephasing length of $L_{deph} \approx 30$ cm is much larger. This is also supported by the fact that the front of the beam is continuously accelerated and accordingly the peak energy constantly increases (see figure 23).
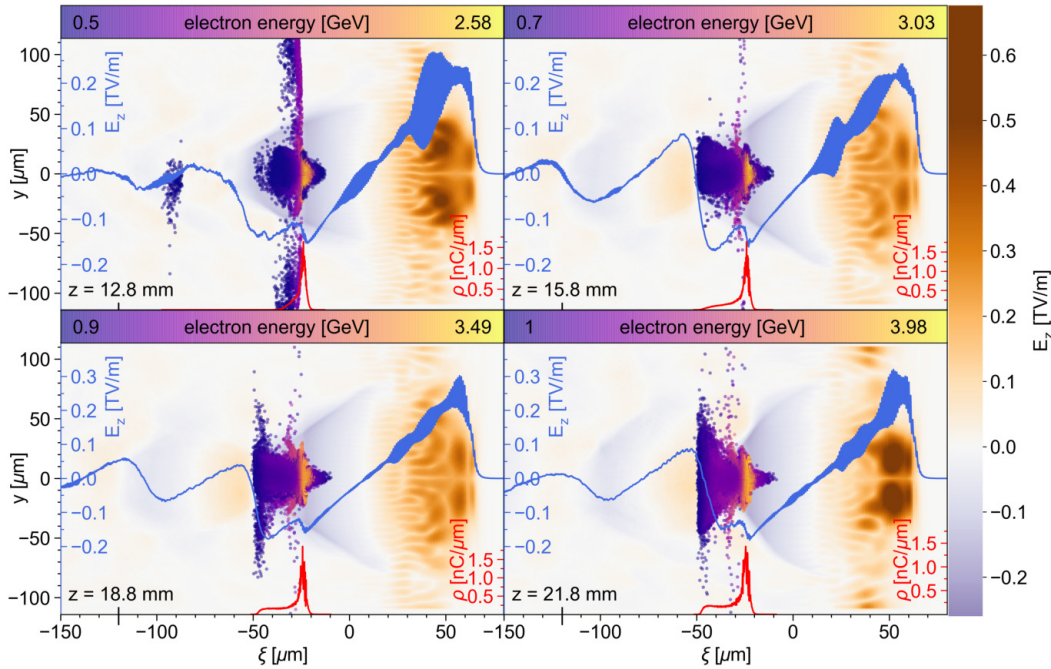

Figure 20: Laser-wakefield acceleration from 13 mm to 22 mm, featuring electrons (color coded dots, top colorbar) above 0.5, 0.7, 0.9, and 1 GeV. The charge of these electrons (red curves), and the amplitude of the longitudinal accelerating field along the central axis (blue curves) are depicted.

Figure 20 shows the acceleration behind the first plasma focus of the driving laser, where some of the recently accelerated electrons are lost in the transverse direction and the large amount of trapped charge significantly lowers the accelerating field and elongates the bubble (upper left subplot). The space that is thereby generated is successively filled with new electrons (see projected charge) until the next, less pronounced plasma focus is reached at about 22 mm. Furthermore, the initially injected charge is situated near a local maximum of the accelerating field, where a comparatively small

portion of the bunch continuously experiences the highest accelerating fields (see figure 24).
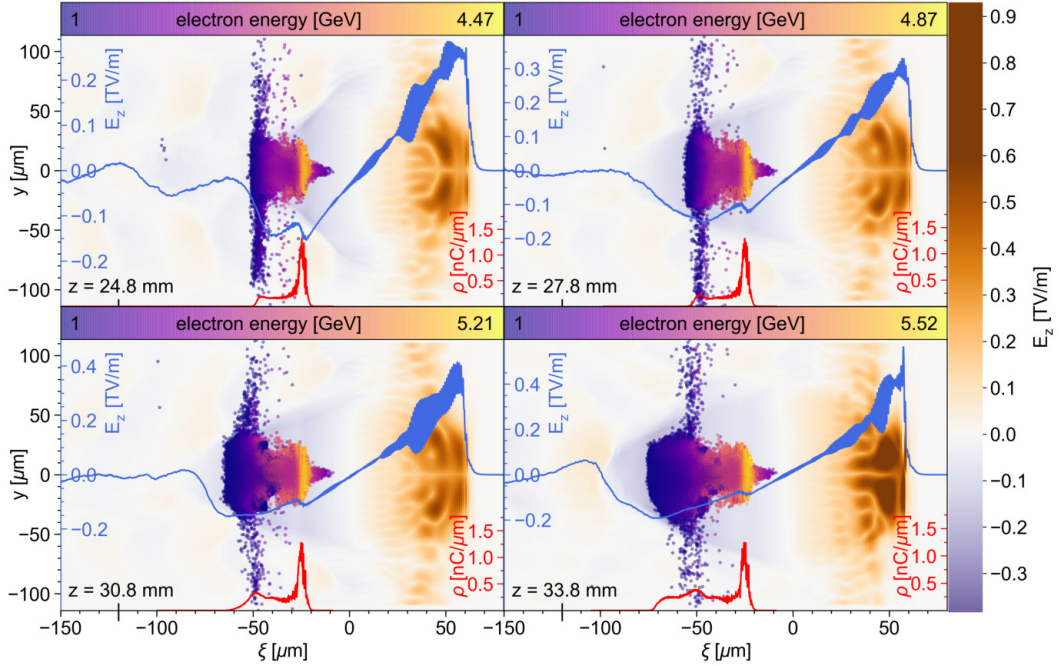

Figure 21: Laser-wakefield acceleration from 25 mm to 34 mm, featuring electrons (color coded dots, top colorbar) above 1 GeV. The longitudinal distribution of these electrons (red curves), and the amplitude of the longitudinal accelerating field along the central axis (blue curves) are depicted.

Next, the ongoing compression of the laser pulse at its front leads to an increasing peak-field strength and significant elongation of the bubble depicted in figure 21. Beginning on the order of nearly 300 GV/m, the laser peak fields quickly rise to about 500 GV/m, increasing the length of the bubble by approximately 50 μm between $z \sim 25$ mm and $z \sim 34$ mm. Because only electrons exceeding 1 GeV are shown, there is an empty part of the bubble behind the shown electron beam that is filled with newly injected electrons that have not reached 1 GeV of energy yet (see figure 21 bottom right). The selected energy of 1 GeV is approximately the threshold that separates electrons from inside the bubble from electrons that are outside the bubble after being accelerated for a short time. The third plasma focus of the laser pulse is reached approximately at the bottom right subplot of figure 21 at about 33 mm, where beam-loading has gradually destroyed the second plasma cavity.

The last part of the simulation is shown in figure 22, which shows the same positions as the bottom row of figure 17. Here, the increase of the amplitude of the laser pulse saturates after approximately 40 mm of acceleration (see figure 18 left), and the large amount of recently self-injected charge is accelerated at a high field strength, attaining energies in excess of 2 GeV within a short distance. At the same point (top right subplot), the depletion of the laser energy begins to stretch the laser pulse as long wave-
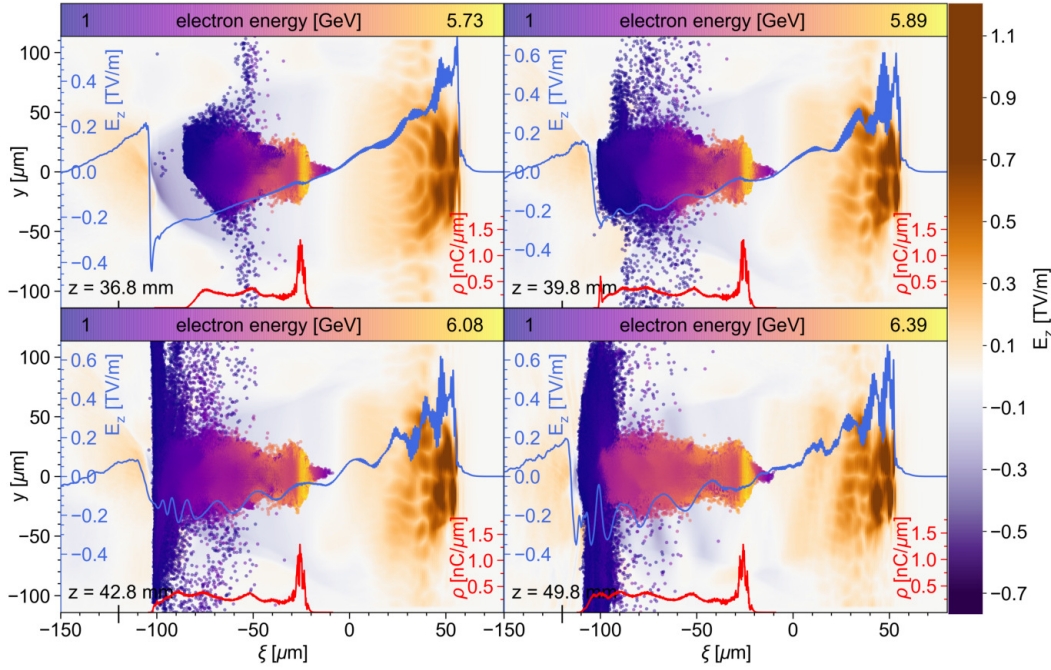
Figure 22: Laser-wakefield acceleration from 37 mm to 50 mm, featuring electrons (color coded dots, top colorbar) above 1 GeV. The longitudinal distribution of these electrons (red lines), and the amplitude of the longitudinal accelerating field along the central axis (blue curves) are depicted.

lengths have a lower velocity [206]. Note, the position of laser foci within the plasma along with increased self injection can also be seen from the smaller maxima in the longitudinal distribution of the charge (red curves), where newly injected charge mostly gets trapped at the back of the electron beam. The elevated energy of the main part of the electron beam, and its increased length is very well suited to run a beam-driven plasma accelerator. Therefore, a closer look at the beam properties and the optimum point for extraction will be considered in the next section.

6.4.1 *Characteristics of the simulation*

In figure 23, the mean energy of 5 µm broad longitudinal slices of the witness beam (see figure 24), and the total peak energy of the witness beam throughout the simulation are depicted. It shows, the constant increase of the maximum energy of the beam (dashed blue line) and its bending towards a saturation that limits the maximum achievable energy presumably to about 7 GeV. The slices are labeled with respect to their co-moving coordinate between $\xi = 50\,\mu m$, and $125\,\mu m$ which shows approximately the total length of the final bunch. For instance, the line $50\,\mu m$ shows all electrons within $\xi = 50 - 55\,\mu m$, where ξ is the distance to the end of the simulation box.

The front of the beam at $\xi = 125\,\mu m$ is injected and accelerated first (the solid lines show the mean energy of the respective slice) and contains the peak energy (blue
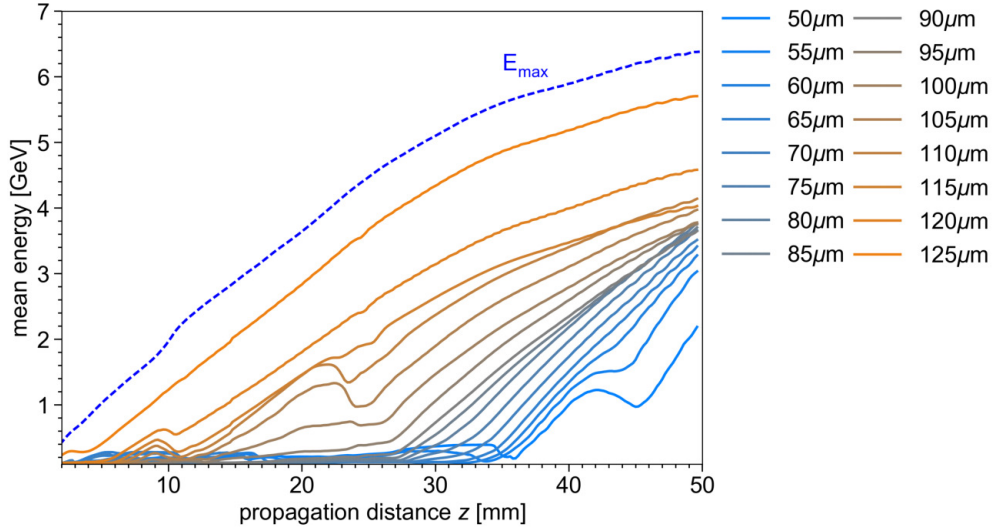
Figure 23: The mean energy of witness beam electrons within $5\,\mu m$ broad longitudinal slices throughout the simulation (color coded, solid), and the maximum energy within the bunch (blue, dashed).

dashed line). Note, the trapping positions of the first electrons in the beam, $\xi \approx 140\,\mu m$, are in front of the electrons with the maximum energy at $\xi \approx 125\,\mu m$. However, these foremost electrons are only a negligible small fraction of the beam and are not included in figure 23 for clarity. Interestingly, these electrons are not injected at the start of the acceleration but at a later point, where the laser amplitude is lower, resulting in a shorter bubble (see figure 24).

The other interesting characteristic that can be extracted from this figure, is the evolution of the length of the plasma cavity. At the beginning, only electrons in between $\xi = 125$ and $130\,\mu m$ gain energy, marking the position of the back of the plasma cavity. Then, electrons within the next three slices are accelerated for a short distance during the first laser focus near $z = 10\,mm$, and subsequently lost again when the bubble shrinks behind the focus. At the end of the simulation, the bubble reaches back to $\xi \approx 50\,\mu m$. Therefore, the bubble stretches for at least $75\,\mu m$ during the simulation, determining the length of the electron beam. It is remarkable that until $z \approx 27\,mm$, the bubble ends at $\xi \approx 95\,\mu m$, but then it rapidly stretches back to $\xi \approx 50\,\mu m$, where also the amplitude of the laser increases quickly. The nonlinear plasma wavelength within the simulation ranged from $\sim 70\,\mu m$ (see figure 19) at the beginning, to $\sim 170\,\mu m$ at $50\,mm$ (see figure 22) after the amplitude of the laser pulse significantly increased and the wave is heavily beam-loaded. Therefore, the nonlinear plasma wavelength could not be predicted accurately by equation (68) with $\lambda_{p,NL} \approx 250\,\mu m$, using $E_{max} = E_0\,(\gamma_\perp - 1/\gamma_\perp) \approx 169.4\,GV/m$ (with $\gamma_\perp = \sqrt{1 + a_0^2/2}$) as the estimate for the maximum electric field strength [231]. The actually measured peak accelerating field strength in the simulation is at about $200\,GV/m$ before the amplitude of the laser in-

creases due to compression of the pulse and increases to about $500\,\mathrm{GV/m}$ at the end of the simulation (see figure 18).

Another piece of information that can be extracted from figure 23, is given by the gradient of the energy, $\frac{\partial W}{\partial z} = eE_z$, that shows the field strength, E_z, at which the electrons are accelerated. Therefore it can be inferred that the later positions ($\xi \sim 50 - 90\,\mu\mathrm{m}$) feel slightly increased accelerating field strength between $\xi \sim 27\,\mu\mathrm{m}$, and $\sim 35\,\mu\mathrm{m}$. This would be expected from the longitudinal component of a plasma wake, but because the charge distribution of the electron beam alters the accelerating field strength as a consequence of beam-loading, it is not trivial that this feature survives. Last but not least, it is visible that at $z \sim 10, 22$, and $z \sim 40\,\mathrm{mm}$, some energy is lost at the rear of the beam. At these positions, charge was lost again after it was temporarily accelerated due to a shrinking bubble which, for the first two positions is caused by the laser de-focusing, and from heavy hosing of the rear part of the beam in the last case.

The development of the longitudinal phase space is shown in figure 24, again at the same positions as in figure 17 to maintain comparability. Also the development of the phase space must be seen in the light of the periodically focusing laser and the connected forward and backwards shifting of the rear end of the bubble. The phase space appears to consist of crescent-like shaped horizontal layers, each created at one self-injection cycle. These structures are generated beginning at the minimum and rising laser field strength, during which the rear end of the bubble is shifted backwards. This injects an increasing number of electrons as the amplitude of the accelerating field increases, and simultaneously gives higher energies to these electrons, while their trapping position is shifted back in conjunction with the rear end of the bubble. When the laser strength decreases again, the injection stops and the already injected charge reacts back onto the length of the bubble, forcing sheath electrons to close the bubble behind the recently trapped charge through its force of repulsion. The next portion of electrons is then inserted at a later position in the following cycle. Note that electrons can also become trapped at the same position at distinct times due to the backwards and forward motion of the end of the bubble, so the electrons are not perfectly ordered in the direction of propagation. For instance, the very front of the beam is injected later, and in front of the part that was injected first (compare figure 19 bottom right, and 20 top right).

To be usable, a drive beam must remain small enough in its transverse extension behind the LWFA stage to be able to drive a PWFA or to be captured by a beam transport element. No less importantly, its direction of propagation must be very well aligned with the optical axis when leaving the plasma. These requirements are not natural to LWFA beams, as they typically exhibit a large divergence, especially when they have been self injected. Unfortunately, the hosing instability of high-charge electron beams inside
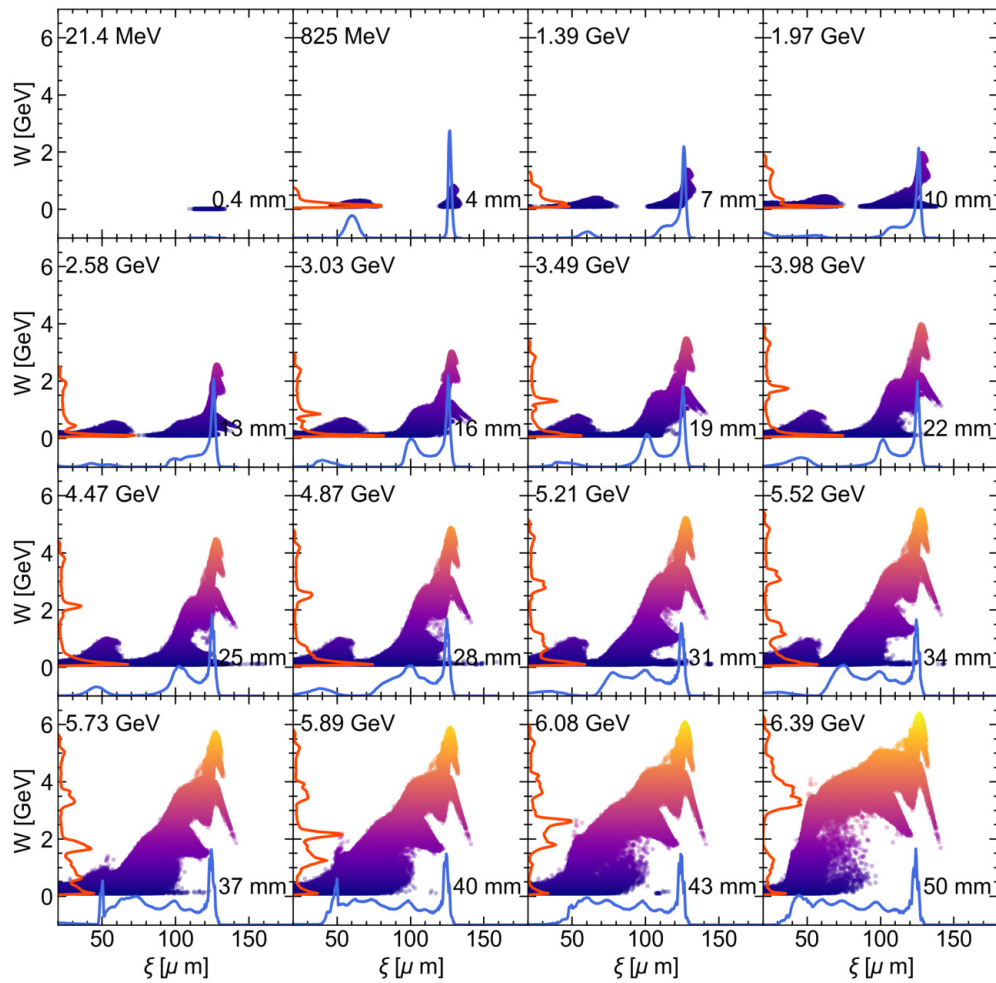
Figure 24: Development of the longitudinal phase space of electrons with more than $100\,MeV$ energy. The maximum energy, and acceleration length are displayed in the top left, and in the bottom right for each subplot. The longitudinal distribution of the charge (blue curves), and the energy distribution (orange curves) are projected onto the respective axes in arbitrary units.

the blowout may also lead a collective oscillation of the beam electrons, resulting in an arbitrary misalignment when leaving the plasma [104, 237].

Within the simulation, this misalignment was measured by the mean transverse momentum and the mean transverse position, shown in figure 25. These two properties are visualized in consecutive, $5\,\mu m$ broad slices of the witness beam (color coding), where just half of the slices of figure 23 are shown for clarity. The rear slices are only interesting from the point on at which their electrons are actually situated within the bubble and undergo acceleration (see figure 23). Therefore, these positions have been extracted from the data shown in figure 23, and the curves in figure 25 have been restricted to start from these positions. From figure 25, it can be seen that the witness beam oscillates with a larger amplitude the further the slice is situated behind (blueish colored) and that the amplitudes increase until $z \approx 40\,mm$. The charge leak that is visible at the same position in figure 23 is based on the catastrophic resonant amplification
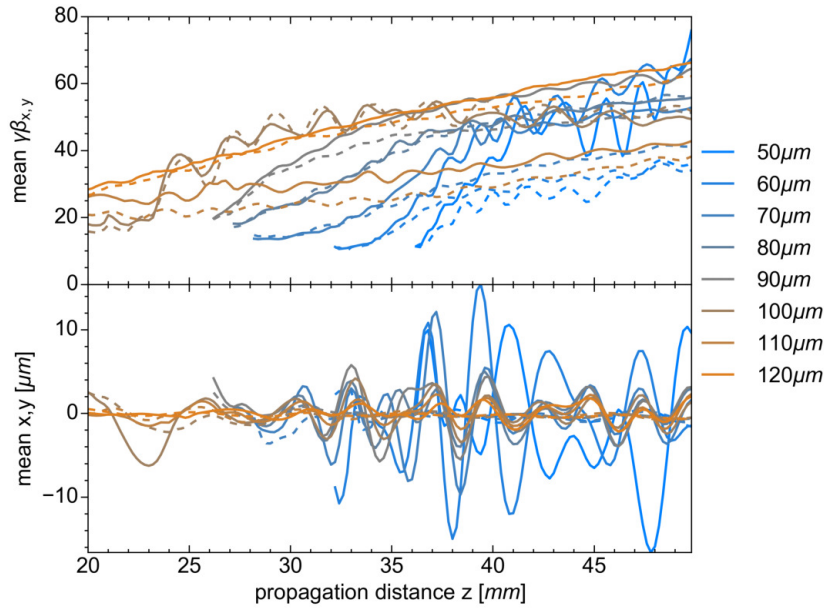
Figure 25: The rise and effects of the beam-hosing instability, visualized by the normalized mean transverse momenta (top), and the mean transverse positions (bottom) of longitudinal 5 µm broad slices of trapped electrons (color coded) in the direction of laser polarization (y, straight) and perpendicular (x, dashed).

of the oscillation amplitude in the last two slices at $\xi = 50$, and $60\,\mu m$ where the mean moment and position suddenly becomes smaller again, after the outermost charge has left the simulation box and is not counted anymore. Note, the oscillations in the plane of the polarization of the laser (y, straight) are substantially larger than the oscillations in the perpendicular plane (x, dashed), which can be seen in both the mean moments (top) and the mean transverse positions (bottom). All these findings suggest that the hosing instability occurred in this simulation.

6.5 ELECTRON BEAM EXTRACTION AND TRANSPORT

The achieved beam, and indeed any typical LWFA beam, is very challenging to transport in a conventional beam line due to its large divergence and energy spread [9, 162, 205]. An alternative solution is provided by the plasma itself, by utilizing the plasma lensing effect. This has the advantage of very strong focusing fields that are radially symmetric, but the focal position still depends on the energy. Using a plasma lens, the goal is to focus the part of the beam that is best suited to drive the plasma wave, and to scatter low-energy electrons away from the axis of propagation. This effect is most effective for long, and thin electron beams, a requirement not necessarily met by a typical LWFA beam. As has been shown in the previous discussed LWFA simulation, the interplay of periodical self-focusing of the laser, followed by increased self injection and elongation of the blowout can result in the formation of long electron beams. Similar

LWFA simulations have been shown by [185], featuring a similar witness-beam phase space and current distribution, and wakefield elongation after a large amount of charge has been self injected.

A typical LWFA beam has a very strong divergence that is introduced by the strong focusing fields inside the plasma and reinforced by its space charge. It will therefore quickly expand after leaving the plasma, which is neither good for being focused by a plasma nor to drive a wakefield. Consideration of the transverse beam size is therefore of crucial importance in a hybrid LWFA-PWFA setup. Within the plasma, the focusing forces increase proportional to the plasma density $F \propto n$ (see equation (117)). Therefore, to focus a strongly divergent beam, high plasma densities are required. On the other hand, focusing forces only arise in regions inside the plasma cavity, which scales inversely with the square root of the plasma density $\lambda_p \propto 1/\sqrt{n}$. As a result, wide beams cannot be focused in a dense plasma because the focusing region is small compared to the beam width. Consequently, the plasma density has to be chosen carefully to include the beam in its focusing region, and to be strong enough to compensate the transverse moment of the beam electrons within the radius of this region.

Extraction of the beam from the LWFA stage is done with a plasma-density downramp, to slowly decrease the powerful focusing forces and result in a less divergent beam. On the other hand, the bunch already expands transversely during the downramp. The downramp length therefore needs to be chosen in such a way that the resulting electron beam has a reduced divergence, but has not blown up too much to be captured behind the plasma. In the present case, it has been chosen to be 1 mm long and to have a cosine-squared shape due to the property of being a realistic profile and being zero after one half period. The exact shape of the downramp is not very important here, as there are no crucial witness-beam properties that needs to be preserved [160]; the divergence and transverse size can be controlled only by the length of the downramp.

In Table 3, the beam parameters for three different extraction points are displayed, involving the separation of the bunch from the background by applying a cut with respect to electron energy. The cut was manually chosen at an energy that only few electrons have and where a physical separation of beam and the background electrons is visible in the phase space (see figure 24). The values of $\langle x' \rangle = \langle p_x/p_z \rangle$, and $\langle y' \rangle$ and the mean position $\langle x \rangle$, and $\langle y \rangle$ with respect to the optical axis are given as a measure of misalignment. Note, the growing imbalance in the direction of LWFA-laser polarization (y) and that the mean energies in the transverse direction are relativistic. Also, the peak current is nearly constant for all considered extraction points and during the acceleration. This is the case because the large amount of charge injected at the very beginning of the acceleration generates the peak current, which does not change much.

The extraction points in Table 3 have been chosen at positions where the requirements for driving a wakefield are roughly fulfilled. Basically, the electron beam has enough energy and charge to drive a plasma wakefield from $z \sim 1.2$ cm onwards, where over

ELECTRON BEAM AT DIFFERENT EXTRACTION POINTS IN THE LWFA

acceleration length	3 cm	4 cm	4 cm	5 cm
energy threshold [GeV]	2	3.12	1.81	2
Q [nC]	7.86	7.96	16.3	24.5
σ_x [µm]	7.63	7.72	8.22	7.13
σ_y [µm]	7.94	8.0	9.36	8.85
σ_z [µm]	7.0	7.81	16.5	23.7
$\langle \gamma_x \rangle$	33.2	41.3	36.1	36.4
$\langle \gamma_y \rangle$	35.8	44.4	40.2	47.2
$\langle \gamma_z \rangle$	6 310	7 970	6 100	7 440
$\langle W \rangle$ [GeV]	3.22	4.07	3.12	3.81
W_{max} [GeV]	5.03	5.85	5.85	6.35
σ_W [GeV]	0.77	0.71	1.08	0.76
$\sigma_W/\langle W \rangle$ [%]	23.9	17.4	34.6	20.1
$\epsilon_{n,x}$ [mm mrad]	273.0	347.8	336.2	287.4
$\epsilon_{n,y}$ [mm mrad]	291.5	377.1	419.9	463.0
I_p [kA]	337.4	329.7	346.6	324.4
$\langle y \rangle$ [µm]	0.28	1.52	2.88	3.13
$\langle x \rangle$ [µm]	0.41	−2.95	−0.28	−0.83
$\langle y' \rangle$ [10^{-4}]	9.12	−11.5	−5.36	14.7
$\langle x' \rangle$ [10^{-4}]	7.11	−0.008	0.91	−0.35

Table 3: LWFA electron-beam parameters at different extraction points, immediately behind a 1 mm long $\cos^2$-shaped density downramp, including the separation of beam electrons from the background with the given energy threshold (first line). $\langle x \rangle$, and σ_x denote the mean value and standard deviation, respectively, and $x' = p_x/p_z$ the divergence.

1 nC of charge exceeds the 3 GeV energy mark. However, with $\sigma_z \approx 7$ µm, the electron beam is very short to drive a PWFA at a reasonable plasma density. A sufficiently long bunch ($\sigma_z > 1$ µm) is required for the last FEL stage and the plasma wave in the PWFA stage must therefore be long enough to allow for a long witness bunch to be accelerated. The length of the drive beam is therefore very important as it determines the applicable densities for PWFA by the resonant condition $\sigma_z \approx \sqrt{2}k_p^{-1} \propto n^{-1/2}$. However, the resonant condition gives only the approximate point of best efficiency of wakefield excitation. The limits where the wakefield can no longer be excited efficiently are approximately reached when the drive-beam duration is below the response time of the plasma, $\sigma_z < k_p^{-1}$, or much longer than half the plasma wakefield wavelength,

$\sigma_z > \pi k_p^{-1}$. This defines a density corridor that is applicable for a given bunch length, σ_z (see figure 26). Based on its properties, the last extraction point at $z = 5\,\mathrm{cm}$ with a sufficiently long bunch, $\sigma_z \approx 23.7\,\mu\mathrm{m}$, and high energy, $W \approx 3.81\,\mathrm{GeV}$, was selected to be best suited as the driver for the PWFA stage.
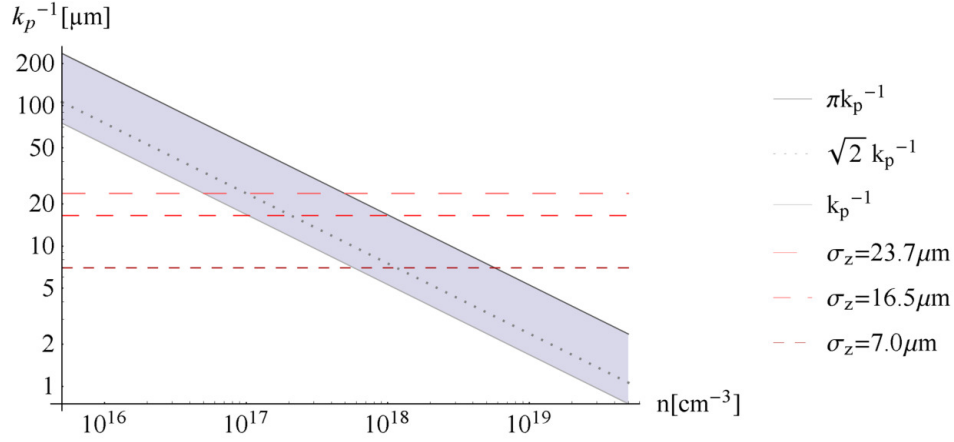

Figure 26: Applicable densities (grayish corridor) for three beam lengths (red dashed) given in Table 3 are shown with the lower density limit defined by the skin depth $\sigma_z > k_p^{-1}$ (black), the resonant condition at $\sigma_z \approx \sqrt{2}k_p^{-1}$ (gray dashed), and the upper density limit at half the plasma wavelength $\sigma_z > \pi k_p^{-1}$ (gray).

Considering the extraction points in Table 3, the optimal density for $\sigma_z = 23.7\,\mu\mathrm{m}$ is $1.0 \times 10^{17}/\mathrm{cm}^3$, for $\sigma_z = 16.5\,\mu\mathrm{m}$, $2.07 \times 10^{17}/\mathrm{cm}^3$, and for $\sigma_z = 7.0\,\mu\mathrm{m}$ the optimal density is $11.5 \times 10^{17}/\mathrm{cm}^3$. Further, the parameter $\tilde{Q} \propto \sqrt{n_p}$ (87) is dependent on the plasma density and for a given electron beam, the plasma response might become linear at low plasma densities, making TH injection impossible. The matched transverse beam size (109) depends on the emittance, which has different values in the x and y directions (see Table 3), resulting in the necessity to match the beam size to two different values in each direction.

In the case of high-current beams, $\tilde{Q} \gg 1$, the plasma response is nonlinear and the nonlinear plasma wavelength $\lambda_{NL} > \lambda_p$ (68) must be considered to estimate the optimal density for the given drive-beam length. Then, also the response time of the plasma is forced to shorten by the strong fields of the drive beam as $k_{NL} \propto 1/\lambda_{NL}$ becomes shorter and the drive beam can be applied in a mismatched condition.

The distance between the two plasma stages is a crucial, yet easily accessible parameter that can be used to adjust the drive-beam width. Simultaneously, it is required for the TH laser to be introduced onto the propagation axis, which limits the laser spot size at this position. For instance, for a 45° angle on-axis mirror, the spot size is restricted to be smaller than the distance between the plasma stages, otherwise the TH laser must be injected from an angle off-axis. The rear side of the mirror—or an additional pinhole—would also block the LWFA laser, which might no longer be needed if the drive beam is capable of self-ionizing. The mirror must then also contain an on-axis aperture to let

the drive-beam electrons pass through. This could block outer electrons and let pass only the core of the beam. This is another way to get rid of electrons with low energies, e. g. when in addition a plasma lens is used.
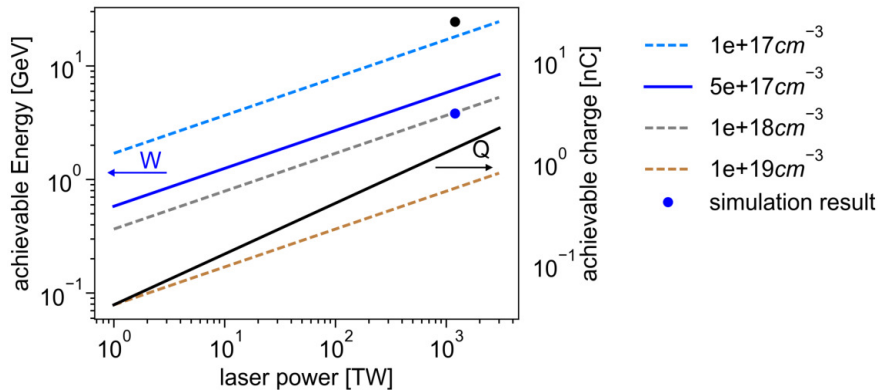

Figure 27: Theoretical scaling of the final bunch energy (85) for different densities (dashed), for the simulated density of $5 \times 10^{17}\,\mathrm{cm}^{-3}$ (blue), and the theoretical scaling of the beam charge (86) (black). The charge (black dot) and energy (blue dot) of the simulation are displayed.

The necessary laser power and plasma density that can produce the charge and energy required for a PWFA drive beam can be estimated using equation (85) and (86). These scaling laws have been used to predict the outcome of the LWFA simulation and are depicted in figure 27. It can be seen that the charge of $24.5\,\mathrm{nC}$ (black dot) resulting from the simulation is substantially underestimated by equation (86) (black line), which predicts only $1.4\,\mathrm{nC}$, while the mean energy of $3.81\,\mathrm{GeV}$ measured in the simulation (blue dot) is overestimated by equation (85), which gives $6.1\,\mathrm{GeV}$ (straight blue line).

This can be understood by noting that the estimate in [146] is based on a non-evolving drive laser and blowout, an approximation that is clearly not fulfilled in this simulation. In fact, as mentioned previously, the trapping mechanism responsible for self injecting the large amount of charge in the simulation relies on the elongation of the plasma cavity, and thus could not have been included with a static approximation. It is obvious that this much bigger amount of charge gained substantially less energy than predicted because of beam-loading effects. The maximum acceleration length, which has been estimated with about $30\,\mathrm{cm}$ from the depletion length, was not fully used at the end of the simulation at $5\,\mathrm{cm}$. The saturating peak energy (see figure 23), however, suggests that a longer simulation would not have increased the energy of the electron beam significantly[1]. As the energy and charge required to drive the PWFA stage, has been achieved at this point, it was not necessary to continue this run.

---

1 Note that in addition, the energy of this electron beam amounts to $\approx 93\,\mathrm{J}$, while the LWFA laser had an energy of $\approx 100\,\mathrm{J}$. Such a high transfer efficiency of the energy is very unlikely and implies a violation of the conservation of energy in the LWFA simulation.

In the presented simulation, the condition for matched self-guided laser propagation, $2\sqrt{a_0} \simeq k_p w_0$ has not been fulfilled exactly ($2\sqrt{a_0} \approx 5.66$ and $k_p w_0 \approx 3.14$) [231], which leaves an important point that could be addressed in future simulations. However, keeping the strongly evolving LWFA-laser pulse more stable is no easy task and makes self injection impossible, i. e. if $P_l = P_c$. The mismatched self guiding of the laser pulse might also have been a reason for the increased amount of self-injected charge. However, this can also be an opportunity to increase or tune the amount of injected charge in self-guided LWFA experiments to meet the requirements of PWFA drivers.

Note that the presented LWFA simulation was also restricted by the available computational methods and resources. In practice, it would be preferable operate at a lower density and laser power to achieve less charge and a higher energy. Because the achievable charge, $Q \propto P_l^{1/2}$, increases faster with laser power than the achievable energy $\Delta W \propto P_l^{1/3}$ and the achievable energy increases $\Delta W \propto n_p^{-2/3}$ with lower density. Operation at significantly lower plasma density would also require external guiding of the laser due to the increasing critical power for self guiding, $P_c \propto n_p^{-1}$. In addition, the efficiency of the plasma accelerator drops with the laser amplitude as $1/a_0$, assuming matched conditions [231].

HIGH-QUALITY ELECTRON-BUNCH GENERATION IN LWFA BEAM-DRIVEN PWFA

In this chapter, the feasibility of the LWFA-produced drive beam for PWFA will be investigated. A cautious approach is crucial when designing the PWFA stage, as the LWFA-beam must not ionize the HIT component. Neither at the start of the second plasma stage, nor during acceleration e.g. when the drive beam is pinched by the plasma focusing forces. An advantage of a high-current drive beam is that no pre-ionization is necessary, which is experimentally very challenging to provide over long distances. To make it easy for the drive beam to ionize, the use of alkali metals—the group of elements with the lowest first-ionization energy—is beneficial as the LIT component. However, alkali metals are not in the gaseous phase under normal conditions and need to be heated to high temperatures to vaporize[167].

In the following, the different kinds of unwanted injection in PWFA will be discussed in order to determine how the bunch must be manipulated between the plasma stages to circumvent this so called "dark current"[150].

7.1 DARK-CURRENT-FREE OPERATION

A feature of the hybrid scheme is that the very front of the LWFA-generated bunch exhibits the highest charge density, as a result of dephasing in LWFA, or as in the simulation shown, because the initial accelerating field is the strongest and able to suck in the most electrons at the very beginning. This high charge is capable of immediately ionizing LIT gas species, so self-ionized scenarios are viable. This is highly advantageous compared to a typical Gaussian beam, where the peak fields are reached only at the bunch center, leaving the bunch front completely unused for acceleration. Other features of this bunch are less advantageous, for example the fact that low-energy electrons are situated at the back of the bunch, where the wakefield can quickly decelerate them until they can become trapped as dark current.

Driver-ionized dark current.

Because the drive beam shows the highest charge density at its front, it will most effectively ionize at this position. During propagation, the approximately $1/k_p$ long head of the drive beam diverges because it is not affected by plasma lensing. This reduces its capability to ionize HIT media, while LIT media can be ionized over long

distances (see figure 28). However, when the drive beam can ionize the HIT medium, for instance at pinching points of drive-beam plasma lensing, dark current may also be injected at later points of the acceleration. To avoid the risk of dark current from HIT-gas ionization for very high-current beams, the bunch charge must be decreased or the bunch width must be increased to reduce the peak fields (see equation (32)). Fortunately, a free drift between the LWFA and the PWFA stage automatically increases the drive-beam width, lowering its peak fields.

Note that if the HIT gas is ionized by the drive beam, the generation of a witness bunch with the TH method could be prevented, because the drive-beam ionization might leave nothing for the trailing TH laser to ionize. Thankfully, the bipolar bunch fields of the drive beam vanish directly on axis and have their maximum at $\approx 1.58\sigma_r$ off axis (see equation (27)), leaving a column of HIT species for the TH laser to ionize, even when the drive-beam fields exceed the HIT. However, this limits the available charge that can be ionized to form the witness bunch.

Wakefield-ionized dark current.

This source of dark current can be avoided by operating at lower plasma density n_p, or using a lower drive-beam peak current I_p, both of which lower the peak-field strengths of the plasma wave. This source of dark current does not necessarily spoil the generation and acceleration of high-quality TH witness bunches, as it occurs only at the peak fields of the wake in the very rear of the blowout, which is typically avoided for acceleration in any case.

Furthermore, the drive beam might looses some charge after a distance and the blowout is therefore shortened. In this case, all charge that is trapped at the very rear runs into the strongly defocusing fields immediately behind the blowout and is thereby blown off axis. Alternatively, ionization by the wakefield can even be exploited to generate and trap electron beams with limited quality utilizing high-current drive beams [154]. The injection of wakefield- or driver-ionized dark current is most likely to occur at positions where the drive beam is at a plasma-lensing focus, and can thus also occur periodically, and after some centimeters of acceleration, even if no dark current was injected at the beginning.

Dark current from drive-beam electrons.

A third source of dark current is the trapping of drive-beam electrons, after they have lost their energy in the decelerating phase of the wakefield. Here, the phase space of a LWFA beam with high-energy electrons at the front, and low-energy electrons at the back (see figure 24) is inappropriate, and low-energy electrons ideally should be removed from the back of the beam before entering the PWFA to avoid this source of dark current. However, the beam is then also shortened, depending on the number of

electrons that are removed, and therefore the reduction of drive-beam electrons must not lead to a drive beam that is too short to drive a wakefield at the needed density.

One possibility to remove electrons, is to use a chicane in a conventional beamline and block part of the beam. However, because of the very large energy spread and divergence, it would be very challenging to manipulate or even transport such a beam with conventional methods [205]. A better approach is to use an underdense plasma to focus the electron beam, where different energies are focused to different positions. This can be exploited to remove low-energy electrons, when only the main part of the electron beam with high-energy electrons enters the PWFA stage focused, whereas low-energy electrons are beyond their focal point and therefore outside the plasma cavity.

Drive-beam electrons can be trapped throughout the entire second half of the blowout, based on their origin, and thus possibly also at the position of the witness bunch. This can result in a large amount of electrons with a lower energy being situated near the witness bunch. Dark current from drive-beam electrons can only be avoided if it is ensured that the tail of the drive beam has only electrons with a sufficiently high energy (see equation (118)). However, it is even possible to use this former unwanted source of dark current to shape the accelerating field acting on the witness bunch in such a way that it reverses its sign and compensates the energy chirp [151], if a sufficient amount of drive-beam electrons is trapped shortly behind the witness bunch. This has high potential to further increase the witness-bunch quality by minimizing the most crucial parameter, the energy spread, at the end of the accelerator. This mechanism is appealing, as it does not need anything additional manipulation, as it is inherently included in the physical process of plasma wakefield acceleration.

In this research, a further source of dark-current was observed in computer simulations that originated from the high current of trapped charge, which, in combination with the wakefield, exceeds the ionization threshold and produces two or even more witness bunches behind the first. This introduces the opportunity to automatically inject bunch trains with only one laser. Finally, it should be emphasized that a big concern was identified to arise from the *hosing instability* of the electron beam in the LWFA stage. This can lead to an axially asymmetric trend in the direction of propagation of the drive beam, or parts of the drive beam, and thus to an unpredictable misalignment at the PWFA stage [104]. Therefore, the electron-hosing instability must be considered a serious thread to the stability of the hybrid LWFA-PWFA scheme and must be taken into account.

7.2 DRIVING A STABLE PLASMA WAVE IN THE BLOWOUT REGIME

The parameters that need to be controlled to drive a stable blowout are the bunch width, its peak current, energy, energy spread, and its divergence. The bunch width ide-

ally should be matched according to equation (109) to not oscillate within the plasma. An unmatched beam will oscillate at the betatron oscillatory frequency $\omega_\beta = ck_\beta = ck_p/\sqrt{2\gamma}$, with period of $\sim \pi/k_\beta$ [104].

The peak current determines the strength of the accelerating field, $E_{z,max} \propto \sqrt{I_p}$, and therefore also the nonlinear plasma wavelength (68). The energy of the drive beam determines the usable acceleration length and its energy spread determines how pronounced it is pinched at a plasma-lensing focal position. A large energy spread leads to a broad spectrum of oscillatory frequencies, $\omega_\beta \propto \gamma^{-1/2}$ within the bunch, resulting in a wider beam waist at its focus. On the other hand, a small energy spread leads to a tighter beam waist, and consequently to a locally increased field strength which might be capable of ionizing second ionization thresholds, and to enlarge the plasma cavity. Both effects—ionization of the HIT gas, and elongation of the plasma cavity—make the acceleration less stable, and crucially affect the witness-bunch quality. A large uncorrelated energy spread therefore stabilizes the acceleration in PWFA, as it mitigates the betatron oscillations in the drive beam.

Finally, the divergence, p_r/p_z, must be low enough so the focusing forces can compensate the transverse momenta of all beam electrons within the blowout radius. Coming from a LWFA stage, the electron beam typically exhibits a very high divergence, which can be mitigated by a long adiabatic downramp, at the expense of a strongly increasing bunch width. The requirement of a compact and simultaneously significantly less divergent drive beam can therefore not be fulfilled without additional beam-transport elements. However, when more charge is generated in the LWFA stage than is needed for PWFA, no additional beam-transport elements are required and the divergence can be exploited as an important feature of the hybrid scheme to reduce the charge and enhance the quality of the driver.

After a free drift between the LWFA and the PWFA stage, the beam diverged and the electrons with low energy and high transverse momentum—and hence high divergence—will be situated at the beam edges with the largest distance from the propagation axis. Because the plasma focuses just the part of the drive beam within the blowout, only the less-divergent and higher-energy electrons in the beam center contribute to drive the wakefield, while the beam electrons that are outside the blowout get lost. This gives the possibility to reduce the effective charge that drives the wakefield by adjusting the distance between the LWFA and the PWFA stage, while simultaneously increasing the mean energy and lowering the divergence of the remaining electrons. In addition, the part of the drive beam that is not focused in the blowout, might ionize further LIT gas and support the generation of a wide plasma channel.

Applying the beam in Table 3 with 5 cm of acceleration and the extremely high peak current of 324.4 kA, a self-ionized PWFA is very well possible. On the other hand, this extremely high-current beam is capable of not only ionizing LIT media very efficiently, but can also ionize the second electron of lithium, which has been observed in computer simulations and is shown in figure 28. Because lithium is the element with the highest second ionization energy, there exists no other HIT species which could be utilized without generating driver-induced dark current. This necessitates either relaxing the peak current or increasing the transverse dimension of the beam.
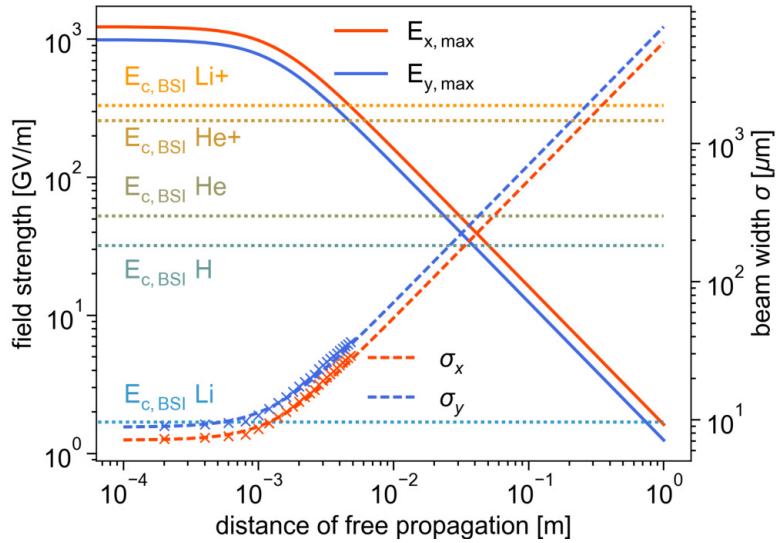

Figure 28: Transverse peak field-strengths for the obtained LWFA beam (see Table 3 at 5 cm) in the x (continuous red curve), and y (continuous blue curve) direction during free drift (using equation (30)), and the critical BSI field values of different species (dotted lines). The development of the transverse size of the electron beam (26) σ_x (dashed red curves) and σ_y (dashed blue curves) are compared to the values of the simulation ("x" markers).

To estimate the capability of the beam to ionize, equation (30) can be compared with the critical BSI field. Note that this is not an exact calculation of whether the beam will ionize a given species, but rather a simple estimate that does not include any temporal dependency in the ionization process.

Figure 28 illustrates the decrease of transverse peak fields during free propagation (continuous curves), which are compared to the critical field strength for BSI (dotted lines) given by equation (55). In this approximation, the bunch fields would no longer ionize Li^+ after 4.7 mm, He^+ after 6.2 mm, helium after 30.9 cm, hydrogen after 50.5 cm and lithium after 96.3 cm. However, as the beam feels focusing forces when entering the plasma, the peak field will increase and may exceed the threshold at a later plasma focus after $\sim \pi/k_\beta$. This figure illustrates that if Li and Li^+ is used as the LIT and HIT

component, the drive beam would no longer ionize Li^+ after approximately $5\,mm$ of free propagation, while it is capable of ionizing Li over approximately $1\,m$. Therefore, after $\sim 6\,mm$ of free propagation, a PWFA-TH scenario is viable using neutral lithium gas. The additional $1\,mm$ of vacuum propagation was found in simulations to be the distance where the plasma focusing of the drive beam no longer results in the ionization of Li^+.

The divergence of the beam in the simulation (see "x" marks in figure 28) was found to be slightly faster than the theoretical divergence of a Gaussian beam as described by equation (26). However, the formula does not include space-charge effects, and the additional push from the high charge must result in a faster diverging beam. Treating LWFA beams as Gaussian shaped in the transverse direction, as done in figure 28, is a fairly good approximation, even if this is not the case in longitudinal direction.

Blumenfeld et. *al.* [21] have examined self-ionized PWFA experimentally using a Gaussian-shaped drive beam in neutral lithium gas at FACET and found that the head of the drive beam erodes slowly, shifting the point of ionization and electron expulsion backwards. In the light of these findings, it is highly advantageous that the front of the LWFA beam exhibits the highest density and energy, resulting in a slowly diverging head with the maximum field strength at the very front, which avoids the erosion of the head. This also provides the most effective ionization and prevents the blowout from shifting backwards during propagation, leading to an extended acceleration length and excitation of a more stable plasma wakefield than that from a Gaussian drive beam. Further stabilization is possible if the drive-beam betatron oscillations in the plasma are reduced by matching its size and divergence to the plasma density, such that the focusing forces cancel the diverging trends in the beam.

7.4   WITNESS-BUNCH GENERATION

Summarizing the results from the previous sections, a simple and realistic scenario was derived, in which the drive beam was extracted from the LWFA stage using a $1\,mm$ long decreasing plasma-density profile with a cosine-squared shape, followed by a $6\,mm$ long free drift. The $1\,mm$ decreasing density profile at the end of the LWFA stage reduces the mean transverse momenta from $\beta_x\gamma_x = -1.63$ to 0.11, and from $\beta_y\gamma_y = 33.1$ to 10.60, while the transverse beam size is enlarged from $\sigma_x = 6.0$ to $7.1\,\mu m$, and from $\sigma_y = 7.5$ to $8.85\,\mu m$. The free drift substantially reduces the amount of low-energy electrons in the beam center and thereby the effective charge that drives the wakefield, because low-energy electrons show nearly the same transverse momenta as high-energy electrons and therefore have a larger divergence. The drift ensures that the HIT component is not ionized by the drive beam, and that no significant number of low-energy drive-beam electrons are trapped as dark current at an early stage of the acceleration.

Within 5 mm of free drift, the drive beam looses approximately 0.68 nC of charge with energies above 2 GeV, 1.95 nC with an energy between 1 and 2 GeV, and 14.36 nC with an energy under 1 GeV through the transverse walls of the simulation box. The remaining low-energy electrons have not been artificially removed from the beam before the PWFA stage, to model a more realistic scenario.

During the drift, the bunch width increases from $\sigma_x = 7.1$ to 34.5 μm, and from $\sigma_y = 8.85$ to 42.9 μm. Further, it was observed in the simulation of the free drift, that the low-energy electrons loose energy, while the high energy of the electrons at the front is not changed significantly. Therefore, the mean energy of the beam with electrons above 2 GeV decreases from 3802.9 to 3728.8 MeV, despite the fact, that low-energy electrons show a stronger divergence and are more likely to be lost. This might be the case because the enormous space-charge of this beam may result in an actual deceleration of the low-energy electrons at the back, as they feel the repulsive force from the charge of the front of the beam. However, it is also possible that the origin of this effect is a numerical inaccuracy. Likewise, the mean transverse-momentum is increased from $\beta_x\gamma_x = 0.11$ to 0.18 and from $\beta_y\gamma_y = 10.60$ to 11.48, possibly by the strong repelling space-charge force of the beam. The expected increase of the mean energy and decrease of the mean divergence after the free drift was therefore not observed and seems to be spoiled by the strong space-charge force of the high-current beam.

The TH-witness-bunch generation mechanism described in section 2.4 can be influenced by many effects, especially when the assumption of a Gaussian beam without inhomogeneities does not hold, as in the present case—or any realistic scenario. Therefore, the best attainable witness bunch, which can be generated using the given drive beam in a PWFA-TH setup will be ascertained by a parameter scan in the following section.

7.4.1   *Scaling of Trojan Horse witness-bunch quality*

Apart from the laser power, a_0, the laser spot radius at focus, w_0, and its FWHM duration, τ, the laser focal position, and time of arrival are crucial parameters that need to be taken into account in the Trojan Horse method. For the following parameter scans, the main focus is on the witness-bunch parameters that are most relevant for the application in a FEL, namely the energy, energy spread, emittance, bunch length and the peak current. First, a scan was performed to identify the center of the blowout by varying the distance of the TH-laser injection positions to the driver (shown in figure 29). Note that the bunch length has been multiplied by 10 in subplot (c) and is therefore shown in units of 0.1μm on the y axis, whereas the trapping position ξ_{trap} and the release position $\xi_{release}$ are in μm, relative to the blowout center.

In this scan, the position of the center of the blowout was determined by the release position that results in the most forward trapping position, and therefore also the
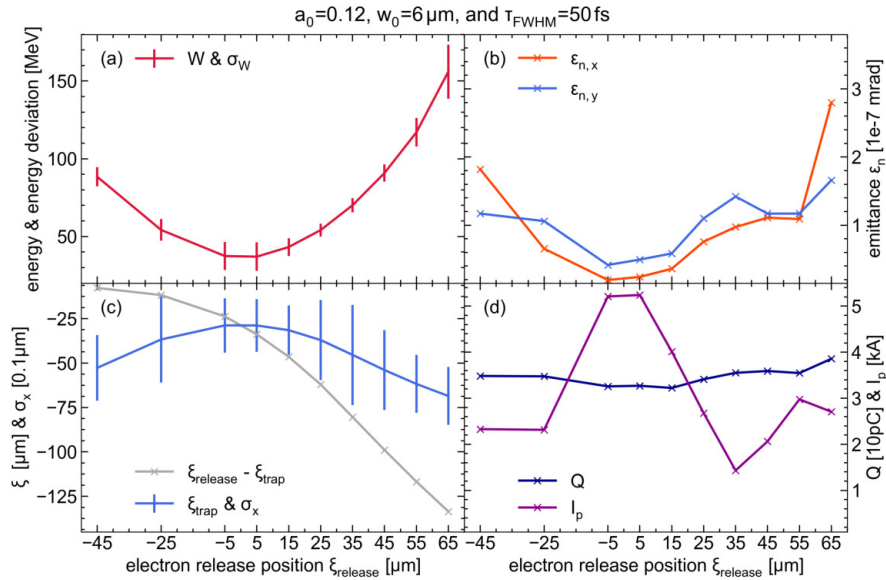
Figure 29: The mean energy (W crimson-colored curve), the energy deviation (σ_W crimson-colored error bars) (a); the emittance in both transverse directions (ϵ_x orange, ϵ_y blue) of the witness bunch (b); the distance between the release, and the trapping position ($\xi_{release} - \xi_{trap}$ [μm] gray curve), the relative trapping position (ξ_{trap} [μm] blue curve) and the bunch length (σ_x [0.1 μm] blue error bars) (c), and the peak current (I_p [kA] dark magenta) and charge (Q [10 pC], dark blue curve) of the witness bunch (d) are displayed against the distance of the TH-laser from the center of the blowout $\xi_{release}$. Note, each "x" symbol marks one simulation, and the other relevant laser parameters that have not been changed are shown at the top.

lowest energy (see figure 29 (a) and (c)). The energy spread and the bunch length are shown as error bars. The bunch length appears to have the reciprocal behavior as the energy spread at earlier trapping positions, so a longer bunch is connected with a smaller energy spread. These two quantities are also given by the standard deviation of the respective projections in figure 30, where it can be seen that the energy distribution of the witness bunch shows a double-peak profile for release positions near the blowout center $\xi_{release} \lesssim |25|$ μm. This profile results in a significantly larger standard deviation, because particles with a larger distance to the mean value have a quadratically larger impact. Except for this distortion that is introduced along with the s-like shape of the phase-space distribution, the trend in the energy spread and bunch length is directed in the opposite direction. Namely, the closer the trapping position to the center of the blowout, the longer the bunch, and the lower the energy spread. For low $|\xi_{release}|$, a high peak current occurs as a consequence of the shorter bunch (see figure 29 (c) and (d)).

The simulation with $\xi_{release} = 35$ μm shows a double-peak profile of the charge distribution (see figure 30), explaining the minimum in the peak current. The emittance is larger the further the trapping position is situated towards the rear of the blowout (large $\xi_{release}$). Interestingly, the influence of phase mixing on the emittance appears
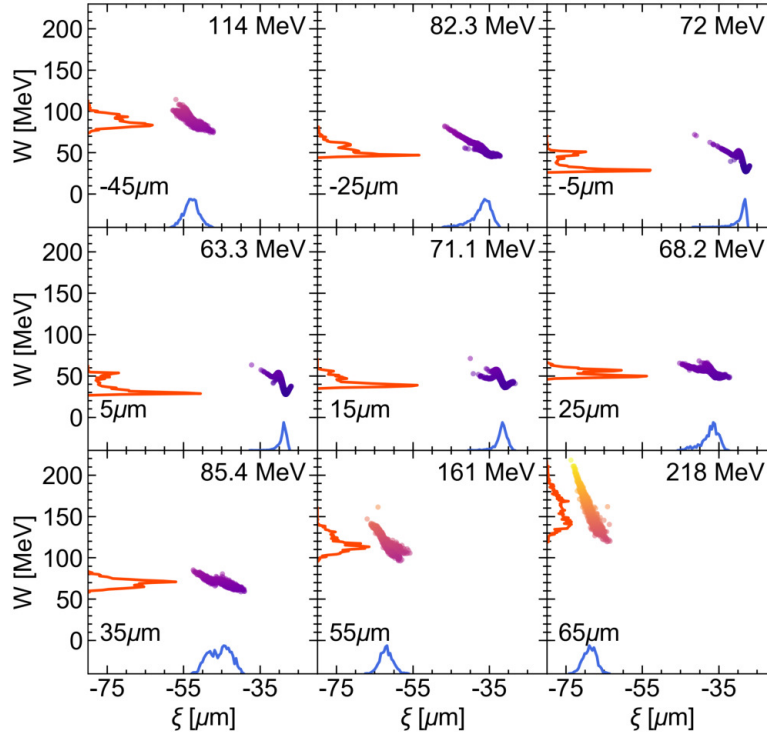
Figure 30: The phase space of witness-bunch electrons (dots, additionally colored by their energy), that are released at different positions ($\xi_{release}$ given at the bottom left of the subplots) with respect to the blowout center, is plotted after $1.6\,\mathrm{mm}$ of acceleration. The mean energy W, the deviation of the energy σ_W, and the bunch length σ_x are displayed in the top right of the subplots. The profile of the energy (orange), and the charge distribution (blue) are projected onto the respective axes in arbitrary units.

to be negligible here, otherwise the emittance should be larger the longer electrons have to travel between the release and trapping position (figure 29 (c) gray curve). The charge is not affected significantly by the release position of the witness electrons. A small increase in charge, however, seems to occur as the combined field strength of the laser pulse and the plasma wave grows with $|\xi_{release}|$.

For release positions at the blowout center, the witness bunch becomes trapped at the most forward possible trapping position $\xi_{trap} \sim -30\,\mu\mathrm{m}$, which is determined by the distance that electrons need to gain a relativistic velocity when being accelerated by the plasma wakefield (see figure 30). Because the accelerating field is approximately linearly increasing from the rear to the center of the blowout, where it is zero, the foremost trapping position is connected with the lowest accelerating field.

The conspicuous s-like shape in the energy of the witness bunch at these foremost trapping positions could be an artificial effect of the computational model. However, the energy modulation is caused by a corresponding modulation of the accelerating field. It is therefore more likely that it has a physical origin and is generated when electrons that have been trapped alter the underlying electric field in such a way that the trapping position of the following electrons is shifted. Their energy gain is then

also different from that of an unloaded wakefield as a consequence of the altered accelerating field. This is supported by the fact that it occurs most prominently at the first trapping positions, where the accelerating field has its lowest amplitude, and the space charge field of the witness bunch is not negligible compared to that of the wakefield. This is also supported by the fact, that the length of the witness bunch is significantly shorter, which is the opposite of the expected behavior (see figure 30 and 29 (c)). Beam-loading can have an influence, if the density of the witness beam $n_b = (Q/e)/((2\pi)^{3/2}\sigma_x\sigma_y\sigma_z)$ is larger than the background density n_p. For the simulation with $\xi_{release} = 5\,\mu m$ this is the case as $n_b \approx 5.89 \times 10^{19}\,cm^{-3} \gg n_p = 1 \times 10^{17}\,cm^{-3}$ (with $Q \approx 32.7\,pC$, $\sigma_x \approx 0.335\,\mu m$, $\sigma_y \approx 0.444\,\mu m$, and $\sigma_z \approx 1.48\,\mu m$). Therefore, the s-like shape of the particle energy seems to be a physical characteristic of the trapping process at low accelerating fields, which are not very efficient for acceleration.
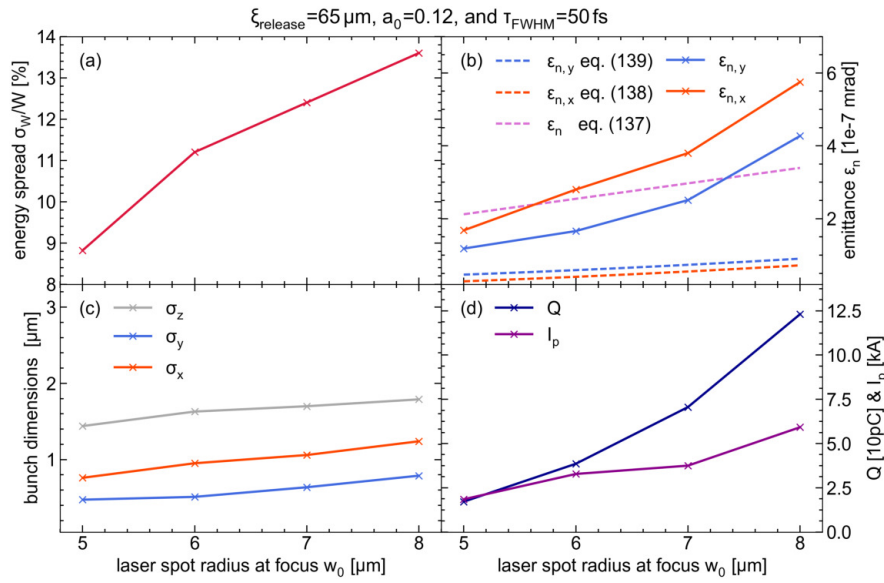

Figure 31: The energy spread (crimson-colored curve) (a); the emittance in both transverse directions ($\epsilon_{n,x}$ orange, $\epsilon_{n,y}$ blue, and ϵ_n magenta-colored curve) of the witness bunch compared to equations (139), (138) and (137) (b); the bunch dimensions in all three directions (c); and the peak current (I_p [kA] dark magenta) and charge (Q [10 pC], dark blue curve) of the witness bunch (d) are displayed against the radius of the laser spot at focus. Every "x" symbol marks one simulation, and the other relevant laser parameters that have not been changed are shown at the top.

In figure 31, the laser-spot radius at focus, w_0, is varied with the electron-release position, being 65 µm before the bubble center, corresponding to the outermost right points in figure 29. At this position, the most energy can be gained, while the emittance is still acceptable—the s-shape-feature of the phase space does not occur at this position. In figure 31 (a), the substantial increase of the energy spread can be seen, while neither the trapping position nor the energy is affected by variation of w_0. Note that increasing w_0 without changing the FWHM duration (τ) or amplitude (a_0) of the laser, simultaneously increases the total laser energy $W_l \propto \tau w_0^2 a_0^2$. The charge (see subplot (d)) and

the emittance (see subplot (b)), increase quadratically with w_0 along with the energy of the laser. However, four points are not enough to determine the growth rate precisely. Compared to the estimates of equation (139), (138) and (137), it must be noted that the trapping position seems to have a considerable influence on the emittance (see figure 29) but is not included in any of the mentioned estimates. Apart from that, the estimated emittances are of the same order of magnitude as the measured emittance, and can reproduce the correct trend.

All three dimensions of the witness bunch slightly increase with w_0 (see subplot (c)), while the charge increases very rapidly with w_0 (see subplot (d)). Note that the charge is displayed in units of $10\,\mathrm{pC}$ and therefore ranging from $17\,\mathrm{pC}$ for $w_0 = 5\,\mu\mathrm{m}$ to $123\,\mathrm{pC}$ for $w_0 = 8\,\mu\mathrm{m}$. This can be understood with the discussion of section 2.4, which showed that the ionization volume becomes longer proportional to the Rayleigh length $z_\mathrm{R} \propto w_0^2$ (see equation (127) and figure 11). Note that the length of the ionization volume does not translate into the length of the bunch, which is mainly defined by the length of the laser pulse (see figure 33). This increases the ionization volume proportional to w_0^2 and the ionized charge increases accordingly. Also, in section 2.4 it was assumed that the initial energy spread is also a function of the length over which the laser ionizes because the first ionized electron has been accelerated over this distance before the last electron is ionized and becomes trapped at approximately the same position. This is an explanation for the rapidly increasing energy spread in subplot (a).
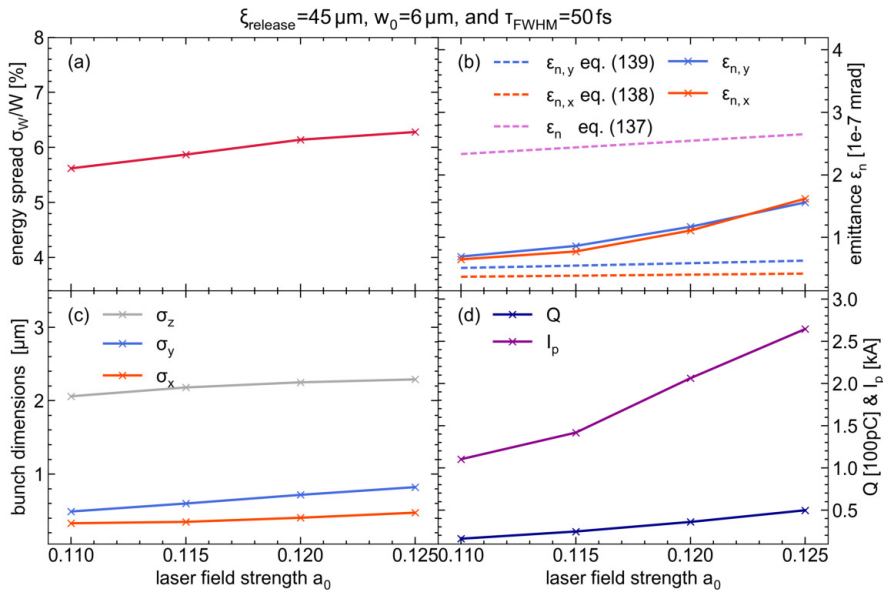

Figure 32: The energy spread (crimson-colored curve) (a); the emittance in both transverse directions ($\epsilon_{n,x}$ orange, $\epsilon_{n,y}$ blue, and ϵ_n magenta-colored curve) of the witness bunch compared to equation (139), (138) and (137) (b); the bunch dimensions in all three directions (c); and the peak current (I_p [kA] dark magenta) and charge (Q [100\,pC], dark blue curve) of the witness bunch (d) are displayed against the normalize amplitude a_0 of the laser. Every "x" symbol marks one simulation, the other relevant laser parameters that have not been changed are shown at the top.

In figure 32, the amplitude of the laser, a_0, is varied, again without changing other parameters. However, in contrast to figure 31, the release position of the electrons was chosen to be $\xi_{release} = 45\,\mu m$, corresponding to the third mark from the right-hand side in figure 29, at a significantly lower emittance and energy level. Again, the emittance increases quadratically with a_0, like the energy of the laser $W_l \propto a_0^2$. The charge substantially increases from $Q \approx 16\,pC$ for $a_0 = 0.11$ to $Q \approx 50$ for $a_0 = 0.125$ again given in units of $10\,pC$, but not as fast as in figure 31.

It is noteworthy that this dramatic increase of the charge does not substantially affect the bunch dimensions (which increase from $\sigma_z \approx 2.06$ to $2.29\,\mu m$, from $\sigma_x \approx 0.33$ to $0.47\,\mu m$, and from $\sigma_y \approx 0.49$ to $0.82\,\mu m$) or the energy spread (which increases from $\sigma_W/W \approx 5.62$ to $6.28\,\%$). The emittance increases by approximately a factor of two (from $\epsilon_{n,x} \approx 6.9$ to $15.6 \times 10^{-8}\,m\,rad$). The estimates of equation 138 and 139 are slightly lower, and underestimate the slope significantly. The simple equation 137 has a more accurate, steeper slope, but overestimates the measured emittance by a factor around two. Neither of the equations show the quadratic growth of the emittance that was observed in the simulations. The peak current increases significantly (from $I_p \approx 1.10$ to $2.64\,kA$), because the charge increases while the bunch dimensions stay approximately constant (similar to figure 31).
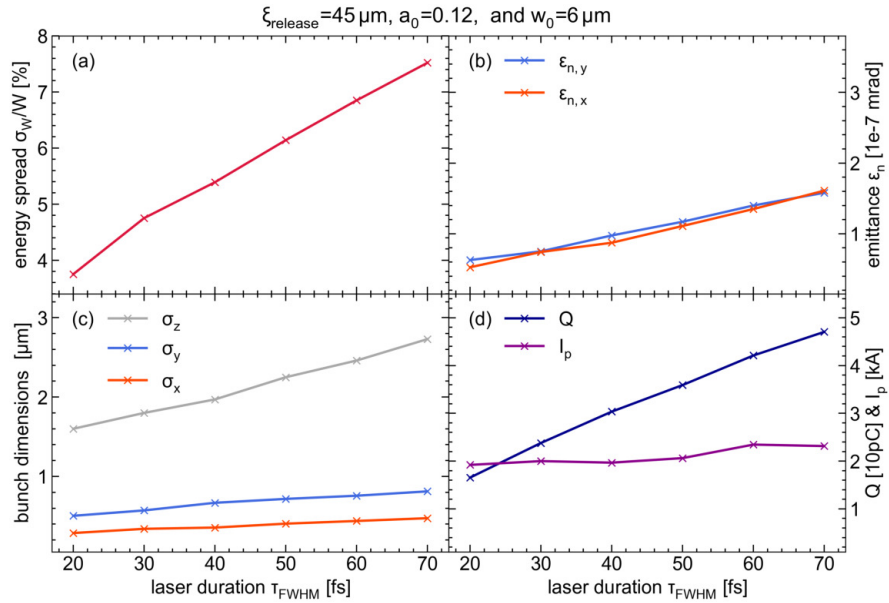
Figure 33: The energy spread (crimson-colored curve) (a); the emittance in both transverse directions ($\epsilon_{n,x}$ red, $\epsilon_{n,y}$ blue curve) of the witness bunch (b); the bunch dimensions in all three directions (c); and the peak current (I_p [kA] dark magenta) and charge (Q [10 pC], dark blue curve) of the witness bunch (d) are plotted against the FWHM-duration of the laser pulse. Every "x" symbol marks one simulation, and the other relevant laser parameters that have not been changed are shown at the top.

Figure 33 shows the change of the witness-bunch parameters when the laser-pulse duration is altered—the remaining parameters are kept as in figure 32, and displayed

at the top of the figure. Just as in the cases where a_0 and w_0 are varied, the laser energy increases with longer laser-pulse duration as $W_l \propto \tau$, yet unlike previous cases, not quadratically but linearly. This leads to an approximately linear increase of the charge (from $Q \approx 16.5$ to $47.0\,\mathrm{pC}$) and the emittance (from $\epsilon_{n,x} \approx 5.26$ to $16.1 \times 10^{-8}\,\mathrm{m\,rad}$), when increasing τ (from $20\,\mathrm{fs}$ to $70\,\mathrm{fs}$). The bunch length significantly increases from $\sigma_z \approx 1.6$ to $2.73\,\mu\mathrm{m}$, where no other laser parameter changed σ_z this much. This, again is consistent with the discussion in section 2.4. As a consequence of the increased bunch length, the total energy spread also increases from $\sigma_W/W \approx 3.75$ to $7.52\,\%$; the fractional energy spread—the energy spread within one slice of the bunch—does not increase significantly.

Summarizing the results from the parameter-scan simulations; the peak current and charge are increased most efficiently by a larger a_0, and w_0 based on the quadratically increasing energy of the laser $W_l \propto \tau w_0^2 a_0^2$. The bunch length is increased most efficiently by a longer laser pulse duration τ, or by shifting the release position towards the blowout center, but simultaneously the total energy spread is increased. The emittance depends greatly on the electron release position, ξ_{release}, and on the laser focal spot size, w_0, and and strength, a_0, and increases less significantly with larger τ.

From the perspective of FELs, where a long bunch with a small energy spread and emittance is required it is therefore favorable to use a long TH-laser pulse. However, from the above parameter scans it also becomes clear that not all parameters can be optimized simultaneously and a trade-off is inevitable. First, the position of electron release was chosen to provide for a high energy gain, at a simultaneously long bunch length and low emittance. Consequently, the release position $\xi_{release} = 45\,\mu\mathrm{m}$ was chosen in between the center of the blowout and the outermost positions where trapping is possible. An order of magnitude lower emittance can be achieved for a central electron-release position (the minimal measured emittance shown in figure 29 is $\epsilon_{n,x} \approx 2 \times 10^{-8}\,\mathrm{m\,rad}$). Exploiting the s-shape-feature at central release positions, a very high peak current is possible (the highest measured peak current is $I_p \approx 5.24\,\mathrm{kA}$). However, the small energy gain combined with the short bunch inhibits proper FEL operation.

The laser waist, $w_0 = 6\,\mu\mathrm{m}$, was chosen at a point where the energy spread and emittance is small, while the peak current and bunch length fulfills the needs of FELs. Note, the simulation series shown in figure 31 uses an electron release position $\xi_{release} = 65\,\mu\mathrm{m}$ different from the one that is chosen here. The laser FWHM duration of $\tau = 50\,\mathrm{fs}$ is chosen to produce a long bunch, while not spoiling the emittance or energy spread too much, and finally, with $a_0 = 0.12$, a sufficiently large peak current is achieved. Alternatively, injection on an ascending density at the very beginning of the plasma stage could be exploited to stretch the length of the witness bunch. With this chosen set of parameters, a long simulation is set up which is illustrated in figure 34 and 35.

7.4.2 *Characteristics of the simulation*

The simulation parameters used are displayed in Table 12 and Table 13. A lithium density of $1 \times 10^{17}\,cm^{-3}$ was chosen to maximize the plasma response $k_p \sigma_z \approx \sqrt{2}$ (see figure 26), while the resulting plasma wavelength of $\lambda_p \approx 105.6\,\mu m$ is large enough to accelerate a fairly long bunch. The width of the drive beam, however, cannot simultaneously be matched to circumvent betatron oscillation in this case, because the matched beam radius would be on the order of meters due to the large emittance (see Table 3). The normalized charge $\tilde{Q} = (Q/e)(k_p^3/n_p) \approx 322 \gg 1$ of the drive beam indicates the capability of driving a strongly nonlinear wakefield. Note that, similar to the equivalent parameter of LWFA, a_0, the transverse size of the beam is not included in this consideration, e. g. a lower density of $0.5 \times 10^{17}\,cm^{-3}$, $\tilde{Q} \approx 227.6$, and $k_p \sigma_z \approx 1.0$. Further, the mean transverse momenta given in Table 3 have been subtracted from all beam electrons, resulting in a beam that is aligned to the propagation axis. The simulation window was chosen to contain the strongly diverging drive beam for the most part, while the chosen resolution was sufficient to resolve the small local peak field strengths. Note, the wavelength of the TH-laser is not resolved and the laser pulse is represented by the envelope of the pulse.

The plasma of this second accelerator stage begins with a 0.5 mm long, linearly ascending density profile, and the ionization laser is focused another 0.5 mm after the plasma density is constantly at $1 \times 10^{17}\,cm^{-3}$. This initial part of the PWFA is illustrated in figure 34, where the situation is shown immediately behind the density upramp in subplot (a), and during the ionization (b) and trapping process (c). The high-current drive beam excites a strongly nonlinear plasma wave of approximately twice the linear plasma wavelength of $\lambda_p \approx 105.6\,\mu m$. Note that the free drift removed nearly all electrons below 1 GeV from the axis (see figure 34 (a)). The outermost electrons have left the simulation box during the free drift, so the remaining electrons are in the rectangular shape of this box when they are loaded in the PWFA stage with an increased size of the simulation box. However this does not change the wakefield, because the cut off is outside of the plasma cavity and the truncated electrons would not have contributed to driving the wakefield.

Subplot (d) in figure 34 shows the point where part of the drive beam (greenish electrons at about 2 GeV) undergoes the first plasma focus near $\pi/k_\beta \approx 6.45\,mm$ after entering the plasma. The peak electric field strengths at this and the following focal points of the drive beam, are below the ionization threshold for the HIT medium, Li^+, because the massively widened beam has lost a considerable portion of its charge. This successfully prevents the injection of dark current that is ionized by the drive beam. Also, the ionization of Li^+ at the rear of the blowout does not inject dark current.

In figure 35, the situation is shown at later points, where the driver (smaller spheres) undergoes further plasma focusing, while the rear part of the drive beam is decelerated and the witness bunch (larger spheres) constantly gains energy up to the GeV level.
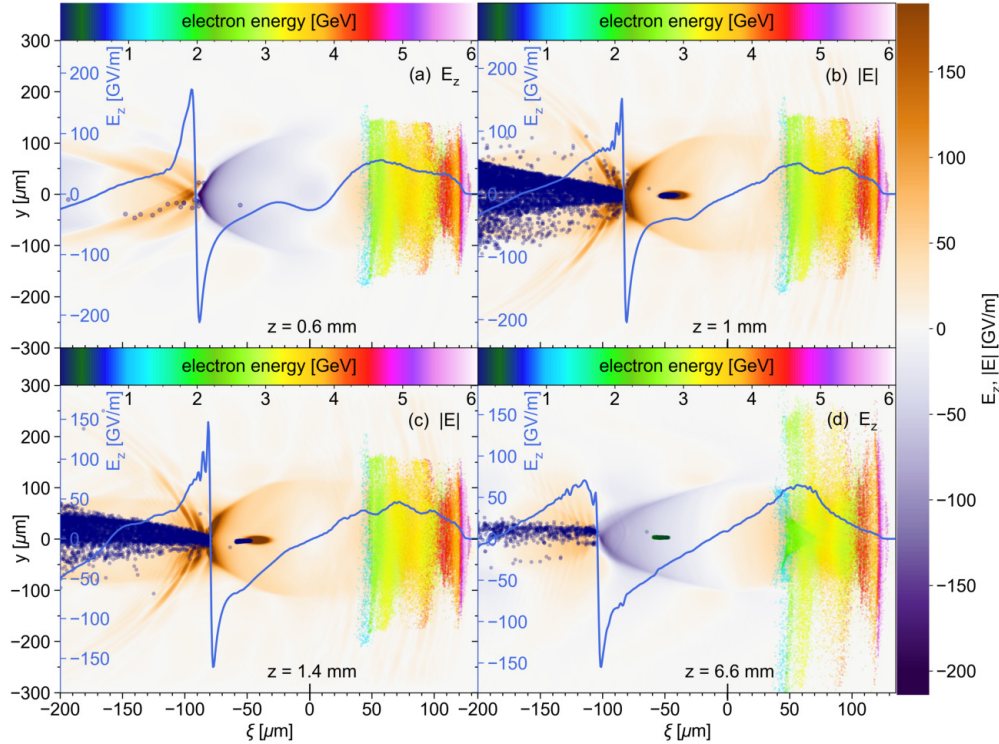
Note that the transverse coordinate, y, is on a different scale than the longitudinal coordinate, ξ, and the blowout is nearly spherical.

Figure 34: The LWFA-generated beam (Table 3) enters a second plasma accelerator stage after 6 mm of free drift through a 0.5 mm long linearly increasing density (a). The electron beam self-ionizes lithium (Li electrons are not shown, electrons from Li^+ ionization and drive-beam electrons within a central slice of $x < |5|\,\mu m$ are depicted as color-coded spheres) and a TH-laser locally ionizes Li^+ (b), generating a high-quality witness bunch that is trapped (c). Part of the electron-drive beam is first focused at $z \approx 6.6\,mm$ by the plasma (d). The central slice of the longitudinal field E_z in (a) and (d), and the magnitude of the electric field $|E|$ in (b) and (d) (right color-bar) are shown. The amplitudes of the longitudinal field along the propagation axis are shown as blue curves.

Subsequently, the electrons at the back of the drive beam have lost so much energy that they move back and become trapped in the accelerating phase of the wakefield behind the witness bunch in the last two subplots. Note, only drive-beam electrons within a central 5 μm broad slice are shown for clarity.

More surprisingly, the main part of the drive beam starts to move off axis, although the mean transverse momentum has been adjusted to be close to zero at the start of the simulation. This movement of the main part is accompanied by a smaller portion of the drive beam that moves into the opposite direction, such that the mean momentum of the beam is still close to zero. This divides the drive beam into two separate parts which are separately focused by the plasma, and that start to drive two parallel wakefields.

The TH witness bunch is pulled off axis with the main part of the wakefield, which then is significantly decreased in size due to the lost drive-beam charge. Note that the splitting of the drive beam is not visible in the x-direction and several other simulations have reproduced this behavior using the same drive beam.
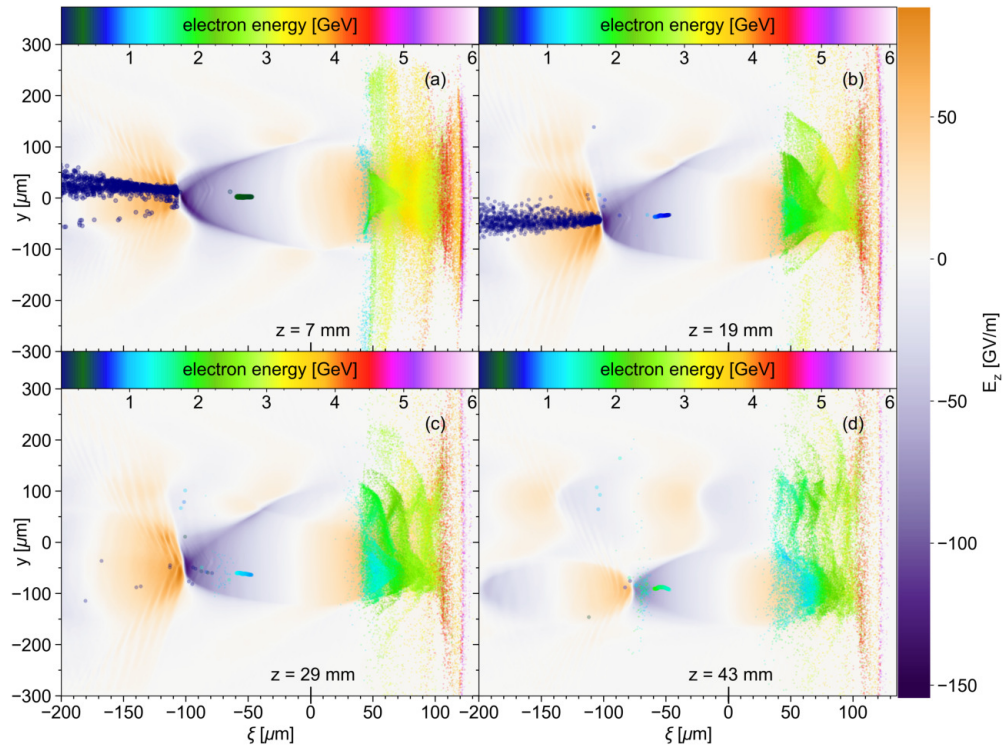

Figure 35: Focusing of the drive beam significantly elongates the wakefield (a), while its head constantly diffracts and its main part begins to move off axis (b). A considerable portion of the driver leaves the main body of the beam and starts to drive a second parallel wakefield (c), (d). Lithium electrons are not shown and drive-beam electrons are shown within a central slice of $x < |5|\,\mu m$. Electrons from Li^+ ionization and drive-beam electrons are depicted as color-coded spheres. The central slices of the longitudinal field, E_z, are shown in the background (right color-bar).

However, this process does not stop the acceleration of the witness bunch and moves it closer towards the rear of the blowout. Interestingly, this does not lead to a higher energy gain or significantly increased energy spread (see figure 36 top). A few millimeters behind the point that is shown in figure 35 (d), the acceleration stops because the shrinking blowout moves the witness bunch out of the focusing and accelerating phase. For a short time during this final phase, the energy chirp of the witness bunch is rapidly reduced as the bunch slips across the point where the gradient of the accelerating field switches its sign. This feature, however, could not be exploited as the strong de-focusing fields at the same positions dramatically increase the emittance and the bunch starts an uncontrolled wiggle motion and is pushed away from the axis immediately thereafter.

Until this point, the energy and standard deviation of the energy grows linearly, while the relative energy spread σ_W/W stays nearly constant at $6.14 - 6.88\%$ (see figure 36 top). Although the acceleration is not influenced when the drive beam is divided into two parts, it leads to a rapid deterioration of the witness-bunch quality as a result of the displacement. The displacement of the wakefield and the witness bunch can immediately be seen by the mean position of the witness bunch (see x, and y in the bottom subplot of figure 36). The direction of this movement clearly is predominantly
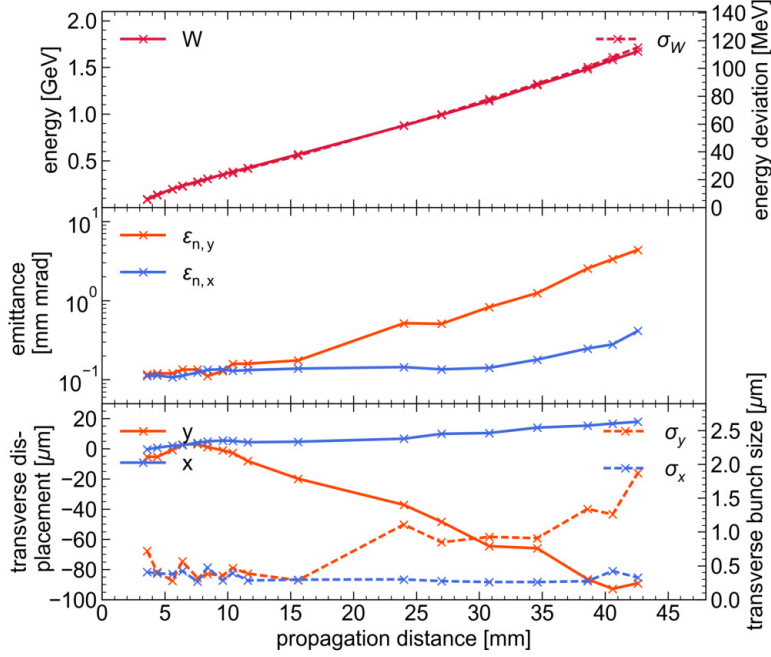

Figure 36: The development of selected parameters is shown for the simulation in figure 34 and 35. The mean energy, W, of the witness bunch (crimson-colored continuous line), and its energy deviation σ_W (crimson-colored dashed line) are shown in the top subplot. During the drift in the y direction, depicted by the mean position of the witness bunch (bottom plot left y-axis, orange continuous curve), the bunch undergoes a meandering motion that leads to a dramatic increase of its width, σ_y (bottom plot right y-axis, orange dashed curve). As a result, the emittance (middle plot, orange curve) dramatically increases from $\epsilon_{n,y} \approx 0.12$ to $4.36\,\text{mm mrad}$ in this direction, while the x-direction is much less affected (blue curves).

in the plane of the polarization of the LWFA laser, y, which also leads to a dramatic increase in the bunch width and the emittance in this direction (orange curves in the middle and bottom subplots). The increase of the bunch width results from the fact that the bunch is significantly longer than broad, and the head is moved off axis time-displaced from the rear. Such that the length partially translates into its width in the direction of the displacement.

Figure 37 shows the development of the longitudinal phase space of the drive beam (smaller spheres) and the small witness bunch at $\xi \sim -50\,\mu\text{m}$ (larger spheres). When comparing the last subplot of figure 24, where the drive beam is shown before exiting
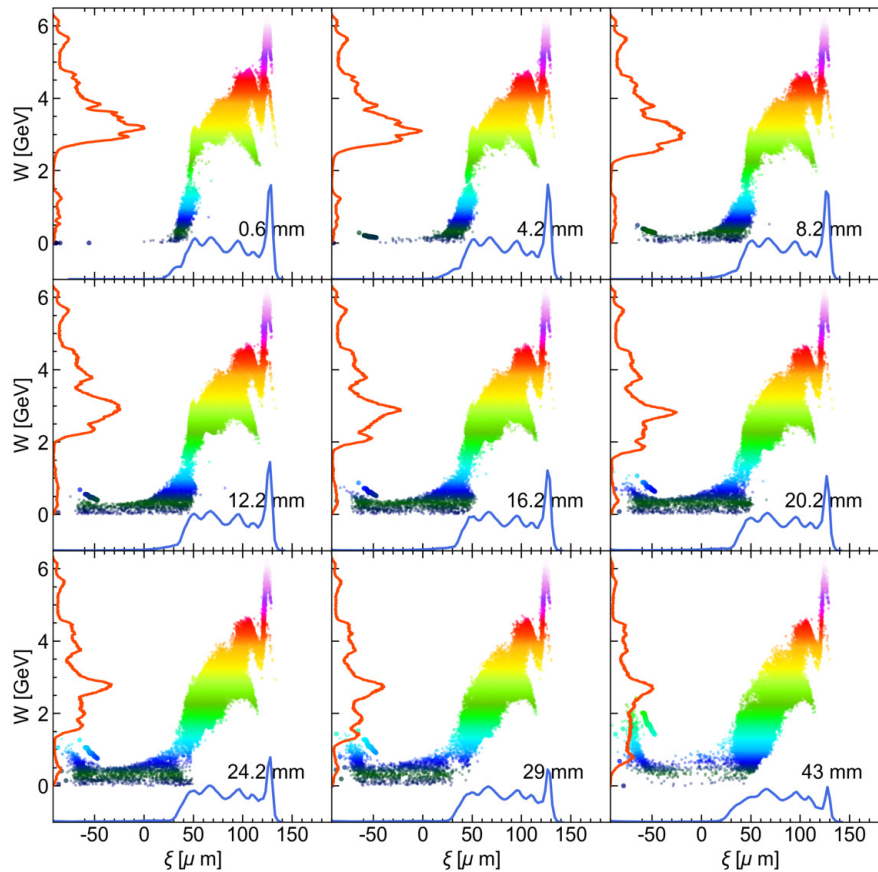
Figure 37: The development of the longitudinal phase space of the witness bunch (larger spheres), and the drive beam (smaller spheres) within the same $x < |5|\,\mu m$ thin central slice as in figure 34 and 35. The energy distribution of the whole beam (orange curves), and the distribution of the drive-beam charge (blue curves) are projected onto the respective axes.

the first plasma stage, and the first subplot in figure 37, where the drive beam has entered the second plasma stage after a 6 mm drift, it can be seen that many low-energy electrons are lost during the drift. However, a small number of electrons with energies below 1 GeV remain. Since they are situated at positions of the strongest decelerating field strengths, they quickly become decelerated and are subsequently trapped at the back of the wakefield. Nevertheless, these trapped beam electrons are spread over a large region within the blowout and do not noticeably interfere with the witness bunch.

The deceleration of the drive beam is clearly visible in the phase space, and from the projection of its energy distribution. The large number of electrons around 3 GeV from the beginning continuously loose energy and start to move into the blowout, while the high-energy electrons at the front of the beam mostly keep their energy but gradually get lost due to their divergence. However, as can be seen from the charge projection, no significant amount of drive-beam charge moves backwards until the end of the simulation, where the rear slope of the distribution of the charge begins to soften.

7.4.3 *Evaluation and summary*

The witness bunch is extracted from the plasma at z=30 mm, the position shown in figure 38 and 39, using a 1 mm long cosine-squared density profile that lowers the density to zero. At this point, the energy is at a sufficiently high level while the emittance, and bunch width, are not too large for application in a FEL (see figure 36). The resulting parameters of the witness bunch, directly behind the plasma exit, are displayed in Table 4.
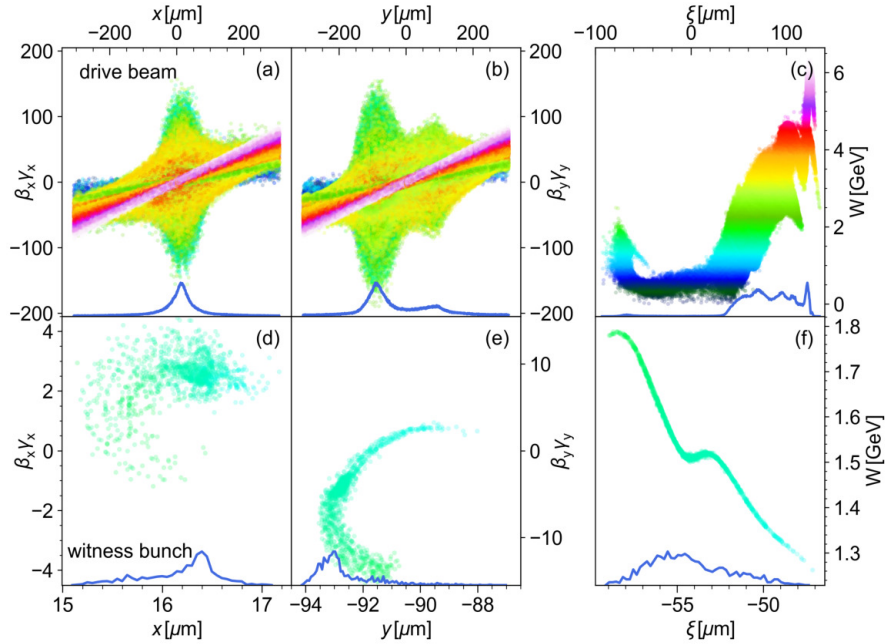

Figure 38: The phase space in all three dimensions for the drive beam (top row) and for the witness bunch (bottom row) at $z = 30$ mm. The projections of the electron distributions onto the spatial axes are shown at the bottom of each subplot in arbitrary units. The scale for the energy (color coding) is the same for every subplot and can be read from the color in subplot (c).

In figure 38, the phase-space distribution of the drive beam (top), and witness bunch (bottom) in all three directions is displayed at the point before it is extracted from the plasma. The vast divergence of the head of the drive beam is visible in subplot (a) and (b), by the wide spread of the electrons over the entire x, and y axes. A different part of the beam with energies from about 2 to 4 GeV (green-, and yellow-colored) is focused by the plasma, and is transversely restricted to the radius of the blowout, despite its very high momentum.

Figures 38 (a) and (b) show that the further the drive-beam electrons are from the central axis, the higher are their transverse momenta. This is because electrons with a high divergence, and thus for a given energy a high transverse momentum, are faster further away from the central axis than electrons with a lower divergence and transverse momentum. Electrons with the same divergence, p_x/p_z, share approximately the

same distance from the central axis. Therefore, high-energy electrons (red- and violet-colored) also have a higher transverse momentum ($\beta\gamma$) than electrons at the same transverse position and a lower energy (see subplot (a) and (b) of figure 38). Finally, the two subplots (a) and (b) show that the drive beam is only split in the y direction. The longitudinal phase space of the entire drive beam is shown in subplot (c). The

WITNESS BUNCH PARAMETERS AFTER A 1 MM LONG DOWN RAMP

W	$1\,130\,\mathrm{MeV}$	mean energy
σ_W/W	6.89%	relative energy spread
$\langle\,\sigma_W/W\,\rangle_{slice}$	0.442%	mean slice energy spread
I_p	$2.05\,\mathrm{kA}$	peak current
Q	$35.9\,\mathrm{pC}$	total charge
σ_z	$2.26\,\mathrm{\mu m}$	longitudinal rms bunch length
$\sigma_x,\,\sigma_y$	$0.29,\,0.93\,\mathrm{\mu m}$	transverse rms bunch lengths
$\epsilon_{n,x},\,\epsilon_{n,y}$	$0.14,\,0.84\,\mathrm{mm\,mrad}$	normalized transverse rms emittances
$\langle\,\beta_x\gamma_x\,\rangle,\,\langle\,\beta_y\gamma_y\,\rangle$	$-0.77,\,-6.07$	mean transverse momenta
$\langle\,x\,\rangle,\,\langle\,y\,\rangle$	$10.3,\,-65.7\,\mathrm{\mu m}$	mean transverse positions
z	$31\,\mathrm{mm}$	point of extraction

Table 4: The resulting witness-bunch parameters from the simulation in figures 34-36 are shown at $z = 31\,\mathrm{mm}$, right after a 1 mm long cosine-squared density profile, at the exit of the plasma. The applied simulation parameters are shown in Table 13. For the calculation of the peak current and the mean slice energy spread, the bunch is divided into $0.5\,\mathrm{\mu m}$ broad slices.

transverse oscillation of the witness bunch, which is induced by the off-axis drift of the drive beam, can be seen in subplots (d) and (e) of figure 38. The oscillation of the witness bunch is predominately in the y direction, along with an offset of $y \approx -93\,\mathrm{\mu m}$, which is approximately at the same position as the peak density of the drive beam (compare subplot (b) and (e)).

The longitudinal phase space of the witness bunch in subplot (f) shows a less pronounced version of the s-like phase space that is discussed in the context of figure 30. Here, the feature is optimized to compensate for the correlated energy spread at the center of the witness bunch.

As can be seen from Table 4, the energy of the obtained witness bunch is well above the 1 GeV level. However, the steep gradient of the accelerating field in combination with the long bunch, lead to a large correlated energy spread that constantly increases during the acceleration (see figure 36). For a FEL, a smaller energy spread is required at higher energy. Therefore, and because the slice energy spread also did not decrease significantly, it was not possible to go to higher energies. It was also not possible to

go to a higher energy in this simulation because of the increasing bunch width and emittance. In practice, the high correlated energy spread must be compensated to fulfill
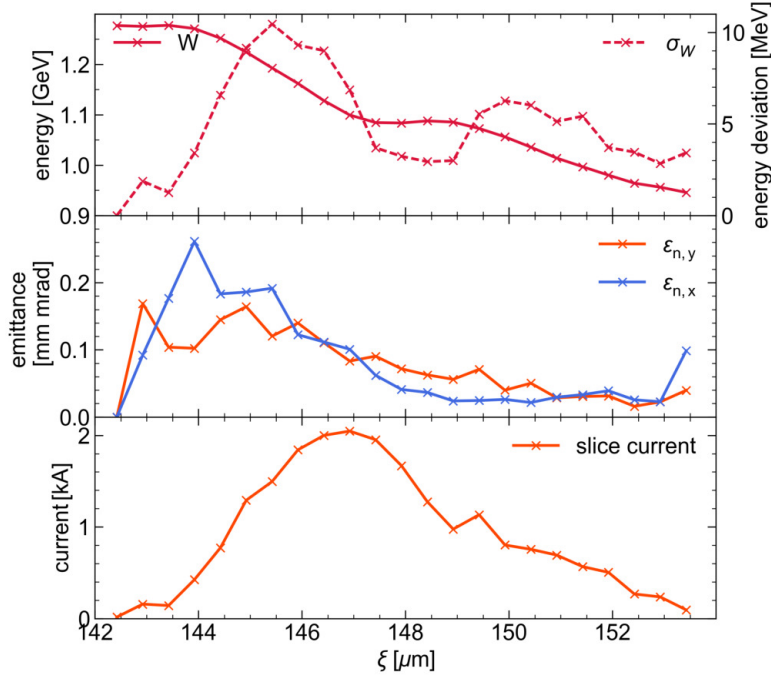

Figure 39: The energy (continuous curve top left axis), standard deviation of the energy (dashed curve top right axis), the emittance in the y (orange curve middle subplot) and the x (blue curve middle subplot) direction, and the slice current of the witness bunch (bottom subplot) are shown along the bunch propagation axis before extraction at 30 mm, using 0.5 μm broad longitudinal slices.

the condition given in equation 177, before the bunch can be utilized in a FEL, e. g. by applying the novel dechirping method introduced by [151]. However, the longitudinal phase space must be approximately linear for this method to be efficient.

In figure 39, the bunch parameters are resolved longitudinally along the bunch axis, by longitudinally dividing the bunch into slices, and evaluating each slice individually. Note, that the values of these parameters depend on the choice of the slices width. Usually, this width is chosen to be about one cooperation length in the context of FELs. However, the cooperation length is dependent on the design of the FEL, which cannot be anticipated at this point. For example, using a slice width of 0.2 μm (instead of 0.5 μm), the mean slice energy spread given in Table 4 reduces from $\approx 0.442\%$ to only $\approx 0.237\%$. Here, the slice width was chosen to result in a continuous curve, with no significant jumps between the slices, while the bunch is reasonably resolved. Bearing this in mind, it can be seen that the slice energy spread shows a pronounced minimum at the position where the energy stays nearly constant, which is also near the peak current of this bunch.

In conclusion, it was found that the inhomogeneous charge and momentum distribution of the LWFA drive beam, in combination with its high divergence, can result in

a significantly changed behavior when driving a wakefield, compared to a Gaussian drive beam. Further, the direction of the polarization of the LWFA laser significantly affects the properties of the following stages in that direction; using a circularly polarized drive laser might solve this issue.

The high divergence of the electron beam could also lead to a severe distortion of the wakefield. Even after the point where the beam has undergone several focuses, it is possible that a large portion of the beam gets lost in the plasma, which itself can be focused to a level where it can drive a separate wakefield. This could be a consequence of the deceleration, which reduces the forward momentum of the beam electrons, while the transverse momentum is not lowered and thereby the divergence, and amplitude of the betatron oscillation is effectively increased. It therefore appears to be very important to enhance the stability and sustainability of the wakefield by matching the transverse size and divergence of the drive beam to the plasma. This requires significantly smaller emittances, which are expected for drive beams with a lower charge. Further, the use of one—or possibly more—plasma lenses in between the LWFA and the PWFA stage might enable the drive beam to be matched.

In general, the electron beam output from a LWFA stage must be expected to show variations of the direction of propagation, in particular when beam instabilities like hosing can occur. This pointing instability also has a crucial influence on the witness bunch in the next plasma accelerator stage, because it leads to an off-axis release of the electrons, or in the worst case, prevents injection. Using a high-current drive beam allows injection to occur within an extended region, first due to a longer nonlinear blowout, and second because the resulting high accelerating fields enable trapping of electrons that are released nearly everywhere in the blowout (see figure 29). Therefore injection and trapping is to a certain extend possible even with misaligned geometry.

However, the off-axis injection increases the emittance and amplifies the transverse oscillation of the witness bunch, leading to intensified betatron radiation, but also increases the pointing instability behind the second plasma stage. Note, that betatron radiation is not included in the PIC simulations because it would require a much smaller resolution, at the level of X-ray wavelengths. The energy loss from betatron radiation can be neglected for on-axis TH injection, and is expected to be on the keV energy level [104].

Last but not least, the separation of witness-bunch, dark-current, and drive-beam electrons needs to be considered. Ideally, the energy of the witness bunch is substantial different from the energy of the other electrons, so a separation with respect to the energy is possible. Another way could be to use a free drift to sort out electrons with higher divergence, e. g. drive-beam electrons, and block electrons that are too far away from the central axis. A third way of separating electrons of different energies is given by the diffraction of the electrons when leaving a plasma with a small angle with respect to its surface [166, 241], similar to the diffraction of a light beam leaving water.

The required plasma profile can be created optically similar to the method introduced in chapter 3. However, all these options might also include either accidentally blocking part of the witness bunch, or at least reducing the quality of the witness bunch.

Similar witness bunches have been produced in further PWFA-TH simulations, all of which show similar quality and the same behavior of the drive beam. Variation of the applied lithium density either results in a smaller plasma cavity, where less driver charge is used to drive the wakefield, or in a larger plasma cavity that cannot compensate the strong divergence of most electrons of the driver. Finally, the bunch that is shown in Table 4 will be used in the third and last step of the simulation setup to produce short-wavelength radiation in an undulator.

GENERATING HIGH-POWER SHORT-WAVELENGTH RADIATION IN AN UNDULATOR

The parameters of the TH-bunch at the plasma exit discussed in the previous chapter are used in the formalism derived by M. Xie [243] to find a combination of undulator period, λ_u, and strength, a_u, for which high-power, short-wavelength radiation can be generated. For this, the conditions 174, 175, 172, and 177 must be fulfilled simultaneously. On the other hand, the undulator period should be $\lambda_u \gtrsim 1\,\mathrm{cm}$ to be manufacturable (an undulator period of $0.5\,\mathrm{cm}$ was produced but required highly advanced methods) and the undulator strength $K = \sqrt{2}a_u$ must be realizable with available techniques and materials. The latter restricts the attainable peak magnetic field, B_0, to a few Teslas [14, 42, 59]. Using the bunch parameters displayed in Table 4 and assuming a compensated energy chirp leads to the possible undulator configuration shown in figure 40, and Table 5. The energy spread of 0.237% is set to the mean slice energy spread for slices with a width of $0.2\,\mu\mathrm{m} \sim L_c$.
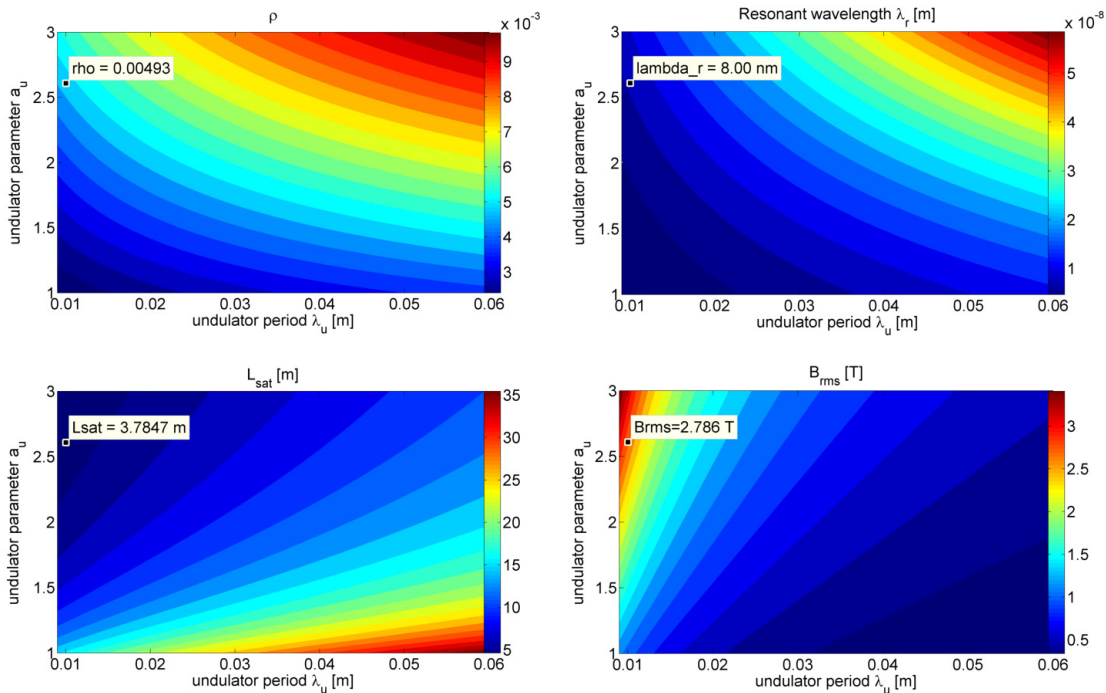

Figure 40: The FEL parameters at $a_u = 2.6$ and $\lambda_u = 1.0\,\mathrm{cm}$ using the undulator design formalism by M. Xie [243] and B. McNeil [158], where the bunch parameters $\gamma = 2211$, $\sigma_\gamma/\gamma = 0.00237$, $I_p = 2203\,\mathrm{A}$, and $\epsilon_{n,x} = 0.137\,\mu\mathrm{m}\,\mathrm{rad}$ are used.

SUMMARIZED FEL DESIGN PARAMETERS

λ_u	1 cm	undulator period	L_g	0.196 m	3D gain length
a_u	2.6	undulator parameter	L_{g0}	0.093 m	1D gain length
K	3.68	undulator parameter	B_{rms}	2.79 T	rms magnetic field
λ_r	8 nm	resonant wavelength	β_{nat}	1.91 m	natural focusing
ρ_{FEL}	0.0049	Pierce parameter	N_u	379	total undulator periods
L_{sat}	3.79 m	saturation length	L_c	0.13 µm	cooperation length
P_{sat}	4.44 GW	saturation power	$L_{s,max}$	3.04 µm	total slippage

Table 5: Possible undulator configuration, displayed in figure 40 based on the formalism by M. Xie [243] and B. McNeil [158].

The restriction $\rho_{FEL} \approx 0.0049 > 2\sigma_\gamma/\gamma \approx 0.0047$ is fulfilled, but for the chosen $\lambda_u = 1\,\text{cm}$, no lower a_u can be used without violating this condition (see figure 40 top left). The number of undulator periods is given by the estimated saturation length $N_u = L_{sat}/\lambda_u \approx 379$; the estimated gain length, including consideration of the energy spread, amounts to $L_g \approx 19.6\,\text{cm}$, whereas the 1D gain length is only $L_{g0} \approx 9.34\,\text{cm}$.

The required magnetic field strength of $B_{rms} \approx 2.79\,\text{T}$ is on the edge of state-of-the-art cryogenic undulators [14, 170] and thus precludes going to higher a_u or lower λ_u (see figure 40 bottom right). To relax the requirement on the high magnetic field strength B_{rms}, a longer undulator period, λ_u, would be required. In this case, however, the slippage would increase to a level that would make the FEL process very ineffective. The maximum slippage of $L_{s,max} \approx 3.0\,\text{µm}$ is slightly larger than the rms length of the bunch $\sigma_z \approx 2.26\,\text{µm}$ (the maximum length of the bunch is 12.0 µm) and the slippage condition, $L_{s,max} = L_{sat}\lambda_r/\lambda_u < \sigma_z$ (174) is therefore not fulfilled. Decreasing the slippage by going to smaller λ_r is prevented because the Pierce parameter then becomes smaller than twice the energy spread of the bunch, violating the important energy-spread condition (172). Going to a shorter undulator period, λ_u, is not possible from the perspective of manufacturability (too high magnetic fields), and increasing λ_u increases $L_{s,max}$, as the resonant wavelength and the saturation length increase simultaneously. The slippage condition could therefore not be fulfilled without violating more stringent restrictions, but it was optimized to result in a small slippage. Also, the condition for transverse overlap of the bunch and the radiation (175), $\epsilon_n \leqslant \lambda_r/4\pi$, cannot be fulfilled with the given bunch, $\epsilon_{n,x} \approx 136 \times 10^{-9} \gg \lambda_r/4\pi \approx 0.64 \times 10^{-9}$.

The gradient of the energy of the witness bunch (energy chirp) is calculated using a linear regression of formula 178, with $\rho_{FEL} = 0.0049$ and $\lambda_r = 8.0\,\text{nm}$, resulting in $\alpha_c \approx 0.15$. Equation (177) then becomes $\frac{\alpha_c}{\sigma_{z,fwhm}}\left(\frac{\lambda_r}{\rho_{FEL}^2}\right) \approx 9.79 > 1$, thus the condition for the maximum allowable energy chirp is violated. Therefore, an un-chirped bunch will be generated in the following for the FEL, assuming that the de-chirping method
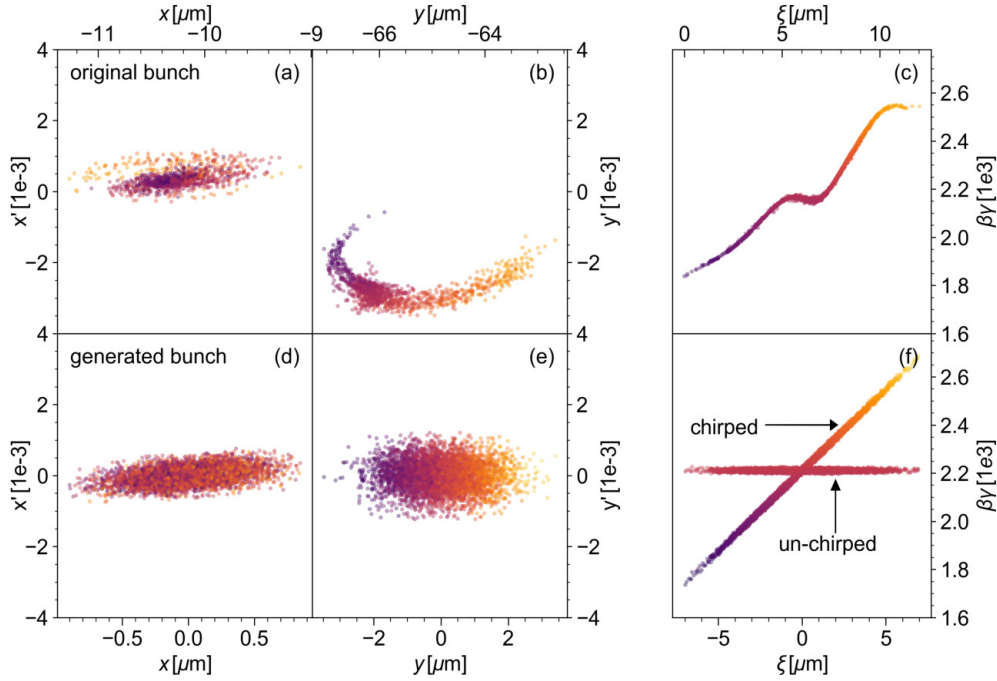
Figure 41: The phase spaces of the simulated PWFA-TH-bunch directly behind the plasma exit (top row), and two generated centered bunches that share the same Twiss parameters and uncorrelated energy spread as the simulated bunch (bottom row). Both generated bunches have the same transverse phase spaces (subplots (d) and (e)). In subplot (f), two generated bunches are shown: one that has an energy chirp that resembles the chirp that was obtained by simulation, and one that has an un-chirped energy distribution. From this subplot, the color coding for every other subplot can be read from the y axis.

from [151] was applied to compensate the energy chirp of the witness bunch. To model the un-chirped bunch that features the same parameters as the obtained PWFA-TH-witness bunch (displayed in Table 6), the tracking code ELEctron Generation ANd Tracking [25] (ELEGANT) was used. The uncorrelated energy spread of this bunch was set to the mean slice energy spread of the original bunch, $\sigma_\gamma/\gamma = 0.0237\%$, using a slice width of $2\,\mu m$, which is slightly larger than the cooperation length, $L_c \approx 0.13\,\mu m$ of the above-discussed undulator configuration. Note, a smaller slice width leads to a smaller slice energy spread.

Besides having virtually the same Twiss parameters as the original bunch, the offsets in the transverse direction and the mean transverse momentum of the original bunch have been subtracted to re-align the generated bunch to the propagation axis. Further, the number of macro-particles was increased in the generated bunch without changing its charge. The phase spaces of the original bunch (top row), and the created bunch (bottom row) are shown in figure 41. In this figure, two bunches are shown that are generated with ELEGANT and have the same transverse phase space. In the longitudinal direction, one bunch has nearly the same energy chirp as the simulated bunch, and the other bunch is assumed to be de-chirped. Therefore, the sole influence of the energy

chirp in a beamline can be seen by comparing both generated bunches, while the effect of the non-Gaussian phase-space distributions and offsets can be seen when the generated, chirped bunch is compared to the original bunch (see figure 44). Because the achieved TH bunch violates the condition for the maximum allowable energy chirp, only the de-chirped bunch will be used as driver in the FEL.

Comparing figure 38 and 41 shows the effect of the applied density downramp at the end of the PWFA stage; the respective parameters before and after the downramp are given in Table 6. From this Table, it can be seen that the normalized emittance grows

TWISS PARAMETERS BEFORE AND AFTER THE PLASMA EXIT

	(α_x, α_y)	(β_x, β_y) [mm]	(ϵ_x, ϵ_y) $[10^{-7}\,\mathrm{m\,rad}]$	(σ_x, σ_y) $[\mu\,\mathrm{m}]$	$(\sigma_{x'}, \sigma_{y'})$ $[10^{-4}]$
before	$(0.028, -0.82)$	$(1.13, 1.90)$	$(1.35, 7.63)$	$(0.26, 0.82)$	$(2.34, 5.56)$
after	$(-0.42, 0.031)$	$(1.34, 2.27)$	$(1.36, 8.43)$	$(0.29, 0.93)$	$(2.33, 4.00)$

Table 6: Twiss parameters of the PWFA-TH bunch before the start of the 1 mm long cosine-square-shaped descending plasma density and after the plasma exit.

slightly and the bunch widths σ_x and σ_y expand, while the transverse momenta $\sigma_{x'}$ and $\sigma_{y'}$ decrease. The Twiss parameters $\alpha_{x,y}$ and $\beta_{x,y}$, as well as the bunch width, $\sigma_{x,y}$, and the emittance, $\epsilon_{x,y}$, are subject to oscillations during the acceleration in the PWFA stage. In addition, these oscillations are superimposed on the transverse drift in the case of the above-discussed PWFA simulation. Therefore, the development of the parameters within the downramp must be seen as a damped continuation of the oscillations within the plasma, featuring a growing bunch width and a decreasing transverse momentum.

8.1   BEAM TRANSPORT AND MATCHING

For the FEL process, it is required that the driving electron bunch is matched to the undulator. Without matching, the vast divergence would result in an extremely short interaction between the bunch and the radiation within the undulator. For a short undulator, natural focusing might suffice to provide the required transverse overlap between the bunch and the radiation, however, it affects only one transverse direction and the beta function still needs to be matched to that of the undulator. External guiding of the bunch within the undulator becomes essential for undulator lengths that are much longer than $\beta^* = \gamma(\sigma_{r,0}^2/\epsilon_n)$ with the beam width at the focus, $\sigma_{r,0}$. The parameters of the bunch at the exit of the plasma (given in Table 6) yield $\beta_x^* \approx 1.37\,\mathrm{mm}$ and $\beta_y^* \approx 2.27\,\mathrm{mm}$, assuming the bunch to be focused at this point. Because the saturation length is at the meter-level and the obtained beta functions are on the millimeter-level,

the beta functions need to be increased by three orders of magnitude and matched to the entrance of the undulator for effective FEL operation.

In the present scenario, external guidance is therefore advisable to achieve the full attainable power output of the bunch. To keep the bunch in a stable and confined trajectory, the undulator is divided into sections of preferably more than a gain length and complemented by a periodic lattice of focusing and defocusing quadrupole magnets in between the sections (see figure 42).
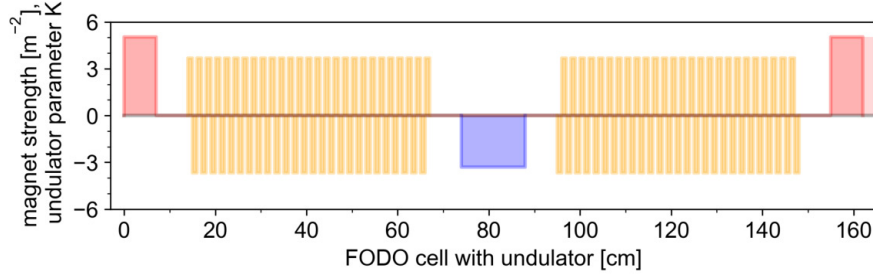

Figure 42: Undulator configuration with external focusing by a FODO structure. The magnetic field strength of the quadrupole magnets and the K parameter of the undulator are proportional to the height of the elements. The corresponding parameters are given in Table 15.

The average beta function, β_{av}, within the FODO cell is connected with the length of one section L_{fodo}, and the ideally small phase advance, μ, via

$$L_{fodo} = \beta_{av} \sin \mu. \tag{181}$$

Obviously, the longer the undulator compared to the total length of the focusing components and drift gaps in between, the more efficient it can amplify the radiation output. Therefore, a large average beta function is favorable to increase the length of one section and therefore the length of the undulators within one section. To achieve a stable, periodic trajectory, the bunch must have precisely defined Twiss parameters at the entrance of the FODO lattice, namely $\alpha_x \approx 0$ and $\alpha_y \approx 0$ and the beta functions must be matched to

$$\beta_x = \beta_{av}(1 - \sin(\mu/2)) \quad \text{and} \quad \beta_y = \beta_{av}(1 + \sin(\mu/2)) \tag{182}$$

when the first quadrupole magnet focuses in the x direction. The bunch must be matched at the center of the first quadrupole, which is ensured by dividing the focusing quads into two equally long parts and starting the section with one half and ending it with the other half (see figure 42). The lengths in the FODO-cell are expressed in units of the undulator period, $\lambda_u = 1.0\,\text{cm}$, to ensure the section is an integer multiple of it.

The millimeter-level beta functions of the bunch behind the plasma must be matched to the values that are given in equation (182), and therefore increased by three orders of

magnitude to allow for a meter-level section length defined by equation (181). Further, the transverse size of the bunch should ideally be small within the undulator while the emittance should not increase significantly in the beamline, to ensure a high amplification ($\rho_{FEL} \propto \sigma_r^{-2/3}$). However, because these parameters are connected via $\beta = \sigma_r^2 / \epsilon_n$, and the emittance cannot decrease within the beamline, the beta function can only be increased along with the size of the beam. Bunch-steering elements are therefore necessary to transport the bunch to, and provide the required parameters at the center of the first quadrupole of the FODO cell. Such a beamline typically consists of a permanent magnet quadrupole (PMQ) triplet to capture and collimate the electron bunch ($\alpha \to 0$) directly behind the plasma, followed by an electromagnet quadrupole (EMQ) triplet to match the Twiss parameters to the required values at the end of the beamline [205].

The large divergence of the witness bunch behind the plasma requires the bunch to be captured as soon as possible, but realistically it is not possible to place strong magnets directly behind a plasma. Also, it is important to leave a sufficiently long gap between the undulator and the quadrupoles in order for their fields not to interfere with each other [251]. These restrictions of the minimum distances, combined with the large divergence, result in an unavoidably wide beam right at the start of the beamline (see figure 43). The bunch can therefore only be collimated with a large transverse size. Then, at least two more triplets would be required to shrink and collimate the bunch [205]. So, instead of using the above-described multi-triplet structure, the bunch size is directly decreased by the first triplet ($\alpha_x > 0$). While optimizing the quad strengths of the second triplet to result in the desired matched bunch behind the beamline. Further, it was found that the first magnet of the second triplet can be omitted and effectively had no influence on the result using ELEGANT.

MATCHING OF THE TWISS PARAMETERS

	$\alpha_{x,y}$	$\beta_{x,y}$ [m]	$\epsilon_{x,y}$ [mrad]	$\sigma_{x,y}$ [μm]
before	$(-0.42, 0.031)$	$(0.0013, 0.0023)$	$(1.36, 8.43) \times 10^{-7}$	$(0.29, 0.93)$
after	$(-0.033, 0.022)$	$(3.14, 1.38)$	$(1.48, 23.9) \times 10^{-7}$	$(14.5, 38.7)$

Table 7: Matching of the Twiss parameters and focusing of the un-chirped bunch, before and after the beam transport line.

The resulting evolution of the bunch parameters is depicted in figure 43, the parameters of the bunch before and after the matching beamline are displayed in Table 7. As can be inferred from β_x and β_y in this Table, the average beta function is $\beta_{av} \approx 2.26\,\mathrm{m}$, resulting in a phase advance of $\mu \approx 0.80\,\mathrm{rad} \approx 45.8°$ and the length of the section is $L_{fodo} \approx 162.11\,\mathrm{cm}$.

The gap between the undulator and the quadrupole magnets is set to $7\,\mathrm{cm}$ to avoid that the magnetic fields interfere while keeping the distance as short as possible to not
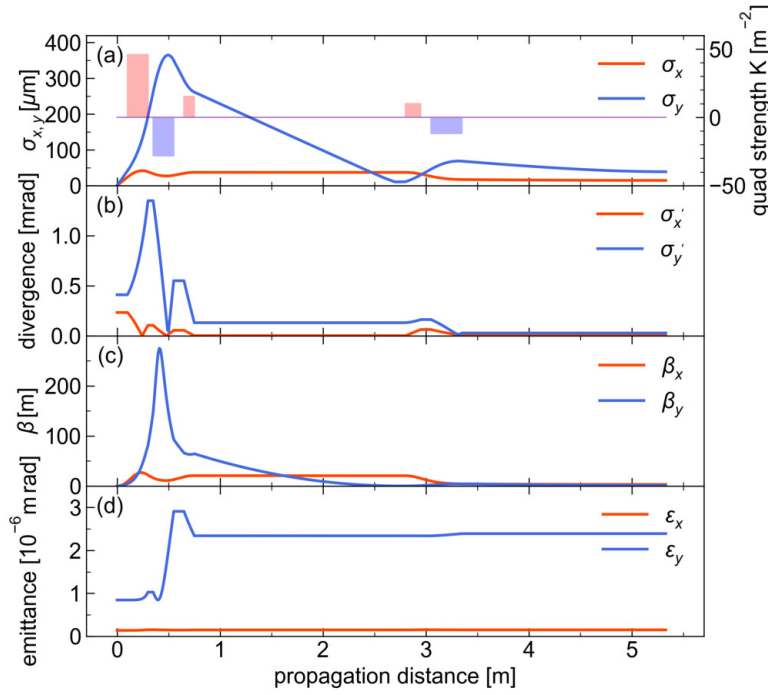
Figure 43: Matching and focusing of the de-chirped bunch in ELEGANT; the initial and final bunch parameters are displayed in Table 7. In the subplot (a), the applied beamline is displayed on the right y axis, where a positive quad strength focuses the bunch in the x direction (red), while a negative quad strength focuses the bunch in the y direction (blue). The bunch width (a), its divergence (b), beta function (c), and the emittance (e) are shown in the direction perpendicular to the polarization of the LWFA and the TH laser (orange) and parallel (blue). The parameters of the beamline are given in Table 14.

disturb the FEL process. The length of the quadrupole magnets of the FODO lattice is set to 14 cm (except for the first and the last quadrupole magnet) for similar reasons (see figure 42). The strengths of the quadrupole magnets, combined with the undulators have been again optimized in ELEGANT to result in a stably periodically focused bunch; the resulting values are displayed in Table 15. When subtracting the drifts ($4 \times 7\,\text{cm}$) and the lengths of the quadrupoles ($2 \times 14\,\text{cm}$) from the given length of the section, $L_{fodo} = 162\,\text{cm}$, the remaining space for one undulator amounts to 53 cm—sufficiently longer than the gain length.

Note, the beamline was adjusted specifically for the un-chirped bunch. As a demonstration of the influence of deviations from the bunch to which the beamline was optimized, the propagation of the original bunch with the high-energy chirp and asymmetric phase space, and the generated bunch with the energy chirp and the centered, Gaussian phase space (see figure 41) are shown in figure 44. Here the emittance grows not merely by a factor of about two, as was the case for the un-chirped bunch, but by two orders of magnitude, as a result of the energy chirp (compare the dashed lines in figure 44 and the continuous lines in figure 43). Further, the beam waist at the focus
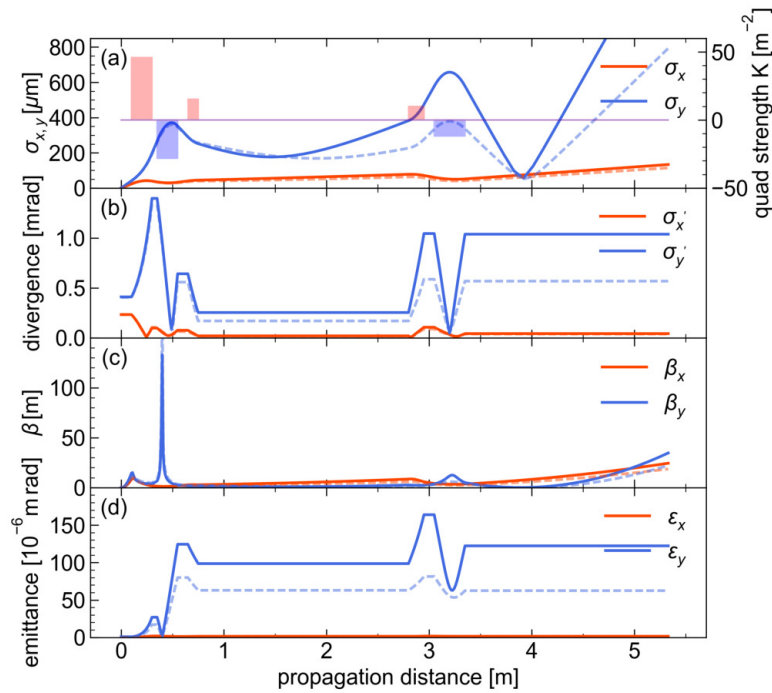
Figure 44: The propagation of the original PWFA-TH bunch (continuous curves) and the generated chirped bunch (dashed curves) in ELEGANT using the focusing and matching beamline of the un-chirped bunch shown in figure 43. In the subplot (a), the applied beamline is displayed on the right y axis, where a positive quad strength focuses the bunch in the x direction (red), while a negative quad strength focuses the bunch in the y direction (blue). The bunch width (a), its divergence (b), beta function (c), and the emittance (e) are shown in the direction perpendicular to the polarization of the LWFA and the TH laser (orange) and parallel (blue). The parameters of the beamline are given in Table 14.

is much broader, resulting from the chromatic aberration induced by the considerably larger energy spread. The original bunch (continuous curve in figure 44) shows a yet more pronounced deviation, worse focusing, and larger emittances. The difference between the continuous line and the dashed line in figure 44 illustrates the difference of the propagation of a Gaussian-shaped, centered bunch to the original asymmetric bunch with large offsets.

Because both conditions that would ensure the transverse (175) and longitudinal overlap (174) of the electron bunch and the radiation pulse could not be fulfilled, the actual gain length is expected to be substantially larger than predicted (see Table 5). Overlap in the transverse direction can be provided by external focusing in the undulator. Consequently, the saturation length and the length of the undulator will be considerably larger than predicted ($L_{sat} \approx 3.8$ m), also increasing the slippage.

8.2 SIMULATION OUTCOME AND DISCUSSION

Combining the results, the full phase space distribution of the matched, un-chirped bunch (see bottom row in Table 7) and the optimized FODO-lattice (see Table 15 and figure 42) was loaded into the FEL-code GENESIS. The resulting parameters along 27
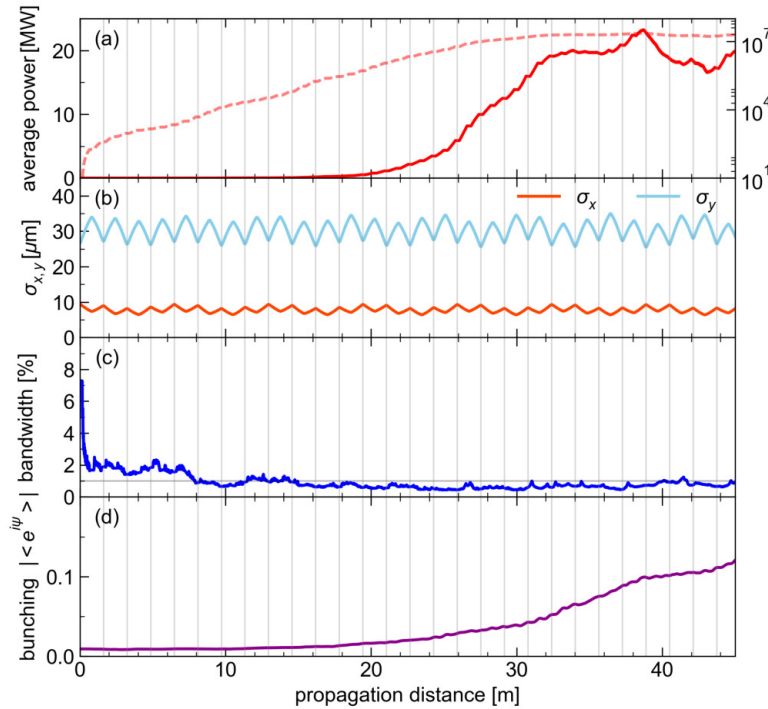

Figure 45: GENESIS simulation of the matched, un-chirped bunch, using the parameters given in Table 16 and using the undulator and FODO-lattice given in 15. In (a), the average power is given on a linear scale (continuous curve) on the left, and on a logarithmic scale (dashed curve) on the right. The bunch is periodically focused (b) and slowly develops micro bunching (c); the bandwidth of the generated radiation decreases under 1% (gray horizontal line) and stays approximately constant (c).

sections are shown in figure 45, where the ends of the sections are depicted by light gray vertical lines.

First, it can be seen that the electron bunch is nicely guided along the undulator by the external focusing, shown in subplot (b). With $\sigma_y \sim 30\,\mu m$, the bunch shows a substantially larger width in the y direction than in the x direction, where $\sigma_x \lesssim 10\,\mu m$. This again is a result of the asymmetry that was induced by the off-axis drift in the PWFA stage and initiated by the stronger momenta in the plane of polarization of the LWFA laser (see figure 25). The substantial increase of the width of the bunch before, and after the beam transport line (see Table 7) compromises the FEL performance by lowering the gain parameter $\rho_{FEL} \propto \sigma_r^{-2/3}$. Therefore, a smaller bunch width would be an important point to address for a better FEL performance. However, as noted before, the bunch width cannot be made much smaller because of the requirement

to simultaneously increase the beta function. Also, focusing the bunch too much will lead to strong diffraction and increase the gain length and therefore reduce the FEL performance again. However, a better aligned, more stable acceleration within the PWFA stage would relax this situation.

In subplot (a) of figure 45, the average power first saturates after about 20 sections, at $z = 32.4\,\mathrm{m}$, with $P_{sat} \approx 19.13\,\mathrm{MW}$ which is dramatically overestimated by the formalism of [243] which gives $P_{sat} \approx 4.44\,\mathrm{GW}$ (see Table 5). The growth of the power is shown on a linear scale (left axis, continuous curve) and on a logarithmic scale (right axis, dashed curve). The peak value of $P_{max} \approx 23.24\,\mathrm{MW}$ is reached after 24 sections at $z = 38.72\,\mathrm{m}$. Thereafter a significant amount of radiation starts to leave the front of the simulation window (see figure 45 (b)) and therefore lowers the average power.

The gain length was estimated as $L_g \approx 0.2\,\mathrm{m}$, while the actually obtained gain length of $L_g \approx 2.8\,\mathrm{m}$ can be deduced from the slope of the approximately linear increase of the power on the logarithmic scale. Accordingly, the estimated saturation length was greatly underestimated, with only $L_{sat} \approx 3.78\,\mathrm{m}$, and became as long as $\approx 38\,\mathrm{m}$ in the simulation. The much longer undulator also significantly advances the slippage, which, for instance can be seen from the moving peak of the power for $z = 32.4\,\mathrm{m}$, $35.64\,\mathrm{m}$, and $39.88\,\mathrm{m}$ (20, 22, and 24 sections) in figure 46 (b). To visualize that the temporal overlap with the generated radiation is therefore very short, also the current distribution of the bunch is shown in this subplot on the right axis. The total slippage at the peak power at $z = 38.88\,\mathrm{m}$ amounts to $31.1\,\mathrm{\mu m}$, which is far beyond the rms-length of the bunch of $\sigma_z \approx 2.26\,\mathrm{\mu m}$. The bandwidth in subplot (c) shows a minimum of $\delta\omega/\omega \approx 0.44\%$ and stays on a constant level under the 1%-mark from about $z = 15\,\mathrm{m}$ onwards. The bunching factor, displayed in subplot (d), is on a low level and increases to slightly over 0.1 as the power increases.

Figure 46 shows the situation along the bunch in subplot (b), and (c), and the spectrum in subplot (a), for different positions within the undulator (after 5, 10, 15, 20, 22, and 24 sections). In the SASE mode, it can be expected that the spectrum counts about as many spikes, as there are cooperation lengths within the bunch length $\sigma_r/L_c \approx 17$ (with $\sigma_z \approx 2.26\,\mathrm{\mu m}$ and $L_c \approx 0.13\,\mathrm{\mu m}$). In subplot (b), the longitudinal profile of the emitted radiation is shown for different times. The profile of the radiated power continuously moves forward and would reach a length of $31.1\,\mathrm{\mu m}$ (or $103.7\,\mathrm{fs}$) at $z = 38.88\,\mathrm{m}$, equal to the accumulated slippage if the simulated window would be large enough. Also, as a result of the slippage, the bunching within the main part of the bunch is low, and only increases at later positions where the emitted radiation is most intense and interacts as it moves outside the bunch in the forward direction.

The overall efficiency achieved within this stage is expected to be on the order of the Pierce parameter $\rho_{FEL} \approx P_{sat}/P_b \approx 0.0049$, whereas the actually achieved efficiency is only $P_{sat}/P_b \approx 7.69 \times 10^{-6}$ (with the power of the electron bunch, $P_b \approx 2.49\,\mathrm{TW}$, and $P_{sat} \approx 19.13\,\mathrm{MW}$). This is owing to the fact that the expected saturation power of
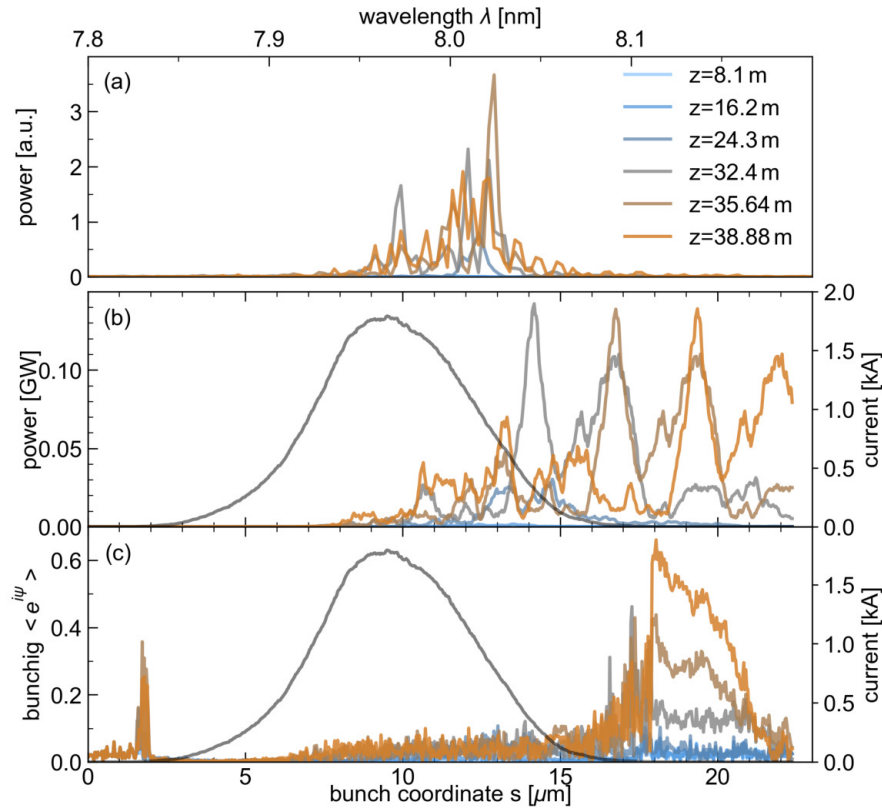
Figure 46: The temporal development (color coding) of the spectrum of the radiation shows a peak at the resonant wavelength $\lambda_r = 8\,\mathrm{nm}$, (a). The power of the emitted radiation shows a poor longitudinal overlap with the current of the bunch (black curve, right y axis), (b). The bunching factor significantly increases only at the very front of the bunch with negligible current, but high radiation power (c)

$P_{sat} \approx 4.44\,\mathrm{GW}$ was not reached. Note that the foremost part of the radiated power leaves the simulation box and reduces the average power from $z \sim 16\,\mathrm{m}$ onwards, due to the slippage. The observed saturation can therefore also be ascribed to the fact that from $z \sim 32\,\mathrm{m}$ onwards, an approximately equal amount of power is generated by the bunch and simultaneously leaves the simulation box in the front. Also the bunching factor, shown in figure 45 (d), indicates that the FEL was not driven to saturation, otherwise the bunching factor would be saturated and decrease slightly delayed to the power. Based on the gain length that was extracted from the simulation $L_g \approx 2.8\,\mathrm{m}$, saturation of the power would not be expected before $20 L_g \approx 56\,\mathrm{m}$.

Despite all these disadvantages, the achievement of mega watts of power at $8\,\mathrm{nm}$ wavelength is a good result that is to a large extent owed to the external focusing, without which the average power was more than three orders of magnitude lower. Saturation within a much shorter distance could be achieved using an external $8\,\mathrm{nm}$ radiation source to seed the FEL process. Such a source could be given by higher harmonic generation, or by the emitted FEL-radiation itself (self-seeding) [45].

In the last chapter of this work, the results will be summarized, the key findings will be emphasized and an outlook of the most promising ways to proceed with this scheme will be given.

CONCLUSION AND OUTLOOK

Hybrid LWFA-PWFA has been investigated and modeled, using fully three-dimensional PIC simulations. Because LWFA simulations are very resource-intensive and time-consuming, only one sufficiently long LWFA simulation that provided the high-current and high-energy electron beam, required to drive a PWFA could be conducted. This electron beam has an extremely high charge and an asymmetric particle and momentum distribution, but in order to produce a realistic scenario it was not replaced by an idealized beam with similar properties. Despite these characteristics of the obtained electron beam, it was possible to drive a PWFA in the blowout regime without ionizing the applied HIT species or injecting dark current. Trojan Horse injection could therefore be successfully applied to inject a high-quality electron bunch.

Although this TH bunch had a low emittance and slice energy spread, and a high peak current, it performed poorly in the FEL due to its high energy chirp. It was therefore assumed that the energy chirp could be removed from the bunch without changing other parameters using the recently introduced plasma-based energy-spread compensation technique [151]. With this, it was possible to achieve satisfactory FEL amplification and a significant amount of power at a wavelength of only $\lambda \approx 8\,\text{nm}$. The feasibility of building an all-optical FEL using the hybrid LWFA-PWFA scheme was therefore successfully demonstrated. However, because this scheme has hitherto not been thoroughly investigated and the number of parameters that must be considered is large, the results obtained can only demonstrate proof-of-principle and leave room for improvement. In the following, some other important points and findings of this thesis will be emphasized and possibilities to enhance the results will be discussed.

Compared to conventional applications, the hybrid scheme requires fundamentally different properties from a LWFA, and experimental campaigns hitherto did not aim at accelerating more charge at the cost of a higher energy spread. However, a high charge and energy is not an issue from the theoretical point of view, as has been shown in this work and other publications [83, 105, 146, 156, 230]

In LWFA, the energy of the electron beam can be increased most efficiently by lowering the plasma density, followed by increasing the laser power (see equation (85)). However, a lower plasma density could not be simulated in this thesis, as the demand for computational resources increases dramatically with lower densities, and the applied density of $n_p = 5 \times 10^{17}\,\text{cm}^{-3}$ was chosen as the lowest practicable. For example, for a peak power of $P \approx 1.2\,\text{PW}$, which was used in the LWFA simulation, the laser would no

longer be self guided ($P_c > P = 1.2\,PW$) for densities below $n_p \approx 2.47 \times 10^{16}\,cm^{-3}$. A lower plasma density would therefore require external guiding of the laser, or a higher laser power to provide for self-focusing. To simulate these low densities, an advanced algorithm was developed [229] and demonstrated [156, 230], where the simulation was conducted in a relativistic frame of reference (a Lorentz-boosted frame) and the wavelength of the laser was increased to lower the required resolution.

For the LWFA simulation in this thesis, a very high laser energy of $W \approx 100\,J$ was therefore used to accelerate a substantial amount of charge to high energies quickly, to allow the high-resolution three-dimensional scenario to be simulated with the available computational resources and methods. The outcome of this simulation of $24.5\,nC$ and $3.81\,GeV$ substantially differed from the expected $1.4\,nC$ of charge and $6.1\,GeV$ of energy, predicted by the scaling laws of Lu et. *al.* [146]. These large deviations are likely to result from a mismatching of the driving laser and from the unavoidable assumption of the theoretical model that the temporal development of the driving laser can be neglected, which was clearly not the case in the simulation. McGuffey et. *al.* [157] also reported deviations from the scaling laws of Lu et. *al.* [146] in their experiments, but found the order of magnitude and trend to be predicted correctly. This illustrates the fundamental need to actually simulate plasma wakefield acceleration to obtain accurate predictions of realistic scenarios. Similar LWFA simulations were reported by Martins et. *al.* [156] and Kalmykov et. *al.* [105], which included oscillations of the spot size of the laser and periodic self-injection, filamentation of the laser pulse, elongation of the bubble and a similar phase space of the self-injected charge.

In the LWFA simulation shown in this thesis, the periodic self-focusing of the driving laser injects large amounts of charge at the focal points. Mitigating the oscillations of the laser by matching its power to the critical power for self focusing, $P_l = P_c$ (see equation (79)), would therefore reduce the amount of self-injected charge. In fact, this would even prohibit self injection, e. g. Froula et. *al.* [69] experimentally determined $P_l \gtrsim 3P_c$ to be the limit for self injection. The condition to match the spot size of the laser and its intensity, $2\sqrt{a_0} \simeq k_p w_0$ [146] was not fulfilled exactly in the LWFA simulation ($2\sqrt{a_0} \approx 5.66$ and $k_p w_0 \approx 3.14$) in order to save laser energy, $W_l \propto w_0^2$. The observed asymmetry between both transverse directions of the electron beam can simply be avoided by using a circularly polarized drive laser in the LWFA stage. Note that the LWFA simulation shown in this work violates the conservation of energy for no obvious reason since the energy of the obtained electron beam of $W \approx 93\,J$ is about the same energy as the driving laser of $\approx 100\,J$. However, besides its enormous charge, this electron beam represents a realistic LWFA beam and can therefore be used to show a realistic hybrid LWFA-PWFA scenario after reducing the charge by the free drift.

For long beams with high charge, as needed for PWFA, the hosing instability is a big challenge and occurs as soon as a small asymmetry induces a variation of the wakefield, which in turn reacts on the beam and the process feeds back on itself. Asymmetry in

the distribution of the charge and momentum of the electron beam must be avoided in the LWFA stage, as otherwise alignment and pointing will become even worse along the subsequent stages. To mitigate hosing, short beams with moderate charge are favored.

For the chosen self-injection mechanism, the resulting energy chirp is positive—the electrons with the lowest energy are situated at the back of the beam—as the electrons in the front are injected first and are accelerated for the longest time. In PWFA, the back of a matched driver experiences the highest decelerating fields (see figure 34) and it would therefore be advantageous if this part also has the highest energy, i. e. a negative energy chirp. Optimal efficiency in the PWFA stage would be achieved when the trend of the decelerating field is matched to the energy-profile of the driving electron beam, such that the driver can deploy as much energy as possible in the plasma wakefield. Such an energy chirp might occur using other injection methods where the beam is injected at once, such as injection by density perturbations as in [65], or ionization injection as in [248], provided self-injection is suppressed, i. e. $P_l \lesssim 3P_c$ [69]. Recently, an innovative new injection method in LWFA, the Self-Truncated-Ionization-Injection (STII), showed very promising results with a negative energy chirp, high charge and optimized beam-loading [44].

To inject a high-quality bunch with the TH method in the PWFA stage, some space is needed for the injection laser to be introduced onto the propagation axis. Injecting the electron bunch at an angle, or with the optical Plasma Torch technique, would allow the LWFA and PWFA stages to be placed immediately next to each other. The scenario that was simulated in this thesis used a long section of free propagation to reduce the charge of the electron beam. After entering the PWFA stage, only the part of the diverging electron beam that is inside the blowout is focused and contributes to driving the wakefield. This has the advantage of simultaneously reducing the mean divergence of the remaining electrons. The optimal amount of drive-beam charge, e. g. for self-ionized PWFA without ionization of a HIT species, can be obtained by simply varying the distances between the plasma accelerator stages. In addition, a plasma lens can be used to enhance this effect and to focus part of the beam.

One further advantage of the hybrid LWFA-PWFA method is the possibility to, at least pre-ionize the beginning of the PWFA stage with the remaining energy of the LWFA laser. This could help to focus the electron driver in the PWFA until its own field strength can provide the pre-ionization of the LIT gas if required. In the PWFA simulations shown in this thesis, only the combination of Li and Li$^+$ could be used due to the high charge of the obtained drive beam, which, without the free drift, would ionize even Li$^+$ (the highest second ionization threshold available). On the other hand, this ensured that the LIT medium, lithium, can easily be self-ionized by the drive beam. If the peak field of the drive beam ionizes the HIT component, a column is left unionized along the axis due to the bipolar electric field that vanishes at the center (see figure 3). In a

more advanced scheme, this spatial restriction of the HIT medium that is available for the generation of the witness bunch could be used to decouple the emittance of the witness bunch from the laser spot size, w_0, in the TH-scheme, and therefore help to decrease the attainable emittance of the witness bunch.

To avoid dark current in the PWFA-TH setup [150], it is important to ensure that the peak field strength of the drive beam stays in between the critical values for the ionization of the LIT and HIT component. The back of the drive beam is decelerated by the wakefield and will move back in the blowout and get trapped at a point, which is determined by the decelerating field and the energy of this part of the driver. Because this form of dark current only occurs shortly before the end of the acceleration, its energy is well below the energy of the witness bunch and therefore well separable. However, it is interesting to consider the potential of this process to even enhance the quality of the witness bunch: when a significant number of drive-beam electrons is trapped right behind the witness bunch, it can invert the gradient of the accelerating field, such that the energy chirp of the witness bunch is compensated, similar to the de-chirping mechanism described in [151]. This mechanism is appealing, as it does not need anything in addition, but is inherently included in the physical process of the plasma wakefield accelerator. The divergence of the drive beam in PWFA effectively increases as a result of the deceleration, which increases the probability for electrons to escape from the blowout transversely (as observed in this thesis). A small initial divergence (and emittance) of the drive beam is therefore also crucial for a long and stable acceleration.

It is typical for electron bunches that are accelerated in a plasma wakefield to have a high divergence as a result of the strong focusing fields and a considerable energy chirp. To effectively apply these bunches in a FEL, the high divergence, and ideally the energy chirp must be reduced. In FELs, the energy of the drive bunch, $W = m_e c (\gamma - 1)$, defines possible resonant wavelengths $\lambda_r \propto \lambda_u / \gamma^2$ ($\lambda_u \gtrsim 1\,cm$ being the undulator period, see equation (153)). To fulfill the resonance condition, $\sigma_\gamma / \gamma < \rho_{FEL}/2$, bunches with a high energy, and hence a small $\rho_{FEL} \propto 1/\gamma$, simultaneously require a low relative energy spread, σ_γ / γ. The energy spread is therefore one of the key parameters, which needs to be as small as possible for a good FEL performance.

To deal with the challenges that electron bunches from plasma wakefield accelerators bring when used in FELs, two approaches are under investigation. One arises from the perspective of FELs, aimed at allowing larger energy spreads in the undulator [147]; the other comes from the perspective of plasma wakefield acceleration, aimed at lowering energy spread of the generated witness bunch [151]. Directly applying electron beams from LWFA in an undulator was experimentally demonstrated in the visible [198] and soft x-ray regime [72] and is under further investigation [232]. However, conventional FELs, which are currently in operation, achieve orders of magnitude higher powers and

shorter wavelengths.

Overall, the simulations conducted here applied a ≈ 1.2 PW laser at a wavelength of 800 nm, to produce x-rays with ≈ 20 MW of power at a wavelength of ≈ 8 nm. Therefore, the feasibility of the hybrid LWFA-PWFA concept was successfully demonstrated and its application in a free-electron laser was shown. The hybrid plasma-wakefield acceleration concept is quickly attracting attention and its experimental realization is currently under investigation. First steps, such as the focusing of an electron-beam from LWFA by a second plasma stage, have been realized [125, 213].

However, plasma wakefield accelerators cannot compete with conventional accelerators to date, and one major reason for this is the large shot-to-shot fluctuations that are typical for plasma-based accelerators. These fluctuations are based on the chaotic behavior of plasmas, i.e. small changes in the initial conditions, such as variations of the laser pulse or fluctuations of the plasma density, might lead to a large change of the result. The stabilization of plasma-based accelerators is therefore a major task that needs to be addressed in the future. For this, extensive, realistic simulations are very important to perform misalignment and perturbation analysis of plasma wakefield accelerators. Apart from the investigation of the stabilization of plasma wakefield accelerators, it is advisable to also search for methods to better deal with these fluctuations in the potential applications.

Part III

APPENDIX

FACILITIES SUITABLE FOR PLASMA WAKEFIELD ACCELERATION

In figure 47, a world map of ultra-high intensity lasers is given, which was shown at the International Committee on Ultra-High Intensity Lasers (ICUIL) in 2010 by C. P. J. Barty (Lawrence Livermore National Laboratory)
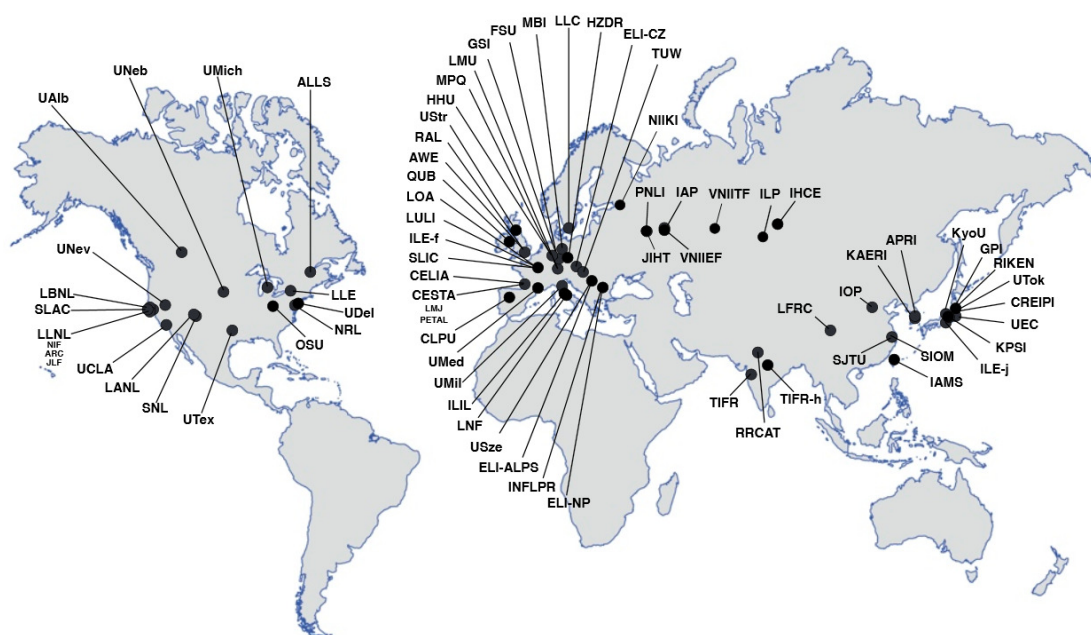
Figure 47: World map of ultra-high intensity lasers. Graphic by C. P. J. Barty, LLNL.

FACILITY	CHARACTERISTICS		
	energy [GeV]	charge [nC]	peak current [kA]
FACET II [246]	10	5	50
CLARA [41]	0.25	0.1	1
ATF II [127]	0.5	0.3	> 1.5
FLASHForward [12]	1.25	0.5	42.5

Table 8: Current specifications of facilities that are used for PWFA, or will be in the near future (non-exhaustive).

LASER, FACILITY, COUNTRY	CHARACTERISTICS			
	$\lambda[\mu m]$	P[TW]	E[J]	$\tau[fs]$
BELLA, LBNL, USA [133][1]	0.8	300	16	40
LOA, FR [149][2]	0.8		6 J	30
JUPITER, LLNL, USA [43][3]	0.8	250		60
JETI40, IOQ, GER[89][4]	0.8		2.5	25
POLARIS, IOQ, GER[5]	1.03	~ 200	17	<100
Texas PW Laser, USA [233][6]	1.05	>1000	190	170
Gemini, RAL, UK [118][7]	0.8	>200	15	30
Vulcan, CLF, UK[8]	1.05	1000	2600	500
CO2 laser, BNL, US [181][9]	~ 10	1000	5	3500
HERCULES, CUOS, USA [157][10]	0.81	300	9	30
PULSER, GIST, Korea [115, 217]	0.8	1100	34	30
ATLAS, LMU, GER [172]	0.8	25	1	40
DRACO, HZDR, GER [50][11]	0.8	150	45	30
ALPHA-X, SCAPA, UK [152][12]	0.8	40 (350)	1.4 (8.7)	35 (25)
FLAME, LNF, IT [136]	0.8	220	7	30

Table 9: Current specifications of laser systems that are used for LWFA experiments (non-exhaustive), potentially many more ultra-high laser systems are available (see figure 47).

1 https://www.lbl.gov/community/bella/
2 http://loa.ensta-paristech.fr/installations_lang_EN_menu_2
3 https://jlf.llnl.gov/
4 http://www.ioq.uni-jena.de/Lasersysteme/JETI.html
5 http://www.ioq.uni-jena.de/Lasersysteme/POLARIS.html
6 http://texaspetawatt.ph.utexas.edu/laser-capabilities.php
7 https://www.clf.stfc.ac.uk/Pages/The-Astra-Gemini-Facility.aspx
8 https://www.clf.stfc.ac.uk/Pages/Vulcan-laser.aspx
9 https://www.bnl.gov/atf/capabilities/CO2laser.php
10 https://cuos.engin.umich.edu/researchgroups/hfs/facilities/hercules-petawatt-laser/
11 https://www.hzdr.de/db/Cms?pNid=2096
12 http://alpha-x.phys.strath.ac.uk/

B

SIMULATION PARAMETERS

SETTINGS OF THE FIRST LASER-DRIVEN PLASMA WAKEFIELD ACCELERATOR		
DRIVING LASER PULSE		
λ_l	0.8 μm	wavelength
τ	78.8 fs	duration
w_0	23.6 μm	focal spot radius
a_0	8.0	normalized amplitude
	y	direction of linear polarization
	100 μm	focal position w.r.t. the start of the plasma
$\mathcal{P}_0$	1.2 PW	peak power
$\mathcal{I}_0$	1.37×10^{20} W/cm²	peak intensity
$\mathcal{E}_0$	32.1 TV/m	peak electric field strength
W_l	100 J	total energy
DERIVED CHARACTERISTIC LWFA PARAMETERS		
Z_R	2.2 mm	Rayleigh length (15)
L_{diff}	6.9 mm	diffraction length (82)
L_{deph}	296.2 mm	dephasing length (83)
L_{depl}	592.4 mm	pump depletion length (84)
$\mathcal{P}_0/P_c$	20 206	critical value for self focusing (79)
n/n_c	18.8	critical density for an underdense plasma (46)
E_0	68.0 GV/m	wave-breaking field strength (56)
$k_p\sigma_z$	1.33	laser duration relative to the plasma cavity dimension

Table 10: Characteristic parameters of the LWFA stage.

SETTINGS OF THE FIRST LASER-DRIVEN PLASMA WAKEFIELD ACCELERATOR

PLASMA SOURCE: NEUTRAL HYDROGEN GAS

n_p	$5 \times 10^{17}\,\mathrm{cm}^{-3}$	hydrogen density
λ_p	$47.2\,\mu\mathrm{m}$	plasma wavelength
ω_p	$40.0\,\mathrm{THz}$	plasma frequency
k_p^{-1}	$7.5\,\mu\mathrm{m}$	plasma skin depth

SIMULATION WINDOW

$\Delta x, \Delta y$	$1.6\,\mu\mathrm{m}$	transverse cell size
Δz	$0.05\,\mu\mathrm{m}$	longitudinal cell size
Δt	$0.167\,\mathrm{fs}$	time step
N_x, N_y	144	transverse number of cells
N_z	4608	longitudinal number of cells
L_x, L_y	$230\,\mu\mathrm{m}$	transverse size of the simulation box
L_z	$230\,\mu\mathrm{m}$	longitudinal size of the simulation box

Table 11: Characteristic parameters of the LWFA stage.

SETTINGS OF THE SECOND PLASMA WAKEFIELD ACCELERATOR

PLASMA SOURCE: NEUTRAL LITHIUM GAS

n_p	$1 \times 10^{23}\,\mathrm{m}^{-3}$	density
λ_p	$105.6\,\mu\mathrm{m}$	plasma wavelength
ω_p	$17.84\,\mathrm{THz}$	plasma frequency
k_p^{-1}	$16.80\,\mu\mathrm{m}$	plasma skin depth

SIMULATION WINDOW

$\Delta x, \Delta y$	$1.6\,\mu\mathrm{m}$	transverse cell size
Δz	$0.64\,\mu\mathrm{m}$	longitudinal cell size
Δt	$1.07\,\mathrm{fs}$	time step
N_x, N_y	384	transverse number of cells
N_z	528	longitudinal number of cells
L_x, L_y	$614.4\,\mu\mathrm{m}$	transverse simulation box size
L_z	$337.9\,\mu\mathrm{m}$	longitudinal simulation box size

Table 12: Simulation parameters of the PWFA stage.

SETTINGS OF THE SECOND PLASMA WAKEFIELD ACCELERATOR

IONIZATION LASER

λ	$0.8\,\mu m$	wavelength
τ	$50.0\,fs$	FWHM duration
w_0	$6.0\,\mu m$	focal spot radius
a_0	0.12	normalized intensity
y		direction of linear polarization
$\mathcal{P}_0$	$1.74 \times 10^{10}\,W$	peak power
$\mathcal{I}_0$	$2.14 \times 10^{20}\,W/m^2$	peak intensity
$\mathcal{E}_0$	$4.82 \times 10^{11}\,V/m$	peak electric field strength
W_l	$0.93\,mJ$	total energy in one pulse

Table 13: Simulation parameters of the PWFA stage.

SETTINGS OF THE ELECTRON-BUNCH TRANSPORT LINE

length [m]	strength [m^{-2}]	description
0.1		initial drift
0.2	45.9	1st focusing quad
0.05		drift
0.2	-28.1	2nd defocusing quad
0.1		drift
0.1	15.25	3st focusing quad
2.05		long drift
0.3	-10.0	4nd defocusing quad
0.1		drift
0.15	11.77	5st focusing quad
1.98		long drift

Table 14: Transport line for the electron bunch, shown in figure 44 and figure 43.

SETTINGS OF THE FREE-ELECTRON LASER COMPONENTS

length [cm]	strength	description
7	19.0 T/m	1st half focusing quad
7		drift
53	$a_u = 2.608$	1st undulator
7		drift
14	-13.0 T/m	defocusing quad
7		drift
53	$a_u = 2.608$	2nd undulator
7		drift
7	19.0 T/m	2nd half focusing quad

Table 15: Undulator and FODO lattice, see figure 42 for a visualization.

SETTINGS OF THE FREE-ELECTRON LASER

DRIVE BUNCH

a_u	2.608	undulator parameter
λ_u	1.0 cm	undulator period
λ_r	8.0 nm	resonance wavelength
γ	2211	Lorentz factor of the bunch
ϵ_x	1.48×10^{-7} m rad	bunch emittance
ϵ_y	23.9×10^{-7} m rad	bunch emittance
I_p	2203 A	peak current

FURTHER GENESIS-SPECIFIC PARAMETERS

SHOTNOISE	1.0	include shot noise for SASE mode
ITDP	1	time resolved simulation
DELZ	$1.0\lambda_u$	integration step
ZSEP	$4.0\lambda_r$	separation of the slices
NWIG	53	number of undulator periods per section
NSEC	27	number of undulator sections
NPART	2048	number of particles per slices
NSLICE	700	number of longitudinal slices

Table 16: GENESIS input parameters. The phase space distribution and the magnetic FODO lattice (see Table 15) is read from external files.

STATISTICAL MOMENTS OF A DISCRETE DISTRIBUTION

The statistical moments of a set of N values, $\{x_1, x_2, ... x_N\}$, are given by

- the n'th raw moment

$$\mu'_n = \langle x^n \rangle = \sum_i P(x_i) x_i^n \tag{183}$$

- and the n'th central moment

$$\mu_n = \langle (x - \langle x \rangle)^n \rangle = \sum_i P(x_i)(x_i - \langle x \rangle)^n, \tag{184}$$

where $P(x_i)$ is a normalized

$$\mu'_0 = \mu_0 = \langle 1 \rangle = \sum_i P(x_i) = 1, \tag{185}$$

discrete probability density function. The expectation value is given by the first raw moment

$$\mu'_1 = \langle x^1 \rangle = \sum_i P(x_i) x_i. \tag{186}$$

Note, the first central moment vanishes $\mu_1 = 0$. In case of macro particles with different weights, the probability function reads $P(x_i) = w_i / \sum_j w_j$ which fulfills the condition $\sum_i P(x_i) = 1$ and determines the *weighted mean* (or expectation) value

$$\langle x \rangle = \frac{1}{\sum_{j=1}^n w_j} \sum_{i=1}^n w_i x_i, \tag{187}$$

where w_i is the number of particles per macro particle. The second central moment is also known as variance

$$\sigma^2 \equiv \mu_2 = \langle (x - \langle x \rangle)^2 \rangle = \frac{1}{\sum_{j=1}^n w_j} \sum_i w_i (x_i - \langle x \rangle)^2, \tag{188}$$

and standard deviation σ. In addition, physical scientists often use the term root-mean-square (rms) as a synonym for the square root of the second central momentum $x_{rms} = \sqrt{\mu_2}$ [67], which is equal to the actual root-mean-square value, $\sqrt{\langle x^2 \rangle} \equiv \sqrt{\mu'_2}$, in case of a centered distribution $\langle x \rangle = 0$. Inserting 187 in 188, another form of the variance can be derived

$$\sigma^2 = \langle (x - \langle x \rangle)^2 \rangle$$
$$= \langle x^2 \rangle - \langle x \rangle^2$$
$$= \frac{1}{\sum_{j=1}^n w_j} \sum_i w_i x_i^2 - \left(\frac{1}{\sum_{j=1}^n w_j} \sum_i w_i x_i \right)^2, \tag{189}$$

which can be used to continuously calculate the variance of a not finished dataset, as no (changing) mean value is needed, hence equation (189) is referred to as *sample variance*. Computationally the variance brings the problem that the term under the square root in equation (188) can be negative due to arithmetic underflow and round-off errors. In addition, this is quite likely, as most x_i are very close to the mean value $\langle x \rangle$. Hence, the representation 189 was used to reckon the variance computationally.

Note, that this definition is a biased estimator for the standard deviation, a unbiased one is calculated by $\sqrt{\frac{n}{n-1}}\sigma$ (in case of $w_i = 1 \ \forall \ i$)

In more than one dimension, statistical moments can be generalized as

- the m,n...'th central moment

$$\mu_{m,n,...} \equiv \langle \, (x_1 - \langle \, x_1 \, \rangle)^m (x_2 - \langle \, x_2 \, \rangle)^n \ldots \, \rangle \tag{190}$$

- the m,n...'th raw moment

$$\mu'_{m,n,...} \equiv \langle \, x_1^m x_2^n \ldots \, \rangle . \tag{191}$$

Considering two dimensional problems (like the emittance $\epsilon \in (x, x')$), the 0th and 1st order raw moments read

$$\mu'_{0,0} = \mu_{0,0} = \sum_i \sum_j P(x_{1,i}, x_{2,j}) = 1 \quad \text{and} \tag{192}$$

$$\mu'_{1,0} = \langle \, x_1 \, \rangle = \sum_i \sum_j P(x_{1,i}, x_{2,j}) x_{1,i} \tag{193}$$

$$\mu'_{0,1} = \langle \, x_2 \, \rangle = \sum_i \sum_j P(x_{1,i}, x_{2,j}) x_{2,j} \tag{194}$$

In 2nd order, the central moments are

$$\begin{aligned}
\mu_{1,1} &= \langle \, (x_1 - \langle \, x_1 \, \rangle) \, \rangle \langle \, (x_2 - \langle \, x_2 \, \rangle) \, \rangle \\
&= \langle \, x_1 \, \rangle \langle \, x_2 \, \rangle - \langle \, x_1 x_2 \, \rangle \tag{195}
\end{aligned}$$

$$\mu_{2,0} = \langle \, (x_1 - \langle \, x_1 \, \rangle)^2 \, \rangle = \langle \, x_1^2 \, \rangle - \langle \, x_1 \, \rangle^2 \tag{196}$$

$$\mu_{0,2} = \langle \, (x_2 - \langle \, x_2 \, \rangle)^2 \, \rangle = \langle \, x_2^2 \, \rangle - \langle \, x_2 \, \rangle^2 \tag{197}$$

where also the mixed moment $\mu_{1,1}$ occurs. And for completeness, the raw moments read

$$\mu'_{1,1} = \langle \, x_1 x_2 \, \rangle \tag{198}$$

$$\mu'_{2,0} = \langle \, x_1^2 \, \rangle \tag{199}$$

$$\mu'_{0,2} = \langle \, x_2^2 \, \rangle \tag{200}$$

With this, it can be seen that the rms emittance is the mixed second-order central moment in two dimensions (x, x').

[1] M. Aicheler, P. Burrows, M. Draper, T. Garvey, P. Lebrun, K. Peach, N. Phinney, H. Schmickler, D. Schulte, and N. Toge. A Multi-TeV Linear Collider Based on CLIC Technology. *CERN-2012-007*, 2012.

[2] A. I. Akhiezer and R. V. Polovin. Theory of Wave Motion of an Electron Plasma . *Sov. Phys. JETP*, 3:696, 1956.

[3] Hannes Alfvén. On the motion of cosmic rays in interstellar space. *Phys. Rev.*, 55:425–429, Mar 1939.

[4] F. Amiranoff, S. Baton, D. Bernard, B. Cros, D. Descamps, F. Dorchies, F. Jacquet, V. Malka, J. R. Marquès, G. Matthieussent, P. Miné, A. Modena, P. Mora, J. Morillo, and Z. Najmudin. Observation of laser wakefield acceleration of electrons. *Phys. Rev. Lett.*, 81:995–998, Aug 1998.

[5] M. V. Ammosov, N. B. Delone, and V. P. Krainov. Tunnel ionization of complex atoms and atomic ions in electromagnetic field. pages 138–141, 1986.

[6] W. An, M. Zhou, N. Vafaei-Najafabadi, K. A. Marsh, C. E. Clayton, C. Joshi, W. B. Mori, W. Lu, E. Adli, S. Corde, M. Litos, S. Li, S. Gessner, J. Frederico, M. J. Hogan, D. Walz, J. England, J. P. Delahaye, and P. Muggli. Strategies for mitigating the ionization-induced beam head erosion problem in an electron-beam-driven plasma wakefield accelerator. *Phys. Rev. ST Accel. Beams*, 16:101301, Oct 2013.

[7] N. E. Andreev, L. M. Gorbunov, V. I. Kirsanov, K. Nakajima, and A. Ogata. Structure of the wake field in plasma channels. *Physics of Plasmas*, 4(4):1145–1153, 1997.

[8] N. E. Andreev, L. M. Gorbunov, P. Mora, and R. R. Ramazashvili. Filamentation of ultrashort laser pulses propagating in tenuous plasmas. *Physics of Plasmas*, 14(8), 2007.

[9] P. Antici, A. Bacci, C. Benedetti, E. Chiadroni, M. Ferrario, A. R. Rossi, L. Lancia, M. Migliorati, A. Mostacci, L. Palumbo, and L. Serafini. Laser-driven electron beamlines generated by coupling laser-plasma sources with conventional transport systems. *Journal of Applied Physics*, 112(4):–, 2012.

[10] T. M. Antonsen and P. Mora. Self-focusing and raman scattering of laser pulses in tenuous plasmas. *Phys. Rev. Lett.*, 69:2204–2207, Oct 1992.

[11] Alexey V. Arefiev, Ginevra E. Cochran, Douglass W. Schumacher, Alexander P. L. Robinson, and Guangye Chen. Temporal resolution criterion for correctly simulating relativistic electron motion in a high-intensity laser field. *Physics of Plasmas*, 22(1):013103, 2015.

[12] A. Aschikhin, C. Behrens, S. Bohlen, J. Dale, N. Delbos, L. di Lucchio, E. Elsen, J.-H. Erbe, M. Felber, B. Foster, L. Goldberg, J. Grebenyuk, J.-N. Gruse, B. Hidding, Zhanghu Hu, S. Karstensen, A. Knetsch, O. Kononenko, V. Libov, K. Ludwig, A.R. Maier, A. Martinez de la Ossa, T. Mehrling, C.A.J. Palmer, F. Pannek, L. Schaper, H. Schlarb, B. Schmidt, S. Schreiber, J.-P. Schwinkendorf, H. Steel, M. Streeter, G. Tauscher, V. Wacker, S. Weichert, S. Wunderlich, J. Zemella, and J. Osterhoff. The {FLASHForward} facility at {DESY}. *Nuclear Instruments and Methods in Physics Research Section A: Accelerators, Spectrometers, Detectors and Associated Equipment*, 806:175 – 183, 2016.

[13] S. Augst, D. D. Meyerhofer, D. Strickland, and S. L. Chin. Laser ionization of noble gases by coulomb-barrier suppression. *J. Opt. Soc. Am. B*, 8(4):858–867, Apr 1991.

[14] J. Bahrdt and Y. Ivanyushenkov. Short period undulators for storage rings and free electron lasers. *Journal of Physics: Conference Series*, 425(3):032001, 2013.

[15] K. L. F. Bane, P. B. Wilson, and T. Weiland. Wake fields and wake field acceleration. *AIP Conference Proceedings*, 127:875–928, 1985.

[16] N. Barov, J. B. Rosenzweig, M. C. Thompson, and R. B. Yoder. Energy loss of a high-charge bunched electron beam in plasma: Analysis. *Phys. Rev. ST Accel. Beams*, 7:061301, Jun 2004.

[17] T. Behnke, J. E. Brau, B. Foster, J. Fuster, M. Harrison, J. Paterson, M. Peskin, M. Stanitzki, N. Walker, and H. Yamamoto. The international linear collider technical design report 2013. Volume 1: Executive summary, The International Linear Collider, 2013.

[18] C. Benedetti, C. B. Schroeder, E. Esarey, and W. P. Leemans. Quasi-matched propagation of ultra-short, intense laser pulses in plasma channels. *Physics of Plasmas*, 19(5), 2012.

[19] V. I. Berezhiani and I. G. Murusidze. Relativistic wake-field generation by an intense laser pulse in a plasma. *Physics Letters A*, 148(6-7):338–340, 1990.

[20] C. K. Birdsall and A. B. Langdon. *Plasma Physics Via Computer Simulation*. Adam Hilger, 1991.

[21] I. Blumenfeld, C. E. Clayton, F.-J. Decker, M. J. Hogan, C. Huang, R. Ischebeck, R. Iverson, C. Joshi, T. Katsouleas, N. Kirby, W. Lu, K. A. Marsh, W. B. Mori,

P. Muggli, E. Oz, R. H. Siemann, D. Walz, and M. Zhou. Energy doubling of 42[thinsp]gev electrons in a metre-scale plasma wakefield accelerator. *Nature*, 445(7129):741–744, February 2007.

[22] I. Blumenfeld, C. E. Clayton, F. J. Decker, M. J. Hogan, C. Huang, R. Ischebeck, R. H. Iverson, C. Joshi, T. Katsouleas, N. Kirby, W. Lu, K. A. Marsh, W. B. Mori, P. Muggli, E. Oz, R. H. Siemann, D. R. Walz, and M. Zhou. Scaling of the longitudinal electric field and transformer ratio in a nonlinear plasma wakefield accelerator. *Phys. Rev. ST Accel. Beams*, 13:111301, Nov 2010.

[23] R. Bonifacio, C. Pellegrini, and L. M. Narducci. Collective instabilities and high-gain regime in a free electron laser. *Optics Communications*, 50:373–378, July 1984.

[24] J. P. Boris and R. A. Shanny. *Proc. 4th Conf. Num. Sim. Plasmas ed*, Naval Research Lab, Washington, DC:3–67, Feb 1970.

[25] Michael Borland. elegant: A flexible sdds-compliant code for accelerator simulation. *Advanced Photon Source*, pages LS–287, September 2000.

[26] T. Bornath and M. Schlanges. Ionization and recombination of excited atomic states in a dense nonideal hydrogen plasma. *Physica A: Statistical Mechanics and its Applications*, 196(3):427 – 440, 1993.

[27] N. Bourgeois, J. Cowley, and S. M. Hooker. Two-pulse ionization injection into quasilinear laser wakefields. *Phys. Rev. Lett.*, 111:155004, Oct 2013.

[28] Richard J. Briggs. Collective accelerator for electrons. *Phys. Rev. Lett.*, 54:2588–2591, Jun 1985.

[29] D. L. Bruhwiler, D. A. Dimitrov, J. R. Cary, E. Esarey, W. Leemans, and R. E. Giacone. Particle-in-cell simulations of tunneling ionization effects in plasma-based accelerators. *Physics of Plasmas (1994-present)*, 10(5):2022–2030, 2003.

[30] A. Buck, M. Nicolai, K. Schmid, C. M. S. Sears, A. Savert, J. M. Mikhailova, F. Krausz, M. C. Kaluza, and L. Veisz. Real-time observation of laser-driven electron acceleration. *Nat Phys*, 7(7):543–548, 2011.

[31] S. Bulanov, N. Naumova, F. Pegoraro, and J. Sakai. Particle injection into the wave acceleration phase due to nonlinear wake wave breaking. *Phys. Rev. E*, 58:R5257–R5260, Nov 1998.

[32] S. V. Bulanov, I. N. Inovenkov, V. I. Kirsanov, N. M. Naumova, and A. S. Sakharov. Nonlinear depletion of ultrashort and relativistically strong laser pulses in an underdense plasma. *Physics of Fluids B*, 4(7):1935–1942, 1992.

[33] S. V. Bulanov, V. I. Kirsanov, and A. S. Sakharov. Excitation of ultrarelativistic plasma waves by pulse of electromagnetic radiation. *JETP Lett*, 50(0):4–25, 1989.

[34] James D. Callen. *Fundamentals of Plasma Physics*. University of Wisconsin, Madison, 2006.

[35] N. Chauvin, O. DelferriÃšre, R. Duperrier, R. Gobin, P. A. P. Nghiem, and D. Uriot. Transport of intense ion beams and space charge compensation issues in low energy beam lines (invited). *Review of Scientific Instruments*, 83(2):02B320, 2012.

[36] M. Chen, E. Esarey, C. B. Schroeder, C. G. R. Geddes, and W. P. Leemans. Theory of ionization-induced trapping in laser-plasma accelerators. *Physics of Plasmas (1994-present)*, 19(3):–, 2012.

[37] M. Chen, Z.-M. Sheng, Y.-Y. Ma, and J. Zhang. Electron injection and trapping in a laser wakefield by field ionization to high-charge states of gases. *Journal of Applied Physics*, 99(5):056109, 2006.

[38] P. Chen, J. M. Dawson, R. W. Huff, and T. Katsouleas. Acceleration of electrons by the interaction of a bunched electron beam with a plasma. *Phys. Rev. Lett.*, 54:693–696, Feb 1985.

[39] P. Chen, J. J. Su, J. M. Dawson, K. L. F. Bane, and P. B. Wilson. Energy transfer in the plasma wake-field accelerator. *Phys. Rev. Lett.*, 56:1252–1255, Mar 1986.

[40] O. Chekhlov R. Clarke E. Divall K. Ertel B. Fell P. Foster S. Hancock A. Langley D. Neely J. Smith C.J. Hooker, J.L. Collier and B. Wyborn. The astra gemini project - a dual-beam petawatt ti:sapphire laser system. *J. Phys. IV France*, 133:673 – 677, June 2006.

[41] J. A. Clarke, D. Angal-Kalinin, N. Bliss, R. Buckley, S. Buckley, R. Cash, P. Corlett, L. Cowie, G. Cox, G. P. Diakun, D. J. Dunning, B. D. Fell, A. Gallagher, P. Goudket, A. R. Goulden, D. M. P. Holland, S. P. Jamison, J. K. Jones, A. S. Kalinin, W. Liggins, L. Ma, K. B. Marinov, B. Martlew, P. A. McIntosh, J. W. McKenzie, K. J. Middleman, B. L. Militsyn, A. J. Moss, B. D. Muratori, M. D. Roper, R. Santer, Y. Saveliev, E. Snedden, R. J. Smith, S. L. Smith, M. Surman, T. Thakker, N. R. Thompson, R. Valizadeh, A. E. Wheelhouse, P. H. Williams, R. Bartolini, I. Martin, R. Barlow, A. Kolano, G. Burt, S. Chattopadhyay, D. Newton, A. Wolski, R. B. Appleby, H. L. Owen, M. Serluca, G. Xia, S. Boogert, A. Lyapin, L. Campbell, B. W. J. McNeil, and V. V. Paramonov. Clara conceptual design report. *Journal of Instrumentation*, 9(05):T05001, 2014.

[42] James E. Clarke. *The Science and Technology of Undulators and Wigglers*. Oxford University Press, 2004.

[43] C. E. Clayton, J. E. Ralph, F. Albert, R. A. Fonseca, S. H. Glenzer, C. Joshi, W. Lu, K. A. Marsh, S. F. Martins, W. B. Mori, A. Pak, F. S. Tsung, B. B. Pollock, J. S. Ross,

L. O. Silva, and D. H. Froula. Self-guided laser wakefield acceleration beyond 1 gev using ionization-induced injection. *Phys. Rev. Lett.*, 105(10):105003, 2010.

[44] J. P. Couperus, R. Pausch, A. Köhler, O. Zarini, J.M. Krämer, M. Garten, A. Huebl, R. Gebhardt, U. Helbig, S. Bock, et al. Demonstration of a beam loaded nanocoulomb-class laser wakefield accelerator. *Nature Communications*, 8, 2017.

[45] M. E. Couprie, A. Loulergue, M. Labat, R. Lehe, and V. Malka. Towards a free electron laser based on laser plasma accelerators. *Journal of Physics B: Atomic, Molecular and Optical Physics*, 47(23):234001, 2014.

[46] R. Courant, K. Friedrichs, and H. Lewy. Über die partiellen differenzengleichungen der mathematischen physik. *Mathematische Annalen*, 100(1):32–74, Dec 1928.

[47] B. M. Cowan, D. L. Bruhwiler, J. R. Cary, E. Cormier-Michel, and C. G. R. Geddes. Generalized algorithm for control of numerical dispersion in explicit time-domain electromagnetic simulations. *Phys. Rev. ST Accel. Beams*, 16:041303, Apr 2013.

[48] B. M. Cowan, D. L. Bruhwiler, E. Cormier-Michel, E. Esarey, C. G. R. Geddes, P. Messmer, and K. M. Paul. Characteristics of an envelope model for laser-plasma accelerator simulation. *Journal of Computational Physics*, 230(1):61 – 86, 2011.

[49] John M. Dawson. Nonlinear electron oscillations in a cold plasma. *Phys. Rev.*, 113(2):383–387, January 1959.

[50] Alexander Debus. *Brilliant radiation sources by laser-plasma accelerators and optical undulators*. PhD thesis, Technische Universitaet Dresden, 2012.

[51] C. D. Decker and W. B. Mori. Group velocity of large amplitude electromagnetic waves in a plasma. *Phys. Rev. Lett.*, 72:490–493, Jan 1994.

[52] N. B. Delone and V. P. Krainov. Tunneling and barrier-suppression ionization of atoms and ions in a laser radiation field. *Physics-Uspekhi*, 41(5):469–485, 1998.

[53] A. Deng, O. Karger, A. Knetsch, Y. Xi, J. B. Rosenzweig, G. G. Manahan, and B. Hidding. E210 experiment. *in preperation*, 2016.

[54] Simone Di Mitri. On the importance of electron beam brightness in high gain free electron lasers. *Photonics*, 2(2):317, 2015.

[55] A. Down, W. Mori, and M. Zhou. Particle beam waist location in plasma wakefield acceleration. *Bulletin of the American Physical Society*, 52, 2007.

[56] B. J. Duda, R. G. Hemker, K. C. Tzeng, and W. B. Mori. A long-wavelength hosing instability in laser-plasma interactions. *Phys. Rev. Lett.*, 83:1978–1981, Sep 1999.

[57] C. G. Durfee and H. M. Milchberg. Light pipe for high intensity laser pulses. *Phys. Rev. Lett.*, 71:2409–2412, Oct 1993.

[58] Albert Einstein. Über einen die erzeugung und verwandlung des lichtes betreffenden heuristischen gesichtspunkt. *Annalen der Physik*, 322(6):132–148, 1905.

[59] P. Elleaume, J. Chavanne, and B. Faatz. Design considerations for a 1 angstrom sase undulator. *Nuclear Instruments and Methods in Physics Research Section A: Accelerators, Spectrometers, Detectors and Associated Equipment*, 455(3):503 – 523, 2000.

[60] E. Esarey, R. F. Hubbard, W. P. Leemans, A. Ting, and P. Sprangle. Electron injection into plasma wakefields by colliding laser pulses. *Phys. Rev. Lett.*, 79:2682–2685, Oct 1997.

[61] E. Esarey, C. B. Schroeder, and W. P. Leemans. Physics of laser-driven plasma-based electron accelerators. *Rev. Mod. Phys.*, 81(3):1229–1285, August 2009.

[62] E. Esarey, P. Sprangle, J. Krall, and A. Ting. Overview of plasma-based accelerator concepts. *Plasma Science, IEEE Transactions on*, 24(2):252–288, Apr 1996.

[63] T.Zh. Esirkepov. Exact charge conservation scheme for particle-in-cell simulation with an arbitrary form-factor. *Computer Physics Communications*, 135(2):144–153, April 2001.

[64] J. Faure, Y. Glinec, A. Pukhov, S. Kiselev, S. Gordienko, E. Lefebvre, J. P. Rousseau, F. Burgy, and V. Malka. A laser-plasma accelerator producing monoenergetic electron beams. *Nature*, 431(7008):541–544, 2004.

[65] J. Faure, C. Rechatin, O. Lundh, L. Ammoura, and V. Malka. Injection and acceleration of quasimonoenergetic relativistic electron beams using density gradients at the edges of a plasma channel. *Physics of Plasmas (1994-present)*, 17(8):–, 2010.

[66] J. Faure, C. Rechatin, A. Norlin, A. Lifschitz, Y. Glinec, and V. Malka. Controlled injection and acceleration of electrons in plasma wakefields by colliding laser pulses. *Nature*, 444(7120):737–739, December 2006.

[67] Klaus Floettmann. Some basic features of the beam emittance. *Phys. Rev. ST Accel. Beams*, 6:034202, Mar 2003.

[68] Klaus Floettmann. Adiabatic matching section for plasma accelerated beams. *Phys. Rev. ST Accel. Beams*, 17:054402, May 2014.

[69] D. H. Froula, C. E. Clayton, T. Döppner, K. A. Marsh, C. P. J. Barty, L. Divol, R. A. Fonseca, S. H. Glenzer, C. Joshi, W. Lu, S. F. Martins, P. Michel, W. B. Mori, J. P. Palastro, B. B. Pollock, A. Pak, J. E. Ralph, J. S. Ross, C. W. Siders, L. O. Silva, and T. Wang. Measurements of the critical power for self-injection of electrons in a laser wakefield accelerator. *Phys. Rev. Lett.*, 103:215006, Nov 2009.

[70] G. Fubiani, E. Esarey, C. B. Schroeder, and W. P. Leemans. Beat wave injection of electrons into plasma waves using two interfering laser pulses. *Phys. Rev. E*, 70:016402, Jul 2004.

[71] G. Fubiani, E. Esarey, C. B. Schroeder, and W. P. Leemans. Improvement of electron beam quality in optical injection schemes using negative plasma density gradients. *Phys. Rev. E*, 73:026402, Feb 2006.

[72] M. Fuchs, R. Weingartner, A. Popp, Z. Major, S. Becker, J. Osterhoff, I. Cortrie, B. Zeitler, R. Hörlein, G. D. Tsakiris, et al. Laser-driven soft-x-ray undulator source. *Nature physics*, 5(11):826–829, 2009.

[73] C. Gahn, G. D. Tsakiris, A. Pukhov, J. Meyer-ter Vehn, G. Pretzler, P. Thirolf, D. Habs, and K. J. Witte. Multi-mev electron beam generation by direct laser acceleration in high-density plasma channels. *Phys. Rev. Lett.*, 83:4772–4775, Dec 1999.

[74] C. G. R. Geddes, C. Toth, J. van Tilborg, E. Esarey, C. B. Schroeder, D. Bruhwilder, C. Nieter, J. Cary, and W. P. Leemans. High-quality electron beams from a laser wakefield accelerator using plasma-channel guiding. *Nature*, 431(7008):538–541, 2004.

[75] C. G. R. Geddes, Cs. Toth, J. van Tilborg, E. Esarey, C. B. Schroeder, D. Bruhwiler, C. Nieter, J. Cary, and W. P. Leemans. Production of high-quality electron bunches by dephasing and beam loading in channeled and unchanneled laser plasma accelerators. *Physics of Plasmas*, 12(5):056709, 2005.

[76] C. G. R. Geddes, Cs. Toth, J. van Tilborg, E. Esarey, C. B. Schroeder, J. Cary, and W. P. Leemans. Guiding of relativistic laser pulses by preformed plasma channels. *Phys. Rev. Lett.*, 95:145002, Sep 2005.

[77] P. Gibbon. *Physics of high-intensity laser-plasma interactions*. Societ'a Italiana di Fisica, 2012.

[78] Brendan B. Godfrey. Numerical cherenkov instabilities in electromagnetic particle codes. *Journal of Computational Physics*, 15(4):504–521, 1974.

[79] Brendan B. Godfrey and Jean-Luc Vay. Suppressing the numerical cherenkov instability in {FDTD} {PIC} codes. *Journal of Computational Physics*, 267:1 – 6, 2014.

[80] A. A. Golovanov, I. Yu. Kostyukov, J. Thomas, and A. Pukhov. Beam loading in the bubble regime in plasmas with hollow channels. *Physics of Plasmas*, 23(9):093114, 2016.

[81] A. J. Gonsalves, K. Nakamura, C. Lin, D. Panasenko, S. Shiraishi, T. Sokollik, C. Benedetti, C. B. Schroeder, C. G. R. Geddes, J. van Tilborg, J. Osterhoff,

E. Esarey, C. Toth, and W. P. Leemans. Tunable laser plasma accelerator based on longitudinal density tailoring. *Nat Phys*, advance online publication, 2011.

[82] A. J. Gonsalves, T. P. Rowlands-Rees, B. H. P. Broks, J. J. A. M. van der Mullen, and S. M. Hooker. Transverse interferometry of a hydrogen-filled capillary discharge waveguide. *Phys. Rev. Lett.*, 98:025002, Jan 2007.

[83] S. Gordienko and A. Pukhov. Scalings for ultrarelativistic laser plasmas and quasimonoenergetic electrons. *Physics of Plasmas*, 12(4):043109, 2005.

[84] J. Grebenyuk, A. Martinez de la Ossa, T. Mehrling, and J. Osterhoff. Beam-driven plasma-based acceleration of electrons with density down-ramp injection at flashforward. *Nuclear Instruments and Methods A*, 740:246–249, 2014.

[85] Julia Grebenyuk, Timon Mehrling, Frank S. Tsung, Klaus Floettman, and Jens Osterhoff. Simulations of laser-wakefield acceleration with external electron-bunch injection for regae experiments at desy. *AIP Conference Proceedings*, 1507(1):688–692, 2012.

[86] A. D. Greenwood, K. L. Cartwright, J. W. Luginsland, and E. A. Baca. On the elimination of numerical cerenkov radiation in {PIC} simulations. *Journal of Computational Physics*, 201(2):665 – 684, 2004.

[87] David J. Griffiths. *Introduction to Electrodynamics (3rd ed.)*. Prentice-Hall, 1998.

[88] Serge Haroche and Jean-Michel Raimond. *Exploring the quantum: atoms, cavities, and photons*. Oxford university press, 2006.

[89] Thomas Heinemann. High-quality radiation from inverse compton scattering using ultralow-emittance electron bunches. Master's thesis, University of Hamburg, Physics department library, 2015. Master thesis, AG Hybrid Plasma Wakefield Acceleration, Prof. B. Hidding.

[90] B. Hidding, M. Geissler, G. Pretzler, K.-U. Amthor, H. Schwoerer, S. Karsch, L. Veisz, K. Schmid, and R. Sauerbrey. Quasimonoenergetic electron acceleration in the self-modulated laser wakefield regime. *Physics of Plasmas*, 16(4):043105, 2009.

[91] B. Hidding, T. Königstein, J. Osterholz, S. Karsch, O. Willi, and G. Pretzler. Monoenergetic energy doubling in a hybrid laser-plasma wakefield accelerator. *Phys. Rev. Lett.*, 104(19):195002–, may 2010.

[92] B. Hidding, G. G. Manahan, O. Karger, A. Knetsch, G. Wittig, D. A. Jaroszynski, Z.-M. Sheng, Y. Xi, A. Deng, J. B. Rosenzweig, G. Andonian, A. Murokh, G. Pretzler, D. L. Bruhwiler, and J. Smith. Ultrahigh brightness bunches from hybrid plasma accelerators as drivers of 5th generation light sources. *Journal of Physics B: Atomic, Molecular and Optical Physics*, 47(23):234010, 2014.

[93] B. Hidding, G. Pretzler, J. B. Rosenzweig, T. Koenigstein, D. Schiller, and D. L. Bruhwiler. Ultracold electron bunch generation via plasma photocathode emission and acceleration in a beam-driven plasma blowout. *Phys. Rev. Lett.*, 108(3):035001–, January 2012.

[94] B. Hidding, J. B. Rosenzweig, Y. Xi, B. O'Shea, G. Andonian, D. Schiller, S. Barber, O. Williams, G. Pretzler, T. Königstein, F. Kleeschulte, M. J. Hogan, M. Litos, S. Corde, W. W. White, P. Muggli, D. L. Bruhwiler, and K. Lotov. Beyond injection: Trojan horse underdense photocathode plasma wakefield acceleration. *AIP Conference Proceedings*, 1507:570–575, 2012.

[95] R.W. Hockney and J. W. Eastwood. *Computer Simulation Using Particles*. Adam Hilger, 1988.

[96] M. J. Hogan, R. Assmann, F.-J. Decker, R. Iverson, P. Raimondi, S. Rokni, R. H. Siemann, D. Walz, D. Whittum, B. Blue, C. E. Clayton, E. Dodd, R. Hemker, C. Joshi, K. A. Marsh, W. B. Mori, S. Wang, T. Katsouleas, S. Lee, P. Muggli, P. Catravas, S. Chattopadhyay, E. Esarey, and W. P. Leemans. E-157: A 1.4-m-long plasma wake field acceleration experiment using a 30 gev electron beam from the stanford linear accelerator center linac. *Physics of Plasmas*, 7(5):2241–2248, 2000.

[97] M. J. Hogan, C. D. Barnes, C. E. Clayton, F. J. Decker, S. Deng, P. Emma, C. Huang, R. H. Iverson, D. K. Johnson, C. Joshi, T. Katsouleas, P. Krejcik, W. Lu, K. A. Marsh, W. B. Mori, P. Muggli, C. L. O'Connell, E. Oz, R. H. Siemann, and D. Walz. Multi-gev energy gain in a plasma-wakefield accelerator. *Phys. Rev. Lett.*, 95:054802, Jul 2005.

[98] M. J. Hogan, P. Emma, R. Iverson, C. O'Connell, P. Krejcik, R. Siemann, D. Walz, B. Blue, C. E. Clayton, C. Huang, et al. High gradient plasma-wakefield acceleration using ultrashort electron bunches. 2001.

[99] M. J. Hogan, T. O. Raubenheimer, A. Seryi, P. Muggli, T. Katsouleas, C. Huang, W. Lu, W. An, K. A. Marsh, W. B. Mori, C. E. Clayton, and C. Joshi. Plasma wakefield acceleration experiments at facet. *New Journal of Physics*, 12(5):055030, 2010.

[100] T. Hosokai, M. Kando, H. Dewa, H. Kotaki, S. Kondo, N. Hasegawa, K. Nakajima, and K. Horioka. Optical guidance of terrawatt laser pulses by the implosion phase of a fast z-pinch discharge in a gas-filled capillary. *Opt. Lett.*, 25(1):10–12, Jan 2000.

[101] Z. Huang and K.-J. Kim. Review of x-ray free-electron laser theory. *Phys. Rev. ST Accel. Beams*, 10:034801, Mar 2007.

[102] J. D. Huba. Nrl plasma formulary. Technical report, Naval Research Laboratory, 2016.

[103] A. Irman, M. J. H. Luttikhof, A. G. Khachatryan, F. A. van Goor, J. W. J. Verschuur, H. M. J. Bastiaens, and K.-J. Boller. Design and simulation of laser wakefield acceleration with external electron bunch injection in front of the laser pulse. *Journal of Applied Physics*, 102(2):024513, 2007.

[104] C. Joshi, B. Blue, C. E. Clayton, E. Dodd, C. Huang, K. A. Marsh, W. B. Mori, S. Wang, M. J. Hogan, C. OĆonnell, R. Siemann, D. Watz, P. Muggli, T. Katsouleas, and S. Lee. High energy density plasma science with an ultrarelativistic electron beam. *Physics of Plasmas*, 9(5):1845–1855, 2002.

[105] S. Y. Kalmykov, S. A. Yi, A. Beck, A. F. Lifschitz, X. Davoine, E. Lefebvre, A. Pukhov, V. Khudik, G. Shvets, S. A. Reed, P. Dong, X. Wang, D. Du, S. Bedacht, R. Zgadzaj, W. Henderson, A. Bernstein, G. Dyer, M. Martinez, E. Gaul, T. Ditmire, and M. C. Downer. Numerical modelling of a 10-cm-long multi-gev laser wakefield accelerator driven by a self-guided petawatt pulse. *New Journal of Physics*, 12(4):045019, 2010.

[106] S. Yu. Kalmykov, L. M. Gorbunov, P. Mora, and G. Shvets. Injection, trapping, and acceleration of electrons in a three-dimensional nonlinear laser wakefield. *Physics of Plasmas*, 13(11):113102, 2006.

[107] S. Karsch, J. Osterhoff, A. Popp, T. P. Rowlands-Rees, Z. Major, M. Fuchs, B. Marx, R. Hörlein, K. Schmid, L. Veisz, S. Becker, U. Schramm, B. Hidding, G. Pretzler, D. Habs, F. Grüner, F. Krausz, and S. M. Hooker. Gev-scale electron acceleration in a gas-filled capillary discharge waveguide. *New Journal of Physics*, 9(11):415, 2007.

[108] T. Katsouleas. Physical mechanisms in the plasma wake-field accelerator. *Phys. Rev. A*, 33:2056–2064, Mar 1986.

[109] T. Katsouleas, S. Wilks, P. Chen, J.M. Dawson, and J. J. Su. Beam loading in plasma accelerators. *Part. Accel.*, 22:81–99, 1987.

[110] Predhiman Kaw and John Dawson. Relativistic nonlinear propagation of laser beams in cold overdense plasmas. *The Physics of Fluids*, 13(2):472–481, 1970.

[111] R. Keinigs and M. E. Jones. Two-dimensional dynamics of the plasma wakefield accelerator. *Physics of Fluids*, 30(1):252–263, 1987.

[112] L. V. Keldysh. ionization in the field of a strong electromagnetic wave. *Sov. Phys. JETP*, 20:1307, 1965.

[113] E. A. Khazanov and A. M. Sergeev. Petawatt lasers based on optical parametric amplifiers: their state and prospects. *Physics-Uspekhi*, 51(9):969, 2008.

[114] W. D. Kilpatrick. Criterion for vacuum sparking designed to include both rf and dc. *Review of Scientific Instruments*, 28(10):824–826, 1957.

[115] H. T. Kim, K. H. Pae, H. J. Cha, I J. Kim, T. J. Yu, J. H. Sung, S. K. Lee, T. M. Jeong, and J. Lee. Enhancement of electron energy to the multi-gev regime by a dual-stage laser-wakefield accelerator pumped by petawatt laser pulses. *Phys. Rev. Lett.*, 111:165002, Oct 2013.

[116] Kwang-Je Kim. Brightness, coherence and propagation characteristics of synchrotron radiation. *Nuclear Instruments and Methods in Physics Research Section A: Accelerators, Spectrometers, Detectors and Associated Equipment*, 246(1):71 – 76, 1986.

[117] N. Kirby, I. Blumenfeld, C. E. Clayton, F. J. Decker, M. J. Hogan, C. Huang, R. Ischebeck, R. H. Iverson, C. Joshi, T. Katsouleas, W. Lu, K. A. Marsh, S. F. Martins, W. B. Mori, P. Muggli, E. Oz, R. H. Siemann, D. R. Walz, and M. Zhou. Transverse emittance and current of multi-gev trapped electrons in a plasma wakefield accelerator. *Phys. Rev. ST Accel. Beams*, 12(5):051302–, May 2009.

[118] S. Kneip, S. R. Nagel, S. F. Martins, S. P. D. Mangles, C. Bellei, O. Chekhlov, R. J. Clarke, N. Delerue, E. J. Divall, G. Doucas, K. Ertel, F. Fiuza, R. Fonseca, P. Foster, S. J. Hawkes, C. J. Hooker, K. Krushelnick, W. B. Mori, C. A. J. Palmer, K. Ta Phuoc, P. P. Rajeev, J. Schreiber, M. J. V. Streeter, D. Urner, J. Vieira, L. O. Silva, and Z. Najmudin. Near-gev acceleration of electrons by a nonlinear plasma wave driven by a self-guided laser pulse. *Phys. Rev. Lett.*, 103:035002, Jul 2009.

[119] A. Knetsch, O. Karger, G. Wittig, H. Groth, Y. Xi, A. Deng, J. B. Rosenzweig, D. L. Bruhwiler, J. Smith, D. A. Jaroszynski, Z.-M. Sheng, G. G. Manahan, G. Xia, S. Jamison, and B. Hidding. Downramp-assisted underdense photocathode electron bunch generation in plasma wakefield accelerators. *arXiv*, pages 1412.4844 [physics.acc–ph], 2014.

[120] I. Kostyukov, A. Pukhov, and S. Kiselev. Phenomenological theory of laser-plasma interaction in bubble regime. *Physics of Plasmas*, 11(11):5256–5264, 2004.

[121] J. Krall and G. Joyce. Transverse equilibrium and stability of the primary beam in the plasma wake-field accelerator. *Physics of Plasmas*, 2(4):1326–1331, 1995.

[122] J. Krall, A. Ting, E. Esarey, and P. Sprangle. Enhanced acceleration in a self-modulated-laser wake-field accelerator. *Phys. Rev. E*, 48:2157–2161, Sep 1993.

[123] Dietrich Kremp, Manfred Schlanges, and Wolf-Dietrich Kraeft. *Quantum Statistics of Nonideal Plasmas*, volume 1. Springer-Verlag Berlin Heidelberg, 2005.

[124] W. Kruer. *The physics of laser plasma interactions*, volume 73. Reading, MA, Addison-Wesley Publishing Co. (Frontiers in Physics.), 1988.

[125] S. Kuschel, D. Hollatz, T. Heinemann, O. Karger, M. B. Schwab, D. Ullmann, A. Knetsch, A. Seidel, C. Rödel, M. Yeung, M. Leier, A. Blinne, H. Ding, T. Kurz,

D. J. Corvan, A. Sävert, S. Karsch, M. C. Kaluza, B. Hidding, and M. Zepf. Demonstration of passive plasma lensing of a laser wakefield accelerated electron bunch. *Phys. Rev. Accel. Beams*, 19:071301, Jul 2016.

[126] T. Kwan, J. M. Dawson, and A. T. Lin. Free electron laser. *Physics of Fluids*, 20(4):581–588, 1977.

[127] Brookhaven National Laboratory. Upgrade and operate the accelerator test facility. *Technical report*, 2014.

[128] L. D. Landau and E. M. Lifshitz. *Statistical Physics. 3rd Edition Part 1*. Butterworth-Heinemann, 2000.

[129] S. Lee, T. Katsouleas, P. Muggli, W. B. Mori, C. Joshi, R. Hemker, E. S. Dodd, C. E. Clayton, K. A. Marsh, B. Blue, S. Wang, R. Assmann, F. J. Decker, M. Hogan, R. Iverson, and D. Walz. Energy doubler for a linear collider. *Phys. Rev. ST Accel. Beams*, 5:011001, Jan 2002.

[130] W. P. Leemans, P. Catravas, E. Esarey, C. G. R. Geddes, C. Toth, R. Trines, C. B. Schroeder, B. A. Shadwick, J. van Tilborg, and J. Faure. Electron-yield enhancement in a laser-wakefield accelerator driven by asymmetric laser pulses. *Phys. Rev. Lett.*, 89:174802, Oct 2002.

[131] W. P. Leemans, C. E. Clayton, W. B. Mori, K. A. Marsh, A. Dyson, and C. Joshi. Plasma physics aspects of tunnel-ionized gases. *Phys. Rev. Lett.*, 68:321–324, Jan 1992.

[132] W. P. Leemans, R. Duarte, E. Esarey, S. Fournier, C. G. R. Geddes, D. Lockhart, C. B. Schroeder, C. Toth, J.-L. Vay, and S. Zimmermann. The berkeley lab laser accelerator (bella): A 10 gev laser plasma accelerator. *AIP Conference Proceedings*, 1299(1):3–11, 2010.

[133] W. P. Leemans, A. J. Gonsalves, H.-S. Mao, K. Nakamura, C. Benedetti, C. B. Schroeder, Cs. Toth, J. Daniels, D. E. Mittelberger, S. S. Bulanov, J.-L. Vay, C. G. R. Geddes, and E. Esarey. Multi-gev electron beams from capillary-discharge-guided subpetawatt laser pulses in the self-trapping regime. *Phys. Rev. Lett.*, 113(24):245002–, December 2014.

[134] W. P. Leemans, B. Nagler, A. J. Gonsalves, Cs. Toth, K. Nakamura, C. G. R. Geddes, E. Esarey, C. B. Schroeder, and S. M. Hooker. Gev electron beams from a centimetre-scale accelerator. *Nat Phys*, 2(10):696–699, October 2006.

[135] R. Lehe, A. Lifschitz, C. Thaury, V. Malka, and X. Davoine. Numerical growth of emittance in simulations of laser-wakefield acceleration. *Phys. Rev. ST Accel. Beams*, 16(2):021301–, February 2013.

[136] T. Levato, M. Calvetti, F. Anelli, D. Batani, R. Benocci, L. Cacciotti, C.A. Cecchetti, O. Cerafogli, P. Chimenti, A. Clozza, N. Drenska, A. Esposito, R. Faccini, S. Fioravanti, A. Gamucci, C. Gatti, A. Giulietti, D. Giulietti, L. Labate, V. Lollo, S. Martellotti, M. Monteduro, E. Pace, N.C. Pathak, L. Pellegrino, F. Piastra, M. Pistoni, G. Di Pirro, R. Di Raddo, U. Rotundo, R. Ricci, M. Richetta, C. Vaccarezza, P. Valente, and L.A. Gizzi. First electrons from the new 220 {TW} frascati laser for acceleration and multidisciplinary experiments (flame) at frascati national laboratories (lnf). *Nuclear Instruments and Methods in Physics Research Section A*, 720:95 – 99, 2013. Selected papers from the 2nd International Conference Frontiers in Diagnostic Technologies (ICFDT2).

[137] F. Li, J. F. Hua, X. L. Xu, C. J. Zhang, L. X. Yan, Y. C. Du, W. H. Huang, H. B. Chen, C. X. Tang, W. Lu, C. Joshi, W. B. Mori, and Y. Q. Gu. Generating high-brightness electron beams via ionization injection by transverse colliding lasers in a plasma-wakefield accelerator. *Phys. Rev. Lett.*, 111:015003, Jul 2013.

[138] C. A. Lindstrøm and E. Adli. Design of general apochromatic drift-quadrupole beam lines. *Phys. Rev. Accel. Beams*, 19:071002, Jul 2016.

[139] M. Litos, E. Adli, W. An, C. I. Clarke, C. E. Clayton, S. Corde, J. P. Delahaye, R. J. England, A. S. Fisher, J. Frederico, S. Gessner, S. Z. Green, M. J. Hogan, C. Joshi, W. Lu, K. A. Marsh, W. B. Mori, P. Muggli, N. Vafaei-Najafabadi, D. Walz, G. White, Z. Wu, V. Yakimenko, and G. Yocky. High-efficiency acceleration of an electron beam in a plasma wakefield accelerator. *Nature*, 515(7525):92–95, November 2014.

[140] J. S. Liu, C. Q. Xia, W. T. Wang, H. Y. Lu, Ch. Wang, A. H. Deng, W. T. Li, H. Zhang, X. Y. Liang, Y. X. Leng, X. M. Lu, C. Wang, J. Z. Wang, K. Nakajima, R. X. Li, and Z. Z. Xu. All-optical cascaded laser wakefield accelerator using ionization-induced injection. *Phys. Rev. Lett.*, 107:035001, Jul 2011.

[141] N. C. Lopes, G. Figueira, L. O. Silva, J. M. Dias, R. Fonseca, L. Cardoso, C. Russo, C. Carias, G. Mendes, J. Vieira, and J. T. Mendonça. Plasma channels produced by a laser-triggered high-voltage discharge. *Phys. Rev. E*, 68:035402, Sep 2003.

[142] K. V. Lotov. Fine wakefield structure in the blowout regime of plasma wakefield accelerators. *Phys. Rev. ST Accel. Beams*, 6:061301, Jun 2003.

[143] K. V. Lotov. Efficient operating mode of the plasma wakefield accelerator. *Physics of Plasmas*, 12(5), 2005.

[144] W. Lu, C. Huang, M. Zhou, W. B. Mori, and T. Katsouleas. Nonlinear theory for relativistic plasma wakefields in the blowout regime. *Phys. Rev. Lett.*, 96(16):165002–, April 2006.

[145] W. Lu, C. Huang, M. M. Zhou, W. B. Mori, and T. Katsouleas. Limits of linear plasma wakefield theory for electron or positron beams. *Physics of Plasmas*, 12(6), 2005.

[146] W. Lu, M. Tzoufras, C. Joshi, F. S. Tsung, W. B. Mori, J. Vieira, R. A. Fonseca, and L. O. Silva. Generating multi-gev electron bunches using single stage laser wakefield acceleration in a 3d nonlinear regime. *Phys. Rev. ST Accel. Beams*, 10:061301, Jun 2007.

[147] A. R. Maier, A. Meseck, S. Reiche, C. B. Schroeder, T. Seggebrock, and F. Grüner. Demonstration scheme for a laser-plasma-driven free-electron laser. *Phys. Rev. X*, 2:031019, Sep 2012.

[148] V. Malka, S. Fritzler, E. Lefebvre, M.-M. Aleonard, F. Burgy, J.-P. Chambaret, J.-F. Chemin, K. Krushelnick, G. Malka, S. P. D. Mangles, Z. Najmudin, M. Pittman, J.-P. Rousseau, J.-N. Scheurer, B. Walton, and A. E. Dangor. Electron acceleration by a wake field forced by an intense ultrashort laser pulse. *Science*, 298(5598):1596–1600, 2002.

[149] V. Malka, S. Fritzler, E. Lefebvre, M.-M. Aleonard, F. Burgy, J.-P. Chambaret, J.-F. Chemin, K. Krushelnick, G. Malka, S. P. D. Mangles, Z. Najmudin, M. Pittman, J.-P. Rousseau, J.-N. Scheurer, B. Walton, and A. E. Dangor. Electron acceleration by a wake field forced by an intense ultrashort laser pulse. *Science*, 298(5598):1596–1600, 2002.

[150] G. G. Manahan, A. Deng, O. Karger, Y. Xi, A. Knetsch, M. Litos, G. Wittig, T. Heinemann, J. Smith, Z. M. Sheng, D. A. Jaroszynski, G. Andonian, D. L. Bruhwiler, J. B. Rosenzweig, and B. Hidding. Hot spots and dark current in advanced plasma wakefield accelerators. *Phys. Rev. Accel. Beams*, 19:011303, Jan 2016.

[151] G. G. Manahan, A. F. Habib, P. Scherkl, P. Delinikolas, A. Beaton, A. Knetsch, O. Karger, G. Wittig, T. Heinemann, Z. M. Sheng, J. R. Cary, D. L. Bruhwiler, J. B. Rosenzweig, and B. Hidding. Single-stage plasma-based correlated energy spread compensation for ultrahigh 6d brightness electron beams. *Nature Communications*, 8:15705, Jun 2017.

[152] Grace G. Manahan. *Studies of transverse properties of relativistic electrons from laser wakefield accelerator*. PhD thesis, University of Strathclyde, 2013.

[153] S. P. D. Mangles, C. D. Murphy, Z. Najmudin, A. G. R. Thomas, J. L. Collier, A. E. Dangor, E. J. Divall, P. S. Foster, J. G. Gallacher, C. J. Hooker, D. A. Jaroszynski, A. J. Langley, W. B. Mori, P. A. Norreys, F. S. Tsung, R. Viskup, B. R. Walton, and K. Krushelnick. Monoenergetic beams of relativistic electrons from intense laser-plasma interactions. *Nature*, 431(7008):535–538, 2004.

[154] A. Martinez, J. Grebenyuk, T. Mehrling, L. Schaper, and J. Osterhoff. High-quality electron beams from beam-driven plasma accelerators by wakefield-induced ionization injection. *Phys. Rev. Lett.*, 111(24):245003–, December 2013.

[155] A. Martinez de la Ossa, Z. Hu, M. J. V. Streeter, T. J. Mehrling, O. Kononenko, B. Sheeran, and J. Osterhoff. Optimizing density down-ramp injection for beam-driven plasma wakefield accelerators. *Phys. Rev. Accel. Beams*, 20:091301, Sep 2017.

[156] S. F. Martins, R. A. Fonseca, W. Lu, W. B. Mori, and L. O. Silva. Exploring laser-wakefield-accelerator regimes for near-term lasers using particle-in-cell simulation in lorentz-boosted frames. *Nat Phys*, 6(4):311–316, April 2010.

[157] C. McGuffey, T. Matsuoka, S. Kneip, W. Schumaker, F. Dollar, C. Zulick, V. Chvykov, G. Kalintchenko, V. Yanovsky, A. Maksimchuk, A. G. R. Thomas, K. Krushelnick, and Z. Najmudin. Experimental laser wakefield acceleration scalings exceeding 100 tw. *Physics of Plasmas*, 19(6), 2012.

[158] B. W. J. McNeil. desxie - an matlab code for solving the free electron laser design formulae of m. xie. 2004.

[159] B. W. J. McNeil and N. R. Thompson. X-ray free-electron lasers. *Nature Photonics*, 4(12):814–821, 11 2010.

[160] T. Mehrling, J. Grebenyuk, F. S. Tsung, K. Floettmann, and J. Osterhoff. Transverse emittance growth in staged laser-wakefield acceleration. *Phys. Rev. ST Accel. Beams*, 15(11):111303–, November 2012.

[161] J. Meyer-ter Vehn, A. Pukhov, and Zh.-M. Sheng. *Atoms, Solids, and Plasmas in Super-Intense Laser Fields*, chapter Relativistic Laser Plasma Interaction, pages 167–192. Springer US, Boston, MA, 2001.

[162] M. Migliorati, A. Bacci, C. Benedetti, E. Chiadroni, M. Ferrario, A. Mostacci, L. Palumbo, A. R. Rossi, L. Serafini, and P. Antici. Intrinsic normalized emittance growth in laser-driven electron accelerators. *Phys. Rev. ST Accel. Beams*, 16(1):011302–, January 2013.

[163] A. Modena, Z. Najmudin, A. Dangor, C. Clayton, K. A. Marsh, C. Joshi, V. Malka, C. Darrow, C. Danson, D. Neely, and F. Walsh. Electron acceleration from the breaking of relativistic plasma waves. *Nature*, 377(6550):606–608, 1995.

[164] Patrick Mora and Thomas M. Antonsen, Jr. Kinetic modeling of intense, short laser pulses propagating in tenuous plasmas. *Physics of Plasmas (1994-present)*, 4(1):217–229, 1997.

[165] W. B. Mori. The physics of the nonlinear optics of plasmas at relativistic intensities for short-pulse lasers. *IEEE Journal of Quantum Electronics*, 33(11):1942–1953, Nov 1997.

[166] P. Muggli, S. Lee, T. Katsouleas, R. Assmann, F. J. Decker, M. J. Hogan, R. Iverson, P. Raimondi, R. H. Siemann, D. Walz, B. Blue, C. E. Clayton, E. Dodd, R. A. Fonseca, R. Hemker, C. Joshi, K. A. Marsh, W. B. Mori, and S. Wang. Collective refraction of a beam of electrons at a plasma-gas interface</title>. *Phys. Rev. ST Accel. Beams*, 4(9):091301–, September 2001.

[167] P. Muggli, K.A. Marsh, S. Wang, C.E. Clayton, S. Lee, T.C. Katsouleas, and C. Joshi. Photo-ionized lithium source for plasma accelerator applications. *Plasma Science, IEEE Transactions on*, 27(3):791–799, Jun 1999.

[168] K. Nakajima, D. Fisher, T. Kawakubo, H. Nakanishi, A. Ogata, Y. Kato, Y. Kitagawa, R. Kodama, K. Mima, H. Shiraga, K. Suzuki, K. Yamakawa, T. Zhang, Y. Sakawa, T. Shoji, Y. Nishida, N. Yugami, M. Downer, and T. Tajima. Observation of ultrahigh gradient electron acceleration by a self-modulated intense short laser pulse. *Phys. Rev. Lett.*, 74:4428–4431, May 1995.

[169] Chet Nieter and John R. Cary. Vorpal: a versatile plasma simulation code. *Journal of Computational Physics*, 196(2):448–473, 2004.

[170] F. H. O'Shea, G. Marcus, J. B. Rosenzweig, M. Scheer, J. Bahrdt, R. Weingartner, A. Gaupp, and F. Grüner. Short period, high field cryogenic undulator for extreme performance x-ray free electron lasers. *Phys. Rev. ST Accel. Beams*, 13:070702, Jul 2010.

[171] J. Osterhoff, A. Popp, Zs. Major, B. Marx, T. P. Rowlands-Rees, M. Fuchs, M. Geissler, R. Hörlein, B. Hidding, S. Becker, E. A. Peralta, U. Schramm, F. Grüner, D. Habs, F. Krausz, S. M. Hooker, and S. Karsch. Generation of stable, low-divergence electron beams by laser-wakefield acceleration in a steady-state-flow gas cell. *Phys. Rev. Lett.*, 101:085002, Aug 2008.

[172] Jens Osterhoff. *Stable, ultra-relativistic electron beams by laser-wakefield acceleration*. PhD thesis, Ludwig-Maximilians-University Munich, 2009.

[173] E. Oz, S. Deng, T. Katsouleas, P. Muggli, C. D. Barnes, I. Blumenfeld, F. J. Decker, P. Emma, M. J. Hogan, R. Ischebeck, R. H. Iverson, N. Kirby, P. Krejcik, C. O'Connell, R. H. Siemann, D. Walz, D. Auerbach, C. E. Clayton, C. Huang, D. K. Johnson, C. Joshi, W. Lu, K. A. Marsh, W. B. Mori, and M. Zhou. Ionization-induced electron trapping in ultrarelativistic plasma wakes. *Phys. Rev. Lett.*, 98(8):084801, 2007.

[174] K. H. Pae, I. W. Choi, and J. Lee. Self-mode-transition from laser wakefield accelerator to plasma wakefield accelerator of laser-driven plasma-based electron acceleration. *Physics of Plasmas*, 17(12):123104, 2010.

[175] A. Pak, K. A. Marsh, S. F. Martins, W. Lu, W. B. Mori, and C. Joshi. Injection and trapping of tunnel-ionized electrons into laser-produced wakes. *Phys. Rev. Lett.*, 104:025003, Jan 2010.

[176] W. K. H. Panofsky and W. R. Baker. A focusing device for the external 350-mev proton beam of the 184-inch cyclotron at berkeley. *Review of Scientific Instruments*, 21(5):445–447, 1950.

[177] W. K. H. Panofsky and W. A. Wenzel. Some considerations concerning the transverse deflection of charged particles in radio-frequency fields. *Review of Scientific Instruments*, 27(11):967–967, 1956.

[178] A. M. Perelomov, V. S. Popov, and Terentev M. V. ionization in the field of a strong electromagnetic wave. *Sov. Phys. JETP*, 23:924, 1966.

[179] Max Planck. über das gesetz der energieverteilung im normalspectrum. *Annalen der Physik*, 309(3):553–563, 1901.

[180] I. V. Pogorelsky, M. Babzien, I. Ben-Zvi, M. N. Polyanskiy, J. Skaritka, O. Tresca, N. P. Dover, Z. Najmudin, W. Lu, N. Cook, A. Ting, and Y.-H. Chen. Extending laser plasma accelerators into the mid-ir spectral domain with a next-generation ultra-fast co 2 laser. *Plasma Physics and Controlled Fusion*, 58(3):034003, 2016.

[181] I. V. Pogorelsky and I. Ben-Zvi. Brookhaven national laboratory's accelerator test facility: research highlights and plans. *Plasma Physics and Controlled Fusion*, 56(8):084017, 2014.

[182] B. B. Pollock, C. E. Clayton, J. E. Ralph, F. Albert, A. Davidson, L. Divol, C. Filip, S. H. Glenzer, K. Herpoldt, W. Lu, K. A. Marsh, J. Meinecke, W. B. Mori, A. Pak, T. C. Rensink, J. S. Ross, J. Shaw, G. R. Tynan, C. Joshi, and D. H. Froula. Demonstration of a narrow energy spread, ~ 0.5 GeV electron beam from a two-stage laser wakefield accelerator. *Phys. Rev. Lett.*, 107:045001, Jul 2011.

[183] A. Pukhov, O. Jansen, T. Tueckmantel, J. Thomas, and I. Yu. Kostyukov. Field-reversed bubble in deep plasma channels for high-quality electron acceleration. *Phys. Rev. Lett.*, 113:245003, Dec 2014.

[184] A. Pukhov and J. Meyer-ter Vehn. Relativistic magnetic self-channeling of light in near-critical plasma: Three-dimensional particle-in-cell simulation. *Phys. Rev. Lett.*, 76:3975–3978, May 1996.

[185] A. Pukhov and J. Meyer-ter Vehn. Laser wake field acceleration: the highly non-linear broken-wave regime. *Applied Physics B*, 74(4-5):355–361–, 2002.

[186] Sven Reiche. Genesis 1.3: a fully 3d time-dependent fel simulation code. *Nuclear Instruments and Methods in Physics Research Section A: Accelerators, Spectrometers, Detectors and Associated Equipment*, 429(1):243 – 248, 1999.

[187] Martin Reiser. Periodic focusing of intense beams. *Part. Accel.*, 8:167–182, 1978.

[188] Martin Reiser. *Theory and Design of Charged Particle Beams*. Wiley-VCH Verlag GmbH & Co. KGaA, 2008.

[189] W. Rittershofer, C. B. Schroeder, E. Esarey, F. J. Gruener, and W. P. Leemans. Tapered plasma channels to phase-lock accelerating and focusing forces in laser-plasma accelerators. *Physics of Plasmas*, 17(6), 2010.

[190] J. B. Rosenzweig, D. Alesini, G. Andonian, M. Boscolo, M. Dunning, L. Faillace, M. Ferrario, A. Fukusawa, L. Giannessi, E. Hemsing, G. Marcus, A. Marinelli, P. Musumeci, B. O'Shea, L. Palumbo, C. Pellegrini, V. Petrillo, S. Reiche, C. Ronsivalle, B. Spataro, and C. Vaccarezza. Generation of ultra-short, high brightness electron beams for single-spike sase fel operation. *Nuclear Instruments and Methods in Physics Research Section A: Accelerators, Spectrometers, Detectors and Associated Equipment*, 593(1):39 – 44, 2008. FEL Fronties 2007.

[191] J. B. Rosenzweig, G. Andonian, P. Bucksbaum, M. Ferrario, S. Full, A. Fukusawa, E. Hemsing, B. Hidding, M. Hogan, P. Krejcik, P. Muggli, G. Marcus, A. Marinelli, P. Musumeci, B. O'Shea, C. Pellegrini, D. Schiller, and G. Travish. Teravolt-permeter beam and plasma fields from low-charge femtosecond electron beams. *Nuclear Instruments and Methods in Physics Research Section A: Accelerators, Spectrometers, Detectors and Associated Equipment*, 653(1):98 – 102, 2011. Superstrong 2010.

[192] J. B. Rosenzweig, N. Barov, M. C. Thompson, and R. B. Yoder. Energy loss of a high charge bunched electron beam in plasma: Simulations, scaling, and accelerating wakefields. *Phys. Rev. ST Accel. Beams*, 7:061302, Jun 2004.

[193] J. B. Rosenzweig, B. Breizman, T. Katsouleas, and J. J. Su. Acceleration and focusing of electrons in two-dimensional nonlinear plasma wake fields. *Phys. Rev. A*, 44(10):R6189–R6192, November 1991.

[194] J. B. Rosenzweig, D. B. Cline, B. Cole, H. Figueroa, W. Gai, R. Konecny, J. Norem, P. Schoessow, and J. Simpson. Experimental observation of plasma wake-field acceleration. *Phys. Rev. Lett.*, 61:98–101, Jul 1988.

[195] James B. Rosenzweig. *Fundamentals of beam physics*. Oxford University Press, 2003.

[196] A. R. Rossi, A. Bacci, M. Belleveglia, E. Chiadroni, A. Cianchi, G. Di Pirro, M. Ferrario, A. Gallo, G. Gatti, C. Maroli, A. Mostacci, V. Petrillo, L. Serafini, P. Tomassini, and C. Vaccarezza. The external-injection experiment at the

sparc_lab facility. *Nuclear Instruments and Methods in Physics Research Section A: Accelerators, Spectrometers, Detectors and Associated Equipment*, 740(Supplement C):60 – 66, 2014. Proceedings of the first European Advanced Accelerator Concepts Workshop 2013.

[197] Ronald D Ruth, PL Morton, Perry B Wilson, and AW Chao. A plasma wake field accelerator. *Part. Accel.*, 17(SLAC-PUB-3374):171, 1984.

[198] H. P. Schlenvoigt, K. Haupt, A. Debus, F. Budde, O. Jäckel, S. Pfotenhauer, H. Schwoerer, E. Rohwer, J. G. Gallacher, E. Brunetti, et al. A compact synchrotron radiation source driven by a laser-plasma wakefield accelerator. *Nature Physics*, 4(2):130, 2008.

[199] K. Schmid, A. Buck, C. M. S. Sears, J. M. Mikhailova, R. Tautz, D. Herrmann, M. Geissler, F. Krausz, and L. Veisz. Density-transition based electron injector for laser driven wakefield accelerators. *Phys. Rev. ST Accel. Beams*, 13(9):091301, Sep 2010.

[200] Peter Schmüser, Martin Dohlus, Jörg Rossbach, and Christopher Behrens. *Free-Electron Lasers in the Ultraviolet and X-Ray Regime*. Societ'a Italiana di Fisica, 2012.

[201] C. B. Schroeder, C. Benedetti, S. S. Bulanov, M. Chen, E. Esarey, C. G. R. Geddes, J.-L. Vay, L.-L. Yu, and W. P. Leemans. Ultra-low emittance beam generation using two-color ionization injection in laser-plasma accelerators. *Proc. SPIE*, 9514:951408–951408–7, 2015.

[202] C. B. Schroeder, C. Benedetti, E. Esarey, and W. P. Leemans. Beam loading in a laser-plasma accelerator using a near-hollow plasma channel. *Physics of Plasmas*, 20(12), 2013.

[203] C. B. Schroeder, E. Esarey, C. G. R. Geddes, C. Benedetti, and W. P. Leemans. Physics considerations for laser-plasma linear colliders. *Phys. Rev. ST Accel. Beams*, 13:101301, Oct 2010.

[204] C. B. Schroeder, C. Pellegrini, S. Reiche, J. Arthur, and P. Emma. Chirped-beam two-stage free-electron laser for high-power femtosecond x-ray pulse generation. *J. Opt. Soc. Am. B*, 19(8):1782–1789, Aug 2002.

[205] M. Sciscio, L. Lancia, M. Migliorati, A. Mostacci, L. Palumbo, Y. Papaphilippou, and P. Antici. Parametric study of transport beam lines for electron beams accelerated by laser-plasma interaction. *Journal of Applied Physics*, 119(9), 2016.

[206] B. A. Shadwick, C. B. Schroeder, and E. Esarey. Nonlinear laser energy depletion in laser-plasma acceleratorsa). *Physics of Plasmas*, 16(5), 2009.

[207] D. J. Spence and S. M. Hooker. Investigation of a hydrogen plasma waveguide. *Phys. Rev. E*, 63:015401, Dec 2000.

[208] P. Sprangle, E. Esarey, J. Krall, and G. Joyce. Propagation and guiding of intense laser pulses in plasmas. *Phys. Rev. Lett.*, 69:2200–2203, Oct 1992.

[209] P. Sprangle, E. Esarey, and A. Ting. Nonlinear theory of intense laser-plasma interactions. *Phys. Rev. Lett.*, 64(17):2011–2014, April 1990.

[210] P. Sprangle, E. Esarey, A. Ting, and G. Joyce. Laser wakefield acceleration and relativistic optical guiding. *Applied Physics Letters*, 53(22):2146–2148, 1988.

[211] Phillip Sprangle, Jonathan Krall, and Eric Esarey. Hose-modulation instability of laser pulses in plasmas. *Phys. Rev. Lett.*, 73:3544–3547, Dec 1994.

[212] Jr. Stanley Humphries. *Charged Particle Beams*. 2002.

[213] S. Steinke, J. Van Tilborg, C. Benedetti, C. G. R. Geddes, C. B. Schroeder, J. Daniels, K. K. Swanson, A. J. Gonsalves, K. Nakamura, N. H. Matlis, et al. Multistage coupling of independent laser-plasma accelerators. *Nature*, 530(7589):190–193, 2016.

[214] Donna Strickland and Gerard Mourou. Compression of amplified chirped optical pulses. *Optics Communications*, 56(3):219 – 221, 1985.

[215] H. Suk, N. Barov, J. B. Rosenzweig, and E. Esarey. Plasma electron trapping and acceleration in a plasma wake field using a density transition. *Phys. Rev. Lett.*, 86(6):1011–1014, February 2001.

[216] G.-Z. Sun, E. Ott, Y. C. Lee, and P. Guzdar. Self-focusing of short intense pulses in plasmas. *Physics of Fluids*, 30(2):526–532, 1987.

[217] Jae Hee Sung, Seong Ku Lee, Tae Jun Yu, Tae Moon Jeong, and Jongmin Lee. 0.1 hz 1.0 pw ti: sapphire laser. *Optics letters*, 35(18):3021–3023, 2010.

[218] Orazio Svelto and David C. Hanna. *Principles of lasers, Fifth Edition*. Springer, 2009.

[219] T. Tajima and J. M. Dawson. Laser electron accelerator. *Phys. Rev. Lett.*, 43(4):267–270, July 1979.

[220] J. Thomas, I. Y. Kostyukov, J. Pronold, A. Golovanov, and A. Pukhov. Non-linear theory of a cavitated plasma wake in a plasma channel for special applications and control. *Physics of Plasmas*, 23(5):053108, 2016.

[221] A. Ting, C. I. Moore, K. Krushelnick, C. Manka, E. Esarey, P. Sprangle, R. Hubbard, H. R. Burris, R. Fischer, and M. Baine. Plasma wakefield generation and electron acceleration in a self-modulated laser wakefield accelerator experiment. *Physics of Plasmas*, 4(5):1889–1899, 1997.

[222] R. M. G. M. Trines and P. A. Norreys. Wave-breaking limits for relativistic electrostatic waves in a one-dimensional warm plasma. *Physics of Plasmas*, 13(12), 2006.

[223] F. S. Tsung, Ritesh Narang, W. B. Mori, C. Joshi, R. A. Fonseca, and L. O. Silva. Near-gev-energy laser-wakefield acceleration of self-injected electrons in a centimeter-scale plasma channel. *Phys. Rev. Lett.*, 93:185002, Oct 2004.

[224] M. Tzoufras, W. Lu, F. S. Tsung, C. Huang, W. B. Mori, T. Katsouleas, J. Vieira, R. A. Fonseca, and L. O. Silva. Beam loading in the nonlinear regime of plasma-based acceleration. *Phys. Rev. Lett.*, 101:145002, Sep 2008.

[225] M. Tzoufras, W. Lu, F. S. Tsung, C. Huang, W. B. Mori, T. Katsouleas, J. Vieira, R. A. Fonseca, and L. O. Silva. Beam loading by electrons in nonlinear plasma wakes. *Physics of Plasmas*, 16(5):056705, 2009.

[226] D. Umstadter, S.-Y. Chen, A. Maksimchuk, G. Mourou, and R. Wagner. Nonlinear optics in relativistic plasmas and laser wake field acceleration of electrons. *Science*, 273(5274):472–475, 1996.

[227] D. Umstadter, J. K. Kim, and E. Dodd. Laser injection of ultrashort electron pulses into wakefield plasma waves. *Phys. Rev. Lett.*, 76:2073–2076, Mar 1996.

[228] J. van Tilborg, S. Steinke, C. G. R. Geddes, N. H. Matlis, B. H. Shaw, A. J. Gonsalves, J. V. Huijts, K. Nakamura, J. Daniels, C. B. Schroeder, C. Benedetti, E. Esarey, S. S. Bulanov, N. A. Bobrova, P. V. Sasorov, and W. P. Leemans. Active plasma lensing for relativistic laser-plasma-accelerated electron beams. *Phys. Rev. Lett.*, 115:184802, Oct 2015.

[229] J.-L. Vay. Noninvariance of space- and time-scale ranges under a lorentz transformation and the implications for the study of relativistic interactions. *Phys. Rev. Lett.*, 98:130405, Mar 2007.

[230] J.-L. Vay, C. G. R. Geddes, E. Esarey, C. B. Schroeder, W. P. Leemans, E. Cormier-Michel, and D. P. Grote. Modeling of 10 gev-1 tev laser-plasma accelerators using lorentz boosted simulations. *Physics of Plasmas*, 18(12), 2011.

[231] J. Vieira, R. A. Fonseca, and L. O. Silva. Multidimensional plasma wake excitation in the non-linear blowout regime. *CERN Yellow Reports*, 1(0):79, 2016.

[232] P. A. Walker, P. D. Alesini, A. S. Alexandrova, et al. Horizon 2020 eupraxia design study. *Journal of Physics: Conference Series*, 874(1):012029, 2017.

[233] X. Wang, R. Zgadzaj, N. Fazel, Z. Li, S. A. Yi, X. Zhang, W. Henderson, Y.-Y. Chang, R. Korzekwa, H.-E. Tsai, C.-H. Pai, H. Quevedo, G. Dyer, E. Gaul, M. Martinez, A. C. Bernstein, T. Borger, M. Spinks, M. Donovan, V. Khudik, G. Shvets,

T. Ditmire, and M. C. Downer. Quasi-monoenergetic laser-plasma acceleration of electrons to 2 gev. *Nat Commun*, 4, June 2013.

[234] P. Weinberger. John kerr and his effects found in 1877 and 1878. *Philosophical Magazine Letters*, 88(12):897–907, 2008.

[235] R. Weingartner, M. Fuchs, A. Popp, S. Raith, S. Becker, S. Chou, M. Heigoldt, K. Khrennikov, J. Wenz, T. Seggebrock, B. Zeitler, Z. Major, J. Osterhoff, F. Krausz, S. Karsch, and F. Grüner. Imaging laser-wakefield-accelerated electrons using miniature magnetic quadrupole lenses. *Phys. Rev. ST Accel. Beams*, 14:052801, May 2011.

[236] R. Weingartner, S. Raith, A. Popp, S. Chou, J. Wenz, K. Khrennikov, M. Heigoldt, A. R. Maier, N. Kajumba, M. Fuchs, B. Zeitler, F. Krausz, S. Karsch, and F. Grüner. Ultralow emittance electron beams from a laser-wakefield accelerator. *Phys. Rev. ST Accel. Beams*, 15:111302, Nov 2012.

[237] D. H. Whittum, W. M. Sharp, S. S. Yu, M. Lampe, and G. Joyce. Electron-hose instability in the ion-focused regime. *Phys. Rev. Lett.*, 67:991–994, Aug 1991.

[238] Helmut Wiedemann. *Particle Accelerator Physics*. Springer-Verlag Berlin Heidelberg, 2007.

[239] Klaus Wille. *The Physics of Particle Accelerators*. Oxford University Press, 2000.

[240] G. Wittig, O. Karger, A. Knetsch, Y. Xi, A. Deng, J. B. Rosenzweig, D. L. Bruhwiler, J. Smith, G. G. Manahan, Z.-M. Sheng, D. A. Jaroszynski, and B. Hidding. Optical plasma torch electron bunch generation in plasma wakefield accelerators. *Phys. Rev. ST Accel. Beams*, 18:081304, Aug 2015.

[241] G. Wittig, O. S. Karger, A. Knetsch, Y. Xi, A. Deng, J. B. Rosenzweig, D. L. Bruhwiler, J. Smith, Z.-. Sheng, D. A. Jaroszynski, G. G. Manahan, and B. Hidding. Electron beam manipulation, injection and acceleration in plasma wakefield accelerators by optically generated plasma density spikes. *Nuclear Instruments and Methods in Physics Research Section A: Accelerators, Spectrometers, Detectors and Associated Equipment*, 829:83 – 87, 2016. 2nd European Advanced Accelerator Concepts Workshop - {EAAC} 2015.

[242] Y. Xi, B. Hidding, D. Bruhwiler, G. Pretzler, and J. B. Rosenzweig. Hybrid modeling of relativistic underdense plasma photocathode injectors. *Phys. Rev. ST Accel. Beams*, 16(3):031303–, March 2013.

[243] Ming Xie. Design optimization for an x-ray free electron laser driven by slac linac. *Proc. 1995 Part. Accel. Conf*, pages 183–185, 1996.

[244] X. L. Xu et al. Phase-space dynamics of ionization injection in plasma-based accelerators. *Phys. Rev. Lett.*, 112:035003, Jan 2014.

[245] X. L. Xu, F. Li, W. An, P. Yu, W. Lu, C. Joshi, and W. B. Mori. High quality electron bunch generation using a longitudinal density-tailored plasma-based accelerator in the three-dimensional blowout regime. *arXiv preprint arXiv:1610.00788*, 2016.

[246] V. Yakimenko, Y. Cai, C. Clarke, S. Green, C. Hast, M. Hogan, N. Lipkowitz, N. Phinney, G. White, and G. Yocky. Facet-ii accelerator research with beams of extreme intensities. pages 1067–1070, 2016.

[247] Kane Yee. Numerical solution of initial boundary value problems involving maxwell's equations in isotropic media. *Antennas and Propagation, IEEE Transactions on*, 14(3):302–307, May 1966.

[248] L.-L. Yu, E. Esarey, C. B. Schroeder, J.-L. Vay, C. Benedetti, C. G. R. Geddes, M. Chen, and W. P. Leemans. Two-color laser-ionization injection. *Phys. Rev. Lett.*, 112:125001, Mar 2014.

[249] P. Yu, X. Xu, V. K. Decyk, F. Fiuza, J. Vieira, F. S. Tsung, R. A. Fonseca, W. Lu, L. O. Silva, and W. B. Mori. Elimination of the numerical cerenkov instability for spectral em-pic codes. *Computer Physics Communications*, 192:32 – 47, 2015.

[250] G. L. Yudin and M. Y. Ivanov. Nonadiabatic tunnel ionization: Looking inside a laser cycle. *Phys. Rev. A*, 64:013409, Jun 2001.

[251] D. Zhou, Y. Chen, J. Tang, and N. Wang. Explicit Maps for the Fringe Field of a Quadrupole. *Conf. Proc.*, C100523:THPD091, 2010.

[252] M. Zhou, C. E. Clayton, C. Huang, C. Joshi, W. Lu, K. A. Marsh, W. B. Mori, T. Katsouleas, P. Muggli, E. Oz, et al. Beam head erosion in self-ionized plasma wakefield accelerators. pages 3064–3066, 2007.

ACKNOWLEDGMENTS

DECLARATION

Eidesstattliche Versicherung

Hiermit erkläre ich an Eides statt, dass ich die vorliegende Dissertationsschrift selbst verfasst und keine anderen als die angegebenen Quellen und Hilfsmittel benutzt habe.

Hamburg, October 2017

_____

Georg Wittig